UNIVERSITÀ DI PARMA

UNIVERSITÀ DEGLI STUDI DI PARMA

DOTTORATO DI RICERCA IN
INGEGNERIA INDUSTRIALE

CICLO XXXIV

Design and Development of Robot for Aseptic Environments

Coordinatore:
Chiar.mo Prof. Gianni Royer Carfagni

Tutore:
Chiar.mo Prof. Alessandro Tasora

Dottorando: Dario Fusai

Anni Accademici 2018/2019 - 2020/2021

Abstract

The world of aseptic industry – mainly constituted by pharmaceutical, food & beverage, and microelectronics process plants – is experiencing unprecedented development due to the pervasive integration of Industry 4.0 paradigms. In this context, the progressive transition to automated manufacturing is characterized by a dual aim: increase of output yield and achievement of superior product sterility. This rapid evolution is currently played in a delicate equilibrium scenario, characterized by the interaction of human and machinery activity. While the former is being progressively discouraged – as one of main sources of contamination –, the expansion of automation is still restrained by the presence of stringent regulations and challenging sterilization treatments.

Robotics is only beginning to tackle with this emerging application field. To date, available commercial solutions are derivated from general-purpose counterparts through a certain extent of modifications; thus, respective offer of well-established mechanical features generally overwhelms more critical hygienic requirements. The motivation of this work is hence rooted on the development of a custom robot architecture that is completely devoted to aseptic industry needs; the devised solution is intended to reside in sterile workplaces, withstand the harsh sterilization cycles of surrounding environment and prevent inflow leakage from pressurized liquid jets. To this purpose, the thesis first explores the vast world of aseptic manufacturing and provides a comprehensive overview of related requirements, best-practice design processes, legislative regulations, decontamination treatments, and state-of-art commercial robotics offer. The core of the work consists in a step-by-step presentation of the aseptic robot development. Starting from the comparative analysis of a number of potential concepts and the kinematic modeling of 6-DOF articulated manipulators, the work addresses the following issues: design of highly-integrated modular drives, selection of appropriate arm geometries and materials, integration of electronics, development of dedicated aseptic junction and sealing solutions, realization of a lightweight multitask end-effector. Finally, the work is complemented by the realization of a custom real-time multibody simulator, which serves as a virtual test bench for proposed mechanical design, and the documented manufacturing of a drive preliminary prototype.

Contents

Nomenclature

$\mathsf{SO}(3)$	Special Orthogonal group, $\mathsf{SO}(3) = \left\{\mathbf{R} \in \mathbb{R}^{3\text{x}3} : \mathbf{R}\mathbf{R}^T = \mathbf{I},\ \ \det(\mathbf{R}) = +1\right\}$
S^3	3-sphere, $\mathsf{S}^3 = \{(x, y, z, t) \in \mathbb{R}^4 : x^2 + y^2 + z^2 + t^2 = 1\}$
n, **s**, **a**	End-effector Normal, Sliding, Approach unit vectors
AGV	Autonomous Guided Vehicle
API	Application Programming Interface
CAD	Computer-Aided Design
CIP	Cleaning-In-Place
COG	Center Of Gravity
DOF	Degree Of Freedom
EHDG	European Hygienic Engineering and Design Group
FDA	Food and Drug Administration
FEM	Finite Element Method
FK	Forward Kinematics
GUI	Graphical User Interface
IDE	Integrated Development Environment
IK	Inverse Kinematics
IP	Ingress Protection (grade)
ISO	International Organization for Standardization
PID	Proportional-Integral-Derivative (controller)
RMS	Root Means Square

SCARA	Selective Compliance Assembly Robot Arm
SIP	Sterilization-In-Place
SLERP	Spherical Linear intERPolation
SQUAD	Spherical QUADrangle interpolation
TCP	Tool Center Point

Preface

The present thesis is the result of a joint collaboration between University of Parma and Sidel.

Sidel [108] is a manufacturing company that provides complete equipment solutions for packaging beverage, food and personal care products using PET, can, glass and other materials. Starting from 2003, the company has joined DeLaval and Tetra Pak to form the Tetra Laval Group, a leading multinational corporation which is significantly active in the field of food & beverage processing and packaging.

Sidel portfolio includes the manufacturing of wide set of automated machinery:

- PET bottles blow-moulding machine;
- liquid product fillers;
- bottle and crate labellers;
- material handling equipment;
- pasteurisers;
- bottle and crate washers;
- end-of-line traditional and robotized palletizers;

Fig. 1 illustrates a typical production line.

The range of treated liquid products is quite vast, and involves the use of standard to aseptic and ultra-clean filling technologies. The offer includes: water, carbonated and non-carbonated soft drinks; sensitive beverages such as milk and juices; liquid dairy products, tea, coffee and edible oils. A summary of the exposed products – organized in different product lines with respect to specific beverage requirements – is reported in Fig. 2.

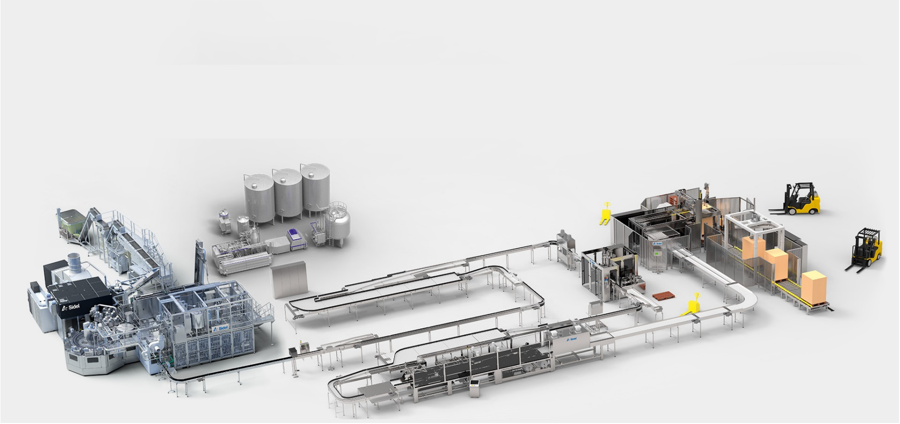

Figure 1: Example of complete Sidel production line [108].

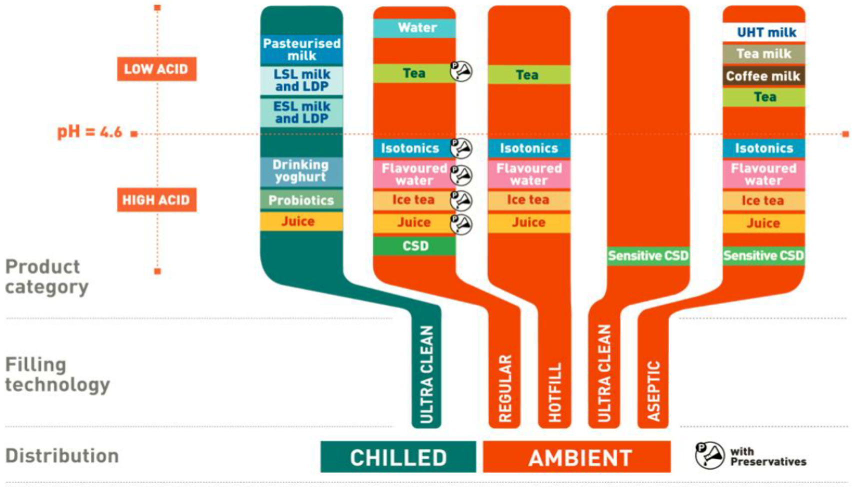

Figure 2: Sidel main product lines in function of beverage requirements [108].

Chapter 1

Aseptic Industry

Many modern industrial fields share the need of a clean environment for proficient manufacturing. While it's true that the non-conformity of a product always constitutes a waste of resources for the manufacturer, some particular cases stand out for the necessity of cleanliness: pharmaceutical, food & beverage, microelectronics, optics and biotechnology facilities are only some of the many existing examples. Industry whose product directly involve people health, such as pharmaceutical and food industry, can not afford to verify the quality of manufacturing by statistical check of batches at the end of production. In fact, the concrete difficulty of tracing and retire a potentially flawed product in the strict time span between commercialization and expiration date immediately shows the paramount necessity of distributing safe environments along all the manufacturing workflow. But also microelectronics industry is gaining more and more interest in clean production. Semiconductors production has been characterized by the continuous strive for material purity and miniaturization: in this context, the tiniest bit of dust can irreparably damage the photoengraving of an entire chip. Aseptic industry was developed to solve these kind of problems. It is based on three main pillars: cleanliness of production environment air, hygienic design of machinery, periodic active decontamination of objects surface. To better understand the drivelines that guide aseptic equipment manufacturing, the key concepts of this vast environment are briefly examined.

1.1 Cleanrooms

A *cleanroom* is a protected environment, built in such a way as to limit the introduction, the generation and the retention of both inanimate and bacterial-carrying airborne particles [53]. To achieve this target, a cleanroom usually imposes a continuous recirculation of clean air, injected through high-quality filters. The room is kept at higher pressure with respect to the surrounding environment to prevent the

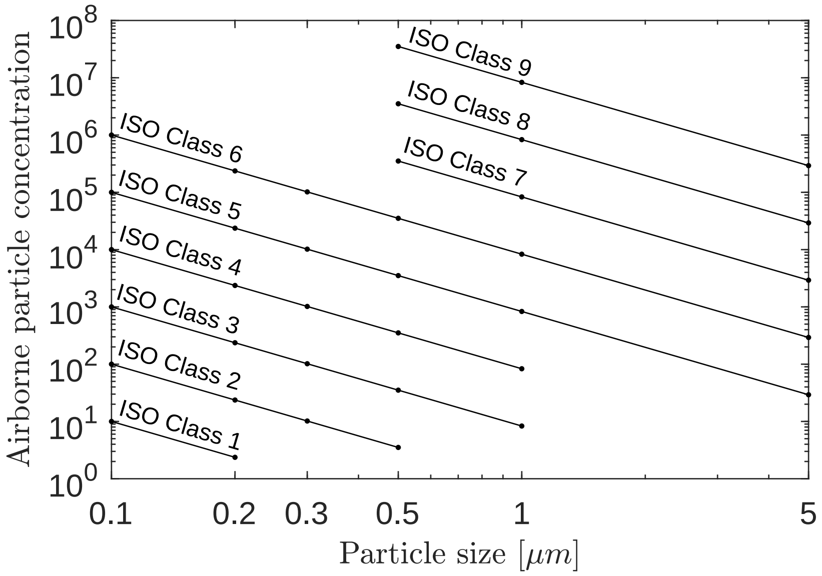

Figure 3: Representation of airborne particulate cleanliness classes according to ISO 14644-1 [53].

entrance of potential contaminants from the outside. Particular care is given to internal surfaces: all the materials must not be prone to particulate generation, must have a high degree of surface finish and must be resistant to the decontaminating agents.

The first formal classification of clean environments was proposed in 1963, with the publication of US Federal Standard 209: its rationale was to classify cleanrooms by the number of 0.5 µm airborne particles present per ft^3 of air. The standard has been updated many times, up to its last metric version 209E, in 1992 [35]. The International Organization for Standardization (ISO) subsequently proposed a similar classification, which replaced national regulations. The new ISO 14644-1 standard classifies cleanrooms on a scale from 1 to 9 (see Fig. 3) by relating airborne particle dimension with their maximum allowed concentration, as in the following equation:

$$C_n = 10^N \left(\frac{0.1}{D}\right)^{2.08} \tag{1.1}$$

where C_n (“classification number”) is the maximum allowed number of airborne particles per m^3 that are equal to or larger than a considered size; N is the ISO classification number of the cleanroom; D is the considered particle size, expressed in µm; 0.1 is a dimensional constant, expressed in µm. Table 1.1 shows a partial comparison between old FED 209E and new ISO classification, with respect to $\geq$0.5 µm particles.

Two main sources of internal contamination are to be minimized: human and

Table 1.1: Comparison between ISO 14644-1 and Federal Standard 209E classification of cleanrooms with respect to concentration of particles equal of larger than 0.5 µm. Potential industrial application fields are also reported [75] [116].

C_n	ISO class	FED class	Potential industrial application
-	ISO 1	-	-
-	ISO 2	-	-
35	ISO 3	Class 1	Integrated circuit manufacturers, submicron scales
352	ISO 4	Class 10	Semiconductor manufacturing plants
3520	ISO 5	Class 100	Bacteria and particulate-free surgical cleanrooms
35 200	ISO 6	Class 1000	High-precision mechanical equipment (e.g. optics, miniaturized bearings, gyroscopes)
352 000	ISO 7	Class 10 000	High-end gearing, general electronics and medical device manufacturing
3 520 000	ISO 8	Class 100 000	Hydraulic and pneumatic equipment assembly
35 200 000	ISO 9	-	-

machinery activities. Machinery-driven particulate generation is highly dependent on design and it usually is quite difficult to be estimated in advance; a broad approximation spans in the range of 100 to 10^6 particles $\geq 0.5\,\mu m$ generated per minute [116]. Human activity has a big impact on overall cleanliness as well: the more people in the environment and the heavier the task is, the poorer quality of the room is. Operations involving simple movements such as knee bending may produce about 8 times more emission than standing still ones [89]. Much of the existing information about human particulate generation are based on study conducted in 1965 by Austin and Timmerman [6], that is still used at present days as general guideline. In that work and later elaborations [87] is shown that the average number of particles $\geq 0.3\,\mu m$ generated per minute by a single person wearing a simple smock, is approximately:

- sitting, standing still: 100 000 particles/min
- intense head, leg, arm, foot movements: 1 000 000 particles/min
- walking at 0.9 m/s: 5 000 000 particles/min
- walking at 2.2 m/s: 10 000 000 particles/min

Other sources [116] estimate that poorly protected people moving in a cleanroom generate on average $2 \cdot 10^6$ particles $\geq 0.5\,\mu m$ per minute, about 300 000 particles

$\geq$ 5 µm per minute and 160 bacteria-carrying particles per minute. However, if the same operators are wearing high-quality protective clothing (such as gauntlets, hoods, coats, boots, goggles), the emission of $\geq$ 0.5 µm particles can be reduced by 50%, the emission of $\geq$ 5 µm particles by 88% and bacteria-carrying particles by 92% [116].

More challenging clean operations require a proper room ventilation system. Ventilation is used to dilute the airborne particulate concentration present in the room and is useful to prevent cross-contamination from other areas of the building as well. In this regard, it is usually adopted a positive 5-20 Pa pressure with respect to adjacent environments [115] [65] [114] to protect critical areas. Ventilation system should also maintain relative humidity below 55% to reduce microorganisms growth [46].

A continuous stream of clean air must be injected through an efficiently-filtered source and subsequently extracted by a dedicated sink at ground. Such industrial end-level air filters are usually composed of several intercepting sheets made of randomly-disposed micro-fibers (such as borosilicate), assembled in several layers and separated by aluminum septa. The international standard ISO 29463-1 [54] classifies these industrial filters in three main categories, with respect to their efficiency against particulate of given dimension (e.g. $\geq$0.3 µm). EPA (Efficient Particulate Air) filters remove from 85% up to 99.9% of airborne particulate; HEPA (High Efficiency Particulate Air) filters remove from 99.95% up to 99.999% of airborne particulate; ULPA (Ultra-Low Penetration Air) filters remove more than 99.9995% of airborne particulate. It is worth mentioning that when properly implemented with photocatalytic oxidation (PCO) processes, HEPA and ULPA filters can be successfully used to neutralize many contaminant bacteria (e.g. Aspergillus Niger, Penicillium Citrinum, Staphylococcus Epidermidis, Bacillus Subtilis) [15].

Ventilation systems may be divided in three main types [116]:

1. *Conventional*: clean air is injected by a single filtered diffuser on the ceiling;
2. *Unidirectional flow*: clean air is injected by many high-efficiency filtered diffusers and flows through the environment in a unidirectional way;
3. *Isolator*: two separate sub-environments are present in the same room, one inside the other. The inner area, completely sealed, forms a protected micro-environment around a critical machinery part, to ensure the highest level of protection against contamination.

The conventionally ventilated cleanroom (see Fig. 4a), having a centralized diffuser on the ceiling, is structurally similar to a common working or office room. However, the main difference is that this type of cleanroom usually has 20-60 complete changes of environment air per hour, while a general-purpose room typically has 2-10. Therefore, the particulate is diluted to acceptable concentration. Conventional ventilation cleanrooms typically reach ISO 7 or ISO 6 class [116].

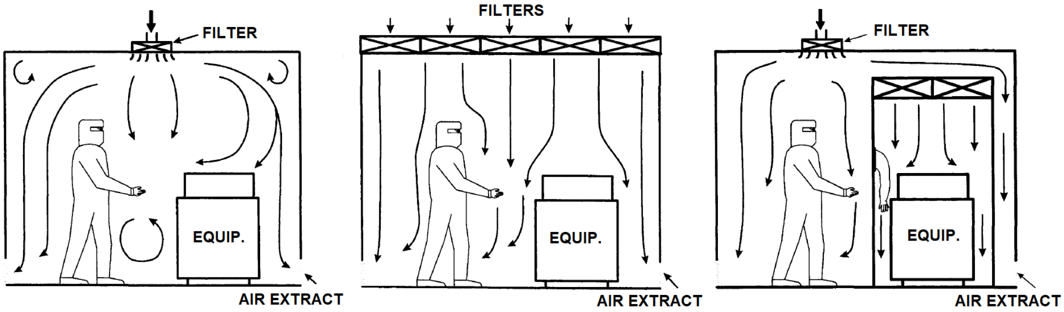

(a) (b) (c)

Figure 4: Main types of cleanroom ventilation: (a) conventional, (b) unidirectional flow, (c) isolator. Adapted from [116].

The unidirectional flow ventilation system greatly increases the overall cleanliness of the room by imposing a quasi-laminar flow in the vertical downward direction. The underlying idea of this system is to remove airborne particles before they can settle onto the internal surfaces rather than impose a generic particle dilution. Air stream velocity is kept as uniform as possible and room air change rate is 10-100 times higher than conventional ventilation system [116]. The theoretical cleanliness level achieved is directly proportional with the imposed air velocity. However, it is worth noting that too high velocity values may be counterproductive as well: in real scenarios, in-room obstruction made by machinery and operators can provoke eddies upon impact with surfaces, resulting in turbulence insurgence and particulate back-flow. Therefore, air velocity is is typically kept in the range between 0.3 and 0.5 m/s [46].

Finally, the isolator system represents the high-end of cleanroom technology. It is used when dangerous or critical tasks have to be performed and a physical barrier is needed to protect operators or products by contamination. Thus, isolators may have two opposite application: to internally confine dangerous particles for operators health or keep contaminant particles outside of a product. An isolator is physically separated from the surrounding environment by interlocked doors and products enter the area through sterilized tunnels. Operators manipulate inner objects from the outside, interacting by the means of fixed and sealed gauntlets, as well as half-suits, for better movement. Cleanliness inside an isolator is assured by the superposition of multiple effects: physical barriers, injection of sterile unidirectional air flow through highly-efficient filtering units (ULPA) and pressurizing system to prevent potential ingress of contaminants from the outside.

1.2 Hygienic design

The second critical requirement of aseptic industry is to design machinery that are compliant with hygienic regulations. As a matter of fact, general-purpose machinery always have to comply with international safety directives (such as EU Machinery Directive [31]). However, for sensitive products there is a further layer of regulations that aims at protecting products and final consumers rather than operators. Most notably, ISO 14159 standard specifies criteria for hygienic safety of machinery and all related requirements [52]. Also, the European Hygienic Engineering & Design Group (EHEDG) consortium provides design guidelines for food industry equipment manufacturers (see for example [18]).

The main rules of hygienic design principally involve equipment surface, shape and material and can be summarized in the following principles:

- all machine parts must be easily accessible and cleanable;
- fluid products must always be in motion;
- dead zones or tight crevices should be avoided;
- external surfaces should be as smooth as possible.

In the following, more detailed guidelines of each category are summarized.

1.2.1 Shapes

The main requirement for hygienic equipment shape is to avoid dead areas and undercuts, i.e. all the spaces wherein a product may be trapped, retained or not completely removed during operation of cleaning [18]. For this reason, all surfaces should be smoothly filleted, without gaps, recesses or crevices (see Fig. 5).

To avoid stagnation of liquid products and accumulation of dust, it is important that every machine area is self-drainable thanks to proper shape; every tank must have a dedicated sink and internal corners should have large-radius fillets. Horizontal external surfaces should be avoided for the same reason: it is always advisable to prefer sloped surfaces, as shown in Fig. 6. Moreover, drains should be designed so to convey soils from sensitive areas to less critical ones; in no case back flow must be allowed. All sharp edges should be chamfered and deburred. In particular, internal corners must be filleted with sufficiently large radii, so to be easily cleanable; appropriate fillet radius for tanks and vessels range from 3 to 6 mm [46].

Ideally, there should be no openings in an hygienically-designed environment. However, it is apparent that the need to manipulate and process products inside such environments impose the design of hygienic doors and windows as well. Both of them have to be properly sealed and the opening mechanism should be considered

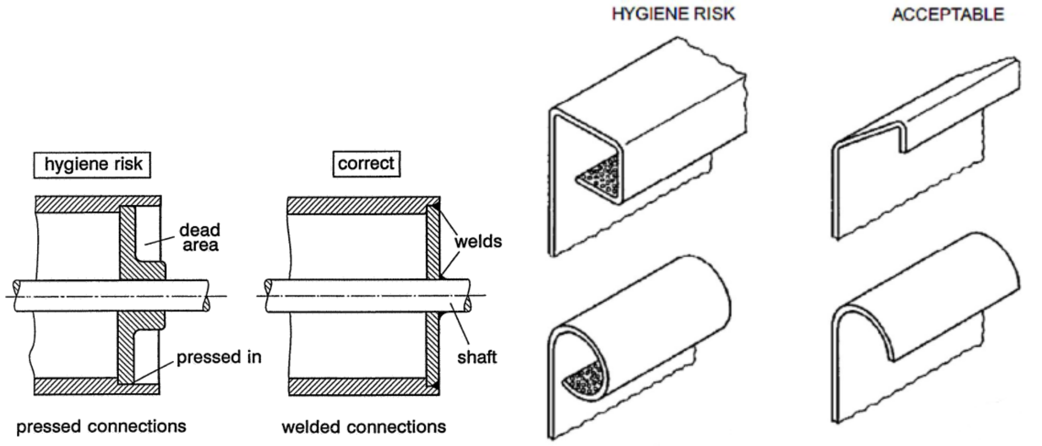

(a) (b)

Figure 5: Hygienic risk due to dead areas. In (a), a pressed connection forming a recess is substituted by an aligned welded joint. In (b) hygienic risks due to horizontal surfaces and undercuts are corrected with properly sloped shapes. Adapted from [18].

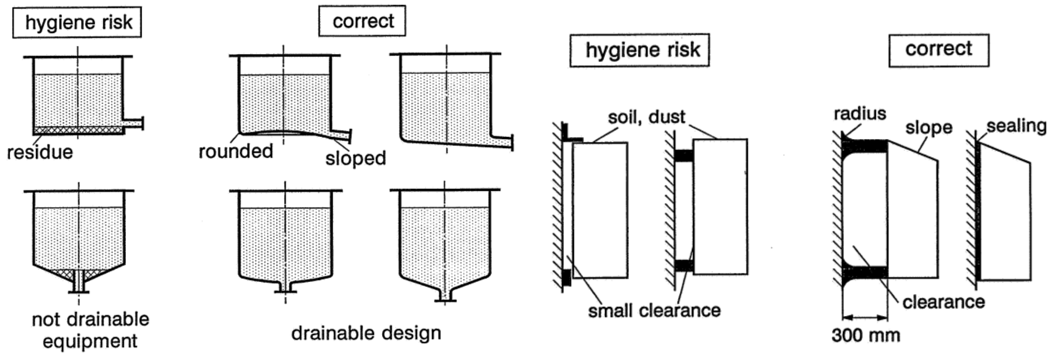

(a) (b)

Figure 6: a) Hygienic design of areas subject to liquids: residues are prevented by dedicated drains at the bottom, rounded corners and sloped floor. (b) Sloped ceilings of equipment and proper clearance from wall prevent dust accumulation and ease cleanability. Adapted from [18].

with great care. For example, externally hinged doors are typically implemented instead of roller-lifting doors, that are prone to bacterial accumulation and are almost impossible to clean. If a door is equipped with windows, they should always be double-glazed in order to prevent condensation [46].

All lubricated components should not be exposed towards the product; when this is not technically possible, there must be a proper sealing to prevent potential leakages. Great care should also be given to electrical cabling. Exposed wires must be avoided because they are almost impossible to clean and they usually do not withstand aggressive chemical decontaminating agents: therefore, cabling should be routed outside production area.

1.2.2 Surfaces and materials

Surfaces must be cleanable, durable and, if necessary, able to withstand the potentially aggressive chemical agents used for disinfection. Surfaces should not be prone to absorption, erosion or corrosion and must not release particulate over time; wetting properties should be cared as well, aiming at the higher hydrophobicity achievable [46].

A critical requirement is to minimize surface roughness and porosity and avoid imperfections like pits and micro-crevices: in fact, at microscopical levels, all asperities constitute a perfect environment for product debris or microbial grappling. As a general rule, all surfaces exposed to product should have a roughness R_a equal to $0.8\,\mu m$ or less [18]; higher roughness values can be accepted if practical tests demonstrate that sufficient cleanliness is achieved nonetheless [18]. However, it is important to highlight the fact that a mere R_a evaluation may be misleading for hygienic assessment. Many sources, such as [32], indicate that the result can be importantly influenced by surface topography and method of producing surface finish (turning, milling, polishing, etc.). It is generally preferable to employ machining processes that produce uniform and parallel grooves rather that irregular pits, which are more difficult to clean. In this sense, with equal R_a values, electro-polishing gives the most hygienic results, followed by insert milling and than spherical milling [13]; refer to Table 1.2 for additional quantitative examples. The most common material used in hygienic applications is stainless steel, for its excellent resistance both to mechanical and chemical aggression and for its compatibility with pharmaceutical or food products. Cold-rolled stainless steel typically possess good roughness and topography properties as well [46]. A common choice is constituted by AISI 316 stainless steel, generally preferred in aseptic processing equipment thanks to its better chemical corrosion resistance with respect to AISI 304 and with no appreciable increase in cost [20].

Hygienic guidelines discourage the use of material coating due to its risk of damaging by wear or collision and consequential detachment of debris. If a surface coating is technically unavoidable, it must be non-toxic, non-absorbent, mechanically stable and made of different color with respect to the underlying material, so that potential erosion areas can be easily seen [18]. Coating used in hygienic applications differ from standard aesthetic coatings by adding a specific function to the underlying surface material: anti-fouling, anti-bacterial, chemical-resistance, wear-resistance or self-cleaning properties are the more frequent cases [47]. For anti-bacterial purposes, two main approaches are present. In one case, coating can have

Table 1.2: Typical R_a surface roughness values obtainable on stainless steel through different processes [103].

Process	R_a [µm]
Cold rolling	0.2 - 0.5
Hot rolling	≥ 4
Glass bead blasting	1.0 - 1.2
Descaling	0.6 - 1.3
Bright annealing	0.4 - 1.2
Pickling	0.5 - 1.0
Mechanical polishing[1]	0.1 - 3.5

[1] Obtained with aluminum oxide or silicon carbide of different (500 - 60) abrasive grit number

a direct biocidal effect by releasing antibiotics or quaternary ammonium or containing silver or copper colloids that inhibit bacterial metabolic system [117]. The latter approach, somewhat preferred in the food & beverage industry, is to avoid biocidal approach and use coating to prevent the adhesion of soil and microorganisms [47]. Another potentially useful application is the "self-cleaning" coating, that actively reduces unwanted particles adhesion through lotus-effect employing superhydrophobic surfaces (i.e. having wetting contact angle ≥150°). In self-cleaning coatings water droplets form almost perfect spheres and can be used to collect soil, thus reducing subsequent cleaning operation times and the overall complexity of the treatments [11].

1.2.3 Joints

As a general rule, it is recommended to use permanently-jointed parts whenever is technically possible. The best way to do so is to employ welding. Great care should be given to superficial polishing of junctures and uniformity; for this reason, it is usually advisable to prefer automatized TIG welding processes, which allows to reach low level of roughness. To avoid gaps prone to debris retaining and are difficult to clean, overlapping plates welding should be avoided; on the contrary, the juncture should be realized by butt-welding of plates on the same level, forming a unique, smooth surface (see Fig. 7a). Welding should also be avoided in sharp internal corners because they would be very difficult to clean: a widely-filleted corner should be designed instead, moving the soldered joint a straight area (see Fig. 7b) Another solution is to employ friction welding which, though having more limited applications, can greatly improve junction hygienicity [112]. In this case, one part is fixed while the other (typically a cylindrical rod or a shaft) rotates; the two pieces are then forced one against the other under high pressure: the consequent friction

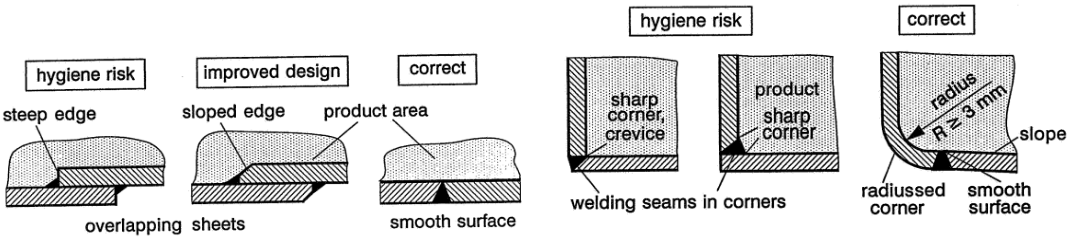

(a) (b)

Figure 7: (a) Overlapping welded sheets should be avoided to prevent gaps and soil accumulation; instead, an aligned smooth surface welded outside the production area is preferred. (b) Corner welding should be avoided in favor of radiussed corners and butt-welding. Adapted from [18].

rapidly brings the material around 1000 °C, thus provoking plastic deformation. After a prescribed time, the rotating piece is abruptly stopped and the junction is completed. The advantage of this solution is the 100% cross sectional weld area, the little presence of porosity and cracks and the easily automatizable and repeatable process [17].

If dismountable joints such as fastened flanges are technically unavoidable, they should always be sealed with proper gaskets and o-rings at their termination: direct metal-to-metal contact is not safe against infiltration and the small gaps between surfaces are very likely to accumulate fouling that is very difficult to clean (Fig. 8a). In this regard, it is important that the equipment is carefully protected against the ingress of both solid and liquid foreign matter. To deal with this problem, the International Electrotechnical Commission introduced a standardized *Ingress Protection* rating (refer to IEC-60529 [50]), which consists of the letters “IP” followed by two digits and a further optional letter. The rating performance increases proportionally to the corresponding number (see Table 1.3 for a brief description); in particular, the first digit indicates the degree of protection against the intrusion of solid objects while the second expresses the protection against liquid ingress. The appropriate IP rating is highly dependent on the application. Electrical equipment should always be certified with IP55 grade at minimum; on the other hand, if equipment is subjected to water jets, IP66 or IP67 classes are strongly recommended. The highest performing rating, IP69K, is suitable to withstand high-pressure and high-temperature water and steam jet cleaning (e.g., in accordance to DIN 40050-9, a 80-100 bar, 80 °C, 14-16 L/min jet from nozzle held at 10-15 cm distance, at various inclinations) [46].

In no case bolted joints can expose the threading to product or sensitive manufacturing space: instead, bolts should be flipped so to expose heads. Screw heads should be mounted with underlying sealings and must not have sockets: domed

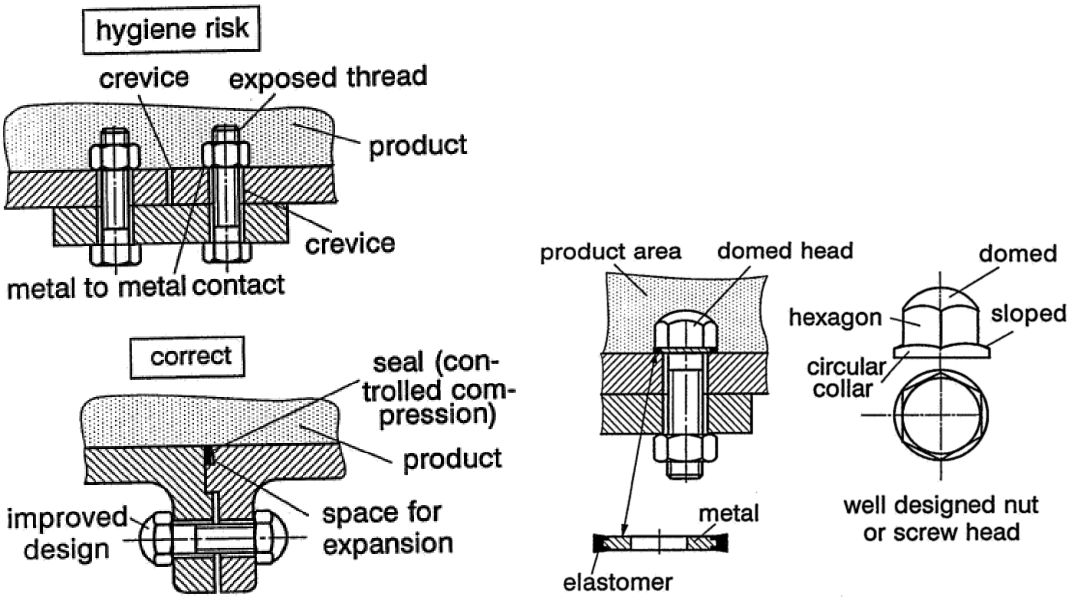

(a) (b)

Figure 8: (a) Direct metal-to-metal junctions and exposed screw threading must be avoided; instead, bolts have to be moved outside production area, preventing leakages and contamination with proper sealings. (b) If the use of bolts inside the production area is technically unavoidable, they must be fastened so to expose the screw head, which is to be designed as a domed hexagon and equipped with an underlying dedicated static seal. Adapted from [18].

hexagonal heads are the standard solution (Fig. 8b).

1.3 Active decontamination

The third requirement of aseptic industry is to actively decontaminate the surface of critical areas. In fact, even if manufacturing takes place inside a clean environment and equipment is hygienically well-designed, organic or inorganic residues may still accumulate after a certain amount of time. This is the typical case of food and pharmaceutical process industries, where liquid products have to be stored into vessels; production is therefore split into cycles which are interspersed by decontamination phases of machinery. A wide variety of industrial physical or chemical decontaminating treatments have been developed for the purpose. In both cases, the underlying principle is the same: to eliminate microorganisms or to inactivate them by blocking their replication capability. The former result is commonly achieved by *denaturation* of microbial proteins: while the primary (peptide) chemical bonds

Table 1.3: Ingress Protection ratings according to IEC-60529 [50].

Dig.	Solid objects: protection vs…
0	no protection
1	objects with $D \geq 50\,\mathrm{mm}$
2	objects with $D \geq 12.5\,\mathrm{mm}$
3	objects with $D \geq 2.5\,\mathrm{mm}$
4	objects with $D \geq 1.0\,\mathrm{mm}$
5	dust-protected
6	dust-tight

Dig.	Water: protection vs…
0	no protection
1	vertically falling water drops
2	vertically falling water drops with tilt up to 15 deg
3	spraying water
4	splashing water
5	water jets
6	powerful water jets
7	temporary immersion in water
8	continuous immersion in water
9	high pressure and temperature water jets

are preserved, the secondary bonds are destroyed; consequently, the protein structures are irreversibly altered and lose the original functionality. Ionizing radiations (i.e. those that possess enough energy to free the electrons of target atoms) easily penetrate microbial cells and inflict a lethal damage. On the contrary, non-ionizing radiations can deteriorate the DNA of microorganisms to a minor extent, thus only preventing replication. Heating is another very common sterilization treatment; despite its cost-effectiveness and intrinsic reliability, it is not applicable to temperature-sensitive products (thermoplastic polymers, electronic devices, etc.). In such cases, the use of chemical agents (in liquid or gaseous form) may become an effective alternative, though they can potentially produce toxic residuals and surface corrosion.

It is apparent that there is no univocal recipe for sterilization and the typical aggressiveness of the involved processes impose great care in the design of aseptic production equipment. For this reason, this section is intended to summarize the main concepts and methodologies that are to be expected in aseptic manufacturing plants.

1.3.1 Basic concepts

To begin with, it is important to clarify the difference between cleaning, decontamination, disinfection and sterilization; these concepts are often used interchangeably in common language, but they actually imply very different industrial processes. *Cleaning* is the action of mechanical removal of dirt, soil and microorganisms from object surfaces; it typically consists of four phases: initial rinse, application of pressurized detergent, final rinse and drying. This process is not intended to actually kill microorganisms, but rather to reduce the risk of spread through their removal. *Decontamination*, on the other hand, should be regarded as a generic treatment that reduces the contamination present on a target object; it results in disinfection or sterilization depending on the residual concentration of microorganisms achieved. *Disinfection* is defined as a process that reduces to a safe level or completely eliminates all pathogenic microorganisms [76]; however, a common disinfection is generally not effective against resilient bacteria and spores. Finally, *sterilization* refers to the use of chemical, physical or other kind of agent in order to completely eliminate any form of microbial life (microbes, bacterial spores, viruses, fungi) [76]. Although sterilization is usually intended as an absolute concept, it is important to note that the result is always limited by the actual possibility of detecting and measuring microorganisms presence.

There are many quantities associated to microbial elimination. Among these, *Log reduction* is probably the most useful; it is a measure of the decontamination level achieved on an object with respect to the concentration of the considered contaminant and it is expressed through the following relation:

$$R = -\log_{10}\left(\frac{C_f}{C_i}\right) \tag{1.2}$$

where R is the Log reduction achieved, C_i and C_f are the initial and final concentration of contaminant, respectively. In a more practical way, the Log reduction can be thought as a percentage of killed microorganisms, where the numerical value of R corresponds to the number of "9" digits in the percentage (e.g. 5-log reduction corresponds to 99.999% of killed bacteria).

Another useful concept is the *decimal reduction time*, usually referred to simply as D value. It expresses the time required at a given set of conditions (often temperature) to reduce a specific microbial population by 90%, i.e. achieving 1 Log reduction. This value is often used to give a rapid characterization of a specific microbial resistance to disinfection: the more time needed (thus the higher the D value associated to a particular bacterium) and the more intense the disinfection process must be; example of typical D values associated to common microorganisms is given in Table 1.4. It should also be noted that the Thermal Death Time (TDT) of microorganisms is a probabilistic concept derived from a theoretical asymptotic exponential curve tending to zero; therefore, in relation with the desired confidence bounds, the sterilization treatment time is selected.

The implementation of an appropriate industrial decontamination treatment it quite a complex task, because it is not trivial to identify the key factors that should drive the process. A simple, yet useful guideline was initially given by *Sinner Circle* in 1960 [100]. This conceptual representation splits the action of cleaning into four contribution (detergent, temperature, mechanical action, time): to preserve the result, the decrease of one factor must be compensated by the increase of the

Table 1.4: Decimal reduction times of common microorganisms subjected to thermal treatment of 121 °C [22].

Species	D [min]
B. polymyxa	0.05
C. botulinum	0.21
B. subtilis	0.7
Clostridium sporogenes	1.5
Desulfotomaculum nigrificans	2–3
T. thermosaccharolyticum	3–4
G. stearothermophilus	4

others. Subsequently, this empirical intuition has been reformulated into more formal approaches, such as energy balance ones. For example, the *decontaminating energy* (i.e. the one required to break chemical, electrostatic and cohesion bonds of soil substrate to object surfaces) can be seen as the sum of injected mechanical, thermal and chemical energy contribution [81]. According to such models, which are now widely accepted in aseptic industry, the whole decontamination process is therefore driven by three main quantities: pressure, temperature and concentration of suitable chemical agents. Mechanical energy is usually introduced through a manually or automatically actuated pressurized liquid cleaning jet. It is worth noting that both pressure extremes present disadvantages. Low-pressure systems (i.e. <2 bar) may lack the necessary energy to remove soil; conversely, too high-pressure ones (e.g. 70-120 bar) can pose threat to both personnel and equipment, due to vibrations and potential erosion of surfaces; a medium-pressure system is usually the optimal solution [46]. Temperature manifests similar side effects: too low values do not carry enough thermal energy to affect soil substrate, while too high ones (>80 °C) may result in condensation (which promotes microbial growth) and thermal shock of component. Again, an intermediate temperature range (such as 50-65 °C) is usually the best compromise [46].

1.3.2 Physical sterilization treatments

A summary of the main physical sterilization treatments is presented in the following.

- *Heat.* Direct application of heat is probably the simplest and most ancient method of sterilization [20]. In fact, beyond a specific temperature, heat produces denaturation (or even coagulation) of microorganism proteins, with a lethal effect that is proportional to temperature itself. Many quantities are used to characterize the process: Thermal Death Point (TDP) is lowest temperature at which all bacteria are killed within 10 minutes; Thermal Death Time (TDT) is the time required to kill the totality of bacteria at a certain temperature; Decimal Reduction Time (DRT), as previously mentioned, is the time required to kill 90% of bacteria population at a certain temperature [37]. The most common heat treatments make use of *saturated pressurized steam* in autoclaves. The transfer of latent heat caused by condensation of hot steam on object colder surface severely increases bacteria temperature, finally getting to their TDT. The typical autoclave cycle requires 121 °C for 15 min at 1 bar [76]; however, more resistant microorganisms such as spores or prions[1] are known to resist such conditions and therefore more severe conditions are applied (e.g. a cycle of 132 °C for 30 min or combination of autoclave and chemical sterilants [91]). A less common way to perform a thermal sterilization is through *dry heat*; the decontamination principle is the same, but it is achieved through simpler and cheaper equipment (hot air ovens). In exchange, the overall process is less effective and therefore longer times and higher temperatures are required (e.g. 180 °C for 30 min or 160 °C for 2 h [32]).

- *Ultraviolet light*, a non-ionizing electromagnetic radiation, is another common example of physical decontamination agent. It has been shown that the portion of E.M. spectrum included in the 100-280 nm (usually referred to as UVC) is lethal to microorganisms, with a maximum bactericidal effect at $\lambda \approx 254\,\text{nm}$ [76]. In fact, proteins and nucleic acids of living organisms absorb UVC light, thus receiving lethal damage their cells. This photochemically-driven mutagenic effect interferes with DNA and RNA replication, ultimately resulting in bacteria inactivation. Two main types of UV treatments have been industrially developed. The first and simpler one is based on the passage of electric current through special glass tubes containing low/medium pressure vapor (e.g. mercury vapor UV lamps); this results in the creation of continuous UV light (hence the name *Continuous Wave UV*, or CWUV). It is a relatively simple and cheap technology and does not raise target temperature, which is useful in case of thermal-sensitive targets. Its penetrating power is quite low and may not be enough to sterilize resistant microbial forms and spores; it can pose health threats if mercury vapor inside lamps is released. All this considered, CWUV is not so used as single sterilizer for equipment but it is rather used as a preprocessor for simple geometries. A possible upgrade is constituted by *Pulsed UV light* (PUV): short UV pulses (e.g. in the range between dozens of µs to hundreds of ms [30] [45]) are produced by Xenon or,

---

[1] Prions are misfolded proteins that manifest corrupted structures and tend to propagate the error to nearby proteins by linking with them. In human and many other organisms, normal prions get "infected" by the misfolded ones and the correct functioning of neural cells is consequently disrupted.

more rarely, Krypton gas lamps. Besides a photochemical effect, shared with CWUV, this treatment adds a photophysical effect by causing direct structural damage to bacterial cells through its high-energy pulses. Moreover, an additional photothermal effect produces instantaneous surface temperature rise of 50-150 °C for very limited layer (e.g. 10 µm thickness); short pulses do not raise mean object temperature, thus thermal-sensitive products are also preserved. In exchange of a better efficacy and higher penetrating effect, PUV equipment and electronics costs are significantly higher. In general, UVC sterilization treatments have proven to be of somewhat limited effectiveness [20], showing variable output Log reduction due to its heavy dependence on many concurrent phenomena. Ray incidence angle and object distance are a determining factor; great care should be given to assess potential shadow areas that can jeopardize the whole process. Object surface properties (such as shape, roughness, hydrophobicity) play a big role too: the more regular and absorbant the surface, the better. Lastly, it is important to highlight that UV rays have different effect against different types of microorganism and, due to their generally-low penetrating power, can be completely ineffective against resistant bacteria (e.g. spores). The high energies required to overcome this problem may affect the target object as well (by discoloring, rendering brittle or deteriorate it).

- *Ionizing radiations* are the electromagnetic waves characterized by short wavelength and very high transported energy; typical examples include γ-rays, X-rays or high-speed electron beams [37]. These radiations have a lethal action due to the ionization of target molecule, i.e. the dislocation of electrons from respective atoms. Two main mechanisms are responsible for decontamination: direct ionization that transfers energy to DNA and proteins and causes their rupture, and indirect ionization that generates and diffuses highly-reactive free radicals (such as OH· and H·). Average doses[1] are about 1-10 kGy [37]. This sterilization treatment is highly effective against microorganisms thanks to its great penetrating power; treatment times are, as a consequence, much shorter than other methods. On the down side, the production of ionizing radiation is highly expensive and may pose serious danger for operators health. Its application in industrial industrial environment is therefore quite sporadic, and is usually limited to the sterilization of critical medical devices.

- *Plasma*, the state of matter in the form of globally neutral ionized gas, is another useful mean of physical decontamination. Ions, electrons, UVC photons, free radicals and neutral reactive species (such as O_3 or H_2O_2) are only part of a long list of its content. Plasma is typically produced by electrical

---

[1] In SI, 1 gray (Gy) represents the transfer of 1 J to 1 kg of matter

discharge between high-voltage electrodes, in which a laminar stream of gas is made to flow. As such, it may be utilized in two main forms: thermal plasma ("hot"), that reach several thousands of Celsius degrees and non-thermal plasma ("cold"), in which electron temperature is far higher than the overall gas temperature[2] (i.e. they are not in thermal equilibrium). Usually, only the latter is employed for industrial decontamination processes, most notably in the form of atmospheric pressure non-thermal plasma (LTAPP) obtained from H_2O_2 gas. Plasma decontamination mechanism has not been thoroughly understood due to many superposing phenomena: lethal damage to microorganism genetic material inflicted by carried UVC radiation (photochemical effect), atom-by-atom erosion of microorganisms through desorption (breaking of chemical bonds), degradation caused by the adsorption of reactive species. Overall, this decontamination treatment is characterized by good microbial reduction, relatively short treatment times (from seconds to dozens of minutes) and no chemical residuals. On the down side, it often causes object's surface to erode and modifies its chemical composition.

A few other physical-based sterilization treatments are available, but their limited efficacy makes them far less common than those summarized above. Among the others, we can mention *microwaves*, whose main decontamination mechanism is based on a thermal effect. *Lasers* superpose thermal, photochemical and photomechanical (rapid microbial cell expansion and ablation) effects; as a side note, it is worth mentioning that lasers are widely used to modify surface hydrophobicity of metals and plastics: hence, they often act as an indirect means of sterilization. Lastly, *ultrasounds* are used to transmit energy through elastic waves; at frequencies higher than 20 kHz they inactivate the microorganisms present in aqueous suspension by cavitation. Mere sonic treatments are not sufficient as single sterilizing method, but can highly increase their efficacy if combined with a chemical treatment.

1.3.3 Chemical sterilization treatments

A summary of the main chemical sterilization treatments is presented in the following.

- *Vaporized hydrogen peroxide* (H_2O_2, usually referred to as VHP) is one of the most common and effective chemical sterilization treatments. Its decontaminating action is based on a powerful oxidation of microbial proteins, enzymes

---

[2] The equivalent temperature associated to the energy of 1 eV corresponds to approximately 11600 K, as in the relation $T_e = k_b T_a$; k_b is the Boltzmann constant, T_e is expressed in J and T_a is expressed in K

and DNA and on the release of free radicals (mostly hydroxyl ·OH) [76] which, anyway, do not leave toxic residuals. VHP efficacy is proportional to both temperature and concentration, but for typical applications it is employed at 35% of concentration and 55 °C. At these conditions VHP it is lethal against a wide number of bacteria; in case of resistant microorganisms such as spores, efficacy can be increased in many ways. One method is to apply external heat (e.g. 60-125 °C hot air flow) after the treatment; this causes the decomposition into water vapor and nascent oxygen with a sterilizing exothermal reaction [20]. The same decontaminating effect may also be achieved by reducing concentration and increasing humidity, up to condensation.

- *Peracetic acid* (CH_3COOOH) is a powerful oxidizing agent and it is particularly effective against of a broad spectrum of microorganisms (bacteria, spores, molds and viruses) [37]. It can be proficiently employed at fairly low temperatures (about 40 °C), so it is widely used to sterilize temperature-sensitive polymers (PET, LDPE, etc.). A typical industrial application is the decontamination of plastic bottles; in this case, the secondary sterile water rinse is no longer required [20]. Peracetic acid is particularly useful because its final decomposition products (i.e. oxygen and water) are non-toxic [76]; nonetheless, it is highly corrosive against metals and its suitable concentration depends on the specific application. It may be used in combination with hydrogen peroxide to complete a product sterilization cycle.

- *Chlorine* and *iodine* compounds are the most common representative of oxidizing halogen-based sterilants [76]. Despite its high efficacy against vegetative cells, chlorine is usually less proficient against resistant microorganisms. In addition, it is highly aggressive against metals and if followed by heating treatments it can cause stainless steel to corrode; AISI 304 is more susceptible to this effect than AISI 316 [20]. Iodine compounds are a valuable alternative and usually perform better at a significantly lower concentration. For example, the same sterilizing effect reached by iodine at 10-25 ppm is possible with 100-200 ppm of chlorine. Although iodine is less corrosive than chlorine, it often produces undesired yellow-to-orange color residuals on object surface [20].

- *Ethylene oxide*, is a particular kind of decontaminating agent, and it is extensively employed in the sterilization of laboratory and medical equipment. Used in form of gas it produces the alkylation of functional groups (amino, carboxyl, hydroxyl), thus blocking the main metabolic processes of contaminating microorganism. Efficacy is approximately proportional to concentration but rapidly increases with temperature. One of its main drawbacks involves the long treatment times required: typically 4 hours at 65 °C plus

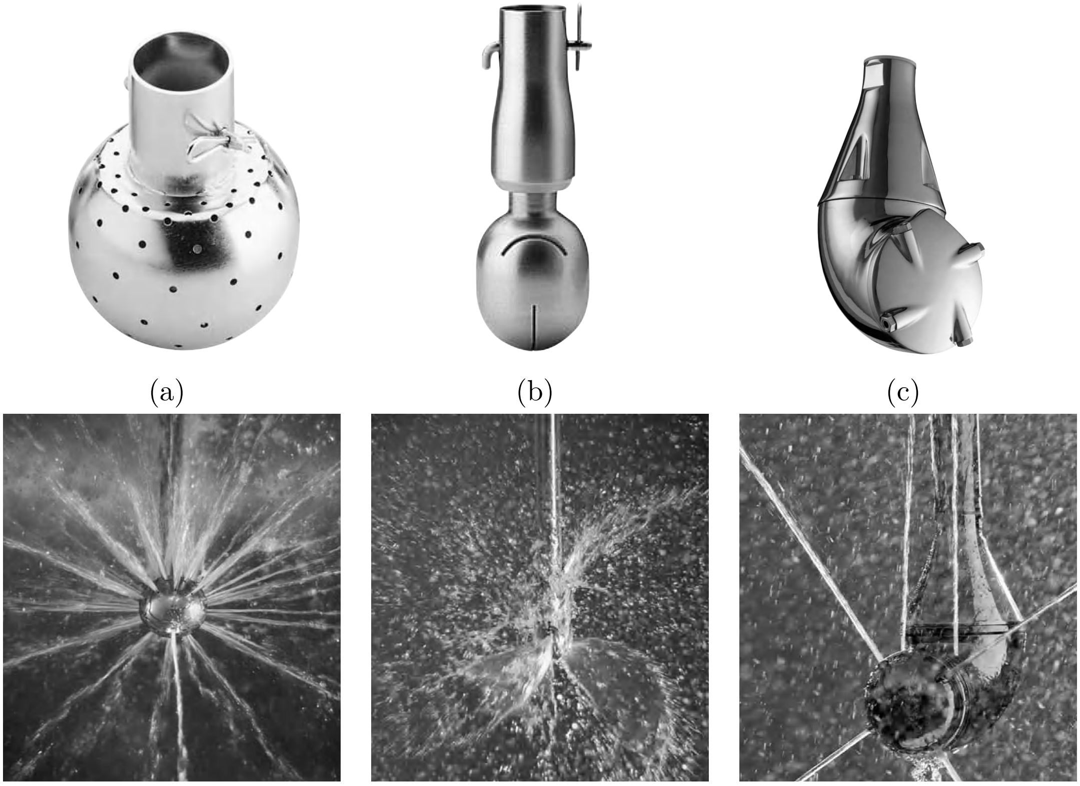

(a) (b) (c)

(d) (e) (f)

Figure 9: Industrial decontamination devices. Static spray ball design (a) and in action (d). Rotary spray head design (b) and in action (e). Rotary jet head design (c) and in action (f). Adapted from [103]

12 additional hours for aeration, in order to eliminate toxic residues from equipment [76].

Many other chemical sterilants are available, but their use is generally less common and delegated to specific purposes. Among them, we can mention Oxonia (a combination of peroxyacetic acid and hydrogen peroxide), Ozone (whose decontaminating mechanism is similar to that of halogen compounds) and some of the highly-aggressive sodium compounds (e.g. sodium hypochlorite and sodium hydroxide) [103].

1.3.4 Industrial implementation

The majority of open surfaces (such as walls, doors, floors, drains) are cleaned with foam detergents followed by disinfectant solutions, in what is usually called an *Open Plant Cleaning* (OPC). The operation is typically performed manually by an operator through dedicated lances. Foams, obtained by water dilution of previously concentrated solutions, are applied for times of 15-30 min [46]. On the contrary, the equipment present inside sterile areas is extensively decontaminated through the *Cleaning-In-Place* (CIP) method, i.e. without dismantling or opening the sterile area and with minimal or absent manual operations [103]. In order to provide sufficient decontaminating energy, two opposite approaches are available: one involves the combination of high flowrate and low pressure, the other the combination of low flowrate and high pressure.

The former approach is reflected by traditional CIP method, which is industrially implemented through the installation of many *static spray ball* devices (see Fig. 9a). As the name suggests, a static spray ball is a fixed spherical liquid distributor mounted on the ceiling of a sterile area in a downward direction and connected to some feeding piping for the input of a cleaning agent. The disinfectant is ejected at a relatively low pressure (e.g. about 2.5 bar [46]) through a limited number of holes drilled on its surface and it is distributed in a preset, specific pattern. This constraint results in poorly controllable decontamination cycles: only a limited set of the surrounding environment points can be directly reached by the jets; instead, remaining surfaces are wet by gravitational pouring or impact bounces. Static spray balls are easy to install and to maintain, and are mostly employed when hygienic requirements and initial investment costs are fairly limited.

Rotary spray heads constitute the natural upgrade of such devices (see Fig. 9b). Despite the numerous design variants available, they all consist of a rotary unit for cleaning agent distribution and an inlet feed pipe. The distributor experiences hydraulic reaction forces due to pressurized detergent expulsion and is consequently put into rotation about the inlet pipe axis. The particular form of openings and holes present on distributor, together with its rotation movement, produce “fan-shaped” jets. This important feature allow rotating spray heads to directly hit all surfaces along their sweep, so that decontaminating effect is not anymore relying on gravitational pouring or bounces. As a consequence, the required quantity of chemical agents is lower and the whole process is faster; hygiene quality is improved as well, thanks to the mechanical abrasion effect (“scrubbing”) added by pressurized jet impact [103].

Finally, the most modern and effective CIP approach – rooted on the lower flowrate and higher pressure paradigm – is realized by the means of *rotary jet heads* (see Fig. 9c). Decontaminating liquid is ejected through the nozzles (e.g. 2-8) of a two-DOF mobile unit; the latter is either actuated by motors or moved by fluid passage through integrated turbines. The combined rotation about vertical and horizontal axes allows to directly reach all the surrounding surfaces; thus, arbitrary trajectories are possible and cleaning is carried out in progressive sweeps (from coarser to finer). Typical jet pressures are in the range of 5-13 bar [46]), with a flowrate of 2-30 m^3/h that effectively decontaminates surfaces up to 2-16 m [103]. Thanks to these advantages, rotary jet head technology minimizes liquid flow and process time (if compared to spray balls), yet reaching the highest CIP cleaning quality available.

1.4 Commercial robots for aseptic industry

The previous sections have shown how human activities have significant impact on workplace contamination; subsequent complex decontamination processes constitute one of the main concerns of aseptic industry in terms of productivity and resources. A natural response to this scenario consists in the progressive automation of cleanliness-sensitive manufacturing processes. Thus, it is not surprising that among the leading robot manufacturers many are currently expanding their portfolio to provide clean-suitable products. The main challenges of this emerging field of automation are related, from a kinematic point of view, by the need of extreme dexterity: the manipulated objects are typically very small (e.g. pharmaceutical test tubes, bacteria sampling tools, small medical devices, microelectronics production tools), trajectories involve both displacement and rotation in 3D space, and working environment is dense of obstacles; as such, a full 6-DOF robot architecture is often required and is in fact the most common solution available on the market. As for the aseptic point of view, the need to minimize airborne particles generation, the requirements in terms of cleanliness of shapes, and material resistance to aggressive decontamination agents pose severe design constraints and result in very different hygienic performances.

The main features of state-of-art commercial aseptic robots are briefly discussed in the following and are summarized in Table 1.5 and Table 1.6. The analysis is performed in terms of eight key quantities: robot arm reach, maximum payload, position repeatability, weight, ISO cleanliness grade, IEC ingress protection class, chemical resistance and overall aseptic design. In particular, six robot models have been compared:

- ABB, IRB-1300 [1]
- Denso, VS-050S2 [25]
- Fanuc, LR-Mate-200iD/7WP [33]
- Kawasaki, MS-005N [57]
- Kuka, KR6-R900-HM [59]
- Stäubli, TX2-60L-Stericlean [102]

First of all, we observe that mechanical performances are in line with those of general-purpose robots; reach is somewhat limited though, and stands on a mean value of 800 mm without end-effector mount. Average payload is about 5 kg, which is sufficient to equip simple grippers and manipulate the typical objects of aseptic industry. Same consideration applies to repeatability, which is in the order of 1/100 mm and allows reliable working operations based on preset programming. In this regard, special mention should be reserved to the Kawasaki model, whose repeatability is one order of magnitude greater than the others; though this robot use might not be advisable in the microelectronic manufacturing field, its application is still suitable to food an pharmaceutical environments thanks to its 7 DOFs, which allow for extended operation flexibility. Since the typical robot applications require for fixed arm mounting, weight is not a primary concern; as such, the proposed models show highly variable weights, in the range of many tens of kilograms 25-75 kg. On the other hand, the implementation of robot on a moving vehicle would allow to cover multiple manufacturing areas with a single arm, thus relaxing the decontamination requirements; in this perspective, the most suitable robot is represented by the Fanuc model, which is the most lightweight.

From the cleanliness point of view, suitable results have been obtained by almost all the manufacturers. Many models exhibit compliance to ISO Class 4 and Class 5 standards, which allow operation in medium-to-high demanding clean manufacturing environments; the only notable exception is constituted by the Kuka model, which does not provide explicit certification in its documentation. The degree of protection against ingress of contaminant significantly varies with the model, as well. Almost all the considered robots present complete protection against dust and solid micro-particles (i.e. at least IP6X), which allows proficient use in microelectronics and optics manufacturing environments. However, some further limitations are present for pharmaceutical and food process applications, whose decontamination cycles are mostly performed through highly-pressurized liquid jets (refer to Section 1.3.4); with respect to these scenarios, IP67 grade or higher is generally required. Only part of the existing industrial robots provide IP67 protection grade along all the arm (namely ABB and Kuka models); others certify IP67 protection only for the terminating part of the robot (wrist), while the rest is partially protected at IP65 (e.g. Denso and Stäubli models); the Fanuc model raises the protection degree to IP69K for the wrist, still protecting the arm at IP67; finally, outstanding ingress protection grade is achieved by the Kawasaki model, which certifies complete IP69K shielding of the robot. Most interestingly, very different chemical resistance is achieved by each commercial robot. ABB and Fanuc models exhibit virtually no resistance to harsh chemical decontaminats due to the lack of proper casings material and surface coverage (i.e. aluminum alloy covered by simple painting). Another part of the available robots certify resistance to at least hydrogen peroxide (H_2O_2), which is probably the most common sterilant in pharmaceutical industries; among them, Denso and Kuka model additionally guarantee suitable resistance to a broader spectrum of aggressive agents. Finally, significant results are achieved by the Kawasaki robot, whose specifically-treated AISI 316 stainless steel casings ensure resistance against virtually all the sterilants used to in aseptic machines.

The last considered parameter concerns the overall hygienicity of robot design. Albeit difficult to formalize in a quantitative way, this feature plays a role of primary importance in aseptic robot selection, as it significantly influences the decontamination processes that have to be implemented. Recalling the principles stated by EHEDG and other hygiene consortium guidelines (see Section 1.2), all surfaces should be easily accessible and cleanable, no hidden areas must be present, profiles should be as smooth as possible, and minimal number of screws should exposed to the environment. The first and most evident hygienic solution that we can observe, and that is adopted by every considered model, consists in the enclosed design of the arm (i.e. no motors or cables are located outside of the casings). Moreover, all the robots achieve sufficient performance in terms of outer surface smoothness, ranging from the lowest results of the ABB model up to highest obtained by Denso and Kawasaki. Unfortunately, some hidden areas may be found in most of the robots as well. In particular, many joints are designed as clevis links, which are prone to contamination accumulation in the narrow space between members and are consequently difficult to sanitize. In this regard, best hygienic performance is achieved by Kawasaki and Stäubli robots that, thanks to their tubular design, provide easy access to all arm surfaces. Lastly, it is easy to observe that the choice of an enclosed design imposes the need of dismountable casings and covers, in order to insert motors and other drive components. The arising issue of exposed screws and sockets inevitably affects all the models, albeit at different extents: ABB and Kuka models have worse performance, as a large number of screws are used to fasten the casings; Denso and Kawasaki robots, on the contrary, manage to minimize the problem.

From the analysis of state-of-the-art commercial aseptic robot offer, we can conclude that multiple solutions are available, but none of them fully satisfies the aseptic requirements. As expected from consolidated firms in the robotics field, all the examined models present extremely good performances from the mechanical point of view (e.g. payload, repeatability). On the contrary, many problems are still present for a proficient integration with harsh aseptic environments due to the relatively young market. In the subsequent chapters, a custom robot design will be proposed to address the problem.

Table 1.5: Specifications of commercial asepticity-oriented robots [1/2].

	ABB IRB-1300	Denso VS-050S2	Fanuc LR-Mate-200iD/7WP
Reach [mm]	900	520	717
Payload [kg]	11	4	7
Repeatability [mm]	0.02	0.02	0.018
Weight [kg]	75	34	25
Cleanliness	ISO Class 4	ISO Class 5	ISO Class 4
Ingress protection	IP67	IP65-IP67[1]	IP67-IP69K[1]
Chemical resistance	None	Good[2]	Very limited[3]
Hygienic design	Poor	Very good	Good

[1] Robot arm - robot wrist. [2] Resistant to H_2O_2, isopropanol, NaOH, formalin, UV.
[3] Not resistant to organic solvents, chlorine, ammine, strong acids.

(a) (b) (c)

Figure 10: Example of commercial asepticity-oriented robots: (a) ABB IRB-1300, (b) Denso VS-050S2, (c) Fanuc LR-Mate-200iD/7WP.

Table 1.6: Specifications of commercial asepticity-oriented robots [2/2].

	Kawasaki MS-005N	Kuka KR6-R900-HM	Stäubli TX2-60L-Stericlean
Reach [mm]	660[1]	902	920
Payload [kg]	5	6	5
Repeatability [mm]	0.10	0.03	0.03
Weight [kg]	50	62	53
Cleanliness	ISO Class 5	-	ISO Class 4
Ingress protection	IP69K	IP67	IP65-IP67[3]
Chemical resistance	Exceptional[2]	Good[4]	Limited[5]
Hygienic design	Very good	Poor	Good

[1] Horizontal reach. [2] AISI 316 stainless steel casings certified for aggressive chemical sterilants. [3] Robot arm - robot wrist. [4] Resistant to H_2O_2, formalin, ammonia, isopropanol, ethanol. [5] Resistant to H_2O_2.


(a) (b) (c)

Figure 11: Example of commercial asepticity-oriented robots: (a) Kawasaki MS-005N, (b) Kuka KR6-R900-HM, (c) Stäubli TX2-60L-Stericlean.

Chapter 2

Custom Robot Concept for Aseptic Industry

2.1 Project design constraints

In this chapter, we introduce the design principles of a custom robot that is able to operate within an aseptic environment and that shares the same sterilization cycles of the surrounding machine. The goal is to develop a solution that is ready for industrial implementation and that realizes a new trade-off between the strengths of commercial robotics and hygienic performance. In this regard, it is important to observe that existing sterile robots are mainly derived – through a certain extent of modifications – from general-purpose counterparts. Therefore, respective offer of well-established mechanical features typically overwhelms more critical hygienic requirements. The present case application is characterized by the need to handle small and lightweight objects, with fairly slow motion and reduced duty cycles. In force of these considerations, the proposed robot intends to maximize hygienic performance at the expense of lower payload and accelerations; moreover, in order to guarantee the realization of complex 3D rototranslation trajectories, our design will focus on a full 6-DOF articulated arm architecture. Actual project design objectives are summarized in Table 2.1 as a list of two categories: quantitative specifications (accompanied by respective target values) and qualitative features (weighted by importance); a brief explanation is also reported in the following.

The first and most important constraint is to design a robot that completely fulfills the hygienic requirements. As such, all external surfaces must be easy to access and clean, should minimize mechanical roughness and be sufficiently smoothed; no hidden areas, recesses or undercuts must be present. The number of exposed bolted connections should be minimized, with particular reference to external screw heads and relative sockets. All dismountable joints, whether they static or dynamic, must be protected through a dedicated bidirectional sealing solution, so to prevent leakage of contaminants from the environment to the robot and vice-versa. Moreover,

Table 2.1: Custom robot design target specifications and features.

Specifications	**Value**
DOFs	6
Reach	800 mm
Payload	2 kg
Repeatability	0.1 mm
Ingress protection grade	IP69K
Chemical resistance	*list*[1]
Features	**Weight**
Hygienic design	3
Enclosed structure	3
High dexterity	3
Durability	2
Small objects manipulation/handling	2
Lightweight design (10-20 kg)	2
Easy to build, install, maintain	1
Least modification to environment aseptic air flow	1

[1] At least H_2O_2, CH_3COOOH, NaOH, HNO_3, UV light.

the arm must be designed as an enclosed structure, since it is subjected to harsh chemical and physical sterilization treatments; hence, all mechanical and electronic parts (e.g. motors, reducers, transmission mechanisms, sensors, wiring) must be contained inside the robot casings. Ingress protection grade should be the highest possible, in order to guarantee sufficient resistance to pressurized liquid decontamination jets; as such, IP69K is chosen as design target for all the arm. Casings overall durability is to be guaranteed by an accurate choice of material and surface treatments, so to avoid both mechanical wear (airborne particulate generation upon impact against repeated pressurized jets) and chemical wear (discoloring or change in material properties). Another important design constraint is to develop a highly-dexterous and slender robot. Since the aseptic industry working environments are typically narrow and dense of obstacles, machines and decontamination devices, the robot must be able to exploit the maximum working volume within the limitations of its reach and minimize self-collision configurations. For the sake of operation flexibility, the robot must be equipped with a slender multitask end-effector that is able to handle and manipulate different objects while minimizing the number of motors and joints. To further improve the overall hygienicity of the solution, it is important that the robot is shaped in such a way as to provoke the least modification to the environment aseptic laminar air flow (see Section 1.1); for the same reason, the number of installed robots should be minimized as well. In this regard, a significant improvement could consist in the development of a single mobile robot which is able to autonomously operate in different workplace areas. To achieve this goal, though, a dedicated locomotion system must be implemented and some additional constraint arise on robot design. First, weight becomes a fundamental parameter of the project: since the packed environment is not likely to accommodate for significant additional locomotion system footprint, the arm must be as lightweight as possible, possibly in the range between 10-20 kg. Secondly, electronic drives must be directly embedded on board the robot, as hygienic requirements impose no wiring outside the enclosed casings. The last project constraint is to develop a design that can be profitably integrated to already-existing industrial environments: as such, the robot is sought to be particularly easy to assemble, install and maintain.

2.2 Aseptic 6-DOF articulated arm concept

In this section a first basic aseptic 6-DOF articulated robot concept is introduced; the drafted solution (see Fig. 12) is intended to illustrate the application of the exposed project objectives and will serve as baseline for subsequent detailed design, which is exposed in the following chapters.

The design starting point is directly drawn from the first requirement. In order to develop a six degrees-of-freedom robot (i.e. those end-effector is able to assume any given 3D translational and rotational configuration within the reach of the arm[1]), at least six independent motor drives must be installed. Any additional motor results in an over-actuated redundant architecture: though allowing for superior flexibility (i.e. the end-effector may reach the same output pose with multiple joint configurations), this solution increases both design complexity and hygienic hazard, and it is consequently discarded.

The conceptualization of the drive structure constitutes the first step of the arm draft. A "lean" design approach should be used as main guideline: given that the minimization of robot members is determinant to improve the overall hygienicity, this component is conceived as a multi-DOF assembly, in which more than one motor is housed. In particular, the drive is shaped as a 2-DOF spherical enclosed structure, in which the motors are installed with perpendicular axis. The described architecture is particularly well-suited for a modular implementation and can be adjusted in size to optimize the arm inertia: three progressively-smaller 2-DOF drives are equipped to realize the total required 6 DOFs. As discussed in Section 1.4, clevis junctions constitute one of the major flaws that afflict available commercial robots. Therefore, the proposed concept is arranged so that the rod

---

[1] Actually, the end-effector possible configurations are progressively limited while approaching the robot workspace extremes, i.e. out of the "dexterous" workspace.

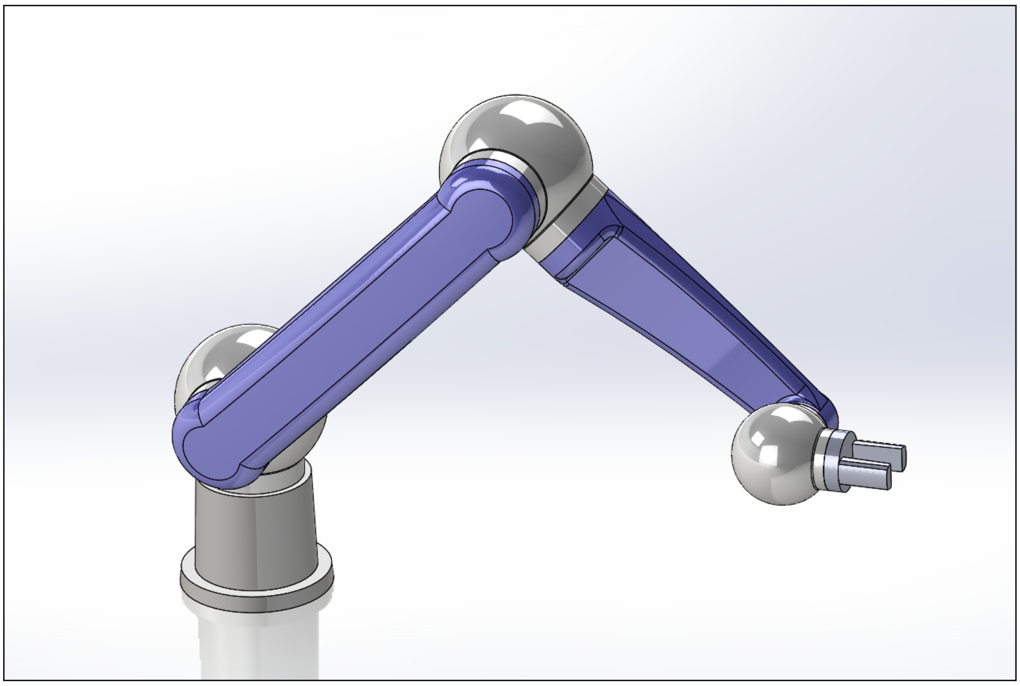

Figure 12: Conceptual 6-DOF aseptic articulated arm. Three 2-DOF spherical casings (grey) are connected to two hollow rods (blue) and a generic gripper.

members (depicted in blue in Fig. 12) are directly connected to the drive casings; a cleaner "tubular"-shaped architecture, having all the external surfaces exposed and easily accessible, is hence obtained.

Another important hygienic requirement consists in the minimization of bolted connections. To pursue this target, the modular motor casing is drafted as a single carved part, with no dismountable covers. Of course, the improved aseptic performance is achieved at the expense of a much greater constructive complication: the lack of fastened parts makes internal components much more difficult to assemble and requires for specific care to be designed. The same approach can be adopted for the arm rods, that are realized as two welded hollow members; in this case, however, most of the interior volume is lost: the peculiar rod elongated shape prevents other components to be housed inside of them. Finally, the presented robot is equipped with an actuated end-effector, which is represented by a generic gripper. Six dynamic sealings, interposed at each joint, complete the assembly.

2.3 Aseptic mobile robot concept scouting

Before proceeding with the detailed design of the exposed arm concept, it is important to further consider one of the main remaining open points: the choice of a fixed or mobile robot solution. Indeed, the design of a profitable locomotion system is strictly dependent on the target working environment configuration and can not be decided in advance. Nonetheless, the implementation of a specific locomotion system, if any, significantly influences the overall robot design constraints and must be taken in serious account, not to preclude any possibility. Therefore, a number of potential mobile robot implementations, suitable to aseptic environments, will be explored in the following. The rest of the project will be based on a precautionary *ready-to* paradigm, i.e. assuming that the developed arm is bound to satisfy the constrains introduced by a mobile implementation.

2.3.1 Autonomous Guided Vehicle

The first presented concept is based on an *Autonomous Guided Vehicle* architecture. As such, the robot arm is installed on a moving vehicle that contains all the equipment needed to operate. Since the robot is not directly connected to the power grid, a dedicated battery pack must be housed on-board. Typically, high-capacity Lithium-ion Polymer cells (*LiPo*) are used for the purpose. In our case, battery can be periodically recharged in a dedicated supply station, directly inside the working environment. To minimize the associated down-times, the recharge phases should occur while the robot is exchanging material with the outside environment and during sterilization phases. Since the AGV locomotion system is linked to the ground by a non-holonomic constraint, an external source of data for is needed for its positioning. In fact, the odometric information gathered by internal motor encoders are not sufficient, due to potential slippage: the robot can not move blindly relying on a preset program. Many on-board artificial vision options are commercially available to solve the problem (e.g. LIDARs and cameras). However, it is probably convenient to exploit the structured characteristic of the environment and use a remote vision to simplify the robot design. Since the workplace is known beforehand, a practical solution is to install a certain amount of fixed cameras inside the workplace and subsequently feedback the robot position via a wireless medium.

As for the locomotion system, two alternative paradigms are available: legs and wheels. The former solution is usually best suited for open unstructured and unknown environments rather than industrial ones. However, the ability to overcome gaps and uneven floors is favorable to aseptic workplaces, since their floors are typically inclined and interspersed with ribs for liquid containment and drainage (see Section 1.2). The increased flexibility is achieved at the expense of a much higher mechanical design and control complexity. Many actuators and joints are required to guarantee motion stability (e.g. four or six legs) and equilibrium may be particularly tough to maintain (see Fig. 13a). To partially mitigate this problem, it may be possible to substitute a fully-motorized leg solution with some planar 1-DOF kinematic linkage leg emulator. Among the others, we can mention Jansen [85], Klann [95] and Ghassaei [39] linkages, in addition to Chebyshev plantigrad

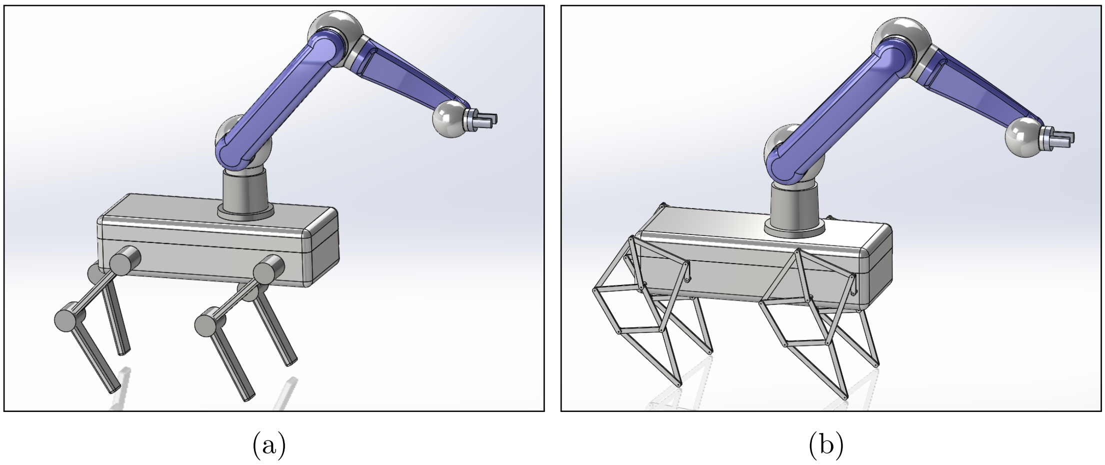

(a) (b)

Figure 13: Legged AGV robot concepts equipped with generic arm: (a) actuated legs and (b) Jansen kinematic linkage locomotion system.

mechanism [69] (an example is drafted in Fig. 13b). However, both proper legs and linkage solutions present a high number of rods and joints exposed to the aseptic environment: this may pose severe hygienic issues and can be difficult to clean effectively. Thus, provided that a sufficiently planar and even floor is available for the application, a simpler wheeled solution is investigated.

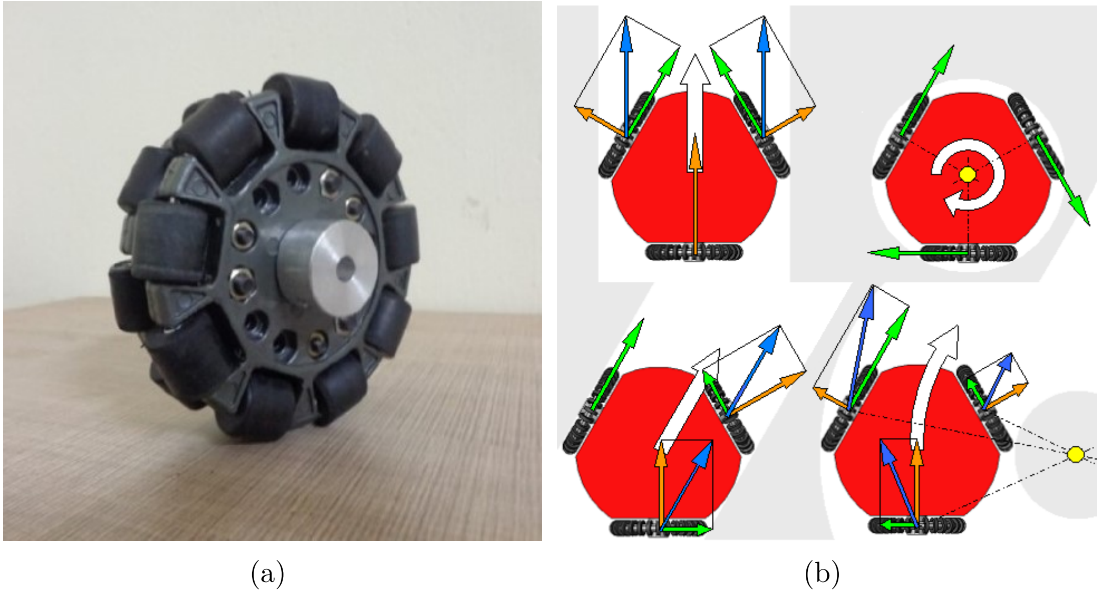

(a) (b)

Figure 14: AGV equipped with *omni wheels*. Adapted from [113].

The wheel-based locomotion system represents the *de facto* standard for industrial AGVs thanks to its simplicity, intrinsic stability and cost effectiveness. As

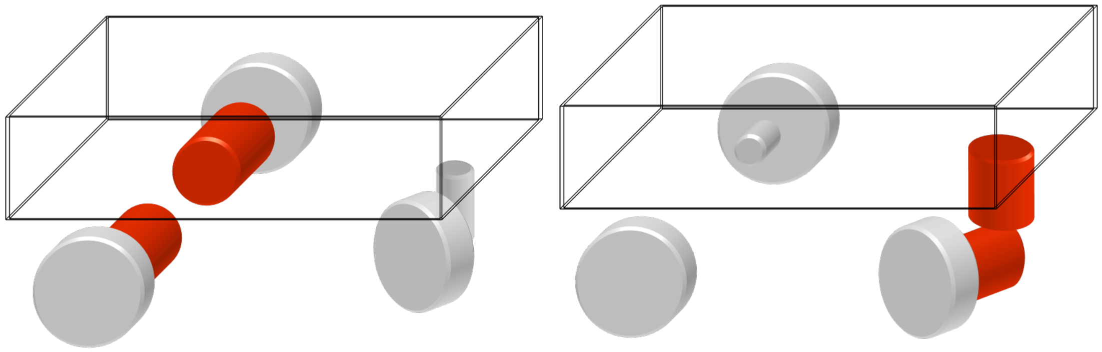
(a) (b)

Figure 15: AGV differential wheels and steerable wheel.

such, many architectures are available, with different degrees of maneuverability. The most dexterous ones make use of at least three “omni wheels” or similar commercial implementations (e.g. *Interrol*, *Mecanum* wheels). A generic omni wheel (see Fig. 14a) is composed of a motor-driven disk and several idle rollers located on its external circumference. These rollers rotate perpendicularly to the disk turning direction: therefore, the wheel is able to both roll on its axis and to slide along it, without opposing resistance. As illustrated by Fig. 14b, proper combination of wheels rotation allows the vehicle to place its instantaneous center of rotation (ICR) in any desired point of the plane. Consequently, the robot is able to perform all possible planar maneuvers (translation, rotation, curves) and probably represents the best choice in terms of obstacle avoidance. Unfortunately, the considerable benefits of this solution are again obtained at the expense of hygienicity: the several wheel rollers require as many exposed revolute joints hubs, which are prone to bacteria accumulation and are almost impossible to clean.

The last considered architecture is based on standard wheels that, while reducing the overall maneuverability of the vehicle (i.e. no transversal sliding is possible), require fewer motors and joints. The minimal solution consists of two motors and three wheels (two of which share the same fixed axis of rotation). As depicted in Fig. 15, the chosen implementation results in *differential* and *steerable* configurations. The first idea (Fig. 15a), typical of industrial AGVs, consists of two fixed-axis motorized wheels and an idle pivoted one (*caster* wheel). It presents many advantages: motors share the same size and both are used for accelerating and turning (hence good vehicle power density); vertical footprint is minimized and ICR can be instantaneously set on a line. However, a major drawback is present: since the caster wheel has passive steering, it can notably get stuck. On the contrary, the steerable configuration (Fig. 15b) allows active control of vehicle trajectory, although only a single motor is actually used for acceleration (worse power density). Anyway, the fact that the front wheel never gets stuck represents a decisive advantage in packed environments; as such, this configuration is further explored so to develop an hygienic version.

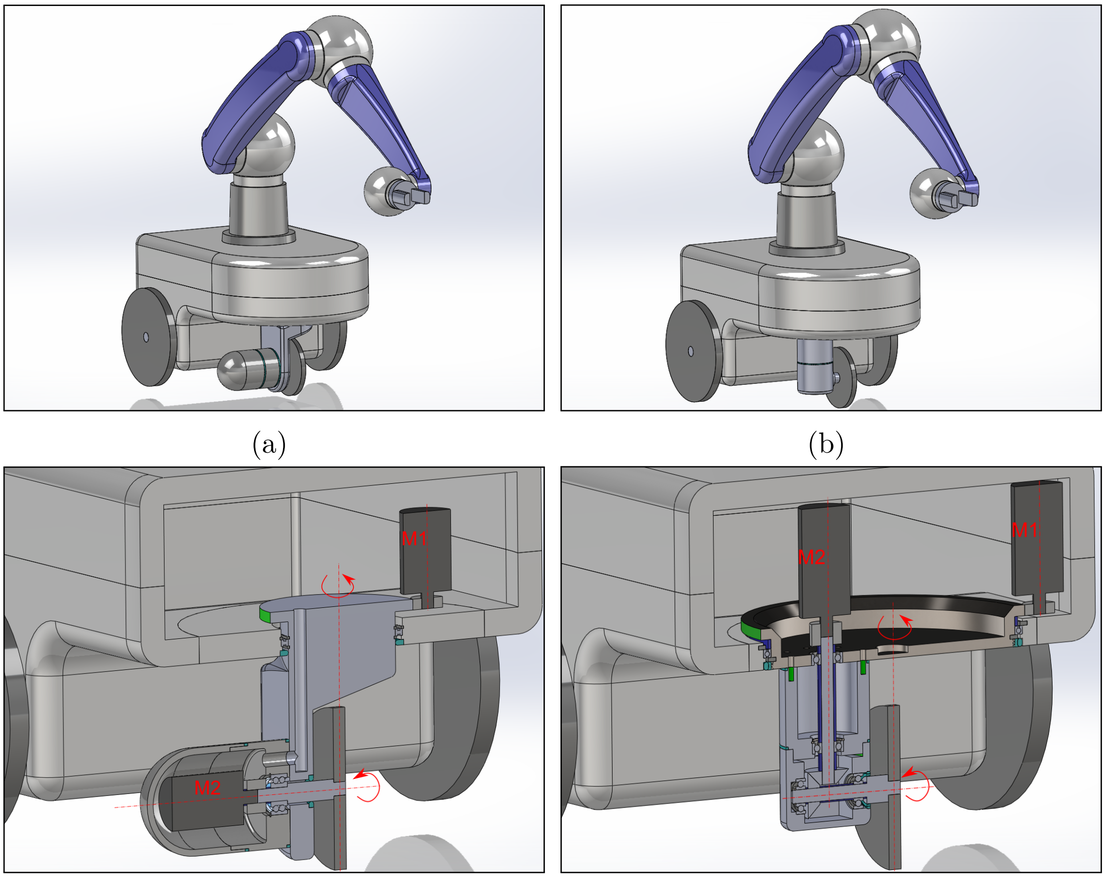

(a) (b)

(c) (d)

Figure 16: Wheeled AGV robot concepts equipped with generic arm: (a) outer and (b) inner locomotion wheel system. Sections (c) and (d) show internal transmission systems for respective solutions.

The first proposed concept is sketched in Fig. 16a and consists of a steerable wheel actuated by both internal and external motors. The steering motor M1 (see Fig. 16c) is placed inside the AGV body and acts through a spur gear transmission, so that no additional reducer is needed. The accelerating motor M2 is placed outside the vehicle, on the steering wheel-carrier structure. Particular care is given to hygienic design: motor casing is rounded and exposes no screws (two sub-parts are fastened together); undercuts and dead areas are minimized; upward horizontal surfaces are suitably inclined; all couplings have dedicated sealings. This solution optimizes motion transmission (each motor is directly connected to its user) and vehicle internal space (which can be used for additional equipment or batteries). On the down side, cable management is rather complicated since M2 wires must pass inside the wheel-carrier structure, from inner vehicle body to external motor casing. The other proposed concept (see Fig. 16b and Fig. 16d) is intended to solve this issue by placing both motors inside the vehicle. Steering is again obtained through a spur gear (M1), while acceleration is exerted through a bevel gear transmission. Though internally more complicated, the wheel-carrier structure is more hygienic and protects transmission from external sterilants.

2.3.2 Gecko

A non-conventional mobile robot may be shaped as a climbing vehicle. The ability to move on both horizontal and vertical surfaces would allow it to completely bypass the many workplace obstacles so to achieve maximum operating flexibility. The few available examples of this kind of robots are typically used to explore the interior of tanks and implement their locomotion system through suction adhesion [82] [77]. Though simple in concept, this solution presents many drawbacks. First, in order to press robot terminations against the wall, an on-board pump is needed; the weight of the pump and the high energy involved to maintain vacuum badly affects battery life performance (i.e. frequent recharges are needed). Secondly, adhesion delay makes locomotion very slow and if any leakage between sucker and wall is present, grip can be lost. Finally, the recirculation of air inside the aseptic environment constitutes a serious hygienic threat and must be avoided at all costs. An alternative solution can be based on magnetic adhesion, which has been explored by some authors (e.g. [98]). Electromagnets are mounted on robot terminations so that it can grip on ferromagnetic surfaces. While improving overall hygienicity, the adhesion energy requirements still constitute a considerable issue. Moreover, the typical aseptic manufacturing area walls are made of AISI 316 stainless steel which is notably non-ferromagnetic (see Section 1.2). Additional ferromagnetic plates may be installed behind the walls as a partial workaround; however, in order to compensate the increased gap, required electromagnetic forces would be higher and the solution would lose much of the sought flexibility. Anyway, it would still not be possible to overcome the glass portholes present on workplace walls.

A completely different approach is to emulate natural climbing animals. Among these, the gecko has attracted much interest due to the high adhesion force-dimension ratio and the ability to attach to almost any surface, regardless of vertical or (downward) horizontal orientation. In particular, it has been proved that the gecko adhesion mechanism is based on molecular van der Waals forces [8]. This *dry adhesion* is made possible through billions of tiny fibers that the animals has on the tip of its toes, which together enormously increase the contact surface area so to achieve a significant action. Once the adhesion mechanism is properly started through a preload on the fibers, it is able to exert forces in the order of $10\,\mathrm{N/cm^2}$ [7]. Since this type of adhesion does not rely on any secretion, the surface material has little

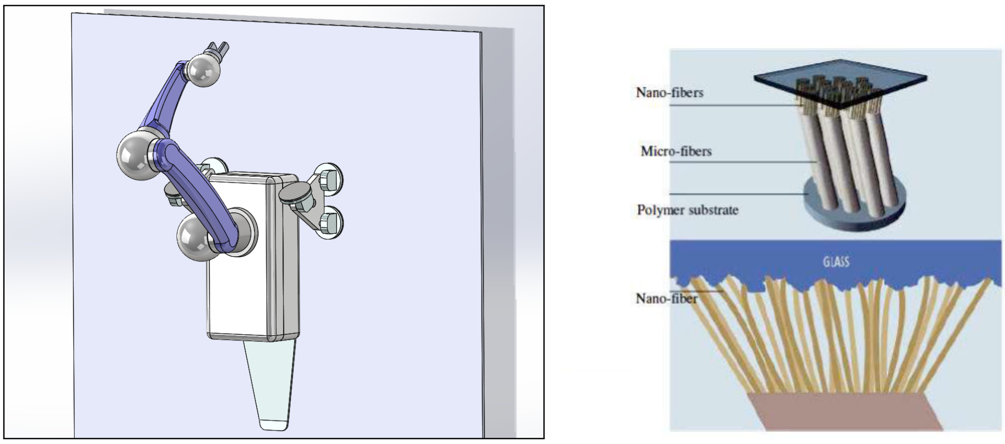

(a)

(b)

Figure 17: (a) Gecko robot concept equipped with generic arm. (b) Micro and nano-scale gecko foot-fibers [73].

effect on it [8]; moreover, the super-hydrophobic properties of natural and synthetic fibers make them independent from dry or wet condition of target surfaces. It should also be highlighted that dry adhesion do not require external energy to be maintained; thus, an artificial vehicle could achieve significant reduction in battery size, increment in payload and less need for recharges. Since attach and detach are performed only by correct inclination of fiber against the surface, both actions are almost instantaneous: locomotion may be sufficiently fast for industrial applications.

Some mobile robot based on such idea have been successfully developed, in different configurations (see for example [73]). Dry adhesion can be exerted by belts mounted on motorized pulleys, so to act as crawlers; however, hygienicity would be irremediably compromised. A more suitable implementation should make use of *whegs* (union of “wheels” and “legs”), at top of which synthetic fibers are disposed (see Fig. 17). Two motors are used in differential configuration to allow straight and curved locomotion; at the end of the two shafts, a proper number of foots are pinned on the rotating structure, so that at least two feet are pressed at the same time against the wall. Preload on feet must be guaranteed by an elastic member of the robot. Instead of a common spring, which is not suitable to aseptic environments, a deformable tail is used. With correct design of tail compliance, distance between contact points and adhesion surface area, a lightweight robot arm could be mounted on top of the exposed structure.

2.3.3 Robot on rail

The last proposed concept is based on a more traditional approach, namely a robot arm installed on a cart that slides along a fixed rail. The main vehicle can be shaped as a sealed box containing supply battery, motors, and drives; suitable slots may be optionally placed on the outer box surface for workplace equipment relocation. If a dedicated station is installed at the end of the rail, it is possible to perform both recharge and sterilization of the robot. The most intuitive way to implement the locomotion system would be to realize a rack-pinion mechanism, which is able to move high loads for arbitrary long paths and allows absolute positioning of the cart. In the contest of aseptic industry, two main drawbacks discourage us to consider the idea. First, it would be very hard to produce teeth adapt to cover sharp curves. Secondly, the rack would be most difficult to clean effectively and would greatly threaten the workplace asepticity. In the present case, a better option is to design a wheeled cart that moves on a smooth rail. Since slippage may occur, a sensor feedback system must be implemented to compensate for positioning uncertainty. A simple and robust solution may be to combine in redundancy odometric data (e.g. collected through multiturn absolute encoders) with a linear pseudo-random code photo-engraved on the rail surface and continuously read by a sensor installed on the cart [24]; alternatively, RFIDs can be inserted in the rail at periodic distances, so to reset potential drifts.

Chapter 3

Mechanical Design

3.1 Kinematic model and analysis

As for any other mechanism, the design of a robot starts from the preliminary identification of its member dimensions and motor sizes. This section is intended to describe the kinematic premises of 6-DOF robot, as well as the main mathematical instruments useful to model it. The information retrieved from this process will constitute the baseline for subsequent detailed implementation.

3.1.1 Mathematical background

The 6-DOF articulated arm consists of a *serial* kinematic chain of bodies, each of which is connected to the others by an actuated revolute joint. In this work, for reasons that will be motivated in Section 3.3 and Section 4.2.1, we will specifically refer to a robot architecture that meets the condition of spherical wrist, i.e. having the last three DOF axes that intersect in a common point.

The first basic problem of robotics involves the transformation of position vectors in different coordinate systems. In particular, it is often useful to express the position of manipulator Tool Center Point (TCP) – which is known in the manipulator local reference frame – with respect to the fixed world coordinate system. From a theoretical point of view, a generic 3D vector can be represented in different frames of reference through the affine transformation

$$\mathbf{p}_{\mathrm{a}} = \mathbf{t}_{\mathrm{ab}} + \mathbf{R}_{\mathrm{ab}}\mathbf{p}_{\mathrm{b}} \tag{3.1}$$

where $\mathbf{p}_{\mathrm{i}}$ denotes the vector in the i frame, $\mathbf{t}_{\mathrm{ab}}$ represents the translation of frame b origin with respect to frame a, and $\mathbf{R}_{\mathrm{ab}}$ is the rotation matrix of frame b with respect to frame a (see Fig. 18). Although efficient to compute (9 multiplications and 9 sums of floating point numbers), the affine transformation is quite unhandy to employ when several consecutive base changes are required. In this scenario,

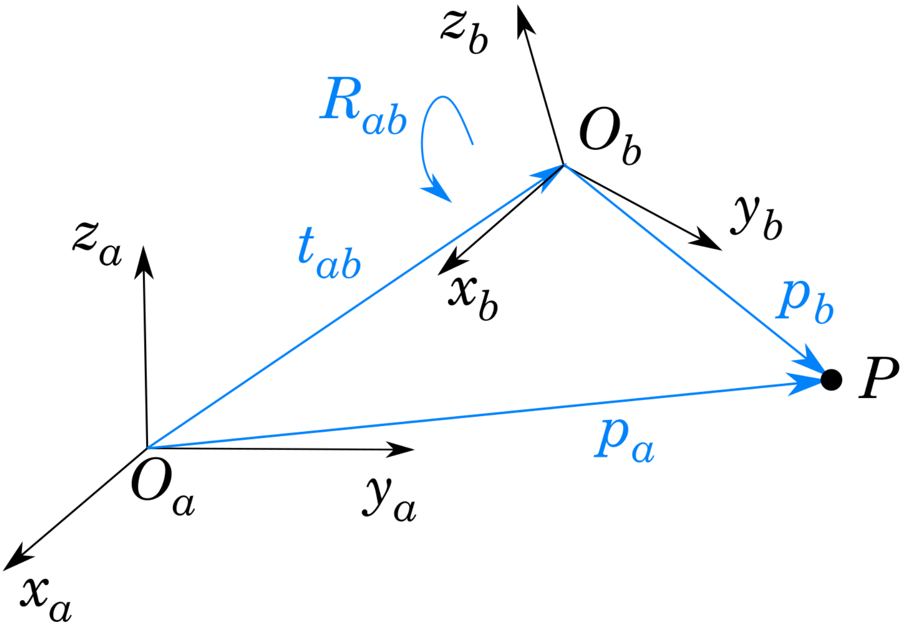

Figure 18: Coordinate system transformation.

typical of robotics, a homogeneous approach is usually preferred: the translation and rotation operations are condensed in a single 4×4 transformation matrix and the position vectors are reshaped into a 4×1 form to preserve dimensional coherence. Consequently, Eq. (3.1) can be reformulated as

$$\underline{\mathbf{p}_{\mathrm{a}}} = \mathbf{H}_{\mathrm{ab}}\underline{\mathbf{p}_{\mathrm{b}}} \tag{3.2}$$

where

$$\mathbf{H_{ab}} = \left(\begin{array}{ccc|c} & \mathbf{R}_{\mathrm{ab}} & & \mathbf{t}_{\mathrm{ab}} \\ \hline 0 & 0 & 0 & 1 \end{array}\right) \qquad \underline{\mathbf{p}_{\mathrm{i}}} = \left(\begin{array}{ccc|c} p_x & p_y & p_z & 1 \end{array}\right)^{\mathrm{T}} \tag{3.3}$$

Multiple subsequent reference conversions are performed by the means of simple matrix pre-multiplications; in return, the computational burden is increased to 16 multiplications and 12 sums per transformation. The robot *forward kinematics* function $f_{\mathrm{FK}} : \boldsymbol{\theta} \mapsto \mathbf{q}$ is easily computed by the means of this instrument; in other words, end-effector configuration $\mathbf{q}$ in Cartesian space can be retrieved for any given configuration of motor rotations $\boldsymbol{\theta}$ in joint space.

The rest of the robot can be modeled as a set of floating reference frames attached to each body and moving together with it. The choice of frames location is arbitrary, but it requires some precautions to be conveniently handled. For example, as a basic approach, each frame could be placed at the center of gravity of the parent robot member. Albeit simple in principle, this method is hardly practical due to

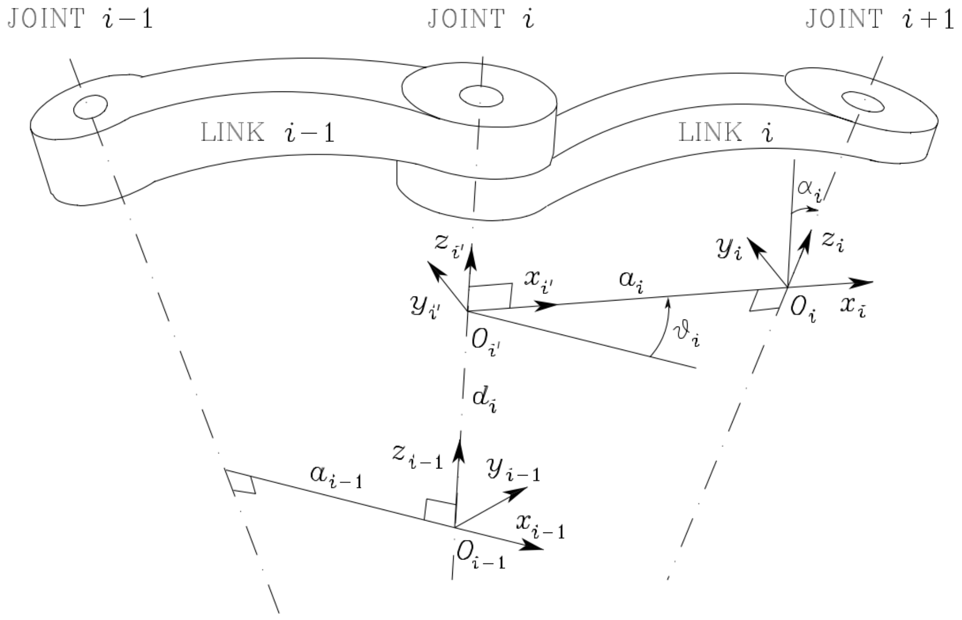

Figure 19: Denavit-Hartenberg notation for link frames selection [99].

the many translational and rotational parameters involved to formulate Eq. (3.5); in addition, any modification made to the robot bodies would impose to recompute the frame positions. A step toward efficiency consists in the choice of the frames along the robot joint axes, possibly at the intersections; even so, the extent of arbitrariness is still quite large. A unified procedure, vastly popular in the fields of robotics and applied mechanics, was introduced by J. Denavit and R. Hartenberg [23]; the main idea of Denavit-Hartenberg notation (D-H) is illustrated in Fig. 19. Given two bodies, Link $i-1$ and Link i, that are connected by Joint i about Axis i, we can define link Frame i through the following recursive procedure:

1. Place axis $\mathbf{z_i}$ along the axis of Joint $i+1$.

2. Retrieve the common normal[1] $\mathbf{n_i}$ to axes $\mathbf{z_{i-1}}$ and $\mathbf{z_i}$. Origin O_i is placed at the intersection of $\mathbf{n_i}$ with axis $\mathbf{z_i}$. In addition, a dummy origin $O_{i'}$ is placed at the intersection of $\mathbf{n_i}$ with axis $\mathbf{z_i}$.

3. Choose axis $\mathbf{x_i}$ along the common normal $\mathbf{n_i}$ and pointing from $O_{i'}$ to O_i.

4. Choose axis $\mathbf{y_i}$ so as to complete a right-handed frame.

---

[1] The common normal between two axes is the line, perpendicular to both, that contains the minimum distance segment between them.

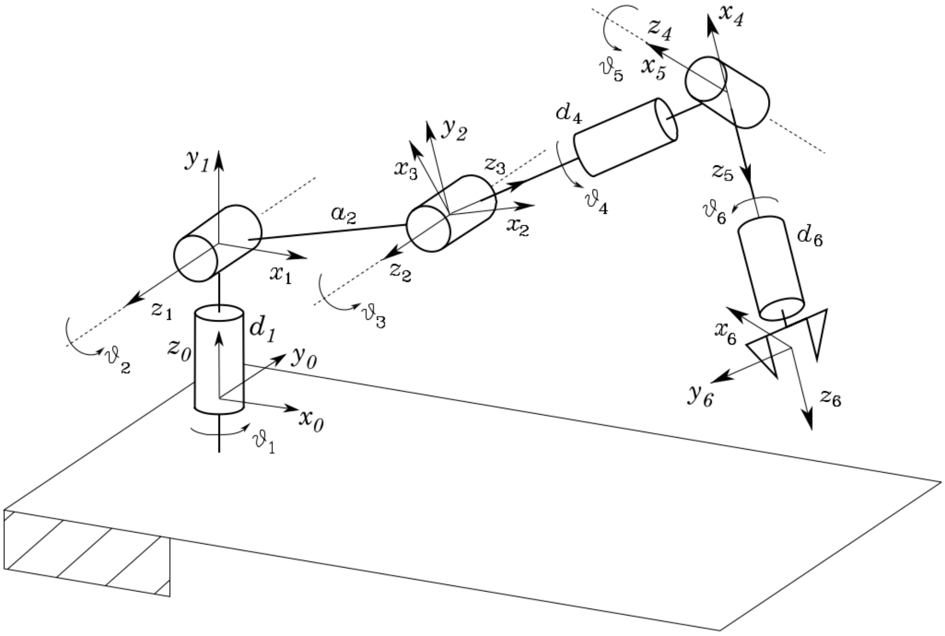

Figure 20: 6-DOF articulated robot kinematic model, with spherical wrist; frames are placed in accordance to Denavit-Hartenberg notation. Adapted from [99].

Though the exposed notation is not always uniquely defined, the potential remaining indeterminacy can be exploited to simplify the procedure. For example, in the case of the first frame, only the direction of axis $\mathbf{z_0}$ is specified: O_0 and $\mathbf{x_0}$ may be arbitrarily chosen. If two consecutive axes are parallel, the common normal is not uniquely defined and O_i can be placed at the most convenient height. Finally, if two consecutive axes intersect, the positive direction of $\mathbf{x_i}$ is arbitrary. Once the link frames have been established, it is easy to express the configuration of frame i with respect to frame $i-1$ through the homogeneous transformation

$$\mathbf{H_{i-1,i}}(\theta_i) = \left(\begin{array}{c|c} \mathbf{R}(\mathbf{z_{i-1}}, \theta_\mathbf{i}) \cdot \mathbf{R_{i-1,i}} & \mathbf{t_{i-1,i}}(\theta_\mathbf{i}) \\ \hline 0 \;\; 0 \;\; 0 & 1 \end{array} \right) \tag{3.4}$$

and complete the kinematic model of the robot; the result is illustrated in Fig. 20. A significant advantage presented by D-H notation is the possibility to easily automate the task. In fact, under the prescribed instructions, the relative transformation between consecutive frames can be expressed by the means of only four parameters:

- link length a_i: distance between $\mathbf{z_{i-1}}$ and O_i (or, equivalently, between $O_{i'}$ and O_i);
- twist α_i: angle between axes $\mathbf{z_{i-1}}$ and $\mathbf{z_i}$ with respect to axis $\mathbf{x_i}$ (positive if counter-clockwise);

- offset d_i: distance between O_{i-1} and $\mathbf{x_i}$ (or, equivalently, between O_{i-1} and $O_{i'}$);
- rotation θ_i: angle between axes $\mathbf{x_{i-1}}$ and $\mathbf{x_i}$ with respect to axis $\mathbf{z_{i-1}}$ (positive if counter-clockwise).

The D-H parameters can be collected in a table to completely describe the robot architecture. Each coordinate transformation is obtained by multiplication of the single transformations as [99]:

$$\mathbf{H_{i-1,i}}(a_i, \alpha_i, d_i, \theta_i) = \left(\begin{array}{ccc|c} \cos\theta_i & -\sin\theta_i\cos\alpha_i & \sin\theta_i\sin\alpha_i & a_i\cos\theta_i \\ \sin\theta_i & \cos\theta_i\cos\alpha_i & -\cos\theta_i\sin\alpha_i & a_i\sin\theta_i \\ 0 & \sin\alpha_i & \cos\alpha_i & d_i \\ \hline 0 & 0 & 0 & 1 \end{array}\right) \tag{3.5}$$

In conclusion, either through Eq. (3.4) or Eq. (3.5) approaches, the TCP of a 6-DOF robot can be expressed in the base absolute reference, at any joint configuration $\boldsymbol{\theta}$, in terms of the following relation:

$$\begin{aligned} \underline{\mathbf{p}_0} &= \mathbf{H}_{06}\underline{\mathbf{p}_6} = \\ &= \mathbf{H}_{01}\mathbf{H}_{12}\mathbf{H}_{23}\mathbf{H}_{34}\mathbf{H}_{45}\mathbf{H}_{56}\underline{\mathbf{p}_6} \end{aligned} \tag{3.6}$$

The results achieved so far can be significantly extended with the introduction of another powerful tool, namely the robot forward kinematics *Jacobian matrix*

$$\mathbf{J}_{\text{FK}}(\boldsymbol{\theta}) = \frac{\mathrm{d}f_{\text{FK}}(\boldsymbol{\theta})}{\mathrm{d}\boldsymbol{\theta}} = \begin{pmatrix} \dfrac{\partial f_{\text{FK}_1}}{\partial\theta_1} & \cdots & \dfrac{\partial f_{\text{FK}_1}}{\partial\theta_n} \\ \vdots & \ddots & \vdots \\ \dfrac{\partial f_{\text{FK}_1}}{\partial\theta_1} & \cdots & \dfrac{\partial f_{\text{FK}_m}}{\partial\theta_n} \end{pmatrix} \tag{3.7}$$

The analytical definition of $\mathbf{J}_{\text{FK}}(\boldsymbol{\theta})$ is conveniently employed when the forward kinematics is sufficiently easy to formulate (e.g. for simple manipulators with limited DOFs). In the opposite, and actually frequent case, the same matrix elements can be obtained numerically by the means of a finite differentiation

$$\mathbf{J}_{\text{FK}}(\boldsymbol{\theta})_{ij} \approx \left(\frac{\Delta f_{\text{FK}}(\boldsymbol{\theta})}{\Delta\boldsymbol{\theta}}\right)_{ij} = \frac{f_{\text{FK}}(\boldsymbol{\theta} + h\mathbf{e}_j)_i - f_{\text{FK}}(\boldsymbol{\theta})_i}{h} \tag{3.8}$$

where h is a small increment (e.g. in the order of $1\mathrm{e}-6$) and $\mathbf{e}_j$ is a unitary vector of the same size of $\boldsymbol{\theta}$ containing 0 in all but j-th position.

Joint space velocities and accelerations of the manipulator can be mapped to the corresponding workspace quantities by simple multiplication of the FK Jacobian matrix:

$$\begin{aligned} \delta\mathbf{q} &\approx \mathbf{J}_{\mathrm{FK}}(\boldsymbol{\theta})\delta\boldsymbol{\theta} \\ \dot{\mathbf{q}} &= \mathbf{J}_{\mathrm{FK}}(\boldsymbol{\theta})\dot{\boldsymbol{\theta}} \\ \ddot{\mathbf{q}} &= \mathbf{J}_{\mathrm{FK}}(\boldsymbol{\theta})\ddot{\boldsymbol{\theta}} + \dot{\mathbf{J}_{\mathrm{FK}}}(\boldsymbol{\theta})\dot{\boldsymbol{\theta}} \end{aligned} \tag{3.9}$$

Finally, we can determine the actions that the motors must exert in order to contrast the external loads applied to the end-effector. If we assume to neglect member weights and inertia actions, the Principle of Virtual Work can be employed to solve the static problem at a configuration of equilibrium. In the above hypothesis, the vector of workspace generalized forces $\mathbf{F}_q$ and the vector of joint generalized forces $\mathbf{F}_\theta$ (actual forces for prismatic joints and torques for revolute joints) are linked by the following equation:

$$\delta W = \mathbf{F}_\theta^T\delta\boldsymbol{\theta} + \mathbf{F}_q^T\delta\mathbf{q} = 0 \tag{3.10}$$

Substituting the first relation of Eq. (3.9) we can re-write

$$\delta W = \mathbf{F}_\theta^T\delta\boldsymbol{\theta} + \mathbf{F}_q^T\mathbf{J}_{\mathrm{FK}}(\boldsymbol{\theta})\delta\boldsymbol{\theta} = (\mathbf{F}_\theta^T + \mathbf{F}_q^T\mathbf{J}_{\mathrm{FK}}(\boldsymbol{\theta}))\delta\boldsymbol{\theta} = 0 \tag{3.11}$$

which leads to

$$\mathbf{F}_\theta^T + \mathbf{F}_q^T\mathbf{J}_{\mathrm{FK}}(\boldsymbol{\theta}) = 0 \tag{3.12}$$

or, equivalently

$$\mathbf{F}_\theta = -\mathbf{J}_{\mathrm{FK}}(\boldsymbol{\theta})^T\mathbf{F}_q \tag{3.13}$$

The negative sign appearing in Eq. (3.13) denotes that, in the adopted convention, $\mathbf{F}_\theta$ is the action applied *by* the motors to reach the equilibrium configuration; thus, an action $-\mathbf{F}_\theta$ is applied *on* the motors.

3.1.2 Preliminary sizing

With the basic mathematical tools described above, we are able to perform a preliminary sizing of robot motors and links, which will guide us in the detailed prosecution of the project.

Recalling the objectives stated in Section 2.1, we begin by assuming that the arm horizontal reach is equal to 800 mm. Consequently, with reference to Fig. 20, the preliminary link lengths are chosen so that $d_1 = 300\,\mathrm{mm}$ and $a_2 + d_4 + d_5 = 800\,\mathrm{mm}$; more specifically, it is assumed that $a_2 = 400\,\mathrm{mm}$, $d_4 = 300\,\mathrm{mm}$, and $d_6 = 100\,\mathrm{mm}$. The robot kinematic description is formulated in accordance to Denavit-Hartenberg notation, whose parameters collection is summarized in Table 3.1.

A basic 3D simulation of the model is presented in Fig. 21, where the robot joints are represented as blue circles, links are depicted as black segments, and the end-effector is marked as a red circle. Fig. 21a shows the robot at its (home) rest configuration, in which $\boldsymbol{\theta} = \mathbf{0}$; the boundary workspace (i.e. the maximum volume reached by the arm at full extension) is highlighted as a blue wireframe sphere

Table 3.1: D-H parameter table of preliminary 6-DOF robot model.

Link	a_i [mm]	α_i [rad]	d_i [mm]	θ_i [rad]
1	0	$\pi/2$	$d_1 = 300$	θ_1
2	$a_2 = 400$	0	0	θ_2
3	0	$\pi/2$	0	$\theta_3 + \pi/2$
4	0	$-\pi/2$	$d_4 = 300$	θ_4
5	0	$\pi/2$	0	$\theta_5 - \pi/2$
6	0	0	$d_6 = 100$	θ_6

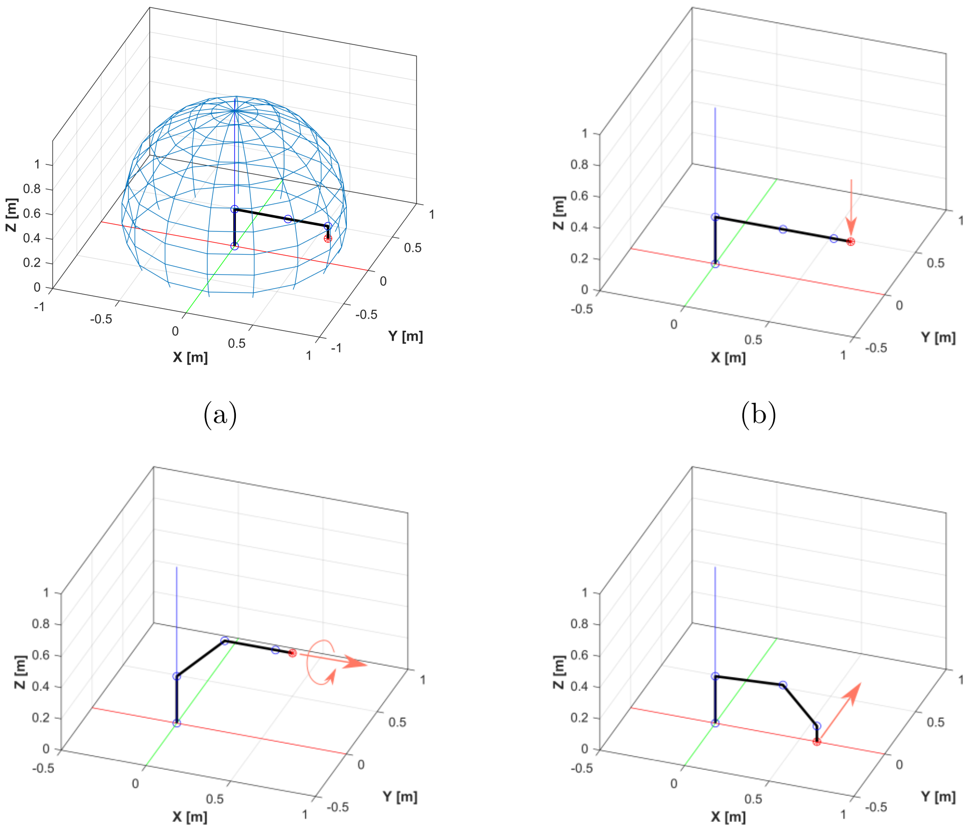

(a) (b)

(c) (d)

Figure 21: Simulated robot model and tested operative scenarios: (a) robot at home configuration, with boundary workspace highlighted in blue; (b) payload sustain at maximum reach; (c) object pulling/threading retrieval; (d) sliding friction pick&place.

with radius $r = 800\,\text{mm}$ and volume $V = \pi(r + d_1)^2\,(r - (r + d_1)/3) = 1.65\,\text{m}^3$. In force of Eq. (3.13), the model is subsequently used to test three different operative scenarios, which the robot is likely to face: maximum payload Fig. 21b, object retrieval Fig. 21c and sliding pick&place Fig. 21d. In the first scenario, a vertical downward force F_z is applied to the end-effector while the arm is extended at its maximum reach. A first contribution F'_z is due to the weight of a gripped object which, in accordance to Section 2.1, is assumed of payload mass $m_p = 2\,\mathrm{kg}$. In addition to this, F_z accounts for the equivalent weight of the part of the arm that is downstream with respect to shoulder joint axis F''_z. With reference to Fig. 20, for the sake of a preliminary analysis, a linear distribution of mass with respect to links lengths is assumed:

$$m_0 = M\frac{d_1}{L_t} \qquad m_1 = M\frac{a_2}{L_t} \qquad m_2 = M\frac{d_4}{L_t} \qquad m_3 = M\frac{d_6}{L_t} \tag{3.14}$$

where M is robot total mass, and $L_t = d_1 + a_2 + d_4 + d_6$ is its total length. With the same rationale, we may estimate the COG distance of this portion of arm as

$$d_{\mathrm{COG}} = \frac{m_1 a_2 + m_2 d_4 + m_3 d_6}{m_1 + m_2 + m_3} \tag{3.15}$$

The equivalent load F''_z, transported to the end-effector is computed with:

$$F''_z = (m_1 + m_2 + m_3)\frac{d_{\mathrm{COG}}}{L_t} g \tag{3.16}$$

Hence, if we assume a payload mass incremented by 50% (for the sake of precaution) and an arm total mass $M = 15\,\mathrm{kg}$ (in the mid-range of project target), we obtain:

$$F_z = F'_z + F''_z = \left[1.5 m_p + (m_1 + m_2 + m_3)\frac{d_{\mathrm{COG}}}{L_t}\right] g = 58.2\,\mathrm{N} \tag{3.17}$$

In the above hypothesis, the required equilibrium motor torques result:

$$\mathbf{F}_{\theta,1} = -\mathbf{J}_{\mathrm{FK}}(\boldsymbol{\theta_1})^T \cdot \begin{pmatrix} 0 \\ 0 \\ F_z \\ 0 \\ 0 \\ 0 \end{pmatrix} = \begin{pmatrix} 0 \\ 46.6 \\ 23.3 \\ 0 \\ 5.8 \\ 0 \end{pmatrix} \mathrm{N\,m} \qquad \text{with } \boldsymbol{\theta_1} = \begin{pmatrix} 0 \\ 0 \\ 0 \\ 0 \\ \pi/2 \\ 0 \end{pmatrix} \mathrm{rad} \tag{3.18}$$

In the second scenario, an axial F_x force is applied to the end-effector in order to simulate the retrieval of an object through a pulling operation (or, analogously, a pushing plug). An additional twisting T_x torque load is superposed as well, so to represent a potential concurrent “threading” resistance. Since the robot is not supposed to perform particularly heavy tasks and the objects involved are fairly light, it is assumed that $F_x = 20\,\mathrm{N}$ and $T_x = 5\,\mathrm{N\,m}$. In this case, the motor torques result

$$\mathbf{F}_{\theta,2} = -\mathbf{J}_{\mathrm{FK}}(\boldsymbol{\theta_2})^T \cdot \begin{pmatrix} F_x \\ 0 \\ 0 \\ T_x \\ 0 \\ 0 \end{pmatrix} = \begin{pmatrix} 0 \\ 5.7 \\ 0 \\ -5 \\ 0 \\ -5 \end{pmatrix} \mathrm{N\,m} \qquad \text{with } \boldsymbol{\theta_2} = \begin{pmatrix} 0 \\ \pi/4 \\ -\pi/4 \\ 0 \\ \pi/2 \\ 0 \end{pmatrix} \mathrm{rad} \tag{3.19}$$

The third and last scenario tests the pick&place relocation of a small object laying on the ground and producing a sliding friction resistance on the end-effector. The object, of nominal payload mass $m_p = 5\,\mathrm{kg}$, is placed at a distance $x = 0.6\,\mathrm{m}$ from the robot base; the static friction coefficient is assumed as a typical dry steel-on-steel value $f_s = 0.75$. The subsequent friction force is $F_y = f_s m_p g = 36.8\,\mathrm{N}$; in this condition, the required torques result

$$\mathbf{F}_{\theta,3} = -\mathbf{J}_{\mathrm{FK}}(\boldsymbol{\theta_3})^T \cdot \begin{pmatrix} 0 \\ F_y \\ 0 \\ 0 \\ 0 \\ 0 \end{pmatrix} = \begin{pmatrix} -22.4 \\ 0 \\ 0 \\ -2.5 \\ 0 \\ -0 \end{pmatrix} \mathrm{N\,m} \qquad \text{with } \boldsymbol{\theta_3} = \begin{pmatrix} 0 \\ 0.06 \\ -0.87 \\ 0 \\ 0.84 \\ 0 \end{pmatrix} \mathrm{rad} \tag{3.20}$$

In conclusion, we assume as preliminary design drives torques the maximum component values that emerged in each tested scenario

$$\mathbf{T} = \max(\mathbf{F}_{\theta,1}, \mathbf{F}_{\theta,2}, \mathbf{F}_{\theta,3}) = \begin{pmatrix} 22.4 \\ 46.6 \\ 23.3 \\ 5 \\ 5.8 \\ 5 \end{pmatrix} \mathrm{N\,m} \approx \begin{pmatrix} 20 \\ 50 \\ 30 \\ 5 \\ 5 \\ 5 \end{pmatrix} \mathrm{N\,m} \tag{3.21}$$

3.2 Custom drive

The design of a custom robot is an iterative process, which concurrently involves the mutual interaction of actuators, joints and links. In this work, the activity is started from the design of the mechanical drives, with respect to which the rest of the robot is going to be shaped. The term *drive* is here used in its largest meaning, i.e. to indicate the assembly including all the mechanical and electrical components needed for motion:

- motor;

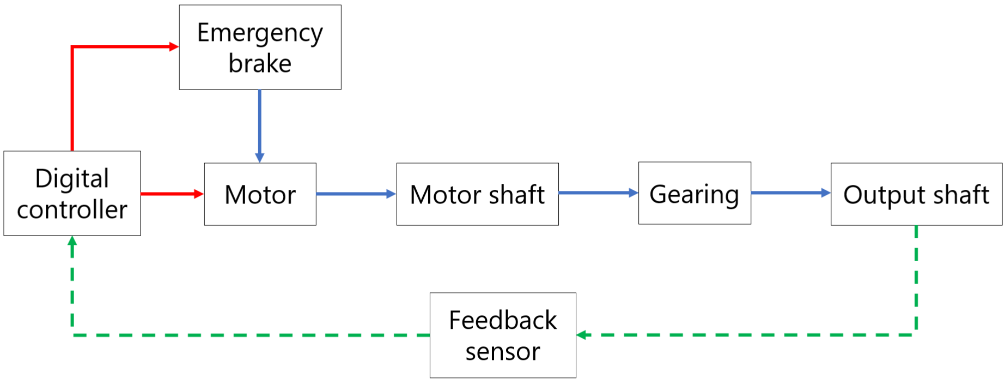

Figure 22: Functional schematics of drive concept. Blue: mechanical energy; red: electric energy; green: information.

- digital controller (or digital drive, or servo drive);
- mechanical transmission (motor shaft, gearing, output shaft);
- feedback sensors;
- emergency brake.

A schematic functional representation is illustrated in Fig. 22. The target application is characterized by precise slow-speed operations, performed by a slender arm: as such, the main objectives of this section is to devise a compact modular, lightweight drive with the highest possible torque density.

3.2.1 Motor scouting

The first step consists in the selection of an appropriate set of motors, which both satisfy the mechanical requirements and, indirectly, move toward the meeting of aseptic constraints. Among the many other technologies available (brushed DC motor, stepper DC motor, asynchronous AC motor, etc.) we restrict the search to brushless DC motors. A BLDC motor is an electronically commutated motor that uses a digital closed-loop controller to switch DC currents in the stator windings, so to produce a rotating magnetic field to which the rotor powerful rare-earth permanent magnets synchronize. In particular, the motor is able to exert a constant-torque profile, proportional to the input current and the number of pole pairs. The advantages of a brushless motor include high torque-to-weight ratio, high speed, fast control of speed and torque, high efficiency, and low maintenance.

Table 3.2: Main specifications of scouted commercial BLDC motors.

	Celera UTO-52	Delta 50BLF15	Exmek TF060	Maxon EC60	Parker PD-04	SDP/SI NH1-D35
Rated current [A]	6.9	4.8	5.7	2.78	1.12	3.07
Rated voltage [V]	50	48	48	48	-	48
Rated torque [Nmm]	353	500	706	319	3000	150
Rated speed [rpm]	4000	3500	2000	3490	500	4800
Torque const [Nm/A]	0.052	0.110	0.124	0.114	2.76	0.042
Weight [g]	176	135	500	333	6300	104
Out diameter [mm]	40.89	50	30.3	60	135	35.6
In diameter [mm]	17.84	30	28.7	20	78	9.73
Length [mm]	17.53	26	36	37	78	26.03
Hall sensors	No	Yes	Yes	Yes	No[1]	No
Torque dens. [Nmm/g]	2	3.7	1.4	1	0.8	1.44
Rating [1-5]	3	4	3	5	1	2

[1] 20-bit absolute encoder equipped.

We begin the scouting of market available solutions by looking for small-sized, frameless, flat BLDC motors that can be easily interfaced to a lightweight, custom geometry housing. A fundamental constraint consists in the need of a hollow design, so to allow internal cable passage throughout the robot (the arm enclosed structure requires that the wiring is routed inside it and traverse the various drives). Additionally, the motor is selected with a low rated voltage as the potential implementation of the robot in a moving architecture would impose the use of a battery supply. Table 3.2 summarizes the specifications of the most promising BLDC motors that satisfy the exposed design restrictions (see also Fig. 23). Indeed, many different sizes are available for each presented manufacturer product family; for the sake of a fair comparison, the same overall size is take in consideration for each of them.

Among the reported products, the Parker model stands out for superior output torque and the presence of an integrated absolute encoder; unfortunately, the great result is obtained at the expense of both size and weight, that are considerably out of the preliminary constraints: the product is therefore discarded. The remaining models present, on the other hand, comparable specifications and require for deeper considerations. A first discriminant is constituted by the presence of integrated Hall sensors, which helps to reduce both design complexity and footprint; for analogous reasons, the presence of an integrated rotor flange is taken into major consideration. Another important selection criterion involves the motor torque constant: a high value results in a better exploitation of battery charge and longer operative service,

(a) (b) (c)

Figure 23: Examples of scouted commercial BLDC motors: (a) Celera UTO-52, (c) Delta-Line 50BLF15, (c) Maxon EC60.

in case of mobile implementation. Lastly, a large motor inner diameter with respect to the overall dimension is preferred, as the same motor can be used to equip more arm joints (provided that the output torque is sufficient). Given the above considerations, the analyzed motors are rated on a scale from 1 to 5; the highest-ranking model, Maxon EC60, is consequently selected as drive motor prototype.

3.2.2 Controller scouting

The world of robotics is characterized by stringent time control frames, typically in the order of 1-10 ms [99]. The use of a suitable digital controller is hence imperative to obtain the demanded position, velocity and acceleration profiles. Many important hardware and software features influence the selection of the drive: nominal and peak output current, control loop frequency, regulation scheme technology (PID, PIV, etc.), real-time fieldbus interface are only part of a much longer list. In the present specific case, two additional constraints limit the potential options. First, unlike common industrial practice, the controller can not be housed inside a dedicated electrical cabinet, but has to be stored directly on board the robot due to its potential mobile implementation; this requirement results in the need of a sufficiently small and lightweight product. Secondly, given the custom nature of the mechanical drive assembly, the controller must retain the flexibility to be interfaced with motors and sensors produced by other manufacturers.

The list of scouted digital drives (see Fig. 24), together with the main respective specifications, is reported in Table 3.6. The products are comparable in sheer technical features and, overall, fulfill the above selection criteria. The ratings are consequently assigned on the basis of weight and footprint considerations.

Table 3.3: Main specifications of scouted commercial motion control digital drives.

	Celera CAP-XCR-C	Delta B400B30	Maxon EPOS4
Rated in voltage [V]	8-60	12-48	10-50
Rated out current [A]	10	10	5
Peak out current [A]	20	28	15
PWM frequency [kHz]	20	40	15
Fieldbus interface	CAN, EtherCAT	CAN, EtherCAT, Modbus	CAN, EtherCAT
Sensor interface	SSI, BiSS	RS422	SSI
Length [mm]	42	139	55
Width [mm]	29	88.8	40
Height [mm]	19.4	30	31
Weight [g]	28	150	58
Rating [1-3]	3	2	3

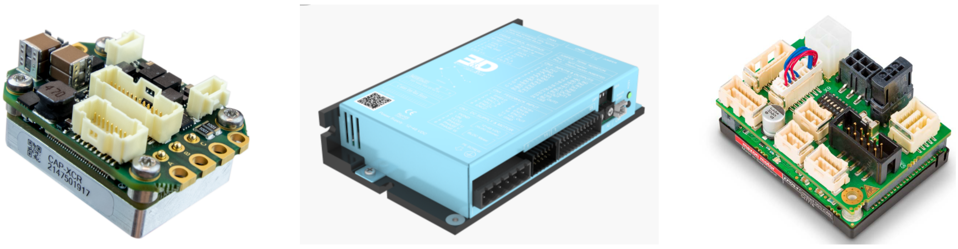
(a) (b) (c)

Figure 24: Examples of scouted commercial digital controllers: (a) Celera CAP-XCR-C, (b) Delta-Line B400B30, (c) Maxon EPOS4.

3.2.3 Gearing scouting

Gearing is a crucial component and its correct selection represents a fundamental step in the realization of a high-performing robot; as such, many concurrent constraints must be taken in consideration. Starting from Table 3.2 data, it is easy to observe that BLDC electric motors are characterized by high rotational speed and negligible output torque. Typical robotics application, on the contrary, require for lower speeds (in the order of 10^1rpm) and much higher torques: consequently, gearing reduction ratio[1] must be very high, in the order of 100:1. In common applications, gearing represents one of the main sources of robot weight; the issue is addressed by the use of high-size motors and external counterweights. In the present case, however, the option is not viable: a compact, lightweight and low rotational inertia product is hence searched. Moreover, the slender and enclosed structure of the target robot requires for a hollow gearing architecture whose input and output shaft are retained coaxial. In order to achieve high robot performance in terms of repeatability and manipulator positioning accuracy, zero-to-minimal backlash must be introduced by the component. Finally, high transmission efficiency is taken in consideration, so to fully exploit motor performance and minimize battery power consumption, if any.

Many architectures are available in the field of gearing transmissions. The option of ordinary spur gears is immediately discarded in force of the limited reduction ratios produced per stage and the considerable weight of the assembly. A viable alternative is constituted by *epicyclic gear trains* (also know as *planetary gearset*). This gearing technology consists of one, or multiple, gears (planet pinion) revolving around a central gear (sun wheel) and constrained into a fixed ring gear; the input motion, provided by the sun, is ultimately transmitted to the output by a pinion-carrying member. Although being frequently used in general-purpose robotics, the planetary gearset is hardly adjustable to a hollow configuration, especially if low outer diameter and multiple stages are required. The appropriate technology, selected for our application, is constituted by strain wave gearing, also known as *harmonic drive* gearing. Harmonic drives are a peculiar category of mechanical gearing, whose transmission principle is based on the elastic deformation of a flexible component (see Fig. 25a) and that are characterized by high positioning accuracy (e.g. 1-2′), low backlash, high torsional rigidity and high load capacity. Only three components are required for the gearing operation

- Wave Generator (WG): elliptical element providing input rotational motion.
- Flex Spline (FS): subtle flexible element deformed by the wave generator during its rotation and providing output rotational motion.
- Circular Spline (CS): fixed outer gear ring, with internal teeth, to which the flex spline is engaged.

While the WG rotates, the contact point of FS and CS teeth progressively move in the opposite direction; if a small difference in the number of teeth is present, huge reduction ratio may be achieved (e.g. in the order of 50:1 to 320:1 per stage), as

---

[1] In this work, the gearing reduction ratio i (input speed vs output speed) will be frequently indicated as a quotient (e.g. 100:1) or simply by the resulting ratio (e.g. 100).

Table 3.4: Main specifications of scouted commercial harmonic drive gearing.

	China Harmonic Drive CHD-32[1]	Harmonic Drive SE CSD-32-2A[2]	Toteltech XSF-32[1]
Gear ratio [-]	120:1	160:1	160:1
Rated torque [Nm]	91	96	137
Backlash [″]	≤20	≤10	≤20
Out diameter [mm]	132	110	110
In diameter [mm]	14	32	18
Length [mm]	27.9	22	44
Weight [kg]	1.92	0.51	0.89
Rating [1-3]	1	3	2

[1] Key connection to shaft. [2] Flange connection to shaft.

enforced by the following relation:

$$i = \frac{z_{FS}}{z_{CS} - z_{FS}} \tag{3.22}$$

An interesting feature possessed by some commercial harmonic drive models consists in the fact that they may be purchased in a *component set* configuration. If this option is adopted, only the three core gearing components are offered, without any additional casing; the creation of appropriate supports and housing is hence delegated to the user. This feature is most convenient for the present custom application: even if more complex design process is required, the shape of the drive assembly can be tailored for the purpose and suitably optimized. The list of commercial products that meet the above requirements is reported in Table 3.4, together with the main technical specifications; Fig. 25 illustrates some of the presented models. The highest score is achieved by the Harmonic Drive SE product, which stands out for all the selection criteria: highest reduction ratio, minimal internal backlash, extremely compact size, low weight, large internal hole diameter; additionally, instead of a key groove, an outer connection flange is provided: this important practical feature helps to reduce backlash during component operation.

3.2.4 Encoder scouting

The feedback of the angular position of a rotating member can be obtained by the means of two main electronic transducers: the resolver and the encoder. The first device is based on electromagnetic induction and consists of a powered winding, rotating with the rotor, and two fixed windings shifted by 90°; the angular position of the rotor is retrieved through the measurement of the concatenated voltage on the fixed winding. Although highly accurate and reliable, this intrinsically

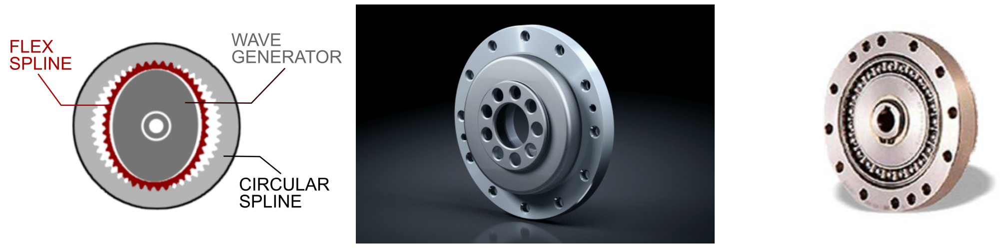

(a) (b) (c)

Figure 25: (a) Harmonic Drive gearing main components: circular spline, wave generator, flex spline. Examples of scouted commercial gearing: (b) Harmonic Drive SE CSD-32, (c) Toteltech XSF-32.

analogical solution is usually quite cumbersome and it is therefore discarded. On the contrary, the encoder consists of a digital transducer of angular position, typically implemented in an optical or magnetic operative principle. In the first case, the light emitted by a fixed source is collected by a dedicate sensor; the two are separated by a rotating disk, integral with the shaft, which has a number of transparent holes on its surface. The count of voltage pulses received by the photo-detector allows the measurement of angular position. Similar scheme is adopted by magnetic-based encoders, which, however, base their measurements on the pulses produced by a magnetized rotating disk. Both of the two technologies can be realized in *incremental* or *absolute* architectures, and may reach comparable performance.

In order to achieve the prescribed positional accuracy and repeatability of the robot, a high-level absolute encoder is required. The main constraints are dictated by the need for: high resolution, hollow and lightweight design, lack of protective casing, and possibility to interface with the selected motor digital controller. The principal solutions emerged from a market scouting are summarized in Table 3.5 and partially illustrated in Fig. 26. The Heidenhain model, despite the great accuracy and resolution shown, is discarded due to its significant dimensions and weight. Other two models, namely the Baumer and Netzer products, constitute potentially viable solutions, but are respectively flawed by excessive outer size (with respect to inner hole) and potentially noisy signal (given the nature of the analog output). The RLS model, fully satisfying both mechanical and electrical requirements, is rated with the highest score.

3.2.5 Drive design

The highest-ranking products that emerged from the above scouting are selected as representatives of the respective commercial models. Consequently, the following model brands will constitute the baseline of the proposed custom drives:

- motor: *Maxon* model;

Table 3.5: Main specifications of scouted commercial absolute encoders.

	Baumer[1] MHAP 100	Heidenhain RCN6310	Netzer DS-90	RLS AksIM-2 80
Type	Magnetic	-[2]	-[3]	Magnetic
Resolution [bit]	17	28	19-21	17-20
Max speed [rpm]	8000	8000	8000	10 000
Accuracy [″]	400	2	36	180
Supply voltage [V]	4.5-30	3.6-14	5	4.5-5.5
Interface	SSI	EnDat	BiSS, SSI	BiSS, UART, PWM, SPI, SSI
Out dimension [mm]	169.5	308	90	90
In diameter [mm]	38	192	50	55
Length [mm]	30	44	10	7.8
Weight [g]	-[1]	6500	55	68
Rating [1-3]	2	1	2	3

[1] Not specified, presumably in the order of 1 kg due to steel and aluminum covers.
[2] Not specified. [3] Proprietary Sine-Cosine analog technology.

(a) (b) (c)

Figure 26: Example of scouted commercial encoders: (a) Hedenhain RCN6310, (a) Netzer DS-90, (b) RLS AksIM-2 80.

- digital controller: *Maxon* model;
- gearing: *Harmonic Drive SE* model;
- encoder: *RLS* model.

The design process starts by taking in consideration the robot most stressed joint, namely the one corresponding to the 2nd DOF (see, for example, Eq. (3.21)). A robot arm is essentially constituted by a serial chain of bodies: as such, the shoulder actuator is permanently subjected to the gravitational and inertial load of all the subsequent members and experiences the most intense duty-cycles. Anyhow, the design principles described in the following do not lose in generality, as the devised architecture is intended to be modular; the remaining drives will be realized by suitable adjustment of components size, with minimal conceptual modifications.

Under these premises, the shoulder drive target torque is assumed so as to compensate the maximum static torque $T_{\text{static}} = 50\,\text{N m}$ that emerged from the mentioned Eq. (3.21). The motor selected for the purpose is *Maxon EC-90*, which has a rated output torque $T_m = 0.453\,\text{N m}$. The highest-performing gearing model that matches motor dimensions is *Harmonic Drive CSD-32*, which is characterized by a reduction ratio $i = 160$. Since T_{static} is inferior to the gearing rated torque $T_N = 96\,\text{N m}$, the model is assessed as suitable for the application. The efficiency of the gearing can be estimated, in function of input motor velocity and operative temperature, through the respective documentation chart [43]. With a motor rated speed $\omega_N = 2630\,\text{rpm}$ and the regimen operative temperature assumed as $T_{\text{op}} \geq 40\,°\text{C}$, the chart returns a gearing efficiency $\eta_{\text{red}} = 0.70$. This data allows us to estimate the rated drive output torque as

$$T_{\text{drive}} = \eta_{\text{red}} i T_m = 0.70 \cdot 160 \cdot 0.453\text{N m} = 50.7\,\text{N m} \tag{3.23}$$

The value obtained is sufficient to sustain the maximum payload at full reach, in nominal conditions (i.e., for an indefinite time); the combination of the specific motor and gearing model presented is therefore accepted.

A first schematic representation of drive core components is illustrated in Fig. 27. The motor stator (orange) is fixed, at its bottom (left in the figure), to a cylindrical (gray) member, which represents the external drive casing. Proceeding to the right, a conceptual motor shaft (light red) is linked to the motor rotor by the means of three screws. It may be noticed that this member, like any other depicted, presents a noticeable hollow cavity in the center; this coaxial hole, shared among the components, is devoted to internal cable passage and must be preserved as large as possible. The hollow harmonic drive gearing constitutes the following component. The orange member (wave generator) is directly fastened to the motor shaft by the means of a flange; the outer gray member (the circular spline) represents the truss member of the gearing and must be fixed, through the appropriate screw holes, to the outer casing. The last gearing member (dark grey) is the flex spline and must be ultimately fastened to the output shaft (light blue).

In order to allow the assembling of the various components, the conceptual external casing subsequently is divided in four sub-parts; in this way, all the needed parts can be inserted, progressively, from left to right. Fig. 28 depicts a refined drive concept based on this idea. It may be noticed that a significant restriction of motor shaft section is needed for the connection to the wave generator. This requirement offers the opportunity to select among two main bearing sizes, which could be placed in the larger or the smaller section of the shaft. The former solution, despite being

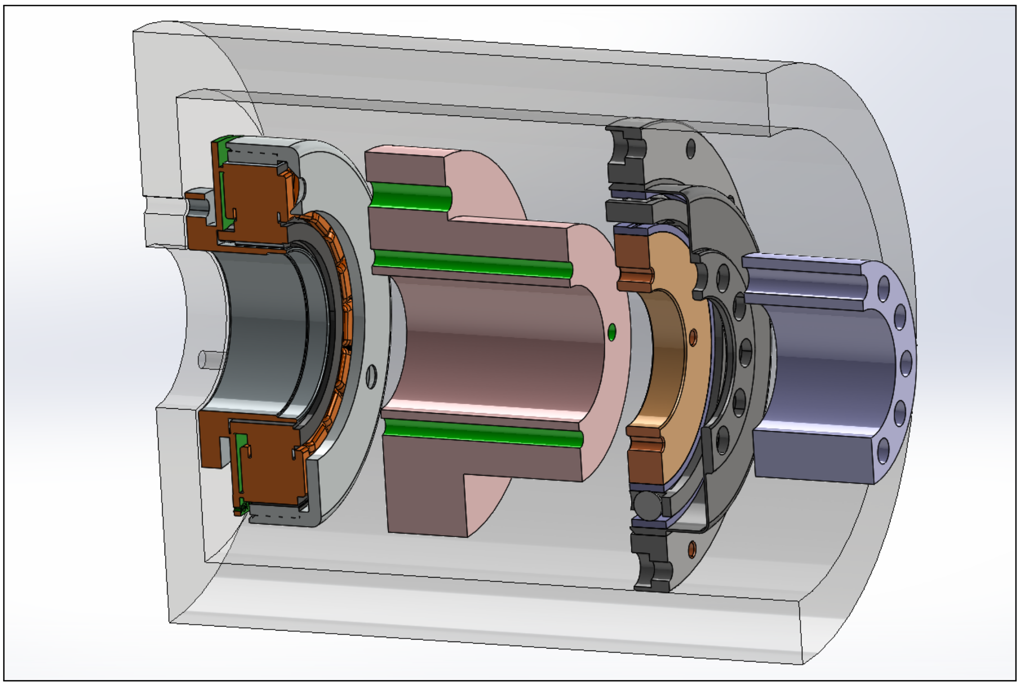

Figure 27: Drive concept exploded view section. From left to right: motor, motor shaft (light red), harmonic drive gearing, output shaft (light blue). Components are housed inside a schematic casing (gray, transparent).

intrinsically suitable for the available housing, is nonetheless discarded for dynamic-based reasons. In fact, it is important to consider that the examined shaft is directly connected to the motor which, before the gearing, is able to exert only a small torque; consequently, the adoption of a higher size bearing, due to the relatively high rotational inertia and increased friction, would significantly deteriorate the motor output performance. The latter solution is hence adopted, and the second sub-casing is modified so to radially protrude and accommodate for bearing little dimension. An opposite consideration is made for the output shaft bearing. The output shaft is, in fact, responsible for the transmission of high-value torques and needs to be as much rigidly supported as possible; consequently, a high internal radius rigid bearing is recommended. The large initial section of the output shaft is subsequently employed to realize a shoulder, which may house the thin absolute encoder magnetic ring. The static reader sensor is conversely mounted to a fixed flange of the fourth, and last, sub-casing.

The following iteration, illustrated in Fig. 29, details the definitive design of the robot shoulder drive. The material selected for the machined components is the aluminum alloy 7075, which is commercially known as *Ergal* and is thoroughly employed in avionics and robotics. This choice is motivated by the great mechanical properties granted by the material, that comprise reduced density ($2.8\,\mathrm{g/cm^3}$), high

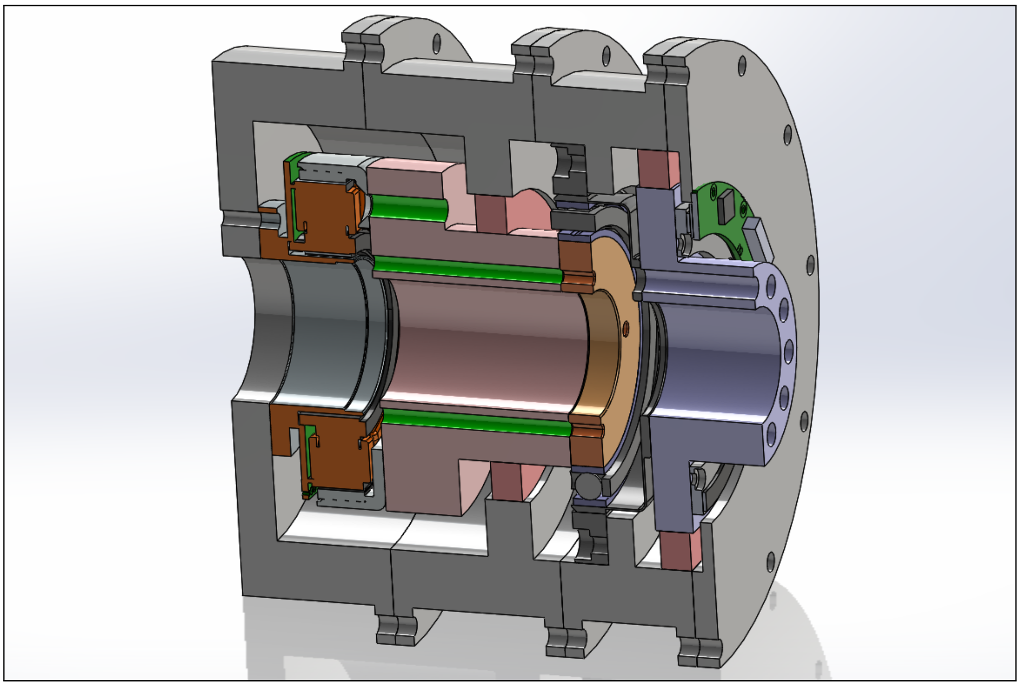

Figure 28: Drive concept refinement. Casing is split into four sub-parts, for easier progressive components assembly from left to right. Bearing locations highlighted in red; encoder directly installed on the output shaft, at extreme right.

ductility and excellent yield strength (550 MPa) [14]. For comparison, a common good structural steel alloy such as C40 (UNI EN 10083), reaches comparable yield strength at the cost of a nearly 3-fold weight increment (7.8 g/cm^3).

Starting from the drive casing, the four sub-parts are designed in such a way as to be progressively mounted from left to right, one after the other (each one presents a dedicated radial centering). By comparing Fig. 30a with Fig. 28, it can be noticed that the three interface flanges, used to connect the parts, have been substituted by a single threaded joint, which packs all of them. In this way, through the simple fastening of the blue-highlighted screws, the casing can be easily assembled in a single operation. A second offset group of screws, highlighted in red in same figure, is included in the rear part of the casing in order to install the whole drive inside the robot body casing. As illustrated, the screwing of these bolts is performed with an Allen wrench that passes through the corresponding holes arranged in the last sub-casing. The operation is most easy, and allows for quick housing and removal of the whole drive for maintenance purposes. As better detailed in following Section 3.3, this solution provides an additional fundamental advantage: the drive can be installed through a single axial operation, acting only on the front side; consequently, no removable covers must be implemented in the outer robot casing in order to access it and hygienicity is significantly improved. As illustrated by

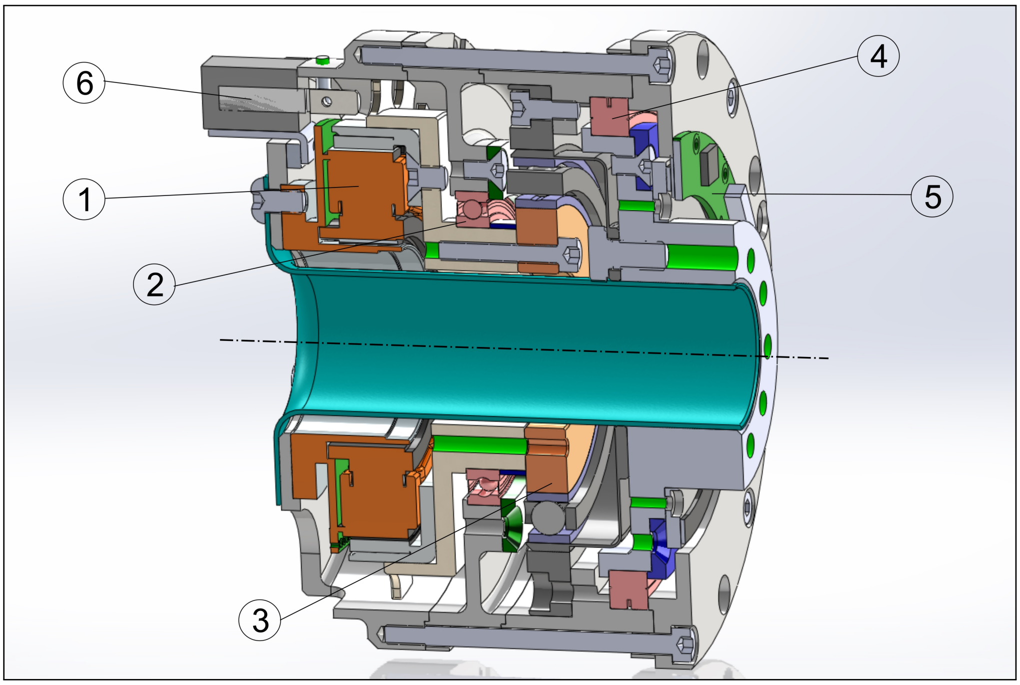

Figure 29: Robot shoulder drive definitive design. Overall section is illustrated: (1) motor, (2) motor shaft bearing, (3) harmonic drive gearing, (4) output shaft bearing, (5) absolute encoder, (6) emergency brake.

Fig. 30b, the rear part of the casing is characterized by multiple circumferential openings. An upper square opening is used to house the drive emergency brake; the remaining set of symmetric openings allows both heat dissipation and motor cable outlet from the drive. An additional unsymmetrical hole, highlighted by a red line, traverses every sub-casing, so to allow the connection of the encoder PCB (installed on the front) with the drive controller (predictably located in the back).

The two shafts are devised as hollow, cylindrical members whose section varies so to fully exploit the axial and radial space inside the casing (a detail is offered in Fig. 31a). In order to minimize any potential source of circumferential backlash, no key or pin solution is used to link with adjacent components; a fastened and radially centered arrangement is utilized instead, whenever possible. Given the short length of the motor shaft and the low actions applied on it, only one bearing is used for its guidance. In particular, a common deep groove thin-section ball bearing is selected, so to support both the main radial loads and the small axial components. Unfortunately, the said bearing may not be lubricated by traditional refurbishment of oil, as the operation could hardly be performed in the proposed enclosed structure and under the compelling hygienic requirements (e.g lack of fastened caps and crevices). Therefore, a permanent grease lubrication is preferred and integrated non-contact NBR seals are equipped on both sides. The

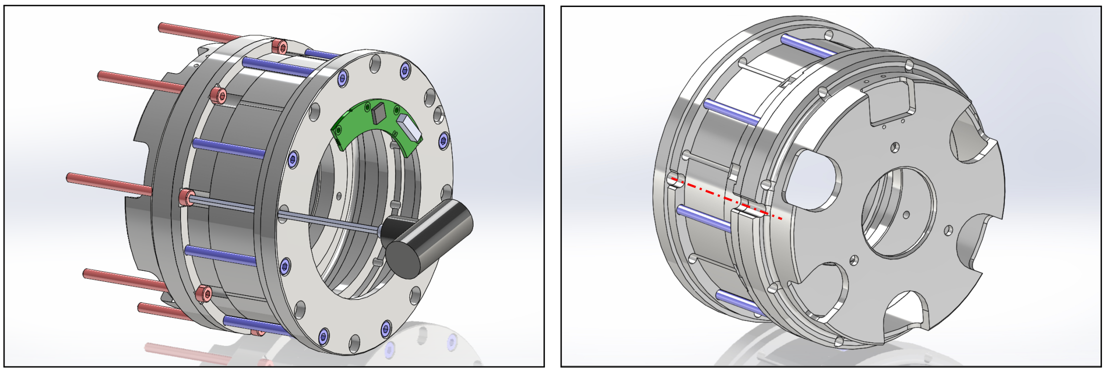

(a) (b)

Figure 30: (a) Detail of the drive casing: blue-highlighted screws are responsible for casing sub-parts assembling; red-highlighted screws, fastened through dedicated holes, allow to secure the drive inside the robot housing. (b) Rear-view detail of casing; unsymmetrical hole for encoder cable passage is highlighted as a red line.

output shaft, on the other hand, is responsible for transmitting the highest loads of the drive and its support must be chosen with particular care. The most common solution to obtain a rigid shaft structure consists in the use of two single-row angular-contact ball bearing arranged in back-to-back configuration (also known as “O arrangement”); analogously, a single double-row angular contact ball bearing could serve the same purpose. In the proposed design, a single thin-section crossed roller bearing is utilized, instead (see Fig. 31b for a schematic comparison). This high-performing solution allows, from one hand, to significantly reduce the overall footprint of the support, thanks to its combined radial and axial load capacity; on the other hand, the intrinsic properties of this device together with the large radius of the selected bearing, allow for great overturning rigidity of the shaft and minimal radial oscillation. The output shaft bearing is permanently lubricated with grease and equips integrated seals on both sides.

An emergency brake is included in the drive assembly, so to intervene in case of power failure and prevent critical arm free falling to the ground. It is important to remember, in this regard, that brushless motors, driven by suitable electronics, are able to work as regenerative brakes for operative decelerations. Since the emergency brake must enter in action only when power is off, a *normally-on* configuration is deemed convenient for the device: an electromagnetic force is responsible for brake disengagement during normal robot operations, while the lack of supply power allows the intervention of an elastic force, previously compensated. Many commercial emergency brakes exist for the purpose; a scouting of the available solutions, however, highlighted that all the examined products lack many of the needed features: hollow design, low weight, reduced footprint, little energy consumption

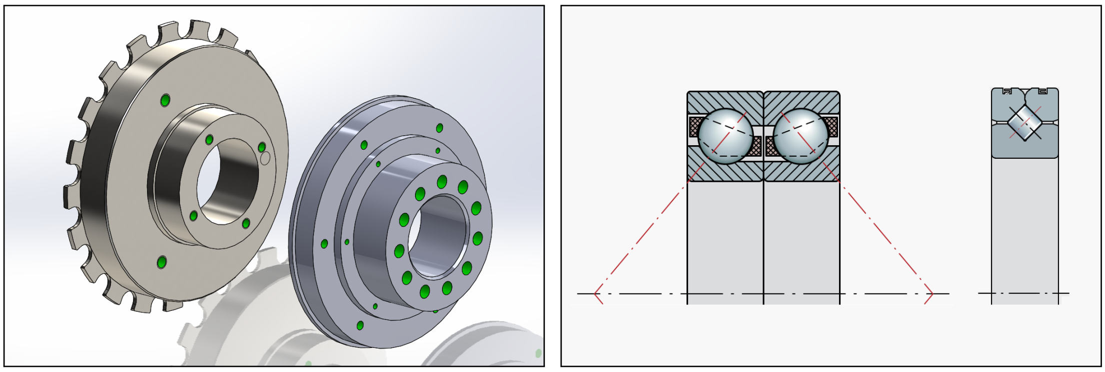

(a) (b)

Figure 31: (a) Drive motor and output shaft detail: large central cavity is devised for internal cable passage; link to adjacent components is performed through the multiple threaded holes present. (b) Schematic comparison between single double-row angular contact ball bearing (left) and thin-section crossed roller bearing (right).

during *on* disengagement phase. Consequently, a custom emergency braking solution is designed for the purpose. A small spring-actuated solenoid is installed in the upper-rear part of the drive; when power is off, a pin is promptly pushed forward and inserted in one of the several circumferential grooves devised in the motor shaft; as a result, the rotor is forcefully blocked by the obstruction offered by pin (see Fig. 32). Indeed, the proposed solution presents both advantages and disadvantages. On the down side, the locking of the motor shaft do not necessarily ensures the stop of the output shaft, as the transmission in-between could fail; a small time lag in actuation and residual backlash is present, anyhow. On the plus side, the shear force acting on the solenoid pin is particularly small, given the the small torque seen on the motor side; this allows for compact and lightweight implementation.

A thin, plastic hollow tube (light-blue in Fig. 29) completes the assembly and is fixed to the rear casing. The rounded shape at the entrance and its soft material are intended to protect the inner cabling traversing the drive from accidental cuts against sharp metal corners or progressive peeling due to joint rotations.

3.2.6 Drive scaling

The guiding principles that were applied to design the above drive can be extended, with minimal conceptual changes, to realize other sizes of the same actuator. In the search of a trade-off between specific joint optimization and simplicity of robot manufacturing, only a subset of the six DOFs are provided with a dedicated drive. In particular, as illustrated in Fig. 33, three exemplars have been devised; these will

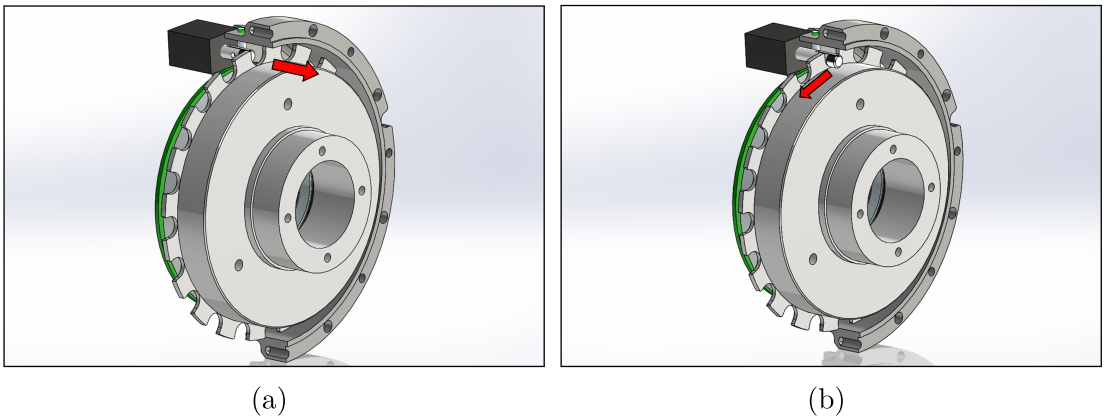
(a) (b)

Figure 32: Partial section detail of custom emergency brake implementation: (a) solenoid pin is retracted during normal robot operation (power on); (b) solenoid pin is extracted and blocks motor shaft through tangential force (power off).

Table 3.6: Summary of designed drives mechanical specifications.

	Size-90	Size-60	Size-45
Max length [mm]	110	103	96
External diameter [mm]	130	106	84
Inner diameter [mm]	28	18	9
Weight [kg]	2.1	1.2	0.8
Motor power [W]	160	100	70
Motor rated torque [N m]	0.453	0.289	0.128
Motor rated speed [rpm]	2630	3740	4860
Gear ratio [-]	160	160	100
Gearing efficiency[1] [-]	0.70	0.70	0.75
Output rated speed [rpm]	16.4	23.4	48.6
Output torque[1] [N m]	50.7	32.4	9.6
Torque density[1] [N m/kg]	24.1	27.0	12.0

[1] At reference motor speed of 2000 rpm.

hereafter be referenced to as *Size-90*, *Size-60* and *Size-45* respectively, in accordance to the equipped motor outer diameter. The rest of the robot will be designed in function of the three actuators, so to achieve the best combination of joint output torque and overall reduction of weight. It is important to stress, in this regard, that the non-linear variation of arm inertia in function of assumed configuration prevents us from using classic 1-DOF sizing approaches based on duty cycle and related RMS torque: the selection of the optimal combination of drives and link lengths constitutes a tough non-linear constrained optimization problem. In the

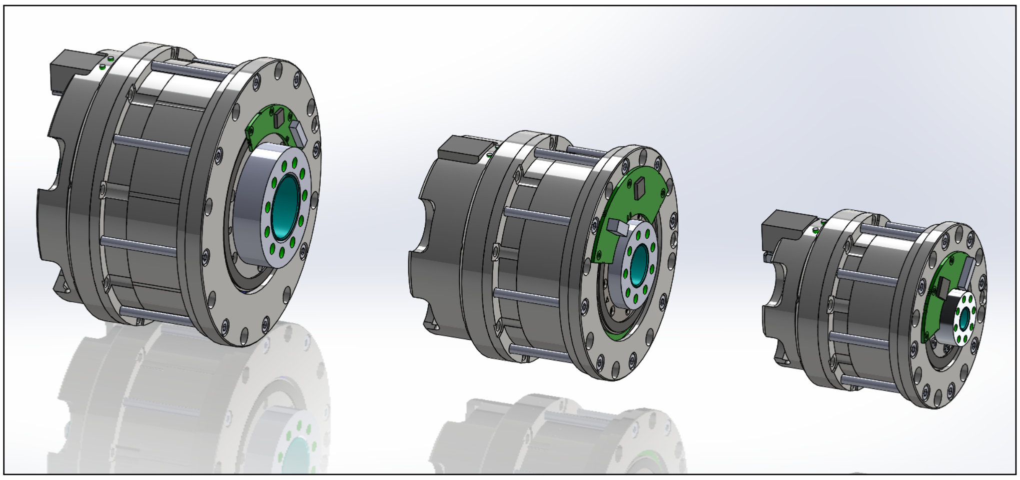

(a)

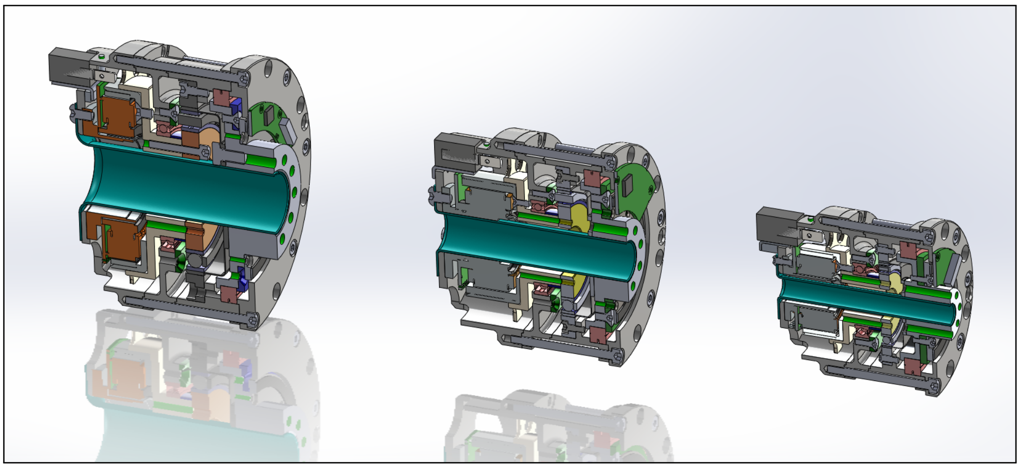

(b)

Figure 33: External view (a) and sectioned view (b) of the three Size-90, Size-60 and Size-45 custom drives designed for the robot.

present work, the design procedure is assisted by concurrent use of simulated test trajectories, which are performed in a dedicated multibody software that will be detailed in Chapter 4.

A final summary of drives mechanical specifications is presented in Table 3.6, while the corresponding bill of materials is reported in Appendix B.

3.3 Casing

The present section is devoted to describe the design process of the robot outer body, henceforth synthetically indicated with the term *casing*. After a premise relative to the selection of material for aseptic robotics, the main guidelines to shape the casing will be presented.

3.3.1 Materials

The selection of a robot casing material is dictated by many concurrent considerations. The first, and most important, constraint, is linked to minimization of *weight*. As previously mentioned, an articulated robot consists of a serial kinematic chain of bodies, in which each member manifests significant static and inertial load on the previous. The increase of motors size required to compensate the weight issue initiates a recursive process which, ultimately, leads to low dynamic performances of the final arm. Therefore, the material is searched with the lowest density possible. A direct implication of lightweight design is the need for high *mechanical strength* of the material. The robot, in fact, must be devised as an enclosed hollow structure, which is able to house all the needed components for its operation (e.g. drives, sensors, wiring). In order to fully exploit the internal volume of the arm and concurrently minimize its weight, the thickness of the casing must be reduced as much as possible; if the material is not to fail, its yield strength must be accordingly high. Moreover, from a practical point of view, the thickness constraint translates into the need for a material that is sufficiently *easy to be machined*. A further implication consists in the need for significant material *stiffness*: the accuracy of manipulator motion is, in fact, inversely proportional to the arm compliance (especially under dynamical loads). Coming to the specific requirements of aseptic industry, the casing material must be evidently resistant to harsh *chemical sterilization* agents (for a detailed list of specific compounds, see Section 1.3 and Section 2.1), so that no appreciable deterioration of robot outer surface can be found during its operative lifespan. The requisite extends to the necessity of a material that is able to withstand the mechanical wear produced by pressurized liquid jets: the production of abrasion airborne particulate must be thoroughly minimized. Finally, as regarding hygiene, the material is compelled to be non-porous (so to avoid potential bacteria proliferation) and compatible with pharmaceutical and food industry applications. A preliminary scouting of the commercial materials that fulfill the exposed requirements, immediately points us in the direction of raw metals or coated ones. A summary of the examined alternatives is reported in Table 3.7 and is detailed below.

AISI 316 stainless steel presumably constitutes the most intuitive option, as it is widely employed in the construction of aseptic machines and it is often recommended in FDA and EHEDG hygienic guidelines (see Section 1.2) for its resistance to chemical sterilizing agents [71] [46] [103]. The material compatibility with sensitive food and pharmaceutical products has been shown in a large number of works (see, for example, [62] [74] [44]) and is demonstrated by its extended use by the leading firms of the field [20]. In terms of sheer mechanical properties, AISI 316

Table 3.7: Summary of scouted casing material mechanical properties.

Property	AISI 316	Ti6-6Al-4V	Ergal
Density [kg/m^3]	8000	4400	2800
Yield strength [MPa]	260-290	830	550
Young modulus [GPa]	193	114	72

steel is characterized by fair performances: with a yield strength attested in the range $S_y = 260 - 290\,\mathrm{MPa}$, and a Young modulus $E = 193\,\mathrm{GPa}$ [14] [101], the material is both durable and stiff. Unfortunately, two important disadvantages undermine steel selection. First, the considerable density $\rho = 8000\,\mathrm{kg/m^3}$ limits the potential usage in the context of robotics; secondly the moderately low machining properties [71] [2] [66] make it difficult to manufacture thin hollow objects.

Titanium alloy Ti-6Al-4V represents a second, interesting, alternative. The alloy is increasingly utilized in a number of different applications, such as avionics, marine constructions, additive manufacturing and biomedical implants. The reason of the extensive material success is rooted on the combination of excellent mechanical performance and reduced weight. In particular, Ti-6Al-4V is characterized by yield strength $S_y = 830\,\mathrm{MPa}$, a Young modulus $E = 114\,\mathrm{GPa}$, and an attractive density $\rho = 4400\,\mathrm{kg/m^3}$ [14]. Additionally, the alloy stands out for its resistance to chemical corrosion, as it is able withstand high concentrations of the most aggressive compounds (e.g. peracetic acid, nitric acid, hydrogen peroxide, sodium hydroxide [21] [93]); the compatibility of the material with pharmaceutical and food process industries is ensured by the wide use in human prosthesis [64]. On the down side, Ti-6Al-4V is not easy to be machined; moreover, even if the raw materials are quite abundant and evenly dispersed on the globe, the final cost of the alloy is significantly high, due to the difficult processes involved in its production [63].

A final alternative is constituted by a superficially treated aluminum 7075 alloy (Ergal). The core material is characterized by an excellent trade-off between yield strength ($S_y = 550\,\mathrm{MPa}$), Young modulus ($E = 72\,\mathrm{GPa}$) and reduced weight ($\rho = 2800\,\mathrm{kg/m^3}$) [14], together with a fairly cost-effectiveness and machining ease. The major material drawback is constituted by the low resistance offered to harsh chemical agents; as such, many different surface processes have been developed to overcome the issue. One frequent procedure consists in aluminum chrome plating. The base material is subjected to the electro-deposition of a thin layer of chromium, whose thickness may vary from $5\,\mathrm{\mu m}$ (light plating) to $0.127\,\mathrm{mm}$ (hard plating) [9]. Despite the achieved corrosion resistance is moderately high [21], the use of this solution in food and pharmaceutical environments is usually strongly discouraged by the regulator authorities; the material, in fact, may release hexavalent chromium particulate, which is highly toxic and potentially carcinogen [90] [41]. A different

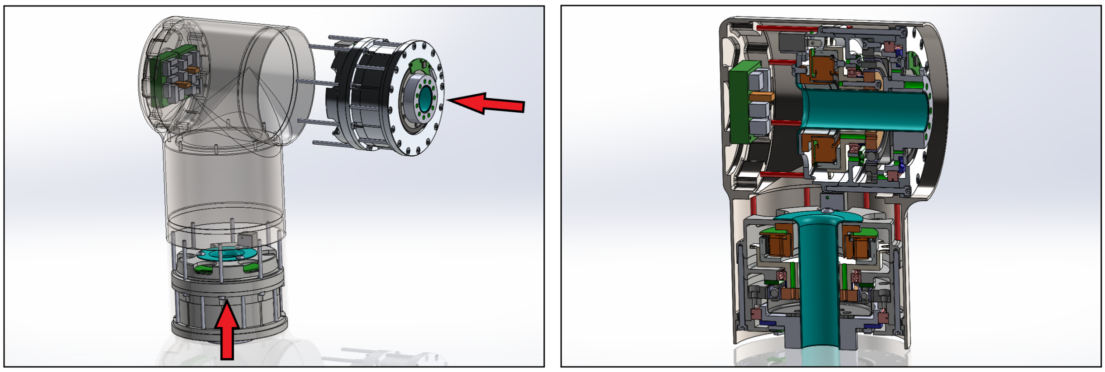

(a) (b)

Figure 34: (a) Exploded view of robot 2-DOF shoulder joint; Size-90 drives are inserted axially. (b) Detailed section of shoulder: drives are fastened to casing through red screws and powered by onboard controllers; wiring passage is ensured by hollow design.

strategy consists in aluminum polymeric coating. One of the most common coating treatments involves the use of PEEK (polyetheretherketone), an organic thermoplastic material with good chemical resistance and mechanical properties (Young modulus $E = 3.6\,\mathrm{GPa}$, ultimate tensile strength $S_{ut} = 90 - 100\,\mathrm{MPa}$) [71] [5]. The main solution disadvantage consists in its intrinsic weakness to mechanical wear: any impact on robot surface, included the ones caused by pressurized jet sterilization, can bring to abrasion of the coating; even if the generated particle is non-toxic, the progressive peeling of material eventually exposes the underneath aluminum to the corroding chemical agents.

At the end of the scouting process, titanium alloy Ti-6Al-4V is assessed as the most suitable option for the aseptic robot casing material. The choice is motivated by the excellent mechanical properties of the alloy, together with the outstanding performance in chemical resistance and food compatibility. If compared to AISI 316, the material has 2.9 times higher tensile strength, which allows for significant reduction of casings thickness; the additional 45% reduction in material density, widens the gap even further. Overall, the above result is judged adequate to compensate the 41% decrease of material stiffness. Symmetrical considerations can be made in the comparison between Ti-6Al-4V and Ergal, since the 36% mass saving granted by the latter is partially mitigated by the greater yield strength and stiffness of the former. Even more importantly, Ti-6Al-4V is characterized by an intrinsically superior chemical resistance, and is not subjected to the risk of coating abrasion over time.

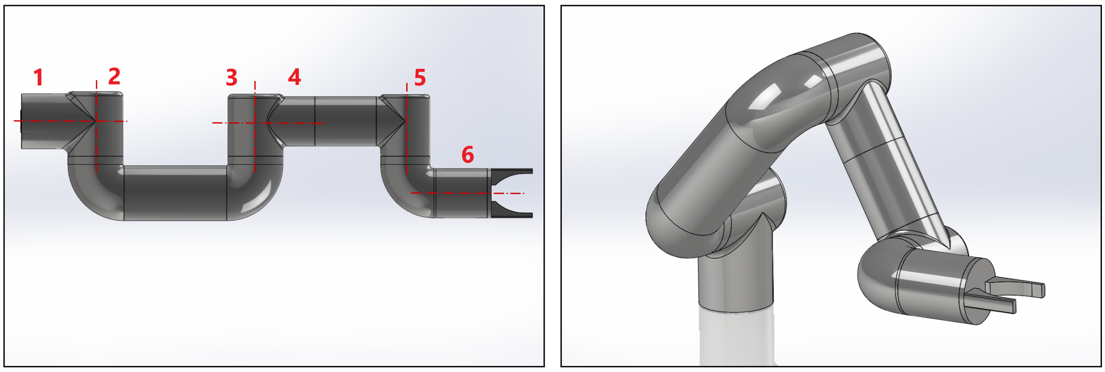

(a) (b)

Figure 35: Robot casing first concept, with generic end-effector equipped. (a) Highlight of drives axes and (b) global view.

3.3.2 Geometries

The shaping of robot body geometry is inspired by the fulfillment of hygienic design guidelines and the considerations exposed in Section 2.2. At first, the shoulder casing is adapted to house two Size-90 actuators; with respect to the concept depicted in Fig. 12, the 2-DOF spherical drive structure is consequently modified into a simpler cylindrical form, which is considerably easier to manufacture. Fig. 34 illustrates the idea: two digital controllers are fastened in the bottom part of the casing, followed by the respective actuators which are axially inserted and fastened through the method discussed in Fig. 30a. It is worth noting that, by the means of the exposed procedure, no removable covers must be implemented to assemble shoulder internal components: the lack of exposed screw heads and interfaces between parts beneficially affects the overall hygienicity. Fig. 34b offers a sectioned view of the assembled shoulder joint. It may be observed that the devised perpendicular arrangement of the drives allows them to be connected to the respective onboard controllers; additionally, the hollow central axes of the two permit the crossing of further wiring, in order to supply the subsequent actuators. The rest of robot casing can be shaped as a tubular assembly that smoothly connects all the required joints. Fig. 35 presents a first potential outcome of the process: elbow and wrist joints reproduce, in a modular approach, the shoulder casing concept; the link members that connect the three joints (namely the biceps and the forearm) are in turn realized as simple cylindrical tubes, which are markedly cost-effective and easy to manufacture. The described geometry is particularly proficient in terms of hygienicity, as all the external surfaces are promptly accessible for cleaning and no areas prone to soil accumulation are present. On the down side, it may be noticed that the exposed concept does not satisfy two important design targets. First, the robot is affected by a significant lateral footprint, which may prevent the

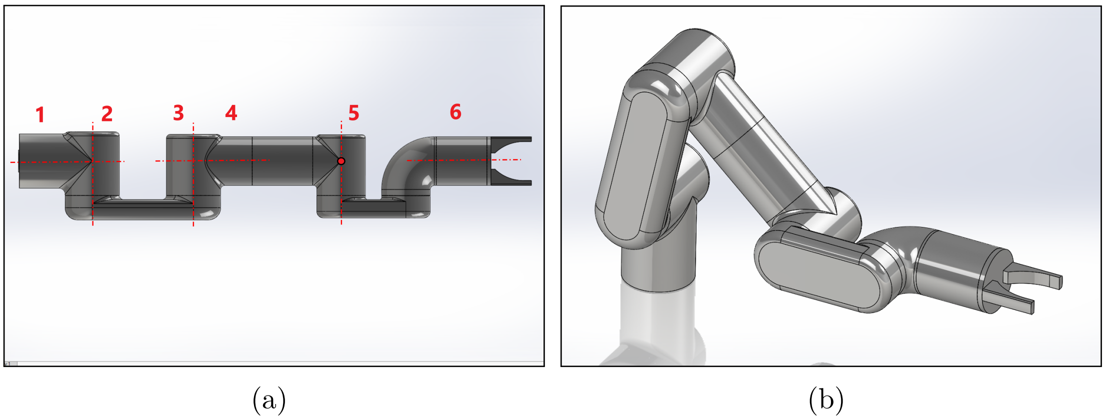

(a) (b)

Figure 36: Robot casing refined concept, with generic end-effector equipped. (a) Highlight of drives axes and spherical wrist center; (b) global view.

manipulator to reach and suitably operate inside narrow workplaces. Secondly, the adopted geometry does not meet the requirements of a spherical wrist, since the three respective motor axes are not incident in a common point.

A refined version of robot casing is presented in Fig. 36. The first difference consists in the noticeable reduction of lateral arm footprint, which is obtained through the introduction of a flat biceps and a revisited wrist. The appreciable result is obtained at the expense of a slightly increase difficulty in components production; nonetheless, the two members may be realized in one-piece by a process of investment casting (which is applicable to the selected Ti-6Al-4V [63]) or by simple welding of two sub-parts along the longitudinal plane. The modifications made to the wrist architecture allow, additionally, to achieve the desired advantageous spherical configuration (see Fig. 36a).

Fig. 37 illustrates the final version of robot casing, in which each joint (shoulder, elbow, wrist) has been optimized in function of the available actuators sizes; a detailed description of robot mass distribution and the explanation of interior sections will be presented in Section 3.7. With respect to the previous form, the last part of the wrist has been reshaped so that the end-effector is the closest possible to the wrist center. This slight modification is responsible for two important results. First, the global center of gravity of the robot is moved closer to shoulder base axis; the dynamic performance of the manipulator is consequently improved. Secondly, the kinematic distance between TCP and wrist center is reduced: the overall ability of the robot to manipulate objects in narrow spaces is accordingly increased.

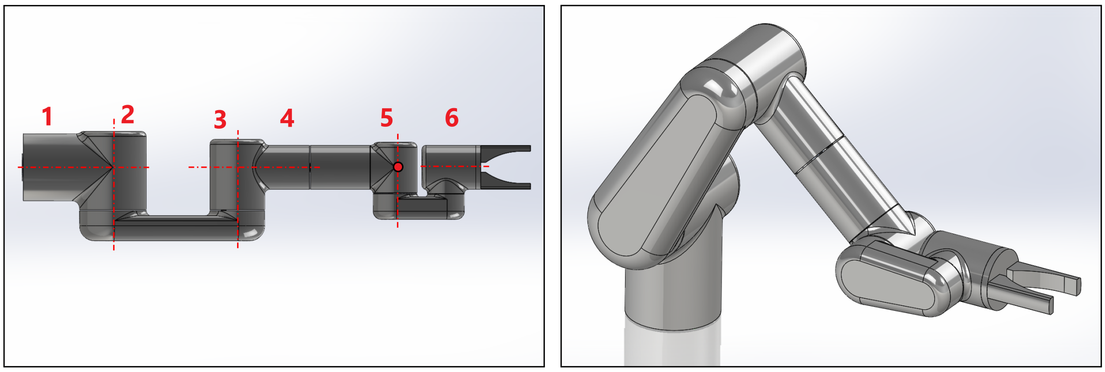

(a) (b)

Figure 37: Robot definitive casing, with generic end-effector equipped. (a) Highlight of drives axes and spherical wrist center; global view (b).

3.4 Sealings

In order to withstand the liquid sterilization treatments of aseptic environments, the robot casing must be protected by an appropriate sealing solution. With particular reference to aseptic industry, sealings are extensively used for two main purposes:

- protect the dismountable mechanical joints from ingress of contaminants;
- avoid the direct metal-to-metal interface between components.

The first function is realized through dynamic seals which, in the case of an articulated arm, involve the protection of every revolute joint. The second task is conversely absolved by static seals (most often by o-rings), which are typically employed to prevent soil accumulation under the exposed screw heads of bolted joints. As for any other robot component, sealings are subjected to the constraints of hygienic design. The first requirement consists in the adoption of a material that is resistant to harsh chemical agents and, in the specific case of food industry, also compliant to the respective regulations (see, for example, [27] [28] [26] [34]). From the implementation point of view, sealings intrinsically constitute a potential source of hygiene hazard, due to the unavoidable grooves required to house them: in this regard, the seals for aseptic environments are required to minimize the presence of crevices, undercuts and generic hidden areas.

3.4.1 Materials

In light of the above considerations, the choice of the appropriate material constitutes the first fundamental step. For this purpose, a synthetic summary of the most important materials for aseptic environments is presented in the following.

NBR and *HNBR*. The Acrylonitrile-Butadiene Rubber (NBR) is one of the most common elastomers for static seals (o-ring) and generic sealing devices. The material is characterized by excellent cost-effectiveness, good mechanical properties, and resistance to a moderate range of temperatures (from −30 °C to 100 °C and up to 120 °C for short periods) [110]. NBR is resistant to many diluted acids [88], but harsher cleaning regimes often result in progressive deterioration of the seal. HNBR constitutes an improved version of the material: the core polymer chain is subjected to a hydrogenation process that increases mechanical properties, temperature range (−20 °C to 150 °C) and chemical resistance (mineral and fuel oils, greases, moderate acids, hydraulic fluids). The versatility of HNBR makes it a useful choice for a wide range of applications [36].

EPDM. The Ethylene-Propylene-Diene Rubber is a versatile unpolar hydrocarbon-based elastomer, characterized by high thermal and chemical resistance. The polymer shows particular good performance against hot water and steam, ozone, alkaline and acidic detergents; as such, it constitutes a suitable choice in most dairy, cleaning and sterilization (CIP/ SIP) process applications [110]. The most important performance limitation is constituted by the ageing effect caused by air. The typical EPDM temperature range spans between −45 °C and 150 °C; if the seal is inserted in a completely inert steam environment, the maximum operative temperature can be raised to 180 °C [36].

FKM. Fluorocarbon, also known with trade name Viton (DuPont) is a fluorinated elastomer characterized by exceptional resistance to chemicals and extreme temperature; though initially introduced for use in aerospace applications, the great properties of the material allowed a progressive spread in automotive, fluid power, chemical processing and food industries. The basis of material strength consists in the incorporation of fluorine, which forms very strong bonds inside the chain. From one side, this process allows FKM to withstand temperatures in the range from −15 °C to 200 °C [36]. In addition, since the chain carbon backbone is fully saturated (i.e. only single bonds between the carbon atoms are contained), no covalent double bonds are present. The lack of double bonds, which are the typical focus for chemical attack, renders the fluorocarbon structure impervious to harmful chemical agents [88] and grants resistance to oxygen, ozone, mineral oils, chlorinated solvents, fuels, steam, and UV light [36]. Overall, FKM results appropriate for use in contact with dairy products and is able to withstand most CIP and SIP media [110]. On the contrary, the polymer is not indicated for phosphate esters, polar solvents, fuels, engine oils, and organic acids [36].

PTFE. Polytetrafluoroethylene (FEP in the ASTM designation or Teflon in the DuPont trade name) is a completely fluorinated polymer (i.e. four fluorine atoms to every two carbon atom) that, together with its numerous commercial derivatives, probably constitutes the most common plastic in sealing technology. Application fields of PTFE include, among the others, automotive and chemical, food and pharmaceutical process industries [110]. The material is produced through free radical vinyl polymerization of the tetrafluoroethylene monomer (TFE) and, in force of its peculiar composition, exhibits outstanding thermal performance (from −250 °C to −250 °C [36]), virtually complete resistance to chemical attack, and very low friction coefficient (0.05-0.15 [49] [67]). The last feature translates in consistent wear resistance and allows proficient use dry-running applications, even at moderate sliding speed; o-rings can be coated with this material for same the purpose [36]. Since PTFE is essentially self-lubricating, its use is most convenient when external lubricants (such as oils and greases) cannot be employed [88]. With respect to other materials, PTFE elasticity is quite low. Consequently, an external "energizing" member is often required to exert a sufficient sealing contact pressure; typical examples of energizing members are metal spring or additional elastomers (such as o-rings) [36]. With reference to chemical resistance, PTFE is inert to almost all acids, alcohols, alkalies, esters, ketones, and hydrocarbons; the most notable weaknesses are related to fluorine, chlorine trifluoride, and molten alkali metal solutions at high pressures [88].

3.4.2 Geometries

Two main paradigms are available for the implementation of dynamics seal: radial and axial contact; a comparison between the two mechanisms is illustrated in Fig. 38. In both cases, the working principle is rooted on the deformation of an elastic member. In the common situation of an elastomer-based seal, the material is characterized by extreme elasticity, which allows even small forces to produce big deformations. As such, seals are installed with interference (typically in the order of 10-30%) [36] in the coupling shaft-groove. The compression force exerted to the seal translates into a high contact force, which provides seal in the direction perpendicular to deformation and prevents fluids from traversing it. In dependence of particular geometry and technology, the sealing action can work only in one verse or both. Elastomeric seals have a high Poisson ratio, proximal to 0.5 [36]: this means that almost the totality of compression in one direction is followed by the elongation in the other. For this reason, grooves must be designed with sufficient space to accommodate for seal expansion and with suitable rounded corners, to avoid cuts. Radial seals represent the most common solution for the protection of rotating shafts and rods. The seal is inserted in a dedicated groove on the shaft or the hub and is ultimately deformed in the direction perpendicular to rotation axis; hence, sealing happens in the direction parallel to this. The working principle of axial seals is analogous, but mirrored: compression is provided in the direction parallel to shaft rotation axis and sealing happens in the perpendicular direction. In this case, grove size must be adapted in function of the expected source of pressure, as well.

The final selection of the appropriate seal solution is a complex task: the choice is strictly dictated by the specific context requirements and is often a matter of

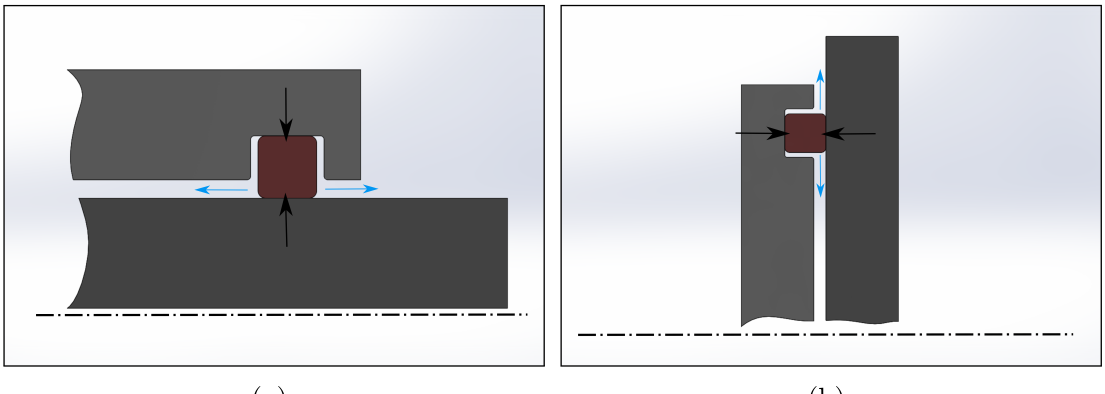
(a) (b)

Figure 38: (a) Radial and (b) axial sealing mechanism. Black arrow indicates direction of compression, blue arrow direction of prevented fluid flow.

experience. It is important to stress, in this regard, that the leading firms in sealing technologies allow the customization of their products, in order to meet the needs of particularly demanding applications; the sealing of an aseptic robot certainly falls in this category. Nonetheless, in the following, some of the standard commercial sealing will be discussed, in order to provide useful guidelines for potential further improvements.

Fig. 39a illustrates a typical example of radial seal for food industry. It consists of a seal ring realized in *Turcon* (a proprietary blend of PTFE and PEEK, with FDA certification for food contact [111]) activated by an elastomeric o-ring, whose compression produces contact pressure. Thanks to the symmetrical cross section, the seal is able to respond to pressure in both directions; in addition, a number of machined grooves on contact surface improves seal efficiency and forms a lubricant reservoir that further reduces friction. The material used has optimal performance against chemical attack, and is able to withstand both high sliding speed (up to 2 m/s) and high external pressure (up to 30 MPa). From mechanical design point of view, the solution is characterized by a mixed performance. From one hand, the seal is handy to employ, as its groove is very simply shaped. From the other hand, however, the consistent radial space to realize its housing translates in increase of casing thickness and, ultimately, additional robot weight. With regard to hygienicity, the solution presents a major problem. In fact, in order to avoid transversal deformation of the contact ring and ensure suitable sealing, the housing must leave a very small gap with respect to the rotating shaft. This gap constitutes a source of contamination accumulation and it is quite difficult to sanitize. Moreover, the radial seal architecture imposes a restriction of rotor member cross section (e.g. biceps with respect to shoulder). This provokes an additional implementation issue: since the robot casing is required to locally maintain a constant external dimension, the moving member casing must re-increase its external diameter after the

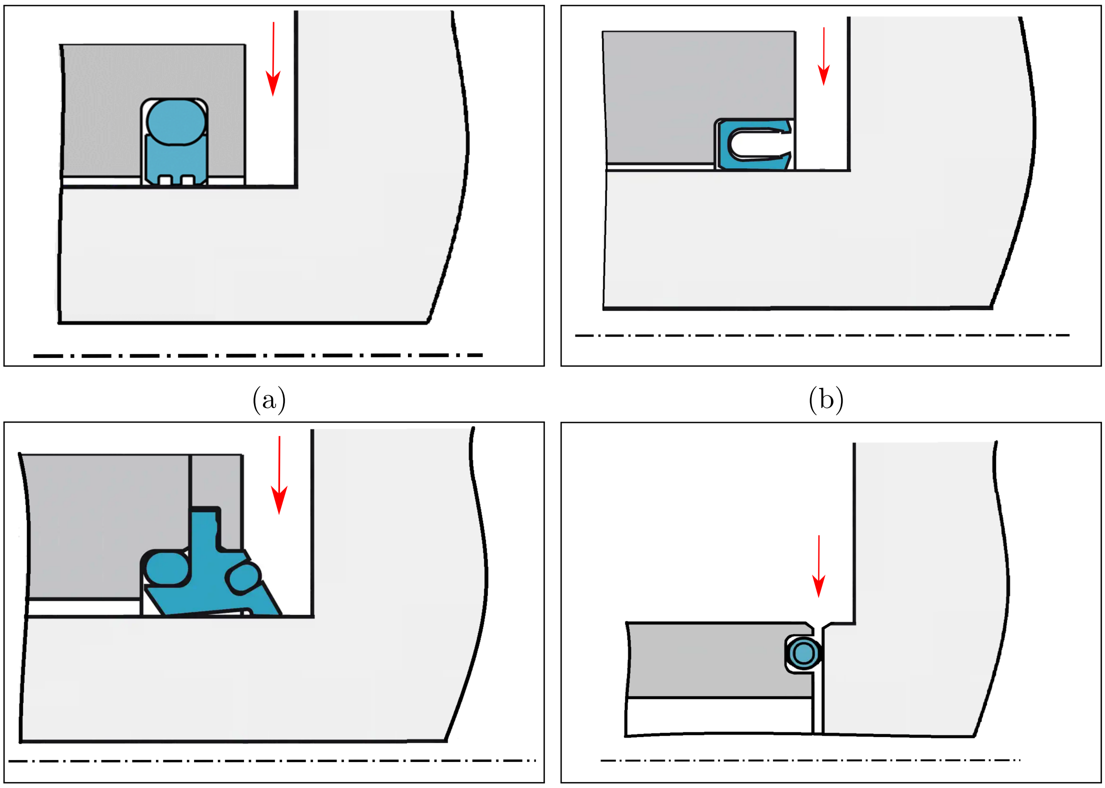

(a) (b) (c) (d)

Figure 39: Comparison of commercial sealing solutions applied to schematic robot joint (e.g. shoulder-biceps): (a) Turcon Roto Glyd Ring, (b) Turcon Variseal, (c) Turcon Excluder SR, (d) FEP O-Ring. Red arrow indicates source of pressure. Adapted from [111]

seal location; an additional hidden area between the two members is created.

A second solution, depicted in Fig. 39b, consists in a Turcon U-shaped sealing element energized by a metallic spring, which produces a radial single-acting sealing effect (i.e. pressure can be sustained only from right to left). The design offers many advantages: very low friction, no stick-slip, high wear resistance, optimal chemical performance, and scraping capabilities. However, even if no gaps are required for its housing, the shape of the seal intrinsically produces a hidden crevice, which is very difficult to reach; additionally, the presence of a metallic spring constitutes a further source of bacteria proliferation.

Fig. 39c presents another alternative. The seal is composed by two double-acting o-rings that energize a Turcon scraper. Mechanical and chemical performances of the element are equivalent to the preceding options. Hygienicity is somewhat improved, though: no undercuts are exposed by the scraper (with the exception of aforementioned hidden area between rotating members). Unfortunately, the

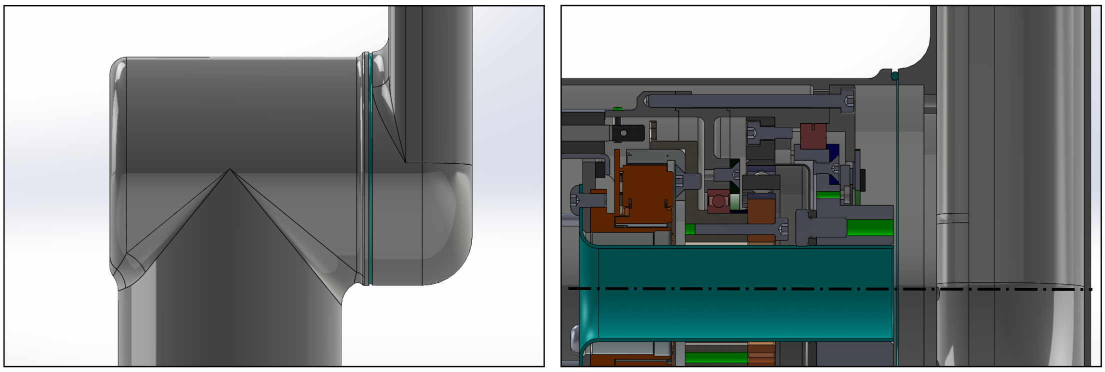
(a) (b)

Figure 40: Example of robot dynamic sealings actual implementation (shoulder-biceps joint): (a) external view and (b) sectioned view.

solution presents an additional design inconvenience: a removable cover is needed to clamp the seal to the rest of the housing. As such, an exposed bolted connection is introduced, together with a direct metal-to-metal interface that must be sealed in turn.

Finally, Fig. 39d depicts an axial sealing solution based on encapsulated o-ring; the core material consists of silicone or fluorocarbon elastomers, while the covering jacket is made of PTFE. Thanks to the particular combination of the two materials, the component guarantees good sealing performance, excellent resistance to chemical agents, and low contact friction. This interesting property allows the seal, typically employed in static applications, to be used in a rotary dynamic context, provided that applied pressures, duty cycles and relative sliding speed are modest (e.g. 3 bar, 0.5 m/s) [36] [4]. If a rotary operation is enforced, the o-ring radial pre-compression must be reduced from standard 25% to 6-14% range, and the sliding contact surface finish must be improved as much as possible (e.g. with $R_a \leq 0.8$) [36] [4]. The axial contact mechanism is greatly beneficial to both mechanical and hygienic design. The solution, in fact, is free from significant undercuts and requires no or limited variations in adjacent members outer diameter. The impact of the small residual gap between o-ring and outer casing surface can be mitigated by a suitable chamfer, which acts as invite for liquid sterilants. In addition, the seal groove is simple to design and requires little radial space on the respective casing; the thickness of the component is consequently minimized, together with weight. On the down side, the production of an adequate sealing action is assured only if enough compression force is exerted between the two involved members. As such, the joint coupling and the relative chain of tolerances must be properly designed to exert a suitable axial force.

After the examination of the main available commercial sealings, the axial o-ring solution is assessed as the most suitable for the custom aseptic robot. The choice is

Table 3.8: Friction torques absorbed by employed seals.

Joint	Joint 1[1]	Joint 2[2]	Joint 3[3]	Joint 4[4]	Joint 5[5]	Joint 6[6]
d_1 [mm]	133.02	133.02	107.62	88.57	88.57	88.57
R_{mean} [mm]	135.64	135.64	110.24	91.19	91.19	91.19
F_c [N]	266.04	266.04	215.24	177.14	177.14	177.14
F_a [N]	26.60	26.60	21.54	17.71	17.71	17.71
T_a [N m]	1.80	1.80	1.19	0.81	0.81	0.81

[1] Ground—Shoulder. [2] Shoulder—Biceps. [3] Biceps—Forearm. [4] Forearm—Elbow. [5] Elbow—Wrist. [6] Wrist—End-effector.

motivated by the seal great hygienic performance and the simplicity of implementation. The requirements of low external pressure, low sliding speed and reduced duty cycles are judged fit for the application [4], as corresponding to the actual context in which the robot is required to operate (see Section 2.1). In addition, it may be observed that the robot is typically not subjected to pressurized sterilization treatments during operative task frames, and vice-versa. In other words, during sterilization cycles, the robot is expected to be still, or moving at reduced speeds; consequently, the joint o-rings re-assume the original static sealing function, which significantly rises the maximum pressure value sustained. The result is obtained at the expense of an increased wear rate. The impact of this issue can be mitigated by the implementation of fast dismountable (i.e. maintainable) robot junctions: Section 3.5 will address the subject. Fig. 40 illustrates the actual implementation of sealing on the robot and the corresponding modifications introduced to the casing to further improve hygienicity.

Finally, an estimation of the friction torques absorbed by joints sealings is presented. With reference to the manufacturer documentation [4], the specific force F_d needed to deform the seal is a function of section chord diameter, hardness, and compression percentage. The set of employed o-rings are characterized by the following data:

- section chord diameter: $d_2 = 2.62\,\text{mm}$;
- hardness: 70 IRHD/Shore A;
- compression: 12%;
- friction coefficient PTFE on Ti-6Al-4V: $f_s = 0.1$ [67].

In the above assumptions, a value $F_d = 2\,\text{N/mm}$ is returned [4]. The net compression force F_c is computed as product of F_d and o-ring internal diameter d_1; the friction torques are hence calculated as $T_a = F_a R_{\text{mean}} = f_s F_c R_{\text{mean}}$, where R_{mean} is the mean radius of the seal. The final results for the six joints are reported in Table 3.8.

3.5 Aseptic junctions

Dynamic junctions represent one of the most delicate areas of an aseptic robot, as they must transmit motion among members while protecting the arm from potential inflow of aggressive sterilants. The common implementation adopted by commercial robots involve the use of internal flanges assembled through bolted connections, subsequently enclosed by removable covers. Although this solution is straightforward and of easy maintainability, hygiene is reduced by the presence of numerous exposed screw heads and sockets (see, for example, Fig. 10 and Fig. 11). This section aims to develop an innovative coupling approach, that might be implemented to improve the preceding. In particular, this aseptic junction architecture proposes to:

- transmit motion between robot members;
- avoid the use of any device that might affect the hygienicity of arm external surface;
- provide suitable axial compression to the implemented o-ring dynamic sealings;
- minimize joint assembling and disassembling time;
- preserve joint hollow design, for wiring passage.

A *compliant clamp unit* is designed for the purpose. The unit working principle is based on the elastic deformation of a number of thin flexible elements. Such deformability allows, from one hand, to assemble the joint without the need of external bolted connections; from the other hand, once a second internal equilibrium state is reached, it produces the residual stress responsible for motion transmission. The four main functional components of the clamp unit, depicted in Fig. 41, consist of an interface disk, a cam-profiled disk, a retain disk, and a compliant disk. The first three parts are linked to the output shaft of a robot drive and are housed in the respective joint casing (omitted in the figure); the fourth part, is conversely fastened to the downstream driven member (omitted as well). Fig. 42 illustrates the assembling order: cam and retain disks are progressively mounted on the interface disk; the provisional assembly is subsequently fastened to the output shaft of a drive through the devised screw holes. At last, the compliant disk is separately fastened to the driven member and enclosed in its casing.

Once the assembling operations have been completed, it is possible to connect the robot junction (see Fig. 43). The compliant disk, together with the surrounding driven member, is brought closer to the drive casing and inserted in the dedicated retain disk slots, until mechanical stop against the interface disk. At this point, the junction is put in operation by rotating the compliant disk in counter-clockwise

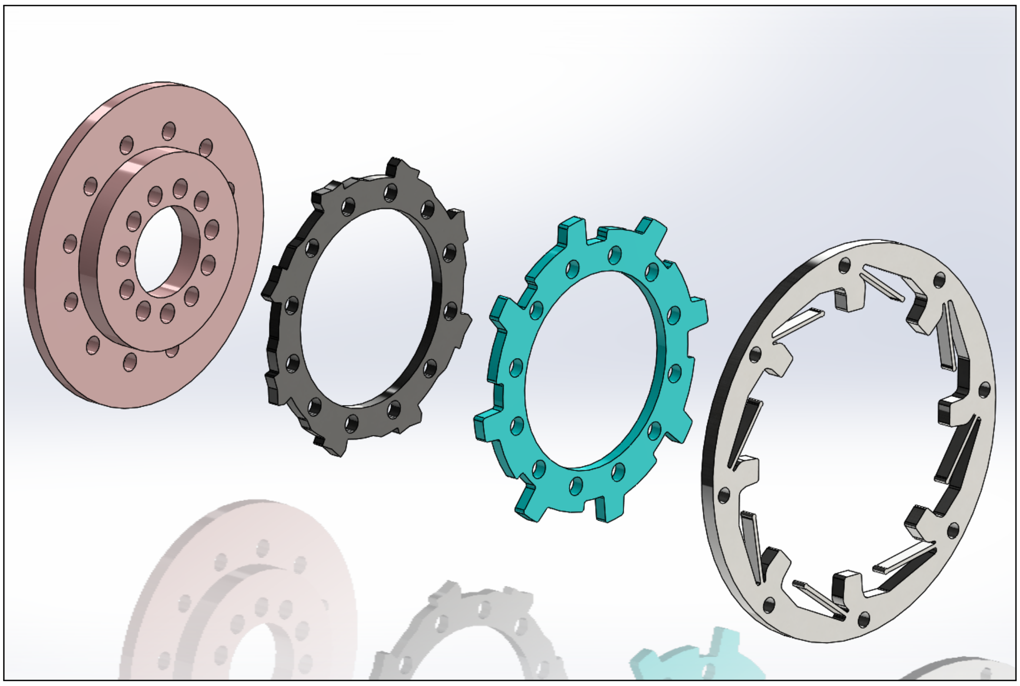

Figure 41: Exploded view of proposed compliant clamp unit parts. From left to right: interface disk (light red), cam-profiled disk (black), retain disk (light blue), and compliant disk (gray).

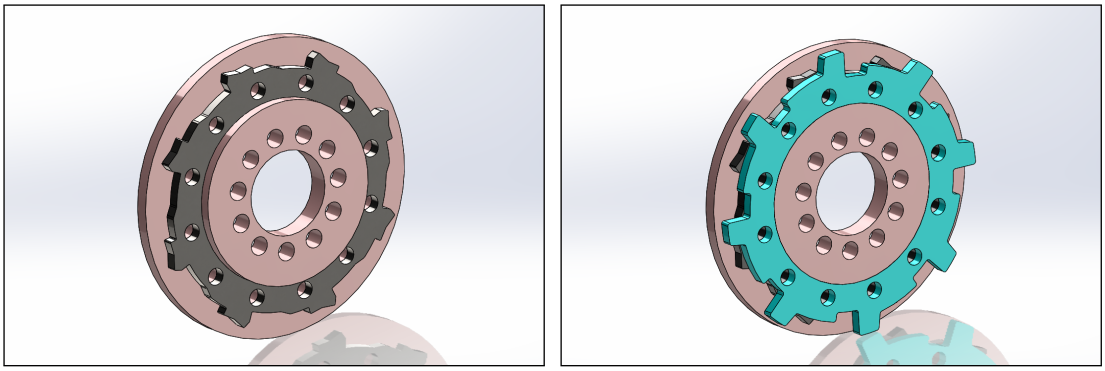

(a)

(b)

Figure 42: Clamp unit rigid sub-assembly mounting order: (a) cam disk is mounted on interface disk, followed by (b) retain disk. The whole sub-assembly is ultimately connected to drive output shaft.

direction. The procedure is illustrated in Fig. 44. The flexible beam (1) is deflected in upward direction by the contact with cam tooth upper profile (2), until the peak is reached. After this point, a descending profile allows partial restoration of beam original height by springback effect and compliant disk tooth (3) contacts

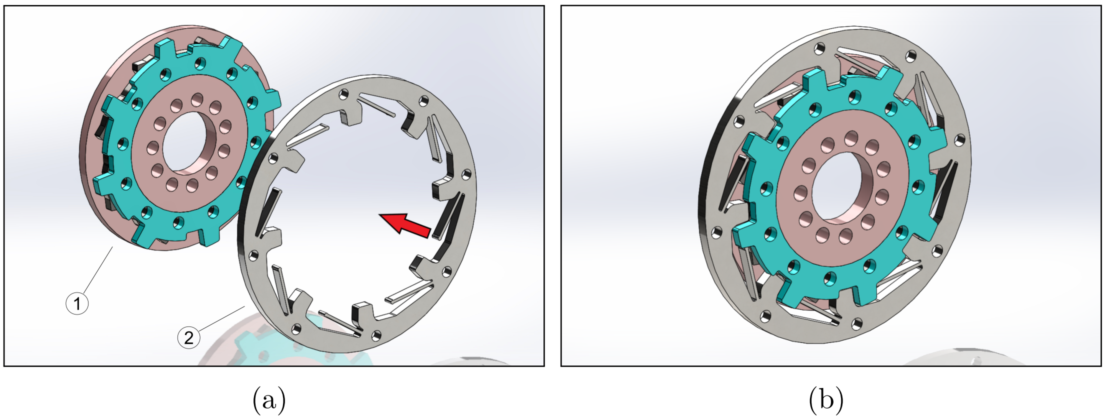

(a) (b)

Figure 43: Insertion of compliant disk (2) to rigid part of the clamp unit (1).

cam disk tooth (2). In this configuration, the two disks are completely locked together. In fact, from one side, the residual bending stress produces a contact force between the beam tip and the cam tooth; the arising friction, together with a suitable inclination of the profile, prevent the beam to overcome the vertical gap in the opposite direction, up to a certain limit. In other words, the cam disk may exert a defined amount of counter-clockwise torque without the flexible beam to bend upward and the tip to slide on the tooth. This principle can be employed to transmit counter-clockwise motion from the outer shaft of a drive (connected to the cam through the interface disk) to a driven robot member (connected to the compliant disk). Conversely, the transmission of a motor torque in the clockwise direction is easily allowed by the rigid contact between teeth (2) and (3). In the radial direction, the relative motion of the two disks is prevented by a calibrated ramp (4) of the cam. Finally, relative the motion of the compliant disk in the figure perpendicular plane is prevented by the obstruction produced by the interface disk and the retain disk (5). This result can be additionally exploited to produce a desired preload on the joint o-ring; the disks thickness, in fact, may be calibrated so that once in operation, the junction exerts a sufficient axial force on the sealing.

The disassembling of the unit, for joint maintenance, is performed through an opposite procedure. The clamp disk is rotated in the clockwise direction, so to produce a tangential sliding force that surpasses the static friction between beam tip and cam tooth. In this way, the beam deflects upward and overcomes the cam tooth peak corner: the compliant disk is consequently freed and can be rotated until tooth (3) arrives in correspondence of retain disk slot (6); finally, the whole driven member may be extracted in the direction perpendicular to figure plane. A summary of junction implementation on the robot is illustrated in Fig. 45.

In conclusion, the devised clamp unit is able to transmit motion from drive to driven member, provided that the friction reaction between cam disk and beams is superior to the maximum torque exerted by the motors. On the contrary, in order

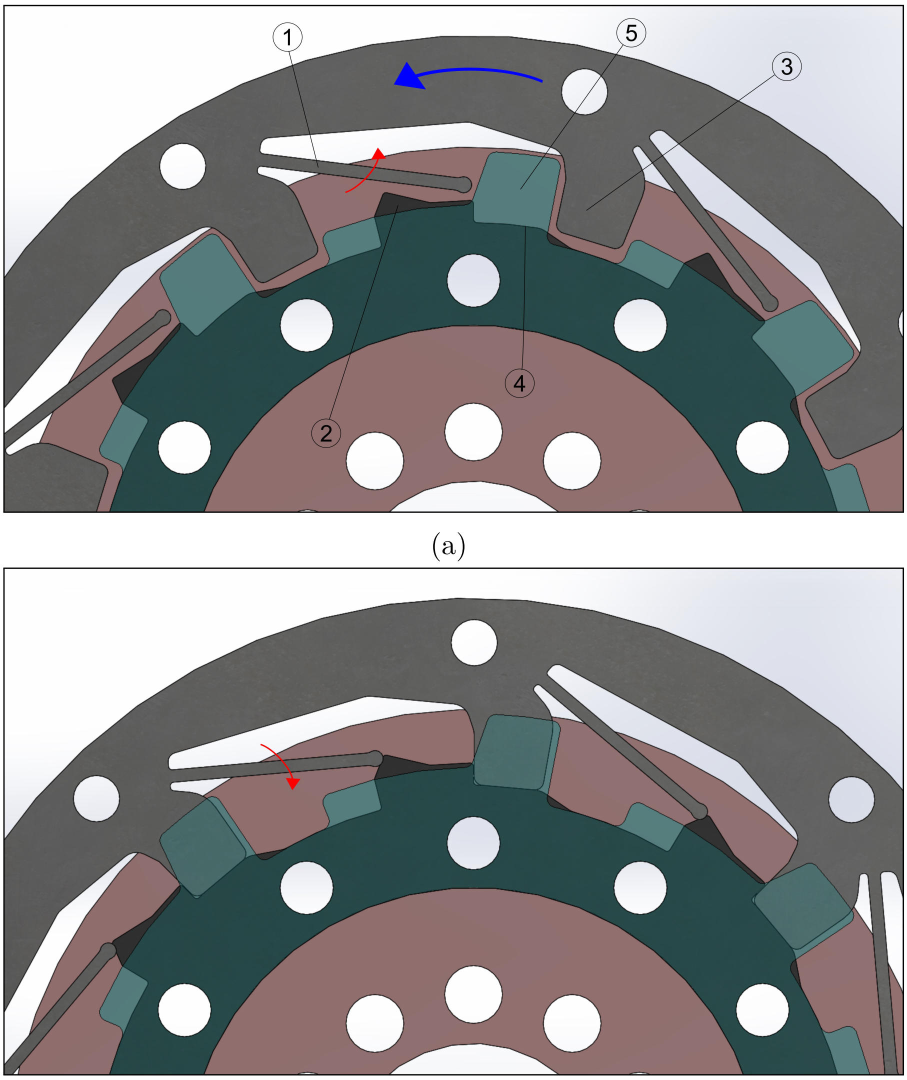

(a)

(b)

Figure 44: Clamp unit working principle. Involved elements: (1) flexible beam, (2) cam tooth, (3) compliant disk tooth, (4) cam ramp, (5) restraint disk tooth. (a) After insertion, compliant disk is rotated in counter-clockwise direction (blue arrow); flexible beam deflects in upward direction (red arrow) following cam tooth profile. (b) Compliant disk is locked: springback of flexible beam (red arrow) and obstruction of compliant disk tooth prevent relative tangential motion.

to separate the unit, a sufficient clockwise “disassembling” torque must be applied. Overall, a useful design relation may be expressed as follows:

$$T_{\text{motor,max}} < T_{\text{disassembling}} < T_{\text{gearing,max}} \tag{3.24}$$

That is: the torque required to disassemble the unit (once in operation) must be

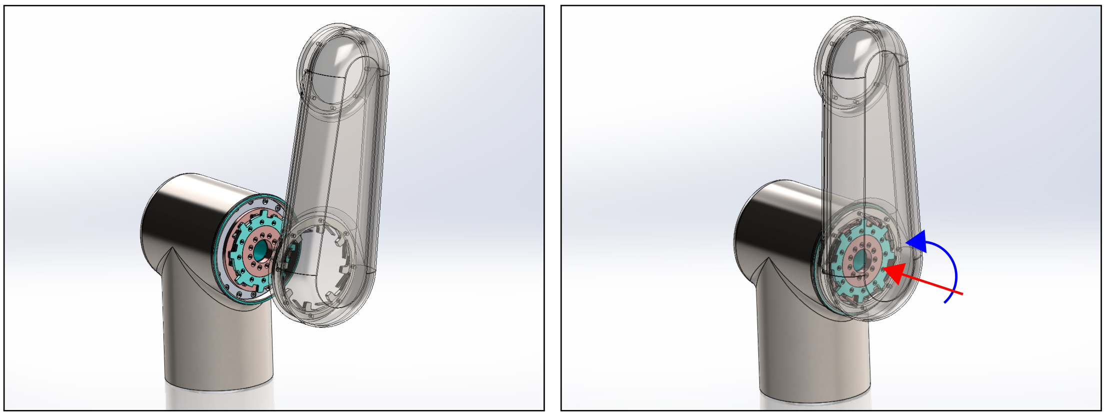

(a) (b)

Figure 45: Implementation of clamp unit on robot through simple manipulation of the external casings. (a) Shoulder and biceps are brought in correspondence; (b) unit is put in operation by axial approach and suitable rotation.

greater that the maximum output torque exerted by the motor; at the same time, the needed disassembling torque must not exceed the maximum value that can be sustained by the drive gearing without damage. Beams number, thickness, length, and inclination must be designed accordingly; Appendix C reports a summary of model and calculations used to size robot clamp units.

A final remark can be made about clamp unit manufacturing. Given the considerable accuracy required to operate correctly, it is advisable that a high-quality process is employed. For the case being, Electrical Discharge Machining (EDM) is judged fit, as both compliant disk and cam disk could be processed by the the same semi-finished plate. As such, the accuracy of the coupling profiles would be greatly increased, and it would be possible to realize very thin beams (e.g. in the order of 0.5 mm) without warps [55].

3.6 End-effector

The last component to design is the robot end-effector. Many commercial products are already available off-the-self; Fig. 46 shows a small summary of the principal offers. It may be noticed that architectures and shapes are widely variable: indeed, the realization of a particular geometry is strictly related to the specific application which the robot is required to perform. In this work, a generic end-effector is presented, with the purpose of manipulating pharmaceutical industry test tubes (see also [84]). Apart from the purely representative task, the main objective of this section is to highlight some useful guidelines with reference to aseptic manipulators design.

(a) (b) (c)

Figure 46: Example commercial grippers: (a) Schunk PGN-plus-E, (b) Festo DHWS, (c) Gimatic GMP-G kit.

Given the fulfillment of hygienic constraints, the proposed concept is based on four key pillars:

- minimization of moving parts;
- multitask operation;
- minimization of weight;
- compact geometry.

The first two points are addressed by the choice of a single actuated claw, combined to a suitable interface geometry. Reduction of weight and compactness are instead pursued by the accurate choice of internal components, the exclusion of every non-fundamental part, and a particularly convenient assembling. Fig. 47 illustrates the design result. The gripper is composed by three separate parts: a casing box, a removable cover, and a moving claw. The last component, responsible for objects manipulation, is shaped as a simple jaw. The rotation in the horizontal plane allows the claw to grip and release the target tubes by friction force. The action is provided by the contact force exerted against a fixed counter-surface, integral to the casing. If the two interface surfaces are suitably shaped, the end-effector is able to manipulate multiple objects and in different attach configurations; an example is offered in Fig. 48. The casing of the end-effector is realized in the same material of the rest of the robot, that is Ti-6Al-4V titanium alloy. It is composed by a main hollow box and a rear circular flange, that allows the connection with the rest of the arm. Fig. 49, presents an overview of box internal components. The source of motion is *Maxon EC-i 30* BLDC motor, which has been selected for a number of important reasons. First, the motor is provided by the same manufacturer of the other robot drives motors; this allows simplified material refurbishment and quicker maintenance operations. Secondly, the motor is characterized by a very thin diameter, a considerable torque density and integrated Hall sensors. Additionally, the output shaft is accessible from both sides; thus, it is possible integrate, with

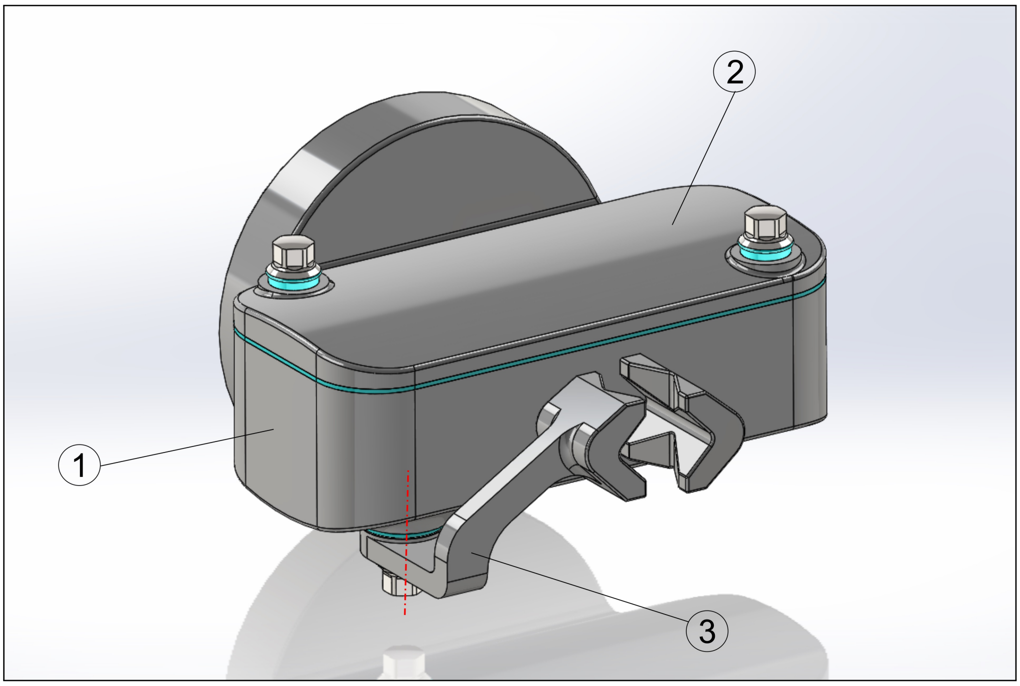

Figure 47: Overall view of proposed end-effector concept for pharmaceutical test tubes manipulation: (1) casing box, (2) casing cover, (3) moving claw. Axis of rotation highlighted in red.

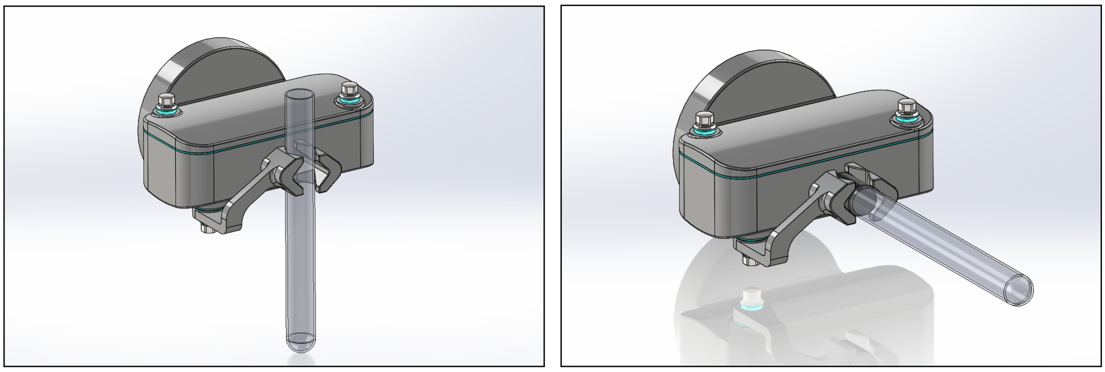
(a)

(b)

Figure 48: Example of end-effector multitasking capability: (a) vertical test tube, (b) horizontal test tube (capped).

significant ease and compactness, a dedicated encoder in the rear part. It may be noticed that no digital controller is present in the assembly: the component is relocated in robot wrist, in order to further reduce inertia and save valuable space. The electrical wiring of motor and accessory sensors is granted by a wide internal opening realized in the connection flange of the casing. Motion transmission

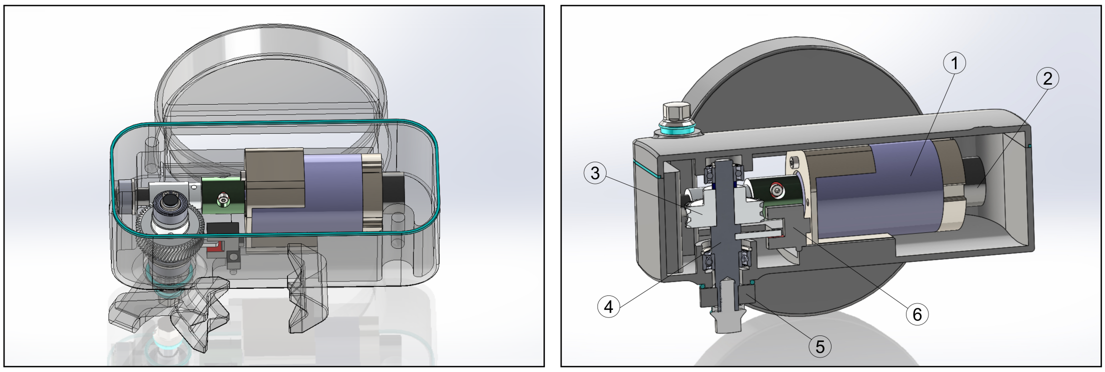

(a) (b)

Figure 49: (a) Overall view of end-effector internal components. (b) Sectioned illustration of motion transmission: (1) motor, (2) encoder, (3) worm gear drive, (4) output shaft, (5) claw, (6) photocell limit switch sensor.

is handled through a worm gear drive, which allows to easily transform motor horizontal rotation into a vertical rotation of the claw; the solution, characterized by a reduction ratio 60:1, is lightweight, compact, and avoids further gearing. Both motor shaft and output shaft are supported by dedicated thin-section ball bearings. The mechanism is completed by a photocell switch sensor, which limits the rotation of the claw and prevents it from colliding. The casing box is closed, at the top, by a removable cover characterized by a rounded upper surface that promotes natural drainage of liquids. The component is fixed to the casing through an aseptic-designed bolted joint: no crevices are present (screw sockets are substituted by extruded support faces), and dedicated static seals are integrated under the rounded screw heads. A gasket in interposed between box and cover to avoid direct metal-to-metal interface and to provide suitable sealing. The claw is implemented in a similar fashion: an aseptic screw, provided with a dedicated sealing, joins the moving member to the output shaft of the box internal mechanism.

Overall, the proposed end-effector weights approximately 0.85 kg, with a center of gravity located 50 mm apart from the connection flange to the robot. The grip force exerted by the claw on a test tube, in the vertical configuration, may be retrieved in function of the motor nominal torque (detailed bill of materials is reported in Appendix B); in particular:

- motor nominal torque: $T_N = 65.4\,\mathrm{N\,mm}$;
- reduction ratio: $i = 60$;
- transmission efficiency: $\eta = 0.9$ (estimation);
- claw lever arm: $b = 29\,\mathrm{mm}$;

- claw contact surface angle: $\alpha = 27.27°$;
- contact friction coefficient: $f_s = 0.2$ (estimation).

Therefore, by conservation of mechanical energy:

$$P_{\text{in}} = \frac{P_{\text{out}}}{\eta} \Rightarrow T_{\text{in}}\omega_{in} = \frac{T_{\text{out}}\omega_{\text{out}}}{\eta} \tag{3.25}$$

or

$$T_{\text{out}} = \eta i T_{\text{in}} = \eta i T_N = 3.53\,\text{N m} \tag{3.26}$$

The contact force results

$$F_c = \frac{T_{\text{out}}}{b\cos(\alpha)} \tag{3.27}$$

and, ultimately, the friction grip force

$$F_g = f_s F_c = f_s \frac{T_{\text{out}}}{b\cos(\alpha)} = 27.4\,\text{N} \tag{3.28}$$

Consequently, the gripper is able to sustain through sheer friction a payload $m_p = F_g/g = 2.8\,\text{kg}$, which is sufficient for the application.

3.7 Robot review

This concluding section presents a final review of the designed aseptic robot.

The overall architecture consists of a 6-DOF articulated arm, equipped with a spherical wrist and a terminating 1-DOF actuated manipulator. From a kinematic point of view, six main members are present: (1) shoulder, (2) biceps, (3) elbow, (4) forearm, (5) wrist, (6) end-effector. With reference to Section 3.2.6, the three designed drive modules have been distributed as follows:

- Ground—Shoulder: Size-90 drive;
- Shoulder—Biceps: Size-90 drive;
- Biceps—Elbow: Size-60 drive;
- Elbow—Forearm: Size-45 drive;
- Forearm—Wrist: Size-45 drive;
- Wrist—End-effector: Size-45 drive.

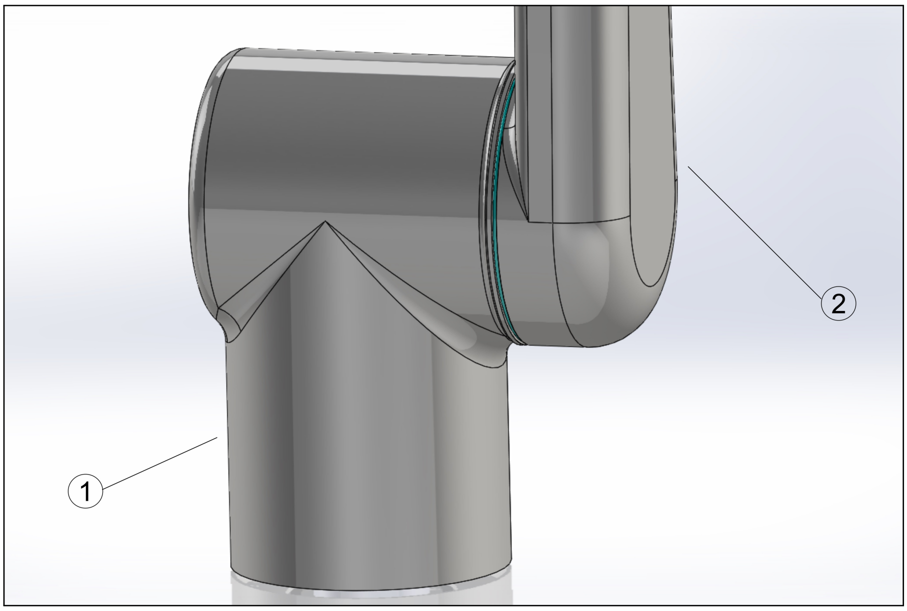

(a)

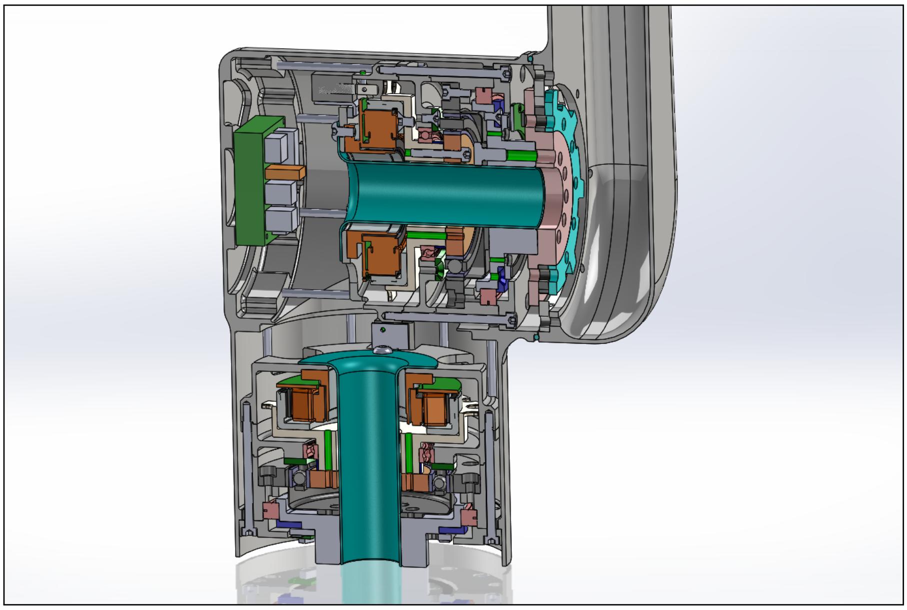

(b)

Figure 50: Robot shoulder joint: (a) external and (b) sectioned view.

Fig. 50 illustrates the final implementation of robot shoulder joint, which is linked to the ground in its lower part. A single casing houses two digital controllers (bolted in a dedicated bottom area) and two corresponding Size-90 drives, for rotation of the robot about the vertical axis (DOF-1) and motion of the subsequent arm in the vertical plane (DOF-2). The drives are inserted axially from the two shoulder casing openings and are subsequently fastened to it; no additional covers are required, nor exposed screws (see also Fig. 34a). The biceps is connected to the horizontal drive output shaft by the means of the described compliant clamp unit (see Section 3.5). This solution allows, from one hand, to transmit motion without the need of external bolted connections. From the other hand, it guarantees sufficient axial preload on the local rotary sealing (o-ring, see Section 3.4) by the means of tolerated chain of dimensions. An internal hollow conduit traverses the shoulder for electric cabling passage; as such, it is possible to wire local controllers and prosecute the routing to subsequent joints through the hollow biceps.

A detailed view of the elbow is offered in Fig. 51. The joint houses, from one side, a Size-60 drive (DOF-3), which is connected to the biceps by the means of a dedicated clamp unit, and realizes motion in the vertical plane. A Size-45 drive (DOF-4) is conversely housed in the casing upper part and constitutes the first actuator of robot spherical wrist; additionally, the drive is coaxial to robot DOF-1 when the arm is at complete vertical extension (see, for example, Fig. 37a). Two digital controllers are fixed to an internal elbow recess, similarly to shoulder assembly. The beginning of the hollow forearm, visible in the upper part of the figure, is ultimately bolted to DOF-4 output shaft by the means of an internal flange (wide openings are present for both cable passage and reduction of inertia). Two rotary axial sealings protect the junctions at both ends.

Finally, an illustration of robot wrist area is presented in Fig. 52. The assembly is composed by three conceptual sub-parts: forearm termination, wrist arm, and wrist drive casing. The forearm termination encloses a Size-45 drive (DOF-5) and realizes the second DOF of the spherical wrist. It may be noticed that its casing is not integral with the hollow forearm tube; the connection is rather performed through direct threading of the two components (secured by a thread-locker), and is externally protected by a static seal. The solution allows, in the assembling phase of the arm, to preemptively reach and fasten the screws that link the tube with DOF-4 (as described earlier). The output shaft of DOF-5 is linked to the wrist (arm) by the means of a third clamp unit; the junction is sheltered by a dedicated rotary axial seal. In order to simplify the manufacturing process, the wrist is produced in two separate pieces (wrist arm and wrist drive casing), subsequently joined by welding. The latter casing houses the last robot actuator (DOF-6), which consists of a Size-45 drive and is ultimately linked to the end-effector by the means of a locked threaded disk. Three digital controllers are contained in this portion of the robot. The first is placed under DOF-5 and is responsible for its power supply; the controller is supported by a thin internal plastic plate, and is facing downward. Through this expedient, the wrist center of gravity is brought closer to the shoulder, so that moment of inertia is slightly reduced; more importantly, it is possible to optimize the use of hollow forearm internal space (otherwise empty) by routing pertaining cables inside it. The last two controllers, housed in the wrist arm, are respectively dedicated to DOF-6 and gripper motor supply; end-effector casing is

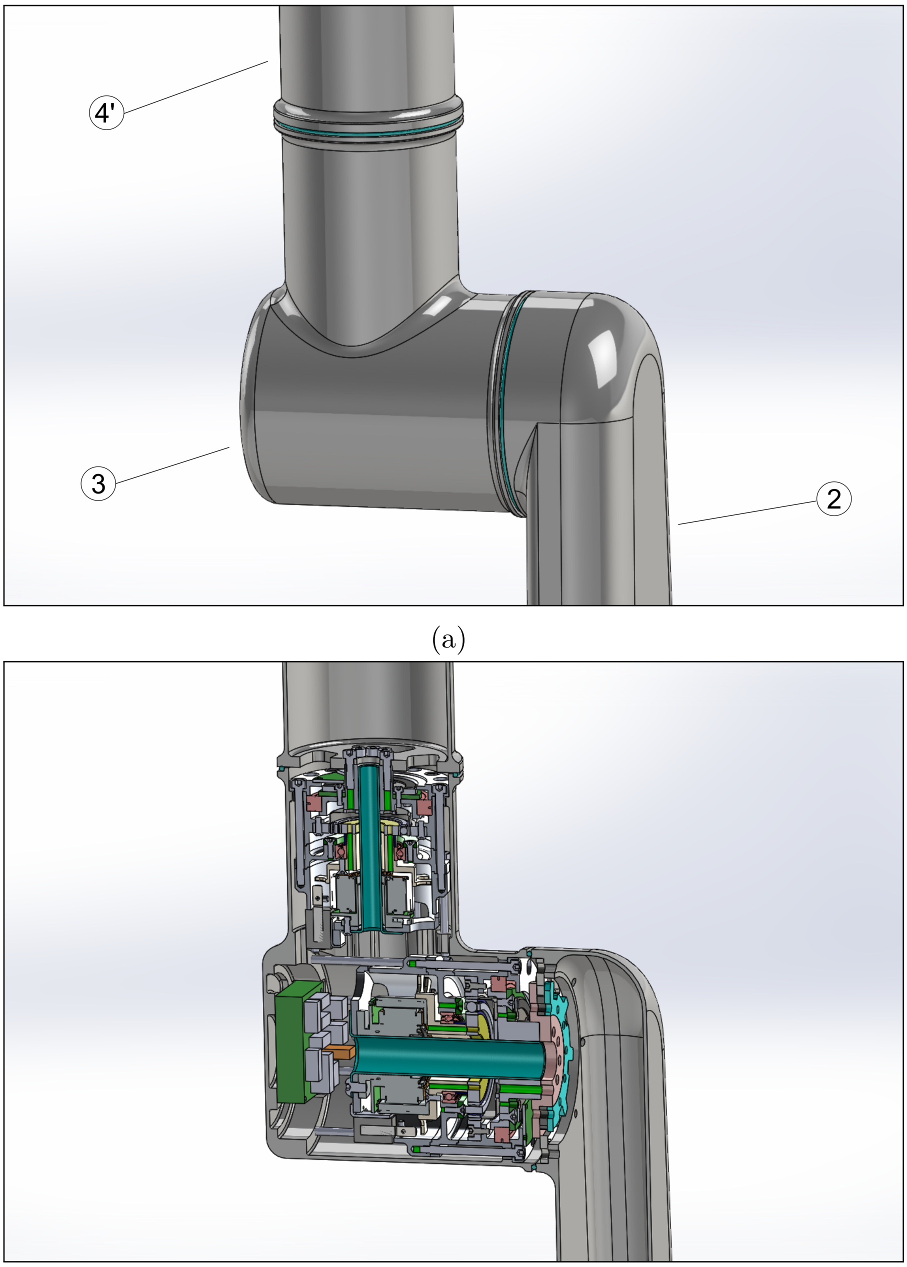

(a)

(b)

Figure 51: Robot elbow joint: (a) external and (b) sectioned view.

consequently reduced in size and inertia.

In conclusion, the main technical specifications of the robot are presented. Mechanical performances of the joints are reported in Table 3.9. Masses are distributed as follows:

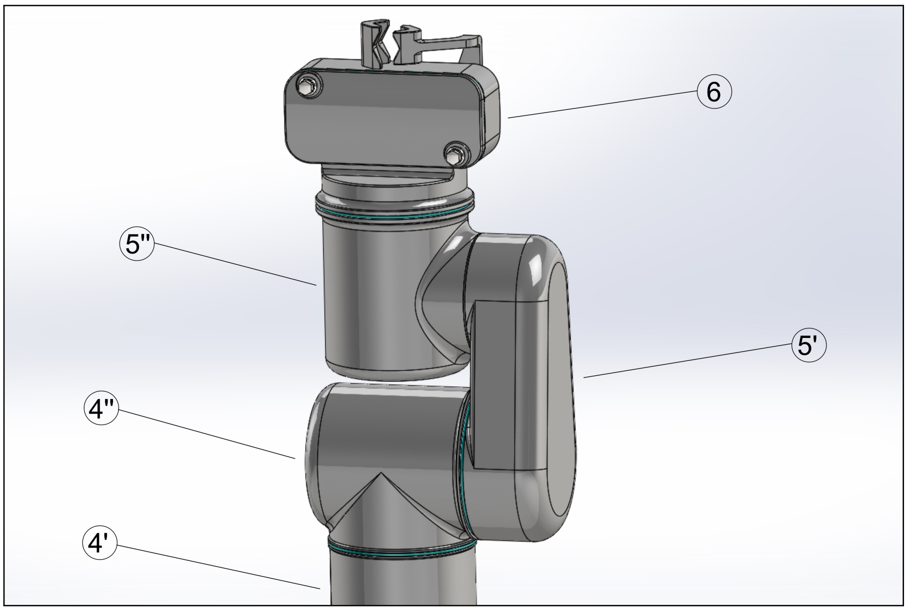

(a)

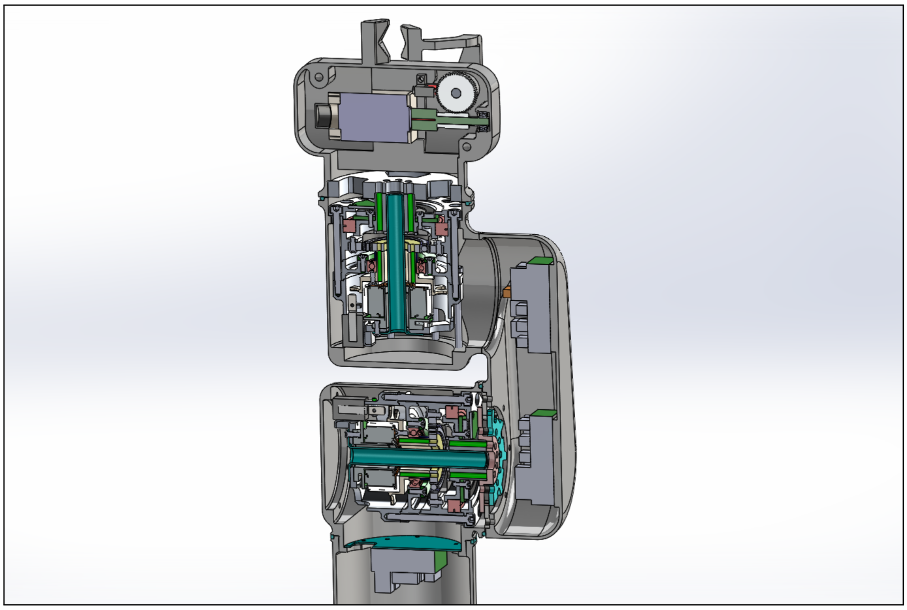

(b)

Figure 52: Robot wrist joint: (a) external and (b) sectioned view.

- shoulder: 6.8 kg;
- biceps: 1.2 kg;
- elbow: 3.4 kg;

Table 3.9: Summary of robot joints specifications.

	DOF 1	DOF 2	DOF 3	DOF 4	DOF 5	DOF 6
Power [W]	160	160	100	70	70	70
Max speed[1] [rpm]	16.4	16.4	21.9	35.0	35.0	35.0
Rated torque[2] [N m]	48.9	48.9	31.21	8.79	8.79	8.79

[1] Average value for grease lubrication; temporary higher peak values allowed.
[2] Net value, accounting gearing efficiency and friction absorbed by sealings at reference motor speed of 2000 rpm.

- forearm: 1.9 kg;
- wrist: 1.8 kg;
- end-effector: 0.8 kg;

The total robot mass results $m_R = 15.9\,\mathrm{kg}$, which is comprised in the prescribed target range. With reference to the kinematic model depicted in Fig. 20, the main robot link lengths are:

- $d_1 = 180\,\mathrm{mm}$;
- $a_2 = 250\,\mathrm{mm}$;
- $d_4 = 303\,\mathrm{mm}$;
- $d_6 = 255\,\mathrm{mm}$;

Consequently, the arm horizontal reach (i.e. the distance measured from DOF-2 axis to TCP) is equal to $r = a_2 + d_4 + d_6 = 808\,\mathrm{mm}$; the full vertical arm reach (i.e. measured from shoulder base to TCP), is conversely equal to $L_t = d_1 + r = 988\,\mathrm{mm}$.

The part of the arm subsequent to the shoulder is characterized by a mass $m_a = 9.1\,\mathrm{kg}$ and a center of gravity located, at full horizontal reach, at $d_a = 424\,\mathrm{mm}$ from DOF-2 axis. Given the data of Table 3.9, the maximum static net payload that the shoulder drive can sustain at full reach, in nominal conditions, may be computed as

$$m_p = \frac{T_2 - m_a g d_a}{g r_h} = 1.3\,\mathrm{kg} \tag{3.29}$$

which is in line with the project target constraints. Indeed, in the presented calculation, the mass of the end-effector was also taken into account. If the same procedure is repeated without this aggravation, m_a and d_a respectively reduce to 8.3 kg and 388 mm, returning a maximum payload of $m_p = 2.2\,\mathrm{kg}$.

A final overview of the designed robot arm is offered in Figs. 53 to 56; structural analysis of main components is reported in Appendix C.

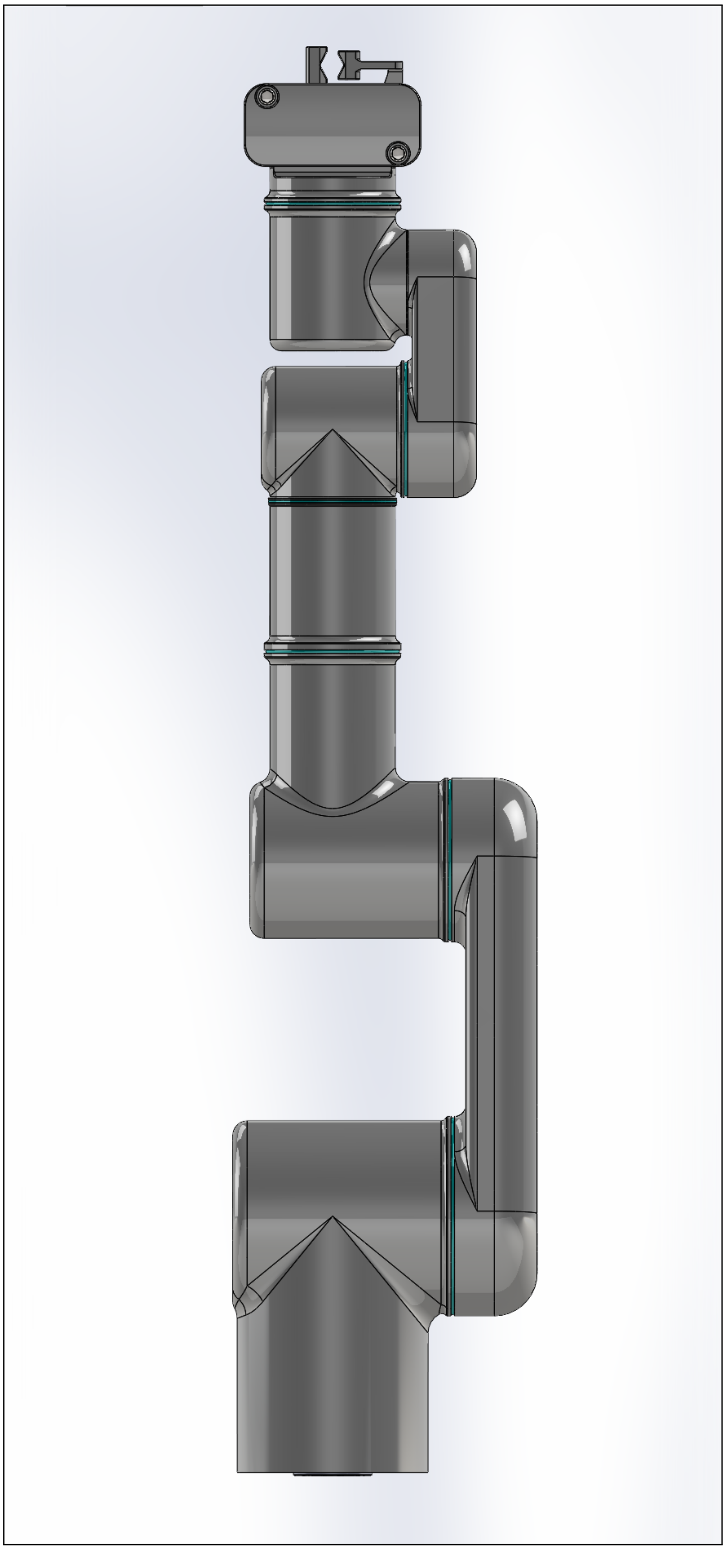

Figure 53: External view of the robot, in full vertical extension.

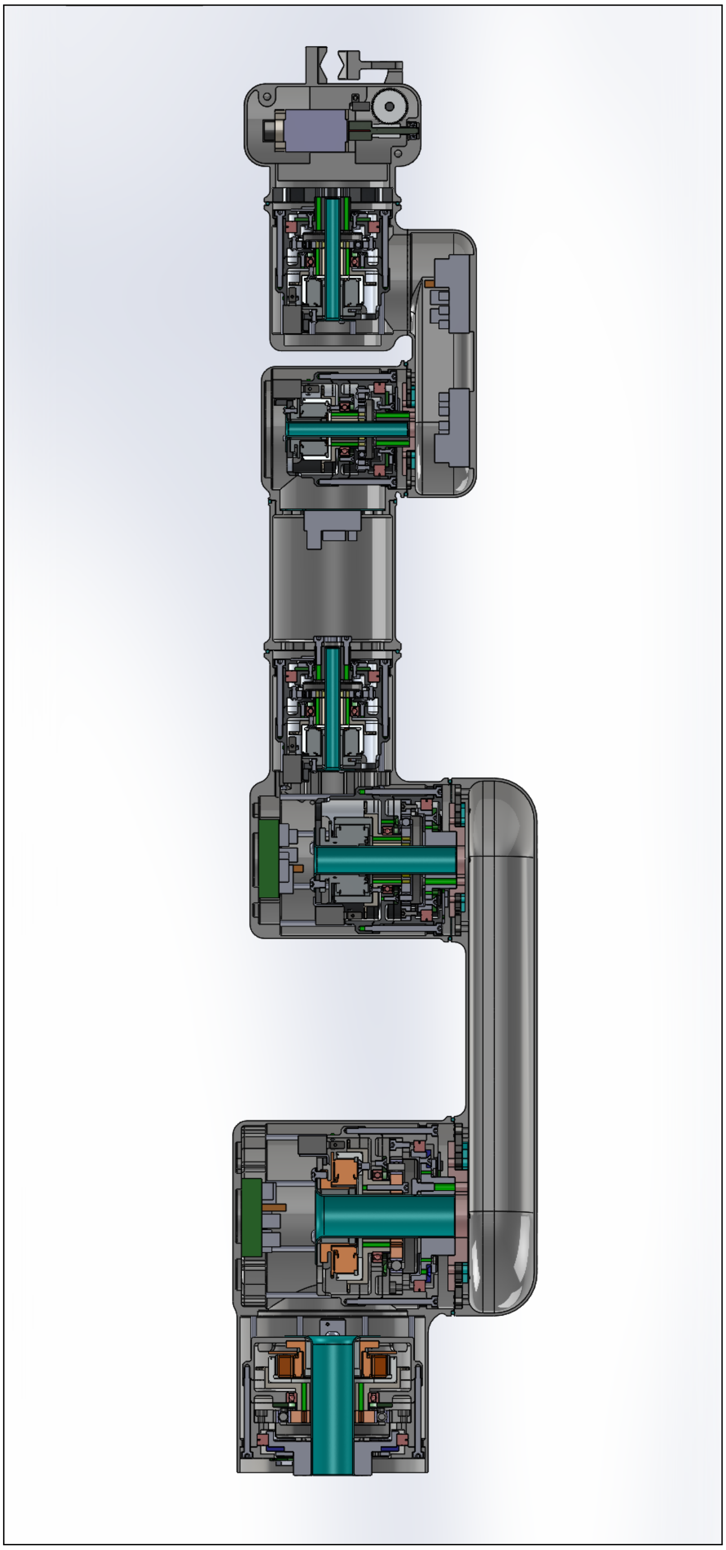

Figure 54: Sectioned view of the robot, in full vertical extension.

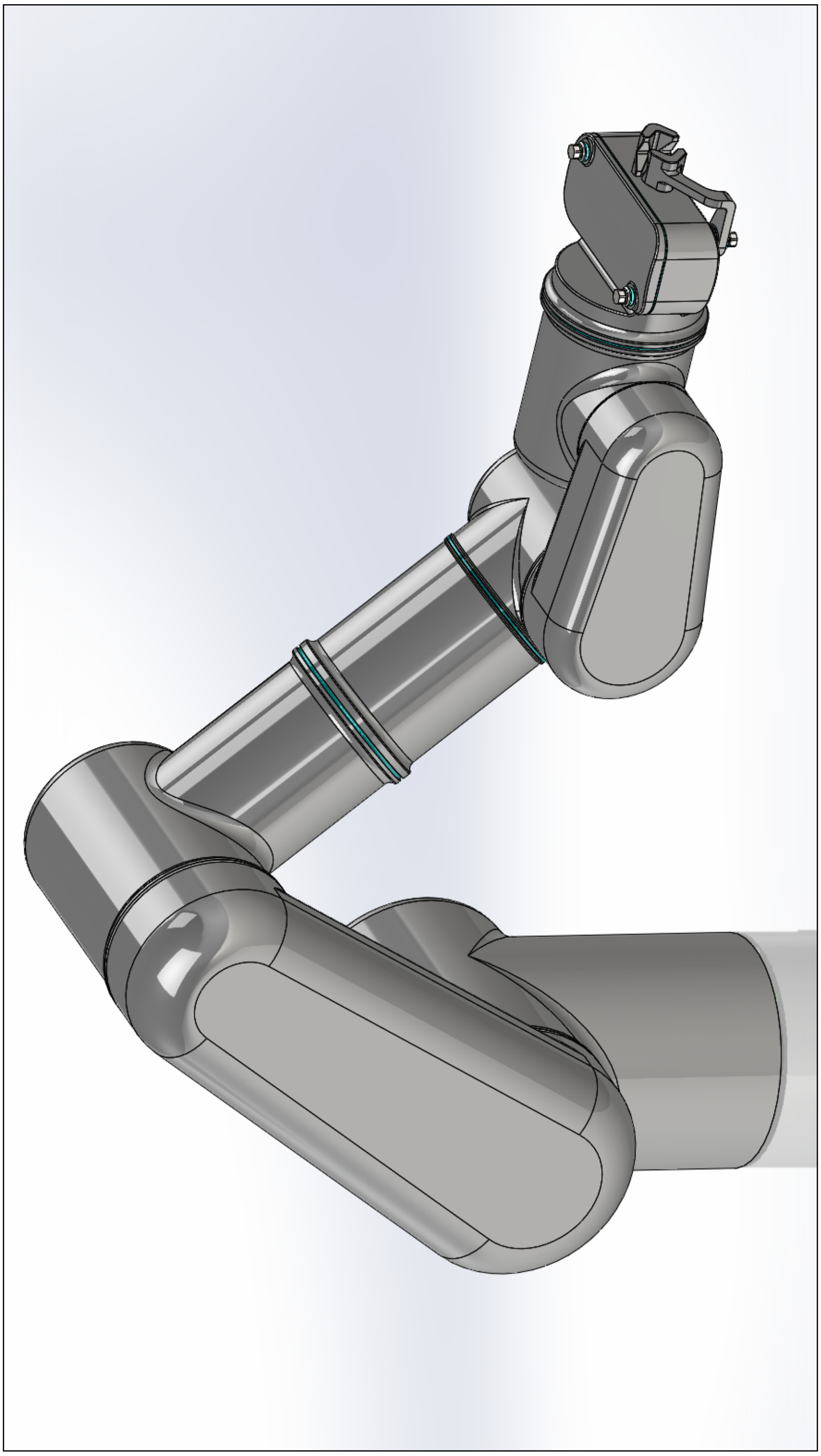

Figure 55: Overall view of the robot, right side.

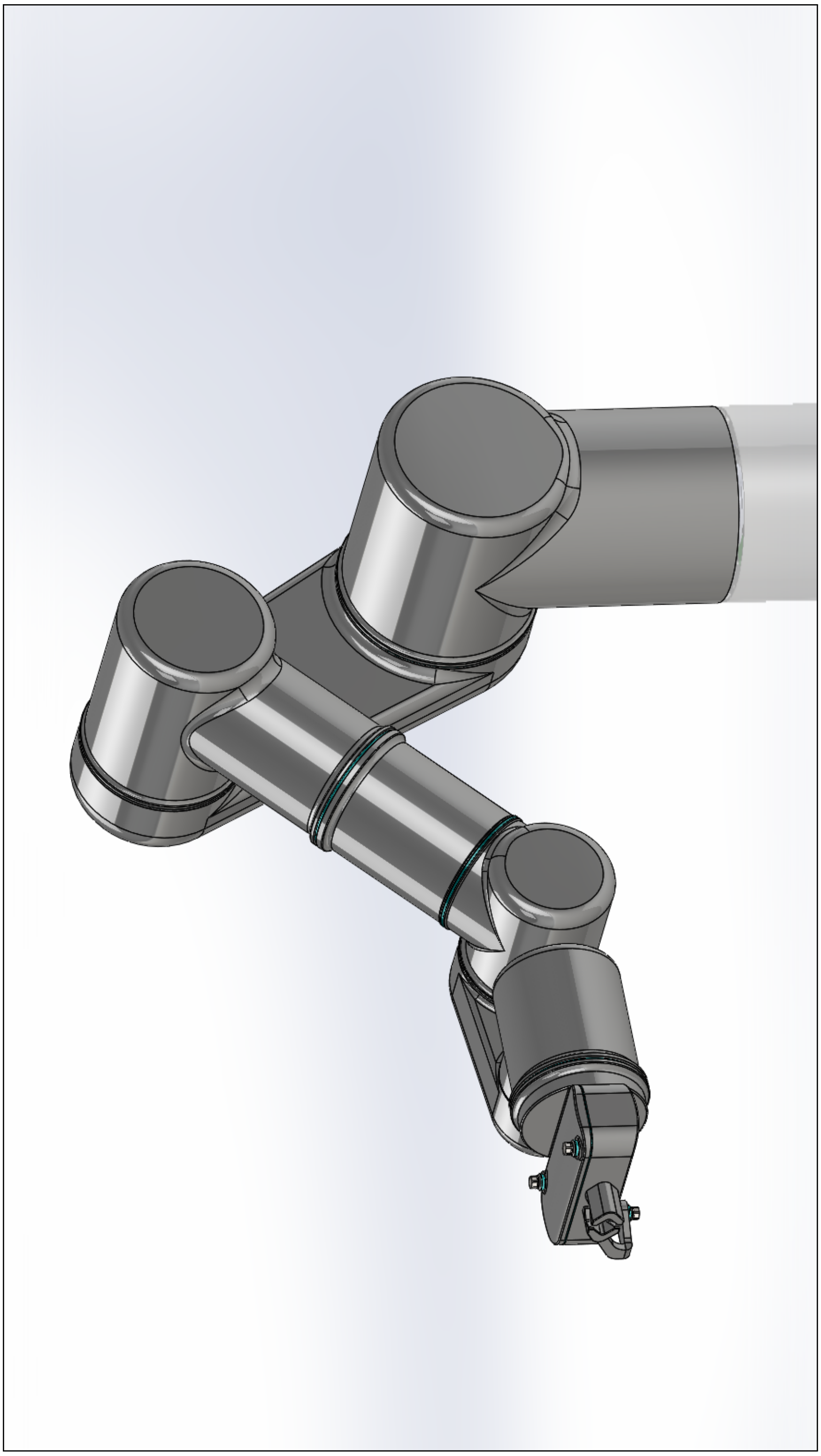

Figure 56: Overall view of the robot, left side.

Chapter 4

Real-time Multibody Simulation

Numerical simulation is a powerful instrument, and is gaining crescent importance in the study of complex mechanical systems.

This chapter describes the development and the application of a custom real-time[1] robot simulator based on multibody dynamics. The software is realized with a dual purpose: to guide mechanical design process, and to serve as a virtual test bench of the robot. More specifically, the simulator is characterized by the following aims:

- verify the mechanical sizing of implemented robot drives;
- visualize a 3D workplace and study the mutual interactions with the robot;
- study and design suitable trajectories and motion laws;
- prepare robot programming in order to shorten subsequent deployment phase.

After a brief summary of the used tools, the main features of the software are presented followed by the achieved results.

4.1 Software implementation

4.1.1 Toolchain

The development of a 3D robot simulator consists of two fundamental steps: realization of a virtual environment and subsequent implementation of tasks (see

---

[1] More specifically, this work focuses on the implementation of a *soft* real-time software, in which the timing constraints are satisfied within the limitations of target machine computational burden.

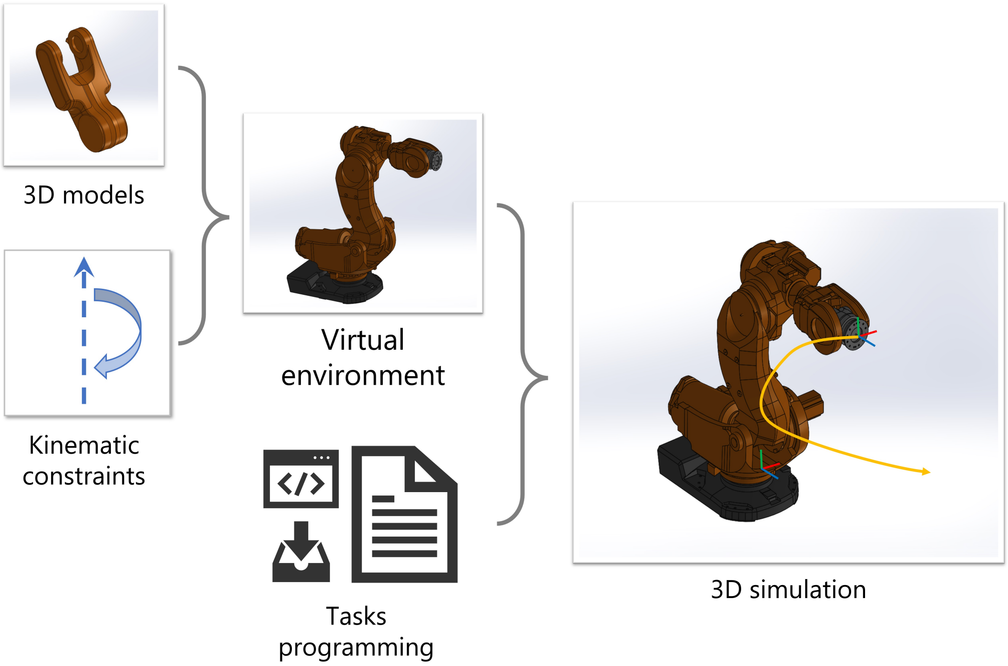

Figure 57: Conceptual bricks of 3D simulation.

Fig. 57). The endpoint is to display the temporal evolution of the system under a given set of inputs, and collect related data.

In the first phase, it is necessary to sub-divide the system in its functional elements. The various bodies are assembled in a hierarchical structure and a set of kinematic constraints are defined among them (mainly lower-pair couplings and actuators). Once the virtual environment modeling is complete, the management of inputs must be programmed. Consequently, it is necessary to implement motion control algorithms, interactions between robot and environment, and a dedicated Graphical User Interface (GUI). The main tools involved consist of:

- a 3D model processor;
- a simulation library;
- a real-time 3D renderer;
- a GUI designer application;
- an Integrated Development Environment (IDE).

In this work, the use of open-source software was selected as a design choice.

First of all, given the multibody nature of the present case application, it is essential to adopt a suitable library for managing kinematics and dynamics of a large number of entities. In particular, the following features are required:

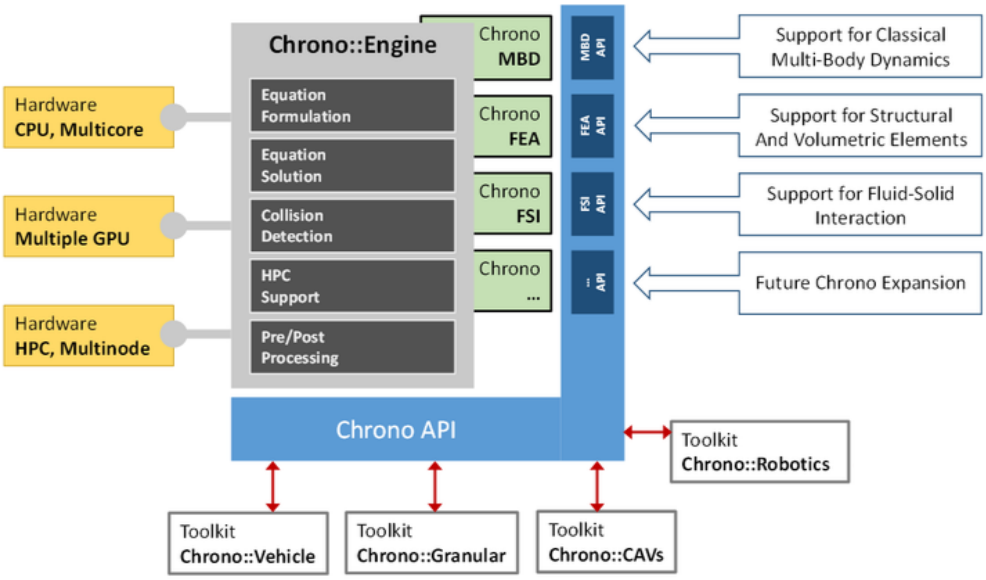

Figure 58: Representation of Chrono::Engine library structure, from API documentation [107].

- faithful representation of underlying physics;
- inclusion of a real-time 3D renderer, or possibility to interface to a third-party one;
- handling of unilateral constraints, contacts and collisions;
- possibility to implement custom algorithms and functions;
- possibility to export data and plots.

Chrono::Engine, an open-source multi-physics modeling and simulation infrastructure, was selected for the purposed [107]. The core of the engine consists of a C++ object-oriented library, which can be included and compiled in custom third-party applications as a middleware (see Fig. 58). In order to display the simulated 3D geometries of the system, the open-source 3D real-time renderer *Irrlicht Engine* was linked to the project [51]. Simulation speed was optimized by the means of an automatic defeaturing pre-process performed through the *Open Cascade* 3D modeling kernel [80]. Finally, the *Qt Designer* library [109] was used to implement a GUI through which the user can interact with the simulation at run-time.

In conclusion, the following workflow is adopted for simulator development:

1. design 3D geometries of robot and environment in a CAD software;

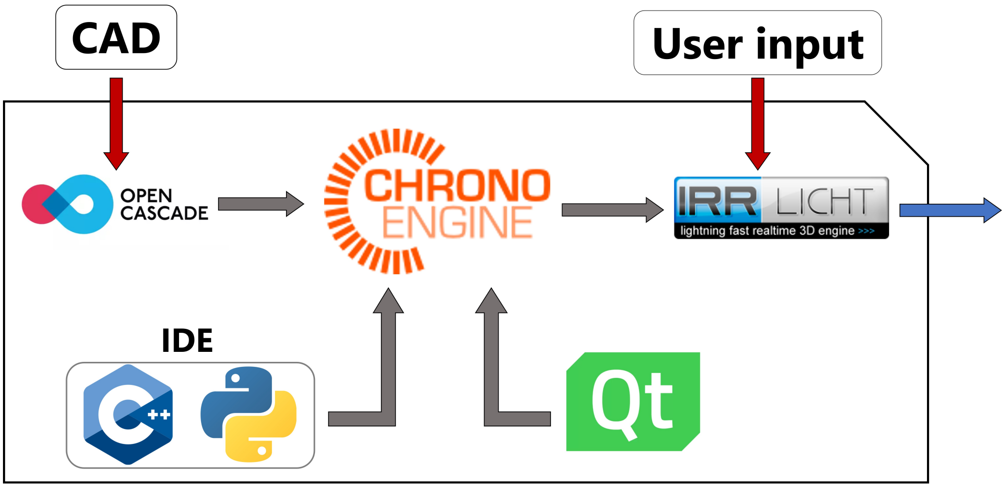

Figure 59: Simulator infrastructure and main development tools.

2. export CAD shapes in a neutral file format;
3. optimize shapes and defeaturing;
4. import shapes as simulation entities, define constraints and assign properties;
5. create classes and methods for system entities interaction;
6. perform simulation;
7. gather results and post-process.

A summary of the involved toolchain is illustrated in Fig. 59.

4.1.2 Virtual environment

The implementation of the software starts from the creation of the virtual environment, which is principally made of the designed robot and a surrounding workplace scenario.

The robot main sub-assemblies (shoulder, biceps, elbow, forearm, wrist, end-effector) are initially rearranged in six corresponding solid entities. In order to keep track of joints location and automatize subsequent creation of simulated motors, a local reference frame is placed at each junction (see Fig. 60a). More specifically, these helper markers are disposed on joints interface plane, and aligned (with local Z) to respective rotation axis. Even if not strictly required, a second set of markers is included in the model. These additional frames, depicted in Fig. 60b, correspond to the Denavit-Hartenberg kinematic model described in Fig. 20 and will serve as base reference for bodies motion control.

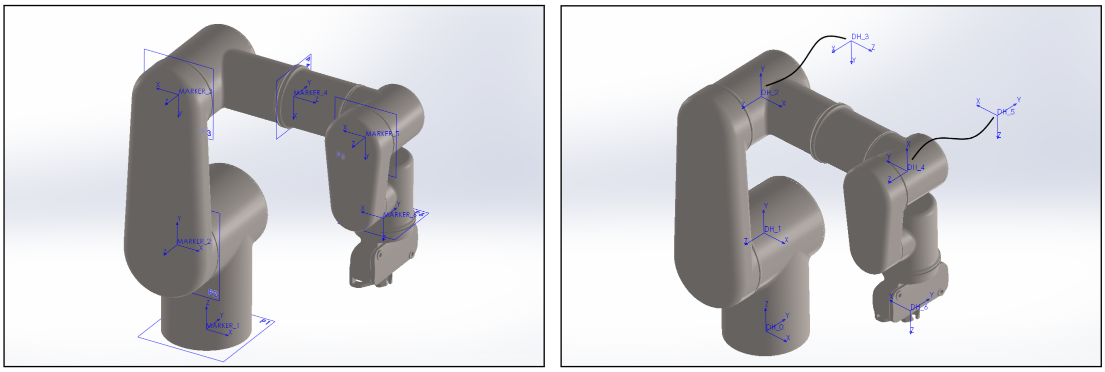

(a) (b)

Figure 60: Robot home configuration, with helper markers highlighted: (a) joint markers and (b) Denavit-Hartenberg markers (frames 3 and 5 shown with fictitious offset).

The next step consists in the 3D modeling of the robot workplace environment. In this work, a pharmaceutical industry process is assumed as example of aseptic application; Fig. 61 illustrates the idea. The environment is composed by four main entities:

1. product injector lance;
2. test tube body;
3. test tube cap;
4. blister of filled test tubes.

The robot, subsequently inserted in correspondence of the highlighted vertical axis, is responsible for the processing of sterile test tubes. More specifically, the robot is required to:

- grip the product injector lance (1) fed by a nearby tank;
- fill the test tube (2) transported by a dedicated conveyor;
- return lance (1);
- stir test tube (2);
- relocate test tube (2) to blister empty slot (4);
- get tube cap (3) from dispenser and plug it into tube (2).

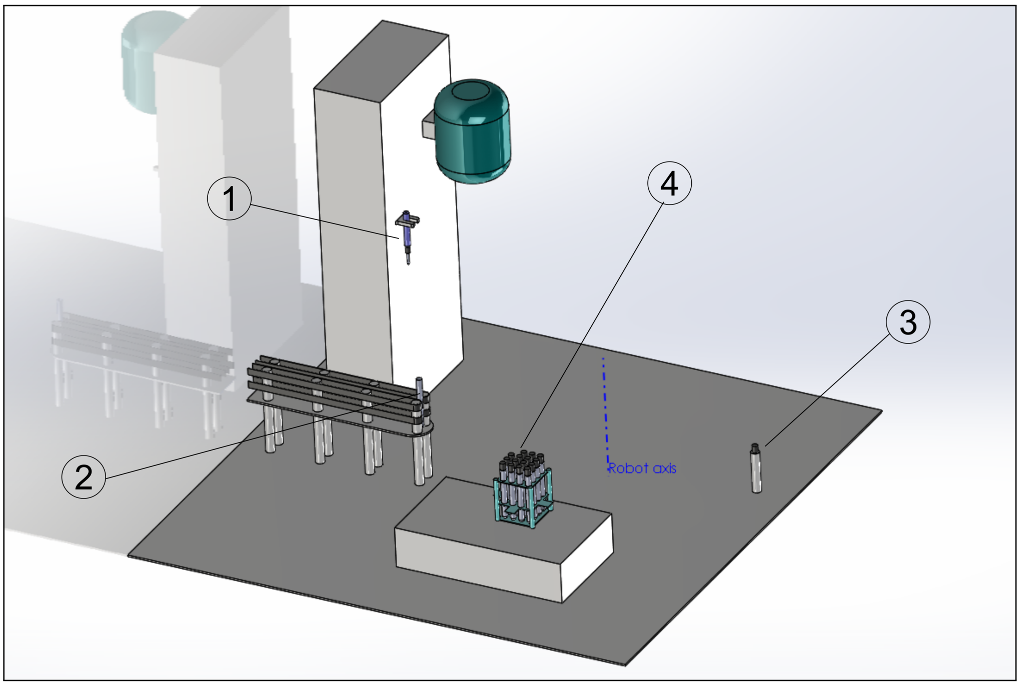

Figure 61: 3D model of assumed workplace scenario: (1) product injector lance, (2) test tube body, (3) test tube cap, (4) blister of filled test tubes.

After the completion of 3D modeling and optimization, robot and scenario shapes are exported in a neutral format (e.g. .obj, .wrl, .ply) and introduced in the simulated environment. Each entity is henceforth managed through the tools provided by the multibody library used. More specifically, every member is associated to a *body* object data structure, which encapsulates mass and inertial properties of the original entity and is able to link a visualization asset corresponding to the imported shape. Kinematic constraints (such as fixtures, revolute joints and prismatic joints) are subsequently introduced in the simulation, so to reproduce the actual scenario behavior. In particular, robot actuators are modeled as rotational motors, which link a slave (driven) member to a master (driver) member with respect to an assigned reference frame axis (aforementioned markers of Fig. 60a are used for the purposed). The rotation angle $\theta(t)$ between the two linked bodies is enforced by the means of a rheonomic constraint and is subsequently controlled through a user-defined function of time $f(t)$.

A rendered frame of the assembled simulated virtual environment is presented in Fig. 62.

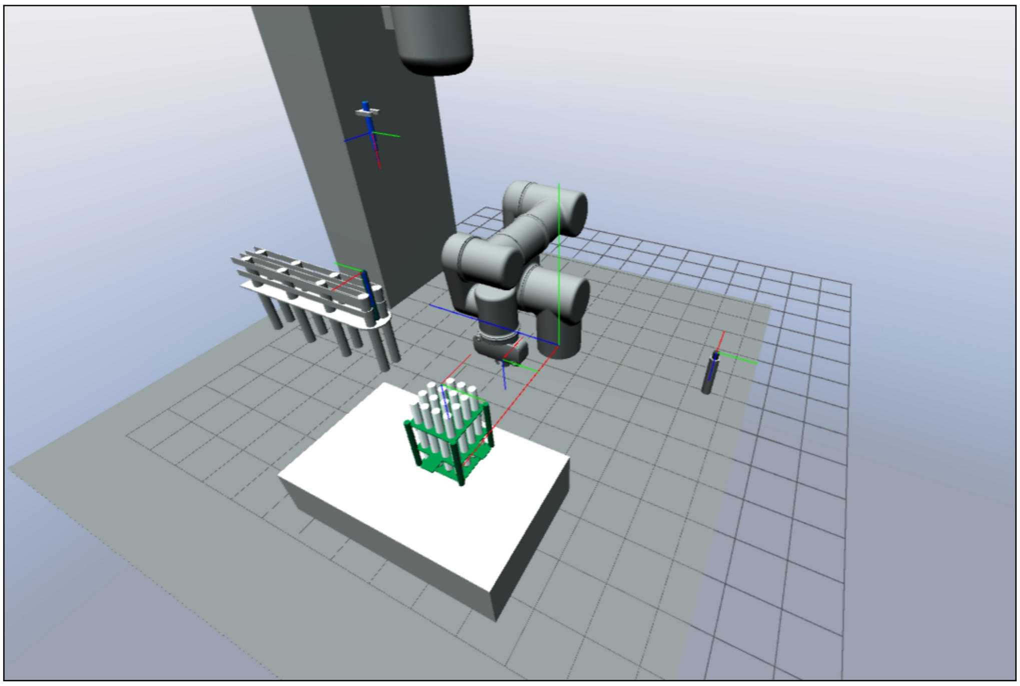

Figure 62: Render frame of simulated virtual environment, with simplified shapes. Significant scenario frames are highlighted.

4.1.3 Tasks programming

Following the design principles of Object-Oriented Programming (OOP, see for example [29]) the simulator is articulated in four main classes, whose interaction constitute the backbone of present software architecture. The Robot class is responsible for automatic import and assembling of arm geometries (from user-defined set of files); inertial properties of respective members, together with motion instructions and simulated data logging, can be imposed by dedicated methods. The Scenario class is devoted to environment shapes import and provides useful methods to access target manipulation objects. The Application class creates a 3D output rendering window that binds all simulated bodies visual assets and displays the temporal evolution of the system. Finally, the GUI class provides a useful virtual panel that allows the user to interact with the simulation at run-time. Fig. 63 illustrates the devised GUI; the underlying intent is to replicate, in a virtual form, industrial robots teach pendant features. More specifically, the virtual controller is organized in three tabs, namely: Forward Kinematics (FK), Inverse Kinematics (IK), and Sequence Control (SEQ).

Forward Kinematics tab (see Fig. 63b) allows the user to control robot motors in joint space by feeding the input to relative rheonomic constraints. In particular, the GOTO data entry area is used for direct “jump” to the inserted angular

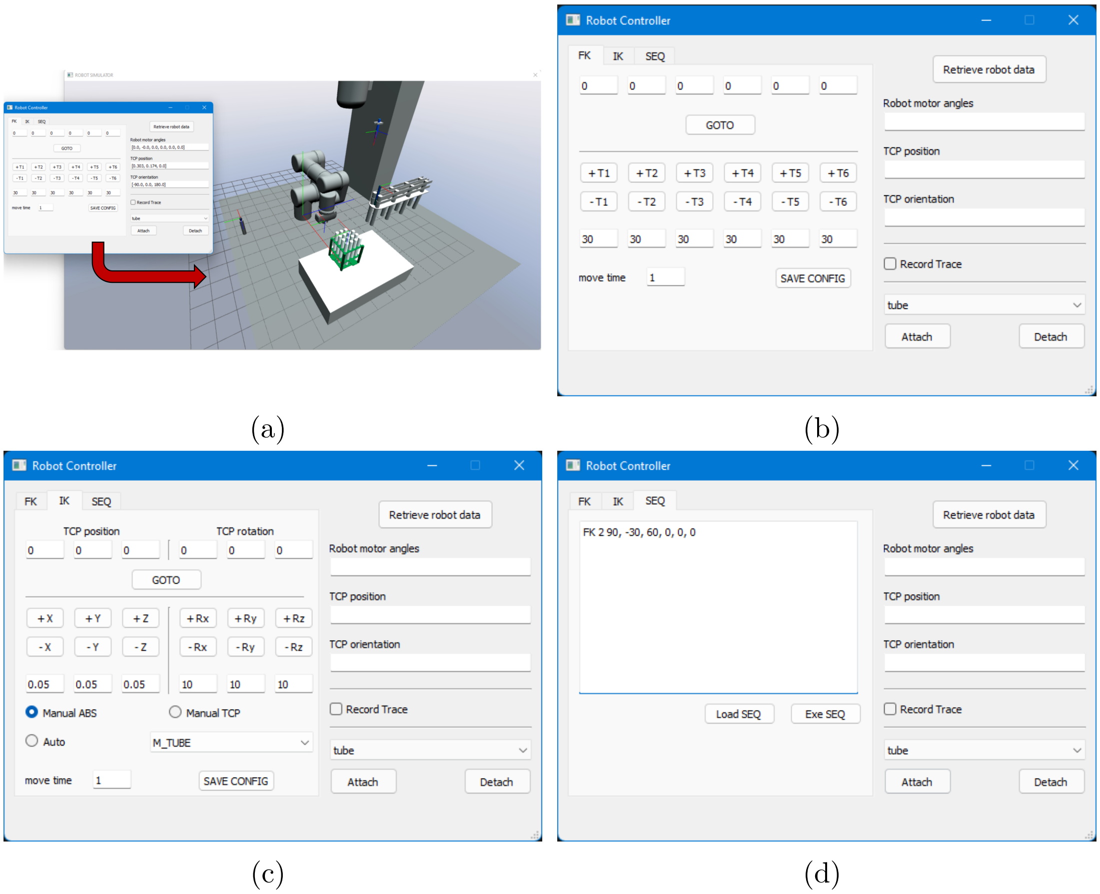

FK 2 90, -30, 60, 0, 0, 0

Figure 63: Simulator GUI panel for run-time control of robot. (a) Overall interaction with render window; (b) Forward Kinematics tab, (c) Inverse Kinematics tab, and (c) Sequence tab.

configuration[1] $\boldsymbol{\theta} \in \mathbb{R}^6$. The area below is conversely devoted to the *Jog* control of each robot axis, whose increment angle may be specifically provided. This feature is particularly useful to test robot motion in the environment, and to assess suitable waypoints that avoid collisions or reach manipulation targets. The tab is complemented by several additional utility features:

- motion time, expressed in seconds, can be imposed through a dedicated input box;
- a side panel allows to display current robot joint angles and TCP position/orientation (expressed as Euler angles of quaternion components) with respect

---

[1] For the sake of simplicity, angle inputs and outputs are expressed in degrees, but are internally managed in radians.

to absolute reference frame;

- motors rotations can be stored in an external file through a dedicated button, so to form a *configurations list* for subsequent use;
- a checkbox allows to record and save to external file robot data traces (i.e. TCP position, motor angles, motor torques as function of simulation time);
- a drop-down list itemizes the scenario manipulable targets, which can be gripped or released by robot end-effector though the relative buttons.

Inverse Kinematics tab (see Fig. 63c) allows to control the robot in Cartesian workspace coordinates; the implementation of related algorithms is described in Section 4.2. As for the FK tab, the user can impose motion via a GOTO instruction or through an incremental jog approach. Three option buttons integrate this functionality:

- Manual ABS: jog is controlled manually, with respect to world absolute reference frame;
- Manual TCP: jog is controlled manually, with respect to local TCP reference frame;
- Auto: robot TCP reaches the target selected in adjacent drop-down list.

Sequence tab (see Fig. 63d) is used to control the robot through a list of instructions, which can be written in the relative text box at run-time or loaded from an external preset file. For the purpose, a dedicated pseudo-language has been developed. The typical instruction line, which is parsed on-the-fly by the GUI class, consists of four entries

[COMMAND] [TIME] [TARGET] [*MOTION LAW*]

In particular:

- COMMAND: defines the action type among FK (arm motion in forward kinematics), IK (arm motion in inverse kinematics), ATTACH or DETACH (grip or release target), PAUSE;
- TIME: time value to perform specified action;
- TARGET: specifies target as array of joint rotations (FK), array of TCP position/orientation (IK), or manipulation object (ATTACH/DETACH);
- MOTION LAW: (optional entry) defines the motion law to employ among the ones described in Section 4.2 (if no value is entered, a constant acceleration law is assumed).

Table 4.1: Example of simulator motion sequence, expressed in designed pseudo-language.

CMD	Time [s]	Target	Motion law
FK	2	90, -30, 30, 0, 0, 0	POLY5
ATTACH	0.5	TUBE	
PAUSE	0.5		
IK	1	0.3, 0.2, 0, -90, 0, 180	POLY5
DETACH	0.5	TUBE	
PAUSE	0.5		
FK	1	0, 0, 0, 0, 0, 0	

An example of motion sequence is provided in Table 4.1. Robot is first controlled in forward kinematics, so to move in 2 s to the specified joint configuration, with a polynomial motion law; the manipulator is then required to grip a target (test tube), pause, and move in inverse kinematics to a second specified location (position/orientation). The sequence is concluded by the release of the target, a pause, and the return to home position in forward kinematics (constant acceleration motion law is assumed as default).

4.2 Motion control

4.2.1 Inverse kinematics

The inverse kinematics problem consists in the determination of the set of joint space variables $\boldsymbol{\theta} = f_{\mathrm{IK}}(\mathbf{q})$ that allow the end-effector to reach a given configuration expressed in workspace (Cartesian) coordinates. The solution to this problem is of fundamental theoretical and technical importance, as it ultimately provides the setpoint required by robot drives. With respect to forward kinematics, though, some additional difficulties are present. As described in Section 3.1, a closed-form formulation of $f_{\mathrm{FK}}(\boldsymbol{\theta})$ function can always be obtained as a combination of affine or homogeneous transformations. On the contrary, the $f_{\mathrm{IK}}(\mathbf{q})$ function is afflicted by the following main issues [99]:

- there might be no admissible solution for the given kinematic structure;
- as the equations to solve are generally non-linear, it may not be possible to find a closed-form solution;
- if solution exists, it may be non-unique or even infinite in number (e.g. for redundant robots).

Consequently, no univocal method is available to analytically solve a generic kinematic structure: the inverse kinematic problem is handled individually, through heuristic algebraic or geometric approaches; alternatively, a numerical procedure is employed.

The proposed 6-DOF articulated robot falls under a special case. In fact, it has been shown that a simple closed-form solution can be found if one of the following conditions is met [86]:

- three consecutive joint axes intersect at a common point;
- three consecutive joint axes are parallel.

In the considered kinematic architecture, the design choice of a spherical wrist fulfills the first requirement; as such, the known "Pieper approach" can be applied [16] [99]. The method consists in a kinematic decoupling of the inverse kinematics problem, which leads to two separate sub-problems: positioning of wrist center W and orientation of the end-effector. Given a demanded output pose

$$\mathbf{H_{06}} = \left(\begin{array}{ccc|c} & \mathbf{R_{06}} & & \mathbf{t_{06}} \\ \hline 0 & 0 & 0 & 1 \end{array}\right) = \left(\begin{array}{ccc|c} \mathbf{n} & \mathbf{s} & \mathbf{a} & \mathbf{t_{06}} \\ \hline 0 & 0 & 0 & 1 \end{array}\right) \tag{4.1}$$

where unit vectors $\mathbf{n}$, $\mathbf{s}$, $\mathbf{a}$ represent the three Normal-Sliding-Approach directions of end-effector in the absolute frame, the following procedure[1] may be applied (see Fig. 64):

1. retrieve wrist center position as $\mathbf{w_{06}} = \mathbf{t_{06}} - d_6\mathbf{a}$
2. solve IK for the first three robot DOFs as $(\theta_1, \theta_2, \theta_3)^{\mathrm{T}} = f_{\mathrm{IK}}(\mathbf{w_{06}})$;
3. retrieve $\mathbf{R_{03}}(\theta_1, \theta_2, \theta_3)$ from known $f_{\mathrm{FK}}(\theta_1, \theta_2, \theta_3)$;
4. determine relative orientation of wrist as $\mathbf{R_{36}} = \mathbf{R_{03}}^{-1}\mathbf{R_{06}} = \mathbf{R_{03}}^{\mathrm{T}}\mathbf{R_{06}}$;
5. extract last three angles $\theta_4, \theta_5, \theta_6$ from $\mathbf{R_{36}}$.

Specific solution to point (2) may be obtained by considering the equivalent 3-DOF articulated arm up to point W [61]. With respect to the configuration assumed in Fig. 64, assume β as the clockwise angle between axis z_0 and a_2, and angle γ as the clockwise angle between a_2 and d_4. In these hypothesis, the projection of this arm in the horizontal x_0–y_0 plane forms a segment of length $\rho = a_2 \sin(\beta) + d_4 \sin(\beta + \gamma)$. Conversely, if we observe the projection on the vertical plane containing point W, the arm is equivalent to a 2-link planar manipulator (i.e. SCARA architecture),

---

[1] As better detailed in the next sections, the simulator handles rotations through quaternion algebra rather than rotation matrices; the proposed scheme outline still holds, though.

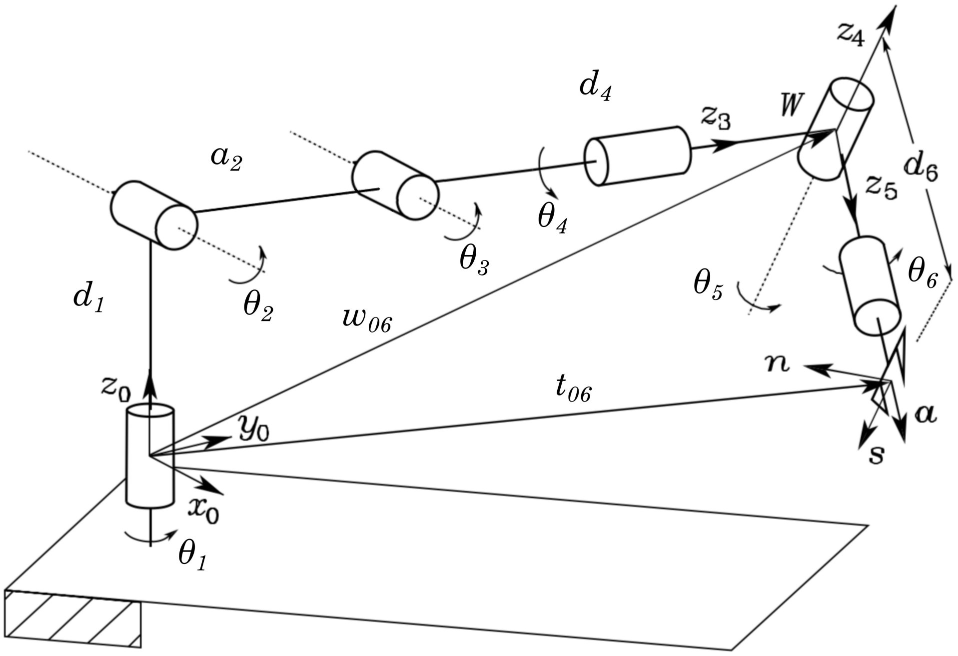

Figure 64: Decoupling approach to solve inverse kinematics problem of 6-DOF articulated arm equipped with spherical wrist. Adapted from [99].

of which the solution is well-known (see, for example, [3]). Gathering the pieces together, we may affirm that

$$\begin{aligned} \theta_1 =& \arctan_2(W_y, W_x) + k\pi & (4.2) \\ \gamma =& \pm \arccos\left(\frac{W_x^2 + W_y^2 + (W_z - d_1)^2 - a_2^2 - d_4^2}{2a_2 d_4}\right) & (4.3) \\ \beta =& \arctan_2(W_x \cos(\theta_1) + W_y \sin(\theta_1), W_z - d_1) + \\ & - \arctan_2(d_4 \sin(\gamma), a_2 + d_4 \cos(\gamma)) & (4.4) \end{aligned}$$

which leads to

$$\begin{aligned} \theta_1 =& \arctan_2(W_y, W_x) + k\pi \\ \theta_2 =& \beta + \frac{\pi}{2} \\ \theta_3 =& -\gamma + \frac{\pi}{2} \end{aligned} \tag{4.5}$$

As two distinct solutions are available for α and γ, the arm has a total of four possible output configurations, illustrated in Fig. 65. The last three angles may be computed by the knowledge of rotation matrix $\mathbf{R_{36}}$. If wrist frames are arranged

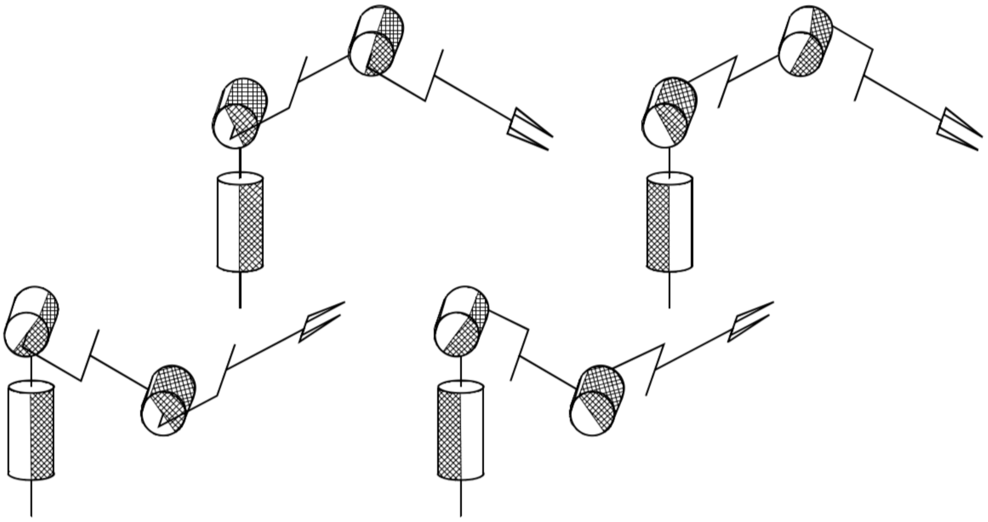

Figure 65: Four possible solution of 3-DOF articulated arm inverse kinematics [99].

as illustrated in Fig. 20, it follows that

$$\mathbf{R_{36}} = \begin{pmatrix} r_{11} & r_{12} & r_{13} \\ r_{21} & r_{22} & r_{23} \\ r_{31} & r_{32} & r_{33} \end{pmatrix} = \\ = \begin{pmatrix} s\theta_4 s\theta_6 - c\theta_4 c\theta_6 s\theta_5 & c\theta_6 s\theta_4 + c\theta_4 s\theta_5 s\theta_6 & -c\theta_4 c\theta_5 \\ -c\theta_4 s\theta_6 - c\theta_6 s\theta_4 s\theta_5 & s\theta_4 s\theta_5 s\theta_6 - c\theta_4 c\theta_6 & -c\theta_5 s\theta_4 \\ -c\theta_5 c\theta_6 & c\theta_5 s\theta_6 & s\theta_5 \end{pmatrix} \tag{4.6}$$

where s and c indicates sine and cosine functions respectively. Therefore, we obtain

$$\begin{aligned} \theta_4 &= \arctan_2(r_{23}, r_{13}) \\ \theta_5 &= \arctan_2(r_{33}, \sqrt{1 - {r_{33}}^2}) \\ \theta_6 &= \arctan_2(-r_{31}, r_{32}) \end{aligned} \tag{4.7}$$

The combination of Eq. (4.5) and Eq. (4.7) provides a complete closed-form solution to robot inverse kinematics problem. Although the procedure is easy to implement and fast to compute, a practical issue arises in its extensive use. The proposed simulator is intended to accommodate for any given 6-DOF robot architecture, so to rapidly test different custom design solutions. It may be noted that the exposed procedure not only is bidden to the adoption of a spherical wrist architecture, but also requires the user to pre-set the Denavit-Hartenberg helper frames of Fig. 60b with great caution. More specifically, if the local frames are not disposed as the ones depicted, or some mistake is unintentionally committed in the procedure, the provided inverse kinematics solution does not apply; an incorrect output configuration is hence obtained. Therefore, for reasons of practical usage convenience, simulation setup speed, and robustness of software, an additional fallback numerical IK solution is implemented.

Many operative algorithms are available in the field (see, for example, [40], [79], [70] or the extensive summary in [56]). In this work, for simplicity of implementation and speed of computation, an iterative method based on Newton-Raphson scheme is employed. In particular, given a target output pose expressed like Eq. (4.1), it is possible to formulate a residual function with respect to current joint variables $\boldsymbol{\theta}$ as:

$$F(\boldsymbol{\theta}) = \begin{pmatrix} t_x - t(\boldsymbol{\theta})_x \\ t_y - t(\boldsymbol{\theta})_y \\ t_z - t(\boldsymbol{\theta})_z \\ \mathbf{n} \cdot \mathbf{n}(\boldsymbol{\theta}) - 1 \\ \mathbf{s} \cdot \mathbf{s}(\boldsymbol{\theta}) - 1 \\ \mathbf{a} \cdot \mathbf{a}(\boldsymbol{\theta}) - 1 \end{pmatrix} \tag{4.8}$$

Eq. (4.8) can be substituted in Eq. (3.8) to obtain an approximate numeric expression of the Jacobian matrix

$$\mathbf{J}(\boldsymbol{\theta})_{ij} \approx \left(\frac{\Delta F(\boldsymbol{\theta})}{\Delta \boldsymbol{\theta}} \right)_{ij} = \frac{F(\boldsymbol{\theta} + h\mathbf{e}_j)_i - F(\boldsymbol{\theta})_i}{h} \tag{4.9}$$

which is subsequently iterated in the form[1]

$$\boldsymbol{\theta}_{k+1} = \boldsymbol{\theta}_k - \mathbf{J}(\boldsymbol{\theta}_{\mathrm{k}})^{-1} F(\boldsymbol{\theta}_k) \tag{4.10}$$

until convergence or maximum number of allowed iterations is reached.

4.2.2 Trajectory planning

The analytical or numerical solution to the inverse kinematics problem allows the robot not only to reach demanded target poses, but also to follow prescribed trajectories. Two main courses of action are available to the simulator user:

- model the trajectories in some external environment (e.g. CAD, IDE), then import into simulation;

---

[1] To improve computation speed and stability, a linear solver is actually employed in place of matrix inversion.

- use the GUI to control the robot at run-time, directly in the simulated environment; define and store desired waypoints, then use the simulator trajectory planning tools.

In both cases, it may be observed that motion control ultimately requires the interpolation of a limited set of given 3D key-frames. In particular, the motion of a 6-DOF manipulator can be expressed through the combination of two continuous curves, one in $\mathbb{R}^3$ for positions and the other in $\mathsf{SO}(3)$ for rotations. The present section is intended to briefly summarize the main concepts involved.

Position interpolation

The first and most basic example of $\mathbb{R}^3$ trajectory consists in the linear interpolation of position vectors. Given a set of prescribed points in absolute space, it is possible to create a polygonal line passing through all by expressing in-between segments in parametric form. For example, given two points P_1 and P_2, and a parameter s, it holds that

$$h = ||\mathbf{p}_{02} - \mathbf{p}_{01}|| \tag{4.11}$$

$$\mathbf{u}_{12} = \frac{\mathbf{p}_{02} - \mathbf{p}_{01}}{h} \tag{4.12}$$

$$\mathbf{p}(s) = \mathbf{p}_{01} + s\mathbf{u}_{12} \qquad s \in [0, h] \tag{4.13}$$

The same may be rearranged in function of time as

$$\mathbf{p}(t) = \mathbf{p}_{01} + s(t)\mathbf{u}_{12} \tag{4.14}$$

From this elementary example, it is apparent that the actual followed trajectory is the result of two elements: a geometric path and a time motion law $s(t)$.

Given a target displacement h and an overall motion time T, the performance required to robot drives is strictly dependent on the adopted motion law. For this reason, a considerable number of options have been proposed in time (see, for example, [92] [68]). The general idea is to formulate a function of time which is specifically designed to minimize some particular quantity related to the actuators (e.g. maximum speed, torque, power or vibrations). The simulator has been provided with four particular motion laws:

- constant acceleration;
- cubic;
- polynomial 3-4-5;
- cycloidal.

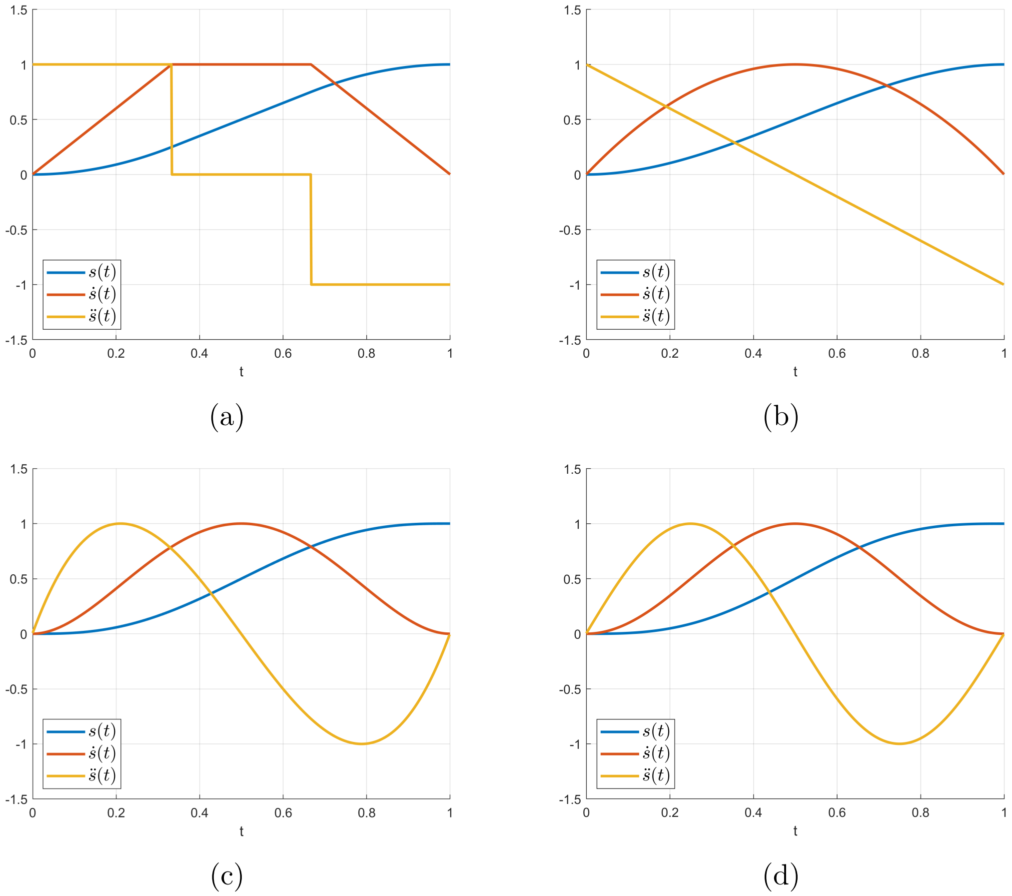

(a) (b)

(c) (d)

Figure 66: Profiles of motion laws implemented in simulator: (a) constant acceleration, here with $t_v = 1/3$ and $t_w = 2/3$; (b) cubic; (c) polynomial 3-4-5; (d) cycloidal. Velocity and acceleration plots are rescaled to unitary amplitude.

In the following, a brief description on the basic formulations is reported for the case of a 1-DOF system. The extension to a multi-DOF kinematic linkage is easily obtainable by suitable remapping of joint interpolation time scales.

The *constant acceleration* motion law (see Fig. 66a) is probably one of the most commonly adopted solutions as it allows to limit the maximum acceleration values in a very simple formulation. If the portion of time t_v devoted to acceleration is assumed as half of the total motion time T, a symmetrical (triangular) velocity profile is obtained; this condition is useful to minimize accelerations, but results consistent peak speed values, which may negatively effect wear and transmission efficiency. Other combinations of t_v and t_w lead to a trapezoidal velocity profile, whose decrease in peak value is exchanged with higher accelerations. In the most general form, the acceleration values are expressed by:

$$\begin{aligned} A &= \frac{2h}{t_v(T - t_v + t_w)} \\ B &= \frac{2h}{(T - t_w)(T - t_v + t_w)} \end{aligned} \tag{4.15}$$

Consequently, the output law results

$$s(t) = \begin{cases} \frac{1}{2}At^2, & t \in [0, tv) \\ At_v\left(t - \frac{t_v}{2}\right) & t \in [tv, tw) \\ At_v\left(t - \frac{t_v}{2}\right) - \frac{1}{2}B\left(t - t_w\right)^2 & t \in [t_w, T) \end{cases} \tag{4.16}$$

In order to mitigate the discontinuity of acceleration presented by the previous option, a polynomial law may be adopted. This kind of law grants a dual advantage: from one hand, the function of time may be formulated in a single expression (contrarily to the piece-wise Eq. (4.16)); from the other hand, the abundance of coefficients allows to tailor the law to the specific needs of the application. A generic polynomial function is expressed as

$$\begin{aligned} s(t) &= c_0 + c_1 t + c_2 t^2 + \cdots + c_n t^2 \\ \dot{s}(t) &= c_1 + 2c_2 t + \cdots + nc_n t^{n-1} \\ \ddot{s}(t) &= 2c_2 + 6c_3 t + \cdots + n(n-1)c_n t^{n-2} \end{aligned} \tag{4.17}$$

If a 3th-degree polynomial is used with the imposition of the following boundary conditions

$$\begin{aligned} s(0) &= 0 & s(T) &= h \\ \dot{s}(0) &= 0 & \dot{s}(T) &= 0 \end{aligned} \tag{4.18}$$

$$\tag{4.19}$$

the following *cubic* motion law is obtained (see Fig. 66b):

$$s(t) = h\left[3\left(\frac{t}{T}\right)^2 - 2\left(\frac{t}{T}\right)^3\right] \tag{4.20}$$

If, on the other hand, a 5th-degree polynomial is used under the following boundary conditions

$$\begin{aligned} s(0) &= 0 & s(T) &= h \\ \dot{s}(0) &= 0 & \dot{s}(T) &= 0 \\ \ddot{s}(0) &= 0 & \ddot{s}(T) &= 0 \end{aligned} \tag{4.21}$$

a *polynomial 3-4-5* motion law is obtained (see Fig. 66c):

$$s(t) = h\left[10\left(\frac{t}{T}\right)^3 - 15\left(\frac{t}{T}\right)^4 + 6\left(\frac{t}{T}\right)^5\right] \tag{4.22}$$

Another useful way to minimize output joint vibrations (i.e. drastic changes in inertial forces caused by acceleration discontinuities), consists in the adoption of harmonic motion laws. Among this broad family of functions, the well-known *cycloidal* law (see Fig. 66d) may be formulated as

$$\ddot{s}(t) = 2\pi\left(\frac{h}{T^2}\right)\sin\left(\frac{2\pi t}{T}\right) \tag{4.23}$$

which, by integration, leads to

$$s(t) = h\left[\frac{t}{T} - \frac{1}{2\pi}\sin\left(\frac{2\pi t}{T}\right)\right] \tag{4.24}$$

The geometric tools provided by the underlying multibody engine [107] have been leveraged to implement additional position interpolation schemes. As such, the simulator is capable to provide a total of five trajectory curves:

- polygonal;
- lines & circular arc fillets;
- B-Splines;
- Bézier curves;
- NURBS.

Fig. 67 illustrates some related examples.

Rotation interpolation

With respect to the generation of $\mathbb{R}^3$ position trajectories – problem that has been extensively addressed in literature – the interpolation of rotations in $\mathsf{SO}(3)$ is a relatively younger subject, which still poses some difficulties [60].

The orientation of solid objects may be expressed in several ways: rotation matrices, axis-angle formalism, Rodrigues vectors and quaternions are only part of a numerous list of possibilities [94] [48]. Each of these representations is characterized by both advantages and drawbacks, hence the most suitable choice depends on the specific application. For example, the well-known rotation matrix parameterization based on Euler angles, results in a straightforward and intuitive approach, which

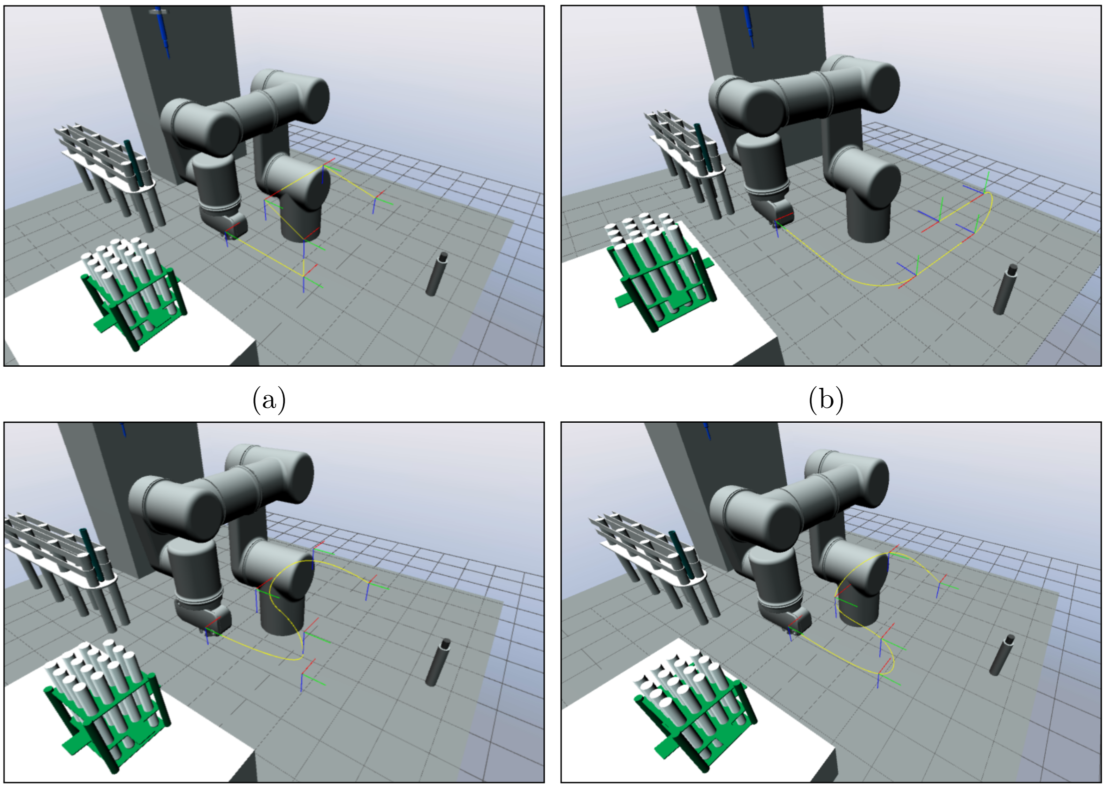

(a) (b) (c) (d)

Figure 67: Example of implemented position interpolation curves (highlighted in yellow): (a) polygonal, (b) lines & circular arc fillets, (c) 2nd-order B-Spline curve, and (d) Bézier curve.

allows to combine successive transformations through simple linear algebra operations. However, any adopted set of angles manifests at least one configuration leading to singularity; thus, such parameterization may be unfit for applications that require extreme robustness (e.g. robotics, avionics, but also computer graphics and simulators). In these fields, a typical better strategy consists in the representation of rotations by means of *unit quaternions* [42]. These mathematical objects possess four components and are usually expressed as hyper-complex numbers in the form $\mathbf{q} = q_0 + q_1\mathbf{i} + q_2\mathbf{j} + q_3\mathbf{k}$. Although being less intuitive and still affected by some drawbacks (e.g. the same orientation may be expressed by two different and opposite quaternions), this formulation provides consistent advantages in the field of rotation interpolation:

- The (slightly) “redundant” formulation of quaternions (4 parameters to map 3 angles) prevents the insurgence of singularity problems.

- A valid rotation is expressed by a quaternion if the latter has unitary norm (hence lies on the surface of a unitary 3-sphere, or *hypersphere*). In contrast, a rotation matrix is required to be orthogonal and with determinant equal to +1.

- From a computational point of view, the normalization of a 4x1 array is much faster than the one of a 3x3 matrix (with Gram-Schmidt or similar algorithms).
- Quaternions only deal with four numbers instead of nine, saving valuable computer memory.

On the basis of the exposed strengths, quaternions are commonly preferred for the generation of 3D rotation curves. As such, they are extensively employed in the core of the Chrono::Engine multibody library [105], and have been consequently leveraged to offer some rotation interpolation scheme in the proposed simulator. In the following, a brief overview of the simulator available methods is presented; for a deeper description of the underlying mathematical aspects, refer to Appendix A.

The first consideration to face in the context of rotation curves is that a naïve interpolation of quaternion components generally leads to incorrect results. For example, given two quaternions $\mathbf{q}_1$ and $\mathbf{q}_2$, the use of a linear formula like $\mathbf{q}(t) = (1-t)\mathbf{q}_1 + t\mathbf{q}_2$ results in non-valid interpolated rotations, since there is no guarantee that unitary norm is preserved in-between; from a geometrical perspective, the linear approach cuts through the hypersphere S^3 instead of lying onto its surface. Consequently, custom interpolation schemes preserving the unit length of $\mathbf{q}(t)$ must be employed; four algorithms have been implemented in the simulator:

- SLERP;
- SQUAD;
- quaternion B-Spline;
- polynomial-filleted SLERP.

The most basic approach implemented is based on the SLERP (Spherical Linear intERPolation) method, proposed by Shoemake in [96]. From a geometrical point of view, the algorithm produces a segment of geodesic on the surface of S^3, which constitutes the shortest possible angular path between two poses; the trajectory is traveled at constant velocity. Given two quaternions $\mathbf{q}_1$ and $\mathbf{q}_2$, and a parameter $t \in [0, 1]$, the algorithm can be expressed in many equivalent forms:

$$\begin{aligned}\mathbf{q}(t) &= f_{\text{SLERP}}(\mathbf{q}_1, \mathbf{q}_2, t) = \\ &= (\mathbf{q}_2{\mathbf{q}_1}^*)^t \mathbf{q}_1 = \mathbf{q}_1({\mathbf{q}_2}^*\mathbf{q}_2)^t = \\ &= \mathbf{q}_2({\mathbf{q}_2}^*\mathbf{q}_1)^{1-t} = (\mathbf{q}_1{\mathbf{q}_2}^*)^{1-t}\mathbf{q}_2\end{aligned} \tag{4.25}$$

where $\mathbf{q}^*$ indicates complex conjugation of $\mathbf{q}$. By the means of quaternion exponential properties, Eq. (4.25) can be reformulated in a geometrical form as

$$\mathbf{q}(t) = \frac{\sin[(1-t)\varphi]}{\sin\varphi}\mathbf{q}_1 + \frac{\sin(t\varphi)}{\sin\varphi}\mathbf{q}_2 \tag{4.26}$$

where $\cos\varphi = \mathbf{q}_1\mathbf{q}_2$. Although the method performs well in the case of two orientations interpolation, the mere replication on multiple frames produces the equivalent of a $\mathbb{R}^3$ polygonal curve, which is characterized by undesirable abrupt velocity spikes at junctions. Some alternative approached have been implemented to overcome the problem.

SQUAD (Spherical QUADrangle interpolation) [97] represents one of the most popular algorithms of computer animation field. The method, obtained by the nested application of SLERP among four control points, constitutes the spherical cubic equivalent of a Bézier curve. Given two extreme quaternions $\mathbf{q}_1$ and $\mathbf{q}_2$, two intermediate quaternions $\mathbf{p}_1$ and $\mathbf{p}_2$, and a parameter $t \in [0,1]$, the interpolated quaternion produced by SQUAD is formulated as:

$$\begin{aligned}\mathbf{q}(t) &= f_{\mathrm{SQUAD}}(\mathbf{q}_1, \mathbf{p}_1, \mathbf{p}_2, \mathbf{q}_2, t) = \\ &= f_{\mathrm{SLERP}}(f_{\mathrm{SLERP}}(\mathbf{q}_1, \mathbf{q}_2, t), f_{\mathrm{SLERP}}(\mathbf{p}_1, \mathbf{p}_2, t), 2t(1-t))\end{aligned} \tag{4.27}$$

To enforce the exact passage among a given list of quaternions $\mathbf{q}_i$, the intermediate $\mathbf{p}_i$ in the span $\mathbf{q}_i, \mathbf{p}_i, \mathbf{p}_{i+1}, \mathbf{q}_{i+1}$ are computed as follows [19]:

$$\mathbf{p}_i = \mathbf{q}_i \exp\left[-\frac{\log(\mathbf{q}_i{}^*\mathbf{q}_{i+1}) + \log(\mathbf{q}_i{}^*\mathbf{q}_{i-1})}{4}\right] \tag{4.28}$$

The third method, available to the simulator from Chrono::Engine API, consists in the use of quaternion B-Splines, in the form proposed in [58]. Given an arbitrary set of n quaternion control points $\mathbf{q}_i$ and a knot vector with t_i knots, the B-Spline basis function $B_{i,k}(t)$ may be computed as $(k-1)$-order piece-wise polynomials with non-zero support in $[t_i, t_{i+k}]$ [60]. If the cumulative form of the basis is defined as

$$\tilde{B}_{i,k}(t) = \sum_{j=1}^{n} B_{j,k}(t) \tag{4.29}$$

the interpolated quaternion results

$$\mathbf{q}(t) = \mathbf{q}_0^{\tilde{B}_{0,k}(t)} \prod_{i=1}^{n} \exp[\log(\mathbf{q}_{i-1}^*\mathbf{q}_i)\tilde{B}_{i,k}(t)] \tag{4.30}$$

The last implemented algorithm is based on a method co-proposed by the writer in [60]. The procedure underlying purpose is to create a quaternion curve that performs a smooth and exact interpolation of an arbitrary set of rotations, without

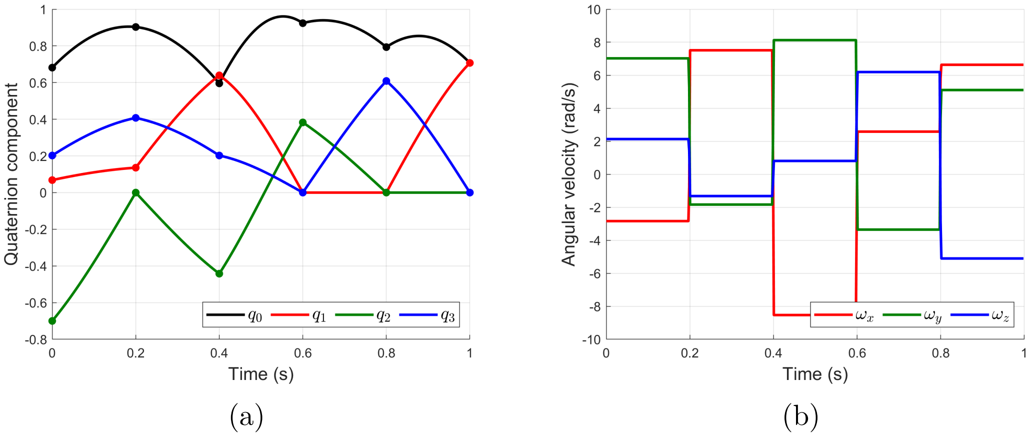

(a) (b)

Figure 68: SLERP: (a) quaternion components and (b) angular velocity profiles [60].

the need for iterative optimization procedures or computational expensive formulations (which characterize many literature methods, e.g. [10], [12], [78]). In other words, the method is mainly addressed to those applications that highly prioritize simple implementation and little computational overhead (like, for example, the present case of real-time multibody simulation). The main objective is to preserve the attractive features of SLERP (i.e. easy algorithm with constant-velocity output trajectory) while overcoming its lack of continuity at curve joints. The target is achieved through a repeated smooth combination of two fundamental ingredients:

- SLERP interpolation segments;
- fillet tracts generated by the means of simple polynomial motion laws.

The duration of these fillets and the angular velocity profiles can be easily and arbitrarily modified by the user to obtain the desired trajectory. The detailed explanation of the algorithm mathematical formulation is presented in Appendix A.

In order to assess the performance of the methods implemented in the simulator, a numerical comparison is proposed in the following. In particular, six rotational key frames are assigned with an interpolation parameter $t \in [0, 1]$; with reference to Figs. 68 to 71, the four components of interpolated quaternions, together with the corresponding angular velocity components, are discussed [60]:

- SLERP exactly passes through all the imposed frames, with no overshoots and minimal angular path. Velocity is piece-wise constant, but presents abrupt discontinuities at curve joints (step variations); consequently, angular acceleration locally presents infinite values. See Fig. 68.
- 2nd-order quaternion B-Spline is significantly smooth, but does not exactly pass through intermediate imposed frames. Velocity is continuous and mainly

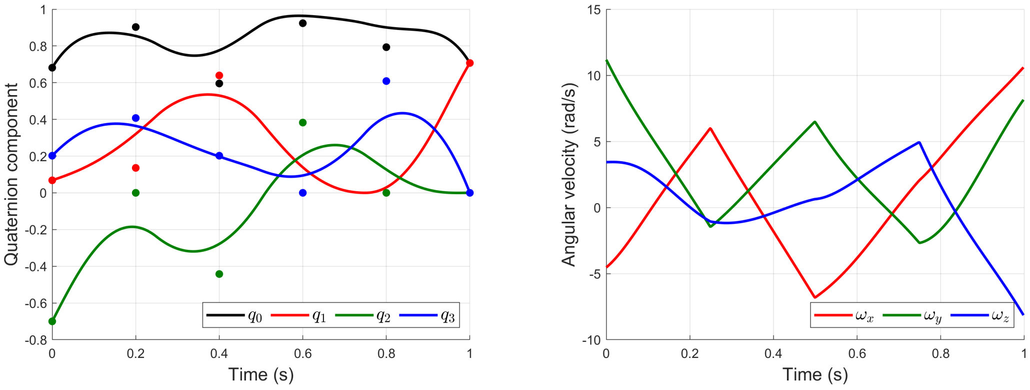

(a) (b)

Figure 69: SPLINE: (a) quaternion components and (b) angular velocity profiles [60].

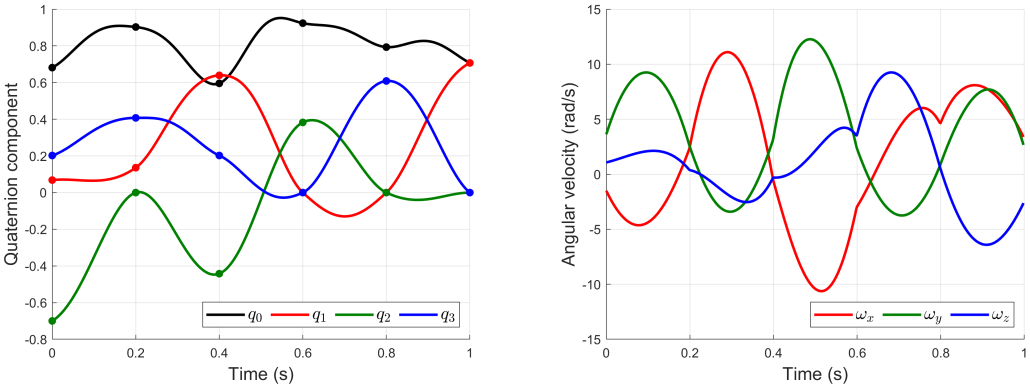

(a) (b)

Figure 70: SQUAD: (a) quaternion components and (b) angular velocity profiles [60].

constituted by linear tracts, but presents drastically rapid changes at curve joints; consequently, angular acceleration is locally very high. See Fig. 69.

- SQUAD exactly interpolates all given frames at the cost of a slight increase of the angular path. Velocity is continuous and smooth, but is characterized by a continuously variable and bouncy trend. See Fig. 70.
- The filleted SLERP method produces a smooth trajectory that exactly interpolates all given poses; modest deviation from minimal SLERP path and slight overshoots at curve joints are present. As for SLERP, constant velocity is preserved during interpolation tracts, here with the advantageous feature

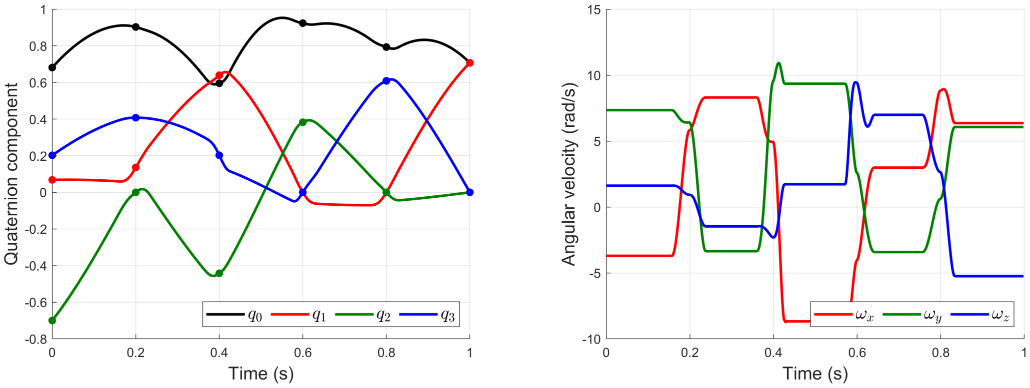

(a) (b)

Figure 71: Polynomial-filleted SLERP: (a) quaternion components and (b) angular velocity profiles [60].

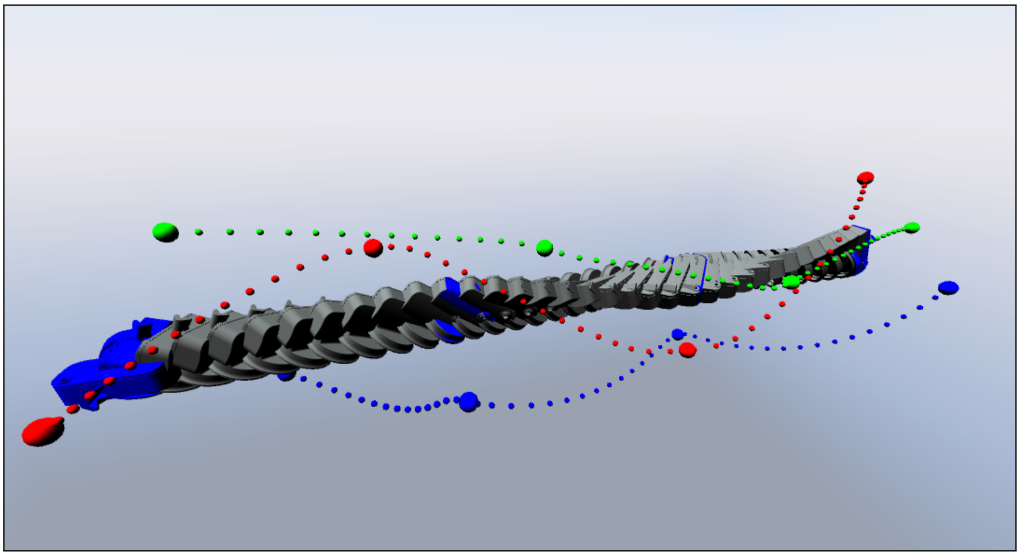

Figure 72: Interpolation of four key-frames performed as combination of linear motion and polynomial-filleted SLERP algorithm; robot end-effector is used as example of body. Assigned configurations are highlighted in blue, while moving body trail is depicted in gray; an additional RGB trail shows the update of body axes and key-frame passage.

of smooth curve connections. Transitions can be arbitrarily adapted to fulfill specific local constraints. See Fig. 71.

Finally, in order to better visualize the concepts exposed, two 3D simulations of

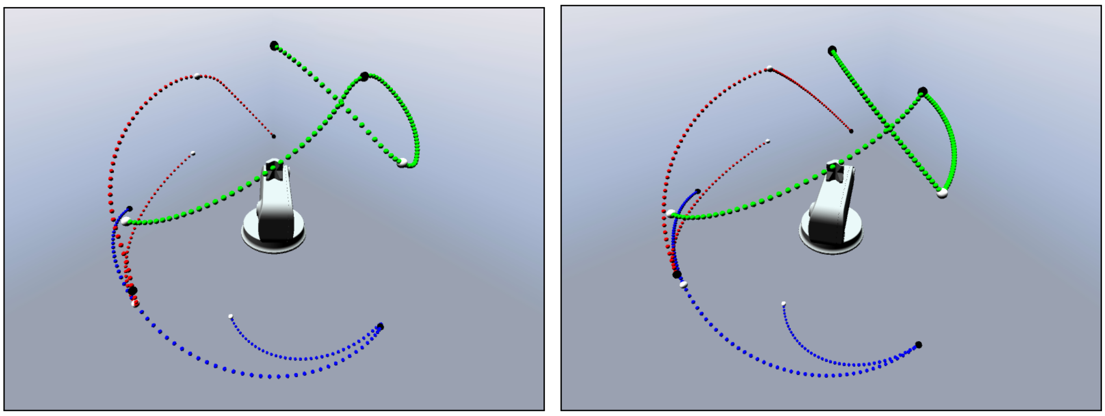

(a) (b)

Figure 73: Simulated comparison between (a) polynomial-filleted SLERP method and (b) pure SLERP interpolation of the same poses of Fig. 72, without spatial motion. The rotating body axes are represented by RGB trails and the passage through the assigned key frames is highlighted as white and black dots.

quaternion interpolation are illustrated. In particular, Fig. 72 depicts the interpolation of four key-frames, performed as combination of linear motion and polynomial-filleted SLERP algorithm. Fig. 73 offers a comparison between the smooth curve obtained by polynomial-filleted SLERP method and the spiky angular path produced by pure SLERP.

4.3 Scenario testing

In conclusion, a comprehensive test of simulator features is proposed; scenario operations described in Section 4.1.2 are used as virtual benchmark for robot motion.

At first, robot inertial properties are set in accordance to the specification listed in Section 3.7. Target test tube is modeled so to reproduce a typical commercial product:

- dimensions: 16x150mm
- material: pyrex (borosilicate glass)
- mass: 50 g (17 g of glass, about 30 g of liquid)

In accordance with the sequence described, four fundamental frames are retrieved from virtual environment:

- product lance;
- test tube;

- test tube cap;
- blister empty slot.

In addition to these, a number of auxiliary poses are defined and stored through run-time interaction with the provided GUI; the helper frames are specifically selected so to avoid collisions during approach to targets. A polygonal trajectory is subsequently generated to connect the complete set of provided control frames; run-time solution to the inverse kinematic problem allows to feed suitable angles $\theta(t)$ to the motors, so that robot TCP follows the curve. In order to allow the end-effector to grip and release a demanded object, a temporary fixture constraint is instantiated on-the-fly among the two bodies; the manipulated object is consequently inserted or deleted from robot hierarchical structure of entities; hence, the inertial effects of the manipulated body can be easily transmitted to the whole kinematic chain.

The simulation is performed with the following setup:

- machine processor: Intel(C) Core i7-10510U, clocked at 1.80 GHz;
- machine RAM: 16 GB;
- timestep: 5 ms;
- time integrator: Linearized Trapezoidal scheme [104];
- linear solver: MINRES [83].

In the described conditions, the simulation proceeds 11% faster than real-time, i.e. with a real-time factor equal to 0.89. An illustration of the robot passing through the exposed main locations is provided in Fig. 74. Finally, Fig. 75 and Fig. 76 report two different motor traces logged at runtime during the simulation (respectively with constant acceleration and polynomial 3-4-5 motion laws); since the RMS value of torque profiles consistently fall under the rated performance of designed actuators (see Section 3.7), robot operation in the scenario is considered successful.

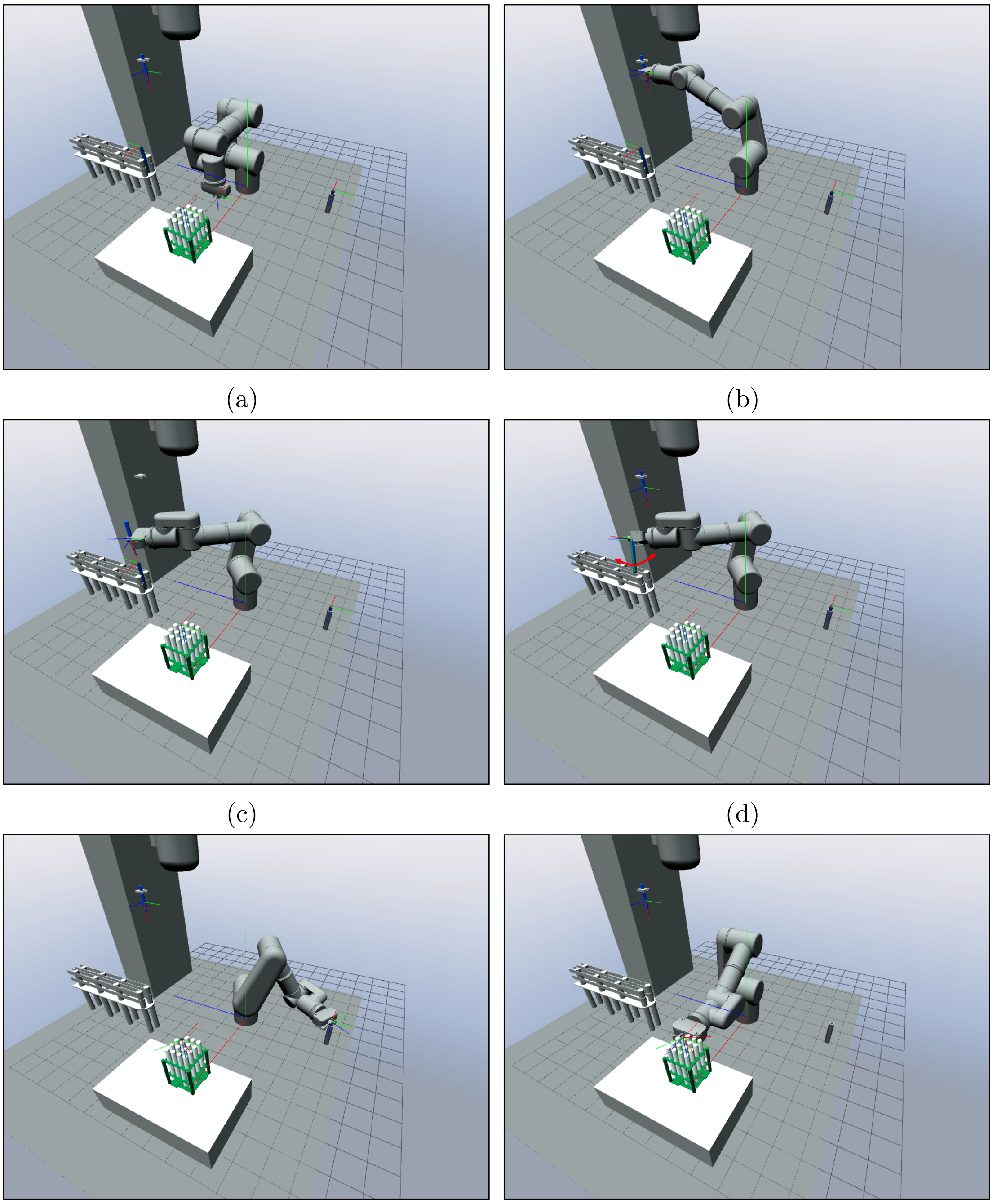

(a) (b)

(c) (d)

(e) (f)

Figure 74: Complete simulation of scenario. Main phases are depicted: (a) home position, (b) product lance retrieval, (c) tube filling, (d) tube stirring (motion highlighted in red), (e) cap retrieval after tube insertion in blister, (f) final capping of test tube.

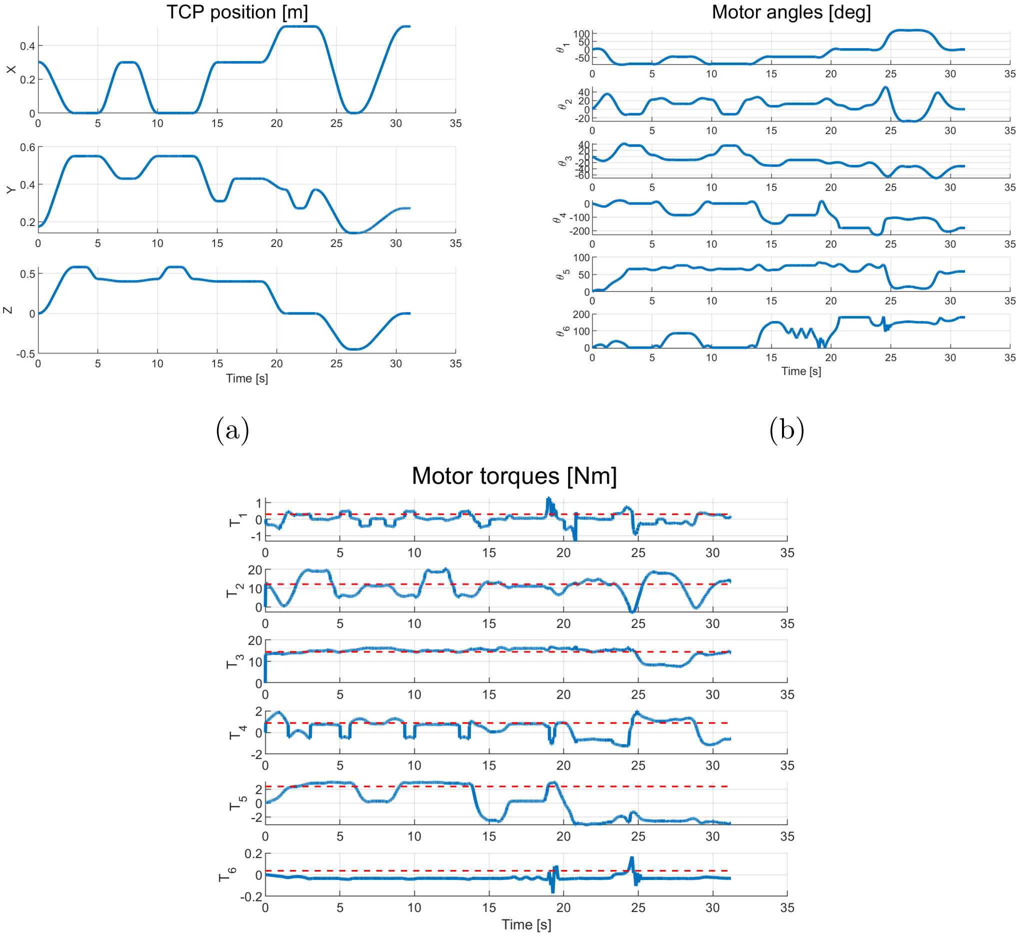

(a) (b)

(c)

Figure 75: Scenario simulation logged data in function of time, with constant acceleration motion law. (a) TCP position in workspace absolute coordinates, (b) joint motor angles, (c) joint motor torques (RMS value highlighted in red).

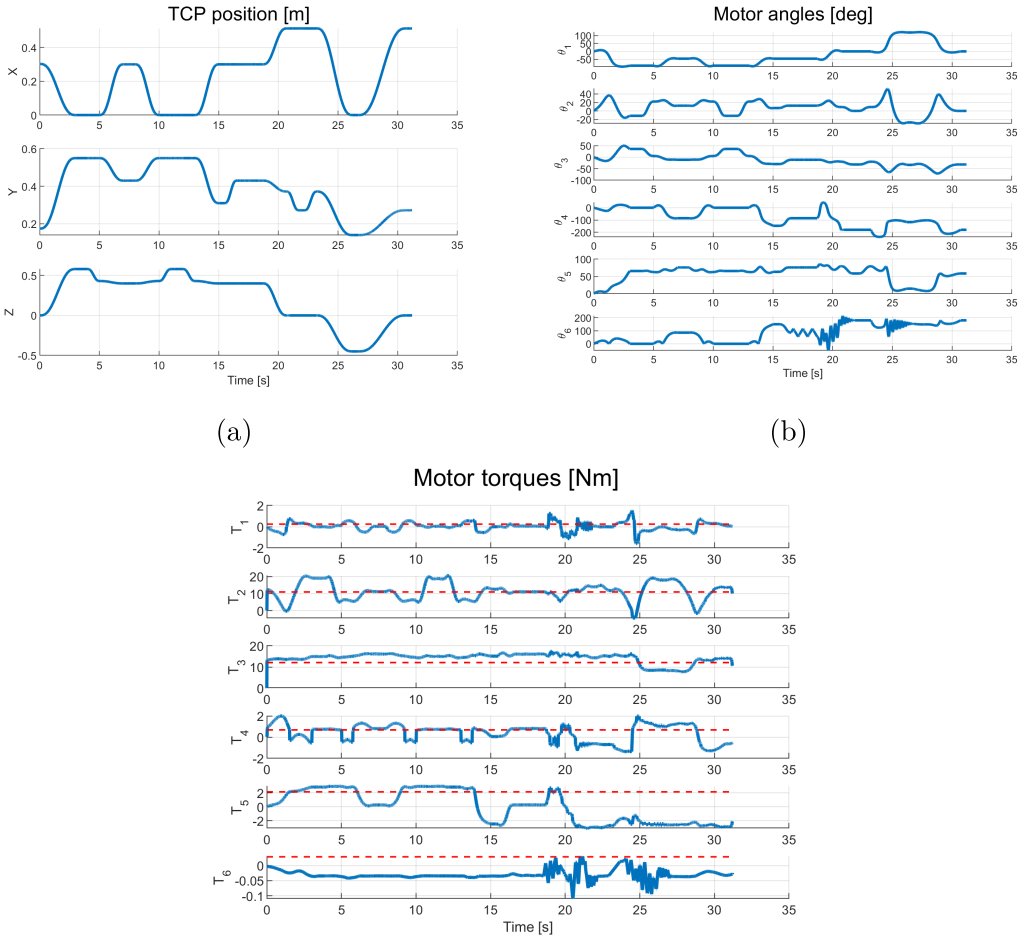

(a) (b)

(c)

Figure 76: Scenario simulation logged data in function of time, with polynomial 3-4-5 motion law. (a) TCP position in workspace absolute coordinates, (b) joint motor angles, (c) joint motor torques (RMS value highlighted in red).

Chapter 5

Drive Prototype Photobook

This final chapter briefly documents, in form of annotated photographs, the realization of a preliminary proof-of-concept of the devised robot drive. The prototype is intended to test the overall actuator mechanical design solutions, assess the feasibility of assembling sequence, and verify communication interface among electronic devices. The item has been manufactured, internally, at University of Parma facilities; for the sake of prototype production speed and cost-effectiveness, no dimensional tolerance, geometric tolerance, or surface finishing was enforced during manufacturing process. Moreover, with respect to the actual drive design presented in Section 3.2.5, two main modifications were introduced:

- *Toteltech XSF-32-160-C-I* gearing was used in place of similar *Harmonic Drive SE CSD-32-160*;
- aluminum alloy 6000 (*Anticorodal*) was used in place of alloy 7075 (*Ergal*).

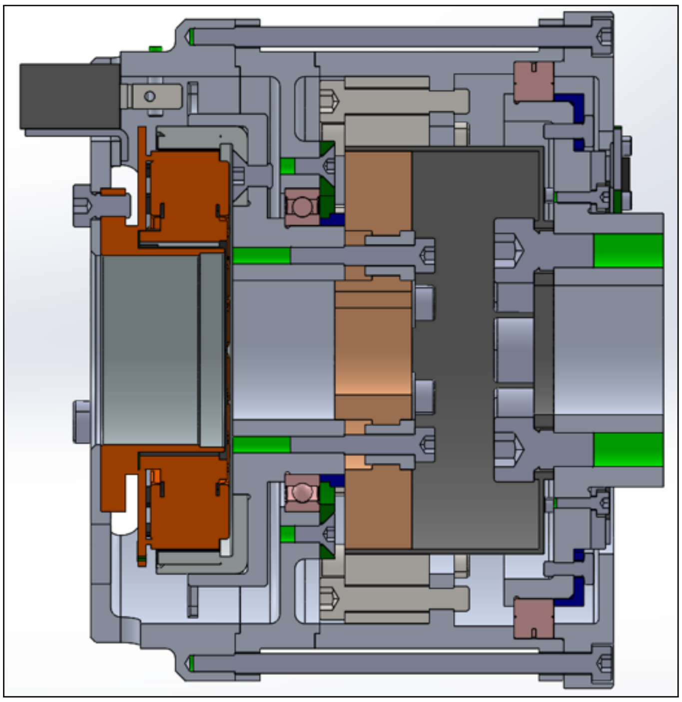

Figure 77: Sectioned view of drive prototype concept.

Figure 78: View of some manufactured parts, with respective drawings.

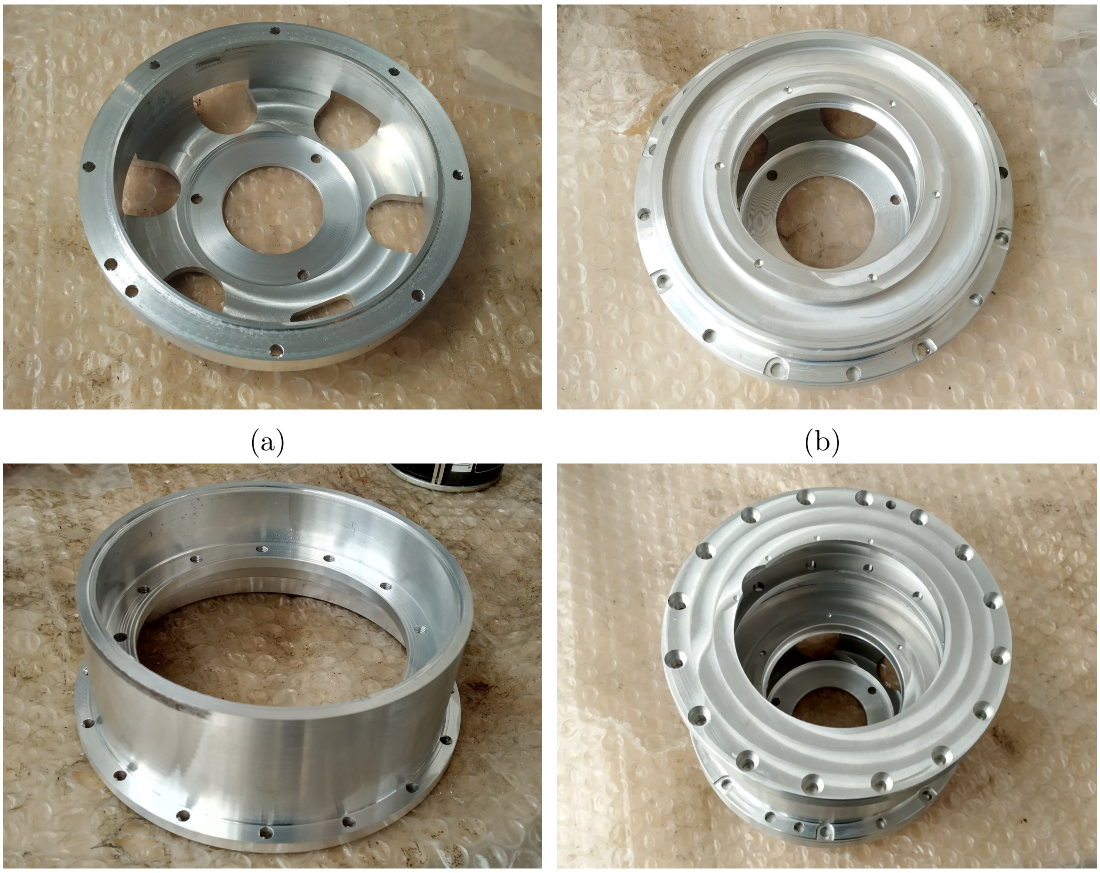

(a) (b)

(c) (d)

Figure 79: Four drive casing sub-parts, dismounted.

(a) (b)

Figure 80: Complete drive casing, unscrewed: (a) side and (b) rear view.

(a) (b)

Figure 81: Complete drive casing, screwed: (a) front and (b) rear view. As described in Section 3.2.5, frontal screws are used to assemble the casing, while rear screws allow to install the drive in robot body casing.

Figure 82: Detail of drive casing installation procedure. A common straight Allen wrench is used to quickly fasten/unfasten the drive to robot casing, without need for removable covers (see also Fig. 30a).

Figure 83: BLDC motor stator windings and magnetic rotor, characterized by hollow and significantly flat design.

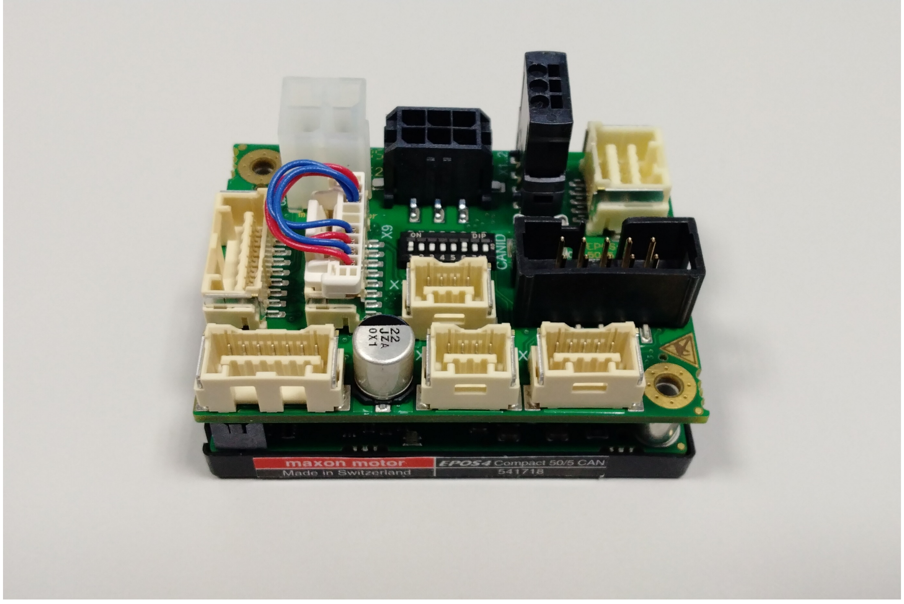

Figure 84: Motor controller, with suitable connectors installed on interface PCB.

Figure 85: Harmonic drive gearing component set parts: wave generator, flex spline, circular spline.

Figure 86: Lubrication of gearing wave generator.

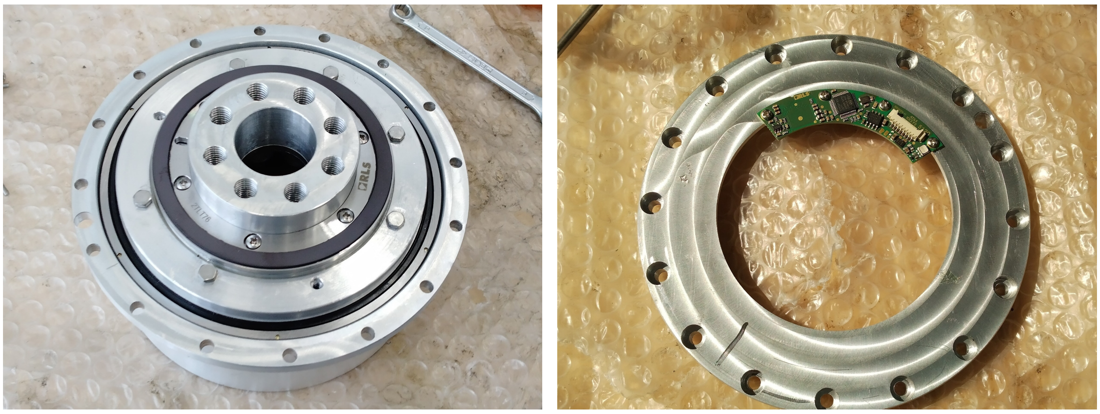
(a) (b)

Figure 87: (a) Absolute encoder magnetic ring, installed on motor output shaft. (b) Absolute encoder PCB read sensor, installed on drive sub-casing 4.

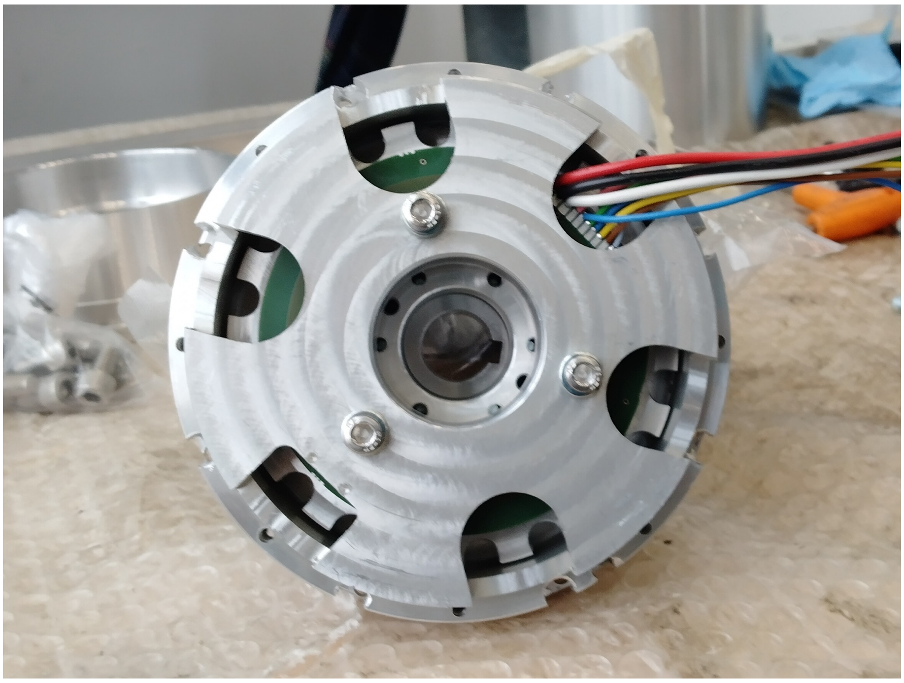

Figure 88: Detail of motor installation in drive casing. Circumferential slots allow to route motor cables outside the illustrated drive; central hollow hole is devoted to wiring of (potential) subsequent actuators.

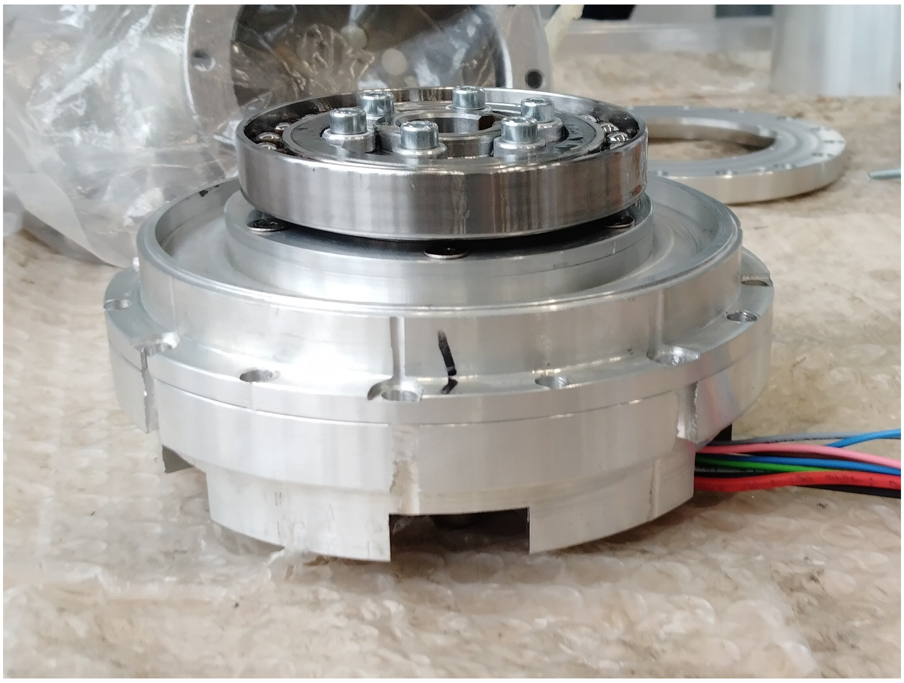

Figure 89: Detail of wave generator installation on motor output shaft.

Figure 90: Complete drive, front view.

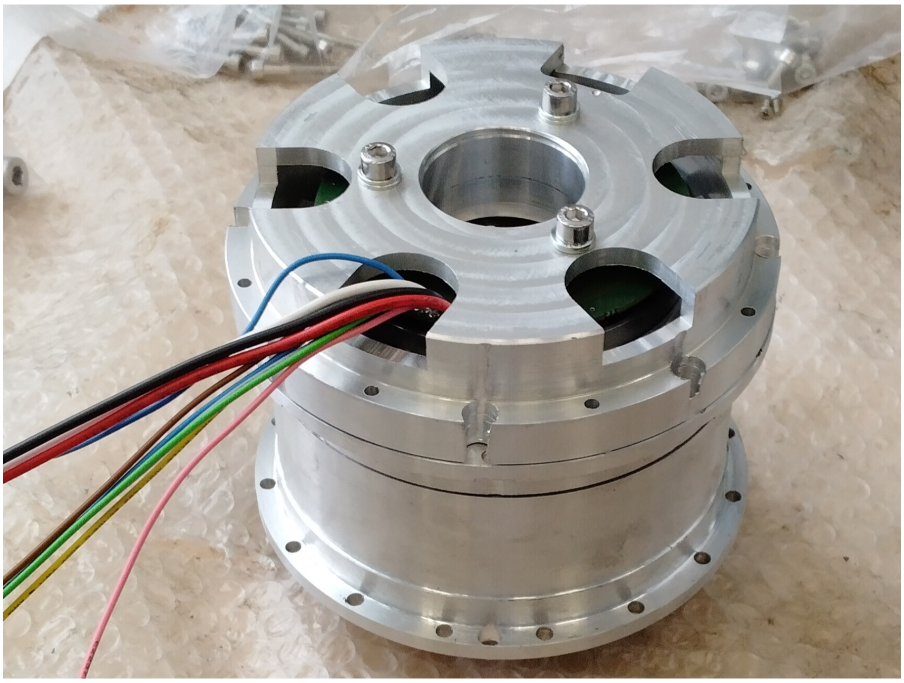

Figure 91: Complete drive, rear view.

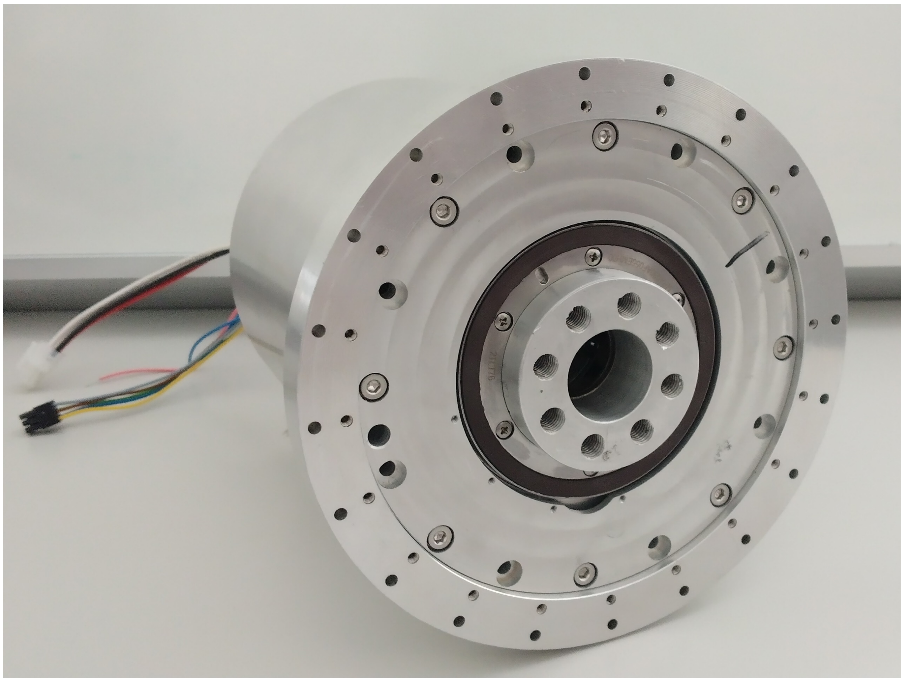

Figure 92: Drive installed in simplified dummy external casing, front view. Note the application of Fig. 82 drive axial mounting solution.

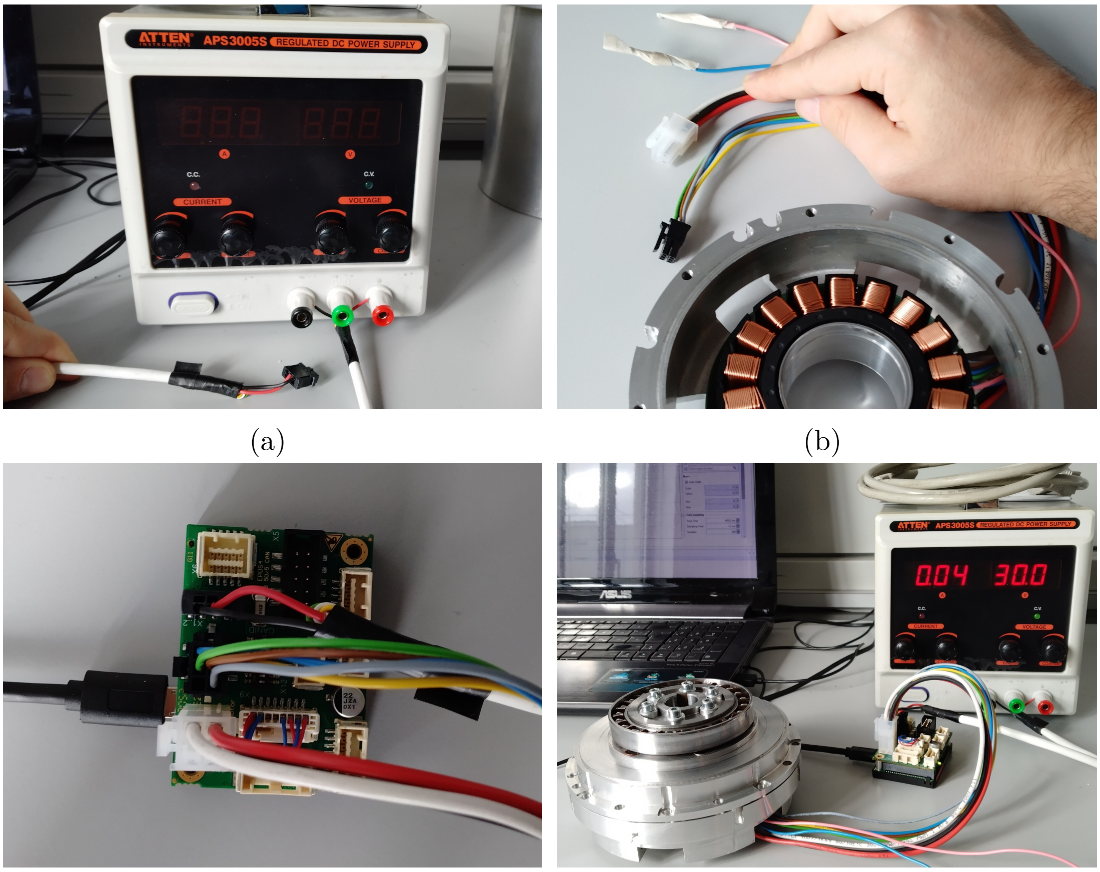

(a) (b)

(c) (d)

Figure 93: (a) Laboratory regulated DC power supply. (b) Motor cable connectors: 3-phase power supply, Hall sensors, thermistor probes (taped). (c) Controller connected to supply power, motor windings, motor Hall sensors, PC USB. (d) Setup for preliminary test of electronics interface and basic drive motor section actuation.

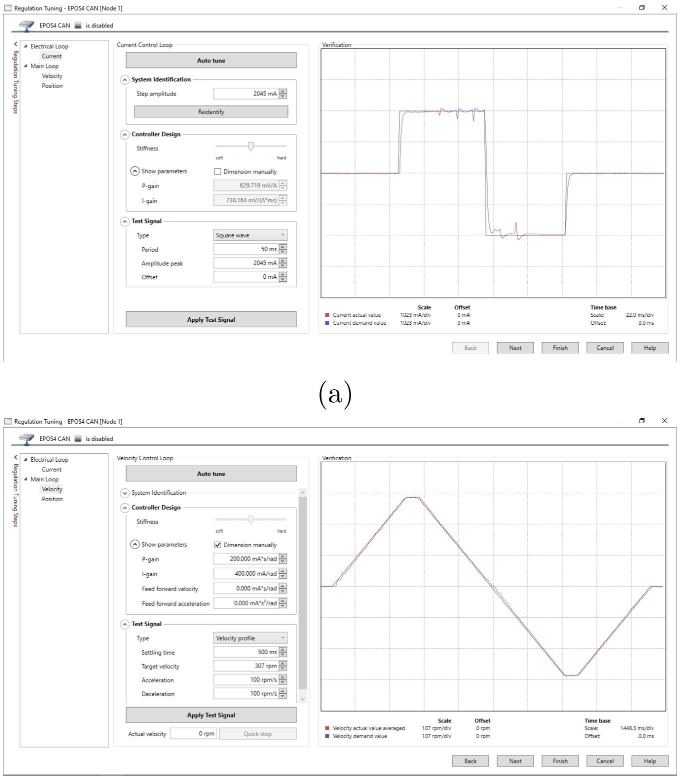

Step amplitude 2045 mA

☐ Dimension manually

P-gain 629.719 mV/A

I-gain 730.164 mV/(A*ms)

Type Square wave

Period 50 ms

Amplitude peak 2045 mA

Offset 0 mA

	Scale	Offset
🟥 Current actual value	1023 mA/div	0 mA
🟦 Current demand value	1023 mA/div	0 mA

Time base
Scale: 22.0 ms/div
Offset: 0.0 ms

(a)

☑ Dimension manually

P-gain 200.000 mA*s/rad

I-gain 400.000 mA/rad

Feed forward velocity 0.000 mA*s/rad

Feed forward acceleration 0.000 mA*s²/rad

Type Velocity profile

Settling time 500 ms

Target velocity 307 rpm

Acceleration 100 rpm/s

Deceleration 100 rpm/s

Actual velocity 0 rpm

	Scale	Offset
🟥 Velocity actual value averaged	107 rpm/div	0 rpm
🟦 Velocity demand value	107 rpm/div	0 rpm

Time base
Scale: 1448.3 ms/div
Offset: 0.0 ms

(b)

Figure 94: Regulation of controller PID constants: (a) current loop output; (b) velocity loop output. Acquisition from Maxon EPOS Studio software.

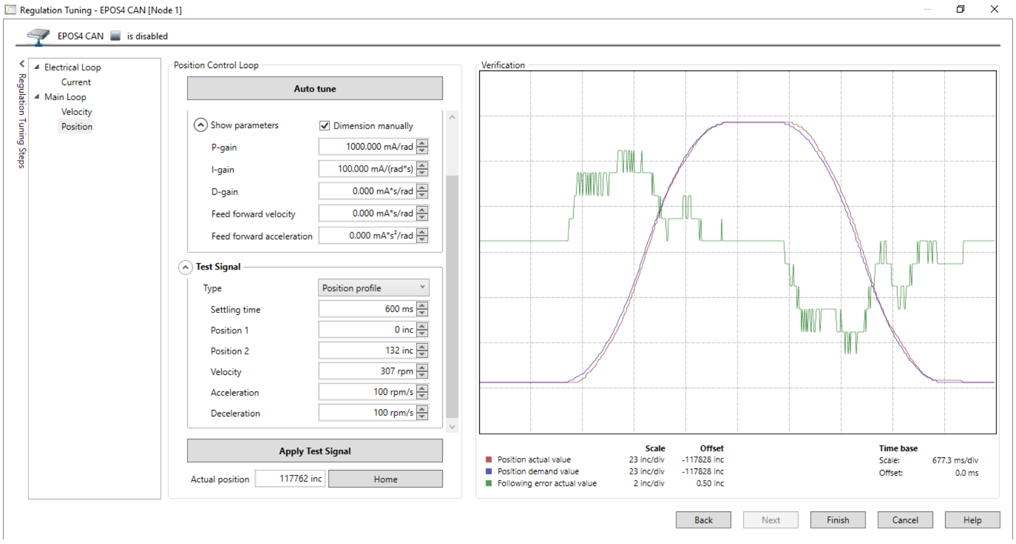

☑ Dimension manually

P-gain 1000.000 mA/rad

I-gain 100.000 mA/(rad*s)

D-gain 0.000 mA*s/rad

Feed forward velocity 0.000 mA*s/rad

Feed forward acceleration 0.000 mA*s²/rad

Type Position profile

Settling time 600 ms

Position 1 0 inc

Position 2 132 inc

Velocity 307 rpm

Acceleration 100 rpm/s

Deceleration 100 rpm/s

Actual position 117762 inc

	Scale	Offset
🟥 Position actual value	23 inc/div	-117828 inc
🟦 Position demand value	23 inc/div	-117828 inc
🟩 Following error actual value	2 inc/div	0.50 inc

Time base
Scale: 677.3 ms/div
Offset: 0.0 ms

Figure 95: Regulation of controller PID position loop and relative output. Acquisition from Maxon EPOS Studio software.

Conclusions

The present work has dealt with the design of a custom 6-DOF articulated robot for aseptic industry applications. The arm was devised with the specific intent to reside in sterile workplaces; as such, the project involved the compliance to stringent hygienic requirements, mainly consisting of: smooth and easily cleanable external robot surfaces (e.g. absence of undercuts or hidden areas, minimization of bolted connections); enclosed arm architecture; capability to withstand the harsh physical and chemical sterilization cycles of surrounding environment; prevention of inflow leakage from pressurized liquid jets.

At first, an overall study of aseptic industry main pillars summarized the regulations, design best-practices, and sterilization treatments involved. A comparative analysis of related commercial robotics highlighted significant offer in terms of mechanical specifications, but somewhat poor hygienic and chemical resistance performances. The custom robot design process took its start from these lacks and specifically addressed the problem of a lightweight architecture, which could lead to a future mobile implementation; a number of potentially suitable concepts were proposed.

Mechanical design of the arm started from the analysis of a basic kinematic model, which was used to test some plausible operation scenarios and assess preliminary target torques. In function of these, the realization of a highly-integrated hollow modular drive – consisting of BLDC motor, harmonic drive gearing, ball and crossed roller bearings, magnetic absolute encoder, digital controller – was proposed, together with relative size scaling for other robot DOFs; the obtained architecture, characterized by a peculiar assembling solution, is housed in the robot without the need for additional removable covers. With regard to arm casing, a tubular geometry was devised, so to avoid the use of classic clevis linkages and to maximize the exposition of outer surfaces. Ti-6Al-4V was selected as casing material; the alloy resulted as the best trade-off between a number of contrasting constraints: reduction of weight, high mechanical strength and stiffness, resistance to chemical corrosion. The realization of hygienic and protected robot junctions – which represent the most vulnerable spot of the arm – was addressed in two phases. From one hand, an innovative compliant clamp unit was proposed to avoid external bolted connections. From the other hand, a number of potential commercial sealing solutions were examined, providing a perspective of the overall related features; PTFE-covered fluorocarbon o-ring seals were implemented. A custom end-effector, aimed at the manipulation of small objects, was developed to complement the robot; the design main features consist of weight and footprint optimization, minimization of moving parts and multitask capabilities.

A custom real-time multibody simulator was developed to guide mechanical design process and to assess its outcome. By the means of a dedicated GUI and provided motion control algorithms, the end-user can interact at run-time with the simulated environment and test robot operation in different scenarios. In the present case, the developed tool was used to verify the correct sizing of devised drives with respect to an assumed aseptic application.

Finally, the actual manufacturing of a preliminary drive prototype was reported. The item allowed to check the correctness of proposed mechanical design, the feasibility of assembling sequence, and the interface between implemented electronic devices.

Overall a slender, highly-hygienic lightweight robot design has been obtained so far. Nevertheless, the work is far from being over, and some open points still need to be addressed in deeper detail. Future interventions will encompass the implementation of customized rotary sealings that are able to overcome the current trade-off between asepticity, size, and dynamic loads. With regard to the presented simulator, automatic obstacle avoidance algorithms will be introduced to speed up path planning. Additionally, *torque actuators* – i.e. exerting a torque $T(t)$ in function of a given setpoint – will replace current implementation, in order to mimic a PID-controlled system; a realistic digital twin, matching the actual specifications of real actuator counterparts, will thus be obtained. Finally, and most importantly, the design requires to be tested on the field; an industrialized version of the prototype will allow to thoroughly characterize the dynamic performance of devised drives, and constitute the base for potential improvements of robot architecture.

Appendix A

Rotation Interpolation

A.1 Quaternions

Quaternions [42] are complex numbers characterized by one real unit and three imaginary units; they are typically written as $\mathbf{q} \in \mathbb{H}$, with q_0, q_1, q_2, $q_3 \in \mathbb{R}$:

$$\mathbf{q} = q_0 + q_1\mathbf{i} + q_2\mathbf{j} + q_3\mathbf{k} \tag{A.1}$$

where the three imaginary units $\mathbf{i}$, $\mathbf{j}$, $\mathbf{k}$ have the following properties:

$$\begin{aligned} \mathbf{i}^2 &= -1 \\ \mathbf{j}^2 &= -1 \\ \mathbf{k}^2 &= -1 \\ \mathbf{i} \cdot \mathbf{j} \cdot \mathbf{k} &= -1 \\ \mathbf{i} \cdot \mathbf{j} &= -\mathbf{j} \cdot \mathbf{i} = \mathbf{k} \\ \mathbf{j} \cdot \mathbf{k} &= -\mathbf{k} \cdot \mathbf{j} = \mathbf{i} \\ \mathbf{k} \cdot \mathbf{i} &= -\mathbf{i} \cdot \mathbf{k} = \mathbf{j} \end{aligned} \tag{A.2}$$

A more compact form is obtained by grouping real and imaginary parts, so that a quaternion results as the combination of a scalar and a vector part:

$$\mathbf{q} = (q_s, \mathbf{q}_v) = (q_s, \mathbf{u}q_v) \quad \mathbf{u} = (i, j, k) \tag{A.3}$$

This notation is very useful to simplify the expression of quaternion multiplication (Hamilton product), that results [48]:

$$\mathbf{pq} = (p_s q_s - \mathbf{p}_v \cdot \mathbf{q}_v, p_s \mathbf{q}_s + q_s \mathbf{p}_v + \mathbf{p}_v \times \mathbf{q}_v) \tag{A.4}$$

Rotations in 3D space can be represented by the means of unit-length quaternions $\mathbf{q} \in \mathbb{H}_1$, $||\mathbf{q}|| = 1$ [48], in which the four scalars q_0, q_1, q_2, q_3 are known as Euler parameters. In this context, Eq. (A.3) can be leveraged to obtain another useful notation of quaternions. In fact, in accordance to polar formulation of common complex numbers, it holds that

$$\mathbf{q} = q_s + \mathbf{u} q_v = \cos\theta + \mathbf{u}\sin\theta \tag{A.5}$$

which, in force of Euler theorem, may be rearranged as

$$\mathbf{q} = \cos\theta + \mathbf{u}\sin\theta = e^{\mathbf{u}\theta} \tag{A.6}$$

From the above relation the definitions of quaternion power and logarithm may be inferred:

$$\mathbf{q}^t = (\cos\theta + \mathbf{u}\sin\theta)^t = \mathrm{e}^{\mathbf{u}\theta t} = \cos(\theta t) + \mathbf{u}\sin(\theta t) \tag{A.7}$$

$$\log(\mathbf{q}) = \log(\cos\theta + \mathbf{u}\sin\theta) = \log\left(\mathrm{e}^{\mathbf{u}\theta t}\right) = \mathbf{u}\theta \tag{A.8}$$

The operation of quaternion conjugation is analogous to that of a common complex number, i.e. it is obtained through change of sign of the imaginary part:

$$\mathbf{q}^* = q_0 - q_1\mathbf{i} - q_2\mathbf{j} - q_3\mathbf{k} \tag{A.9}$$

A consequent important property involves the product of a quaternion and its conjugate, which results in a real term:

$$\begin{aligned} \mathbf{q}\mathbf{q}^* &= \mathbf{q}^*\mathbf{q} \\ &= q_0^2 + q_1^2 + q_2^2 + q_3^2 = s \in \mathbb{R} \end{aligned} \tag{A.10}$$

The above equation may be used to define the norm of a quaternion, which is analogous to the euclidean norm in $\mathbb{R}^4$:

$$||\mathbf{q}|| = \sqrt{\mathbf{q}\mathbf{q}^*} = \sqrt{q_0^2 + q_1^2 + q_2^2 + q_3^2} \tag{A.11}$$

The same property may be seen in reverse:

$$\sqrt{\mathbf{q}\mathbf{q}^*} = \mathbf{q}^*\mathbf{q} = ||\mathbf{q}^2|| \tag{A.12}$$

which brings to

$$\mathbf{q}^{-1} = \frac{\mathbf{q}^*}{||\mathbf{q}^2||} \tag{A.13}$$

The property is most useful for the sake of computational efficiency, as for a unit-length quaternion, the inverse coincides with the conjugate:

$$||\mathbf{q}|| = 1 \implies \mathbf{q}^{-1} = \mathbf{q}^* \tag{A.14}$$

By leveraging the preceding equations, it is possible to prove that the rotation of a vector, expressed as pure quaternion $\mathbf{p} = (0, \mathbf{p}_v)$, is given by [19]:

$$\mathbf{p}' = \mathbf{q}\mathbf{p}\mathbf{q}^* \tag{A.15}$$

Given a rotation of angle φ about axis $\mathbf{u}$, the corresponding quaternion is retrieved through:

$$\mathbf{q} = \begin{pmatrix} q_0 \\ q_1 \\ q_2 \\ q_3 \end{pmatrix} = \begin{pmatrix} \cos(\varphi/2) \\ u_x \sin(\varphi/2) \\ u_y \sin(\varphi/2) \\ u_z \sin(\varphi/2) \end{pmatrix} \tag{A.16}$$

Finally, a rotation matrix is constructed from a unit quaternion through the following formula:

$$\mathbf{R}(\mathbf{q}) = \begin{pmatrix} q_0^2 + q_1^2 - q_2^2 - q_3^2 & 2(q_1 q_2 - q_3 q_0) & 2(q_1 q_3 + q_2 q_0) \\ 2(q_1 q_2 + q_3 q_0) & q_0^2 - q_1^2 + q_2^2 - q_3^2 & 2(-q_1 q_0 - q_2 q_3) \\ 2(q_1 q_3 - q_2 q_0) & 2(q_1 q_0 + q_2 q_3) & q_0^2 - q_1^2 - q_2^2 + q_3^2 \end{pmatrix} \tag{A.17}$$

Vice versa, if a rotation matrix is given, the corresponding quaternion components may be retrieved through:

$$q_0 = \frac{1}{2}\sqrt{R_{11} + R_{22} + R_{33} + 1} \tag{A.18}$$

$$q_1 = \frac{R_{32} - R_{23}}{4q_0} \tag{A.19}$$

$$q_2 = \frac{R_{13} - R_{31}}{4q_0} \tag{A.20}$$

$$q_3 = \frac{R_{23} - R_{12}}{4q_0} \tag{A.21}$$

$$\tag{A.22}$$

which are valid for $q_0 \neq 0$. In the case that $q_0 = 0$, it holds that:

$$\begin{cases} 4q_2 q_3 = R_{32} + R_{23} \\ 4q_1 q_3 = R_{13} + R_{31} \\ 4q_1 q_2 = R_{12} + R_{21} \end{cases} \tag{A.23}$$

Consequently:

$$q_1 = \pm\sqrt{\frac{R_{11} + 1}{2}} \quad q_2 = \pm\sqrt{\frac{R_{22} + 1}{2}} \quad q_3 = \pm\sqrt{\frac{R_{33} + 1}{2}} \tag{A.24}$$

A.2 Polynomial-filleted SLERP

In this section, the main outline of the polynomial-filleted SLERP algorithm is discussed; for a thorough description, refer to the original source [60].

A.2.1 Interpolation between 2 poses

The smooth transition from a starting quaternion $\mathbf{q}_{01}$ to final quaternion $\mathbf{q}_{02}$ may be obtained through a suitable rotation of angle $\overline{\varphi}$ around a unit vector $\mathbf{u}$; the idea is graphically illustrated in Fig. 96a. If we denote $\mathbf{q}_{ij}$ as the orientation of frame (j) with respect to frame (i), we can write

$$\overline{\mathbf{q}}(\mathbf{u}_{(0)}, \overline{\varphi})\mathbf{q}_{01} = \mathbf{q}_{02} \qquad \overline{\mathbf{q}}(\mathbf{u}_{(0)}, \overline{\varphi}) = \mathbf{q}_{02}\mathbf{q}_{10} \tag{A.25}$$

being $\mathbf{q}_{ji}$ the inverse of $\mathbf{q}_{ij}$. The rotation axis $\mathbf{u}$ and angle $\overline{\varphi}$ can be retrieved using Eq. (A.16). The generic intermediate quaternion $\mathbf{q}$ between the two given poses is equivalently expressed through one of the following relations:

$$\mathbf{q} = \mathbf{q}_{01}\overline{\mathbf{q}}(\mathbf{u}_{(1)}, \varphi) \qquad \mathbf{q} = \overline{\mathbf{q}}(\mathbf{u}_{(0)}, \varphi)\mathbf{q}_{01} \qquad \varphi \in [0, \overline{\varphi}] \tag{A.26}$$

If rotation is applied at constant velocity for a time T, the angular velocity vector $\boldsymbol{\omega}$ expressed in frames (0) and (1) is given by:

$$\omega_{(0)} = \mathbf{u}_{(0)}\frac{\overline{\varphi}}{T} \qquad \omega_{(1)} = \mathbf{u}_{(1)}\frac{\overline{\varphi}}{T} \tag{A.27}$$

Conversely, if a specific law is adopted for variation of φ, the preceding equations define the average value $\|\boldsymbol{\omega}\|$ around the same $\mathbf{u}$.

A.2.2 Interpolation between 3 poses

To obtain the connection of three poses – i.e. starting from frame (1), passing through frame (2) and arriving to frame (3), see Fig. 96b – it is possible to replicate the above strategy twice. However, following this approach, it is necessary to perform a smooth stop and restart in coincidence of frame (2) in order to preserve the continuity of angular velocity. The main concepts exposed in the following focus on a way to circumvent this requirement.

Approximate method

The first step consists in the generation a trajectory from frame (1) to frame (3) passing near frame (2) (see Fig. 97a). This is an approximate solution to the exposed problem.

We initially observe that frames (2) and (3) can be reached from the previous frames by suitable rotations $\overline{\alpha}$ and $\overline{\beta}$ around depicted axes $\mathbf{u}_1$ and $\mathbf{u}_2$

$$\mathbf{q}_{02} = \mathbf{q}_{01}\mathbf{q}_{12} \qquad \mathbf{q}_{12} = \overline{\mathbf{q}}(\mathbf{u}_1, \overline{\alpha}) \tag{A.28}$$

$$\mathbf{q}_{03} = \mathbf{q}_{02}\mathbf{q}_{23} \qquad \mathbf{q}_{23} = \overline{\mathbf{q}}(\mathbf{u}_2, \overline{\beta}) \tag{A.29}$$

Therefore, the following equation describes the trajectory connecting pose (1) with

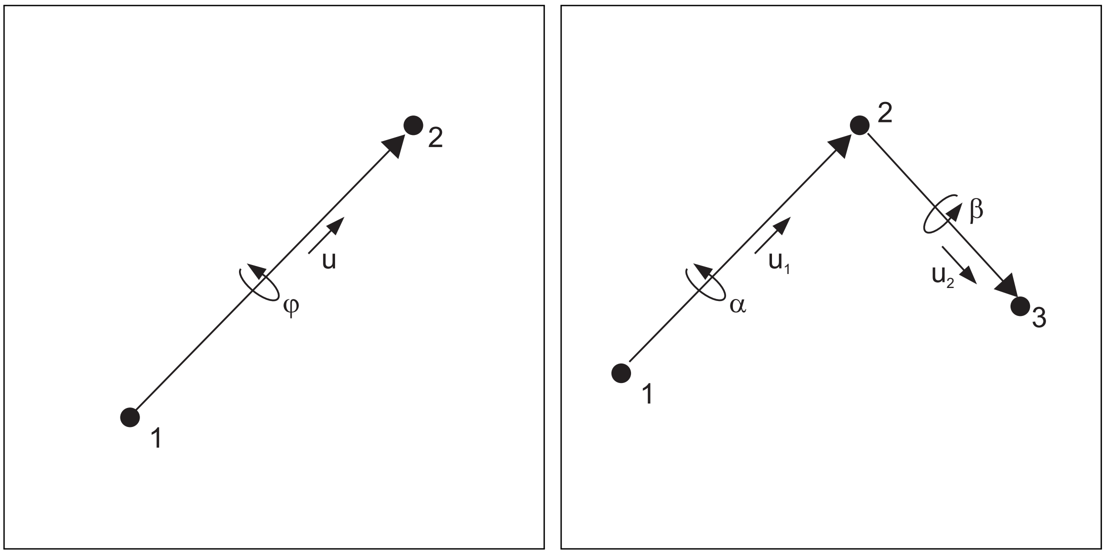

(a) (b)

Figure 96: (a) Conventional representation of an angular motion between two frames, consisting in a rotation of angle φ about a fixed rotation axis $\mathbf{u}$. (b) Conventional representation of an angular motion between three frames, starting from frame (1) and ending to frame (3) while passing through frame (2).

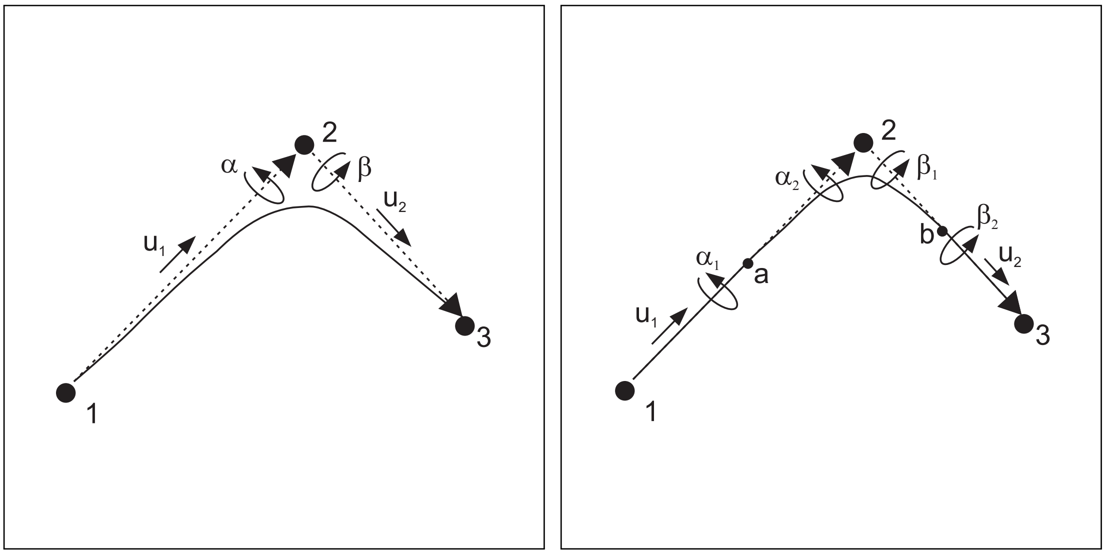

(a) (b)

Figure 97: (a) Approximate angular trajectory between three frames (first definition). (b) Approximate angular trajectory between three frames (variant to pass closer to intermediate frame).

pose (3)

$$\mathbf{q} = \mathbf{q}_{01}\overline{\mathbf{q}}(\mathbf{u}_{1(1)}, \alpha)\overline{\mathbf{q}}(\mathbf{u}_{2(2)}, \beta) \qquad \alpha \in [0, \overline{\alpha}], \beta \in \left[0, \overline{\beta}\right] \tag{A.30}$$

where $\alpha = \beta = 0$ gives $\mathbf{q} = \mathbf{q}_{01}$, while $\alpha = \overline{\alpha}$ and $\beta = \overline{\beta}$ gives $\mathbf{q} = \mathbf{q}_{03}$. To pass near frame (2) it is necessary to assign suitable initial and final conditions to the variation law of α and β. More specifically, it is necessary that the variation of α is fast in the first tract, and slow in the second one; conversely, β should vary slowly in the first part and quickly in the final part. The purpose is achieved by adopting a law like the following:

$$\alpha(t) = \overline{\alpha}s_1(t) \qquad \beta(t) = \overline{\beta}s_2(t) \qquad t \in [0, T] \tag{A.31}$$

$$\dot{s}_1(0) > 0 \qquad \dot{s}_1(T) = 0 \qquad \ddot{s}_1(0) = \ddot{s}_1(T) = 0 \tag{A.32}$$

$$\dot{s}_2(0) = 0 \qquad \dot{s}_2(T) > 0 \qquad \ddot{s}_2(0) = \ddot{s}_2(T) = 0 \tag{A.33}$$

In order to pass closer to pose (2) we may adopt the following strategy (see Fig. 97b)

- perform an initial rotation α_1 around a $\mathbf{u}_1$ and reach frame (a);
- move from frame (a) to (b) using the algorithm of Eq. (A.30) with rotations α_2 and β_1
- conclude motion from frame (b) to (3) rotating around $\mathbf{u}_2$ by an angle β_2.

The mentioned operations are performed assuming $\overline{\alpha} = \alpha_1 + \alpha_2$, $\overline{\beta} = \beta_1 + \beta_2$. Thus, the trajectory is generated by the following three steps:

$$\text{step 1:} \quad \mathbf{q} = \mathbf{q}_{01}\overline{\mathbf{q}}(\mathbf{u}_1, \alpha) \qquad \alpha \in [0, \alpha_1] \tag{A.34}$$

$$\text{step 2:} \quad \mathbf{q} = \mathbf{q}_{01}\overline{\mathbf{q}}(\mathbf{u}_1, \alpha_1)\overline{\mathbf{q}}(\mathbf{u}_1, \alpha)\overline{\mathbf{q}}(\mathbf{u}_2, \beta) \qquad \alpha \in [0, \alpha_2] \qquad \beta \in [0, \beta_1] \tag{A.35}$$

$$\text{step 3:} \quad \mathbf{q} = \mathbf{q}_{01}\overline{\mathbf{q}}(\mathbf{u}_1, \overline{\alpha})\overline{\mathbf{q}}(\mathbf{u}_2, \beta_1)\overline{\mathbf{q}}(\mathbf{u}_2, \beta) \qquad \beta \in [0, \beta_2] \tag{A.36}$$

Steps 1 and 3 are classical SLERP interpolations segments, smoothly connected by Step 2. If the following conditions are imposed to the laws in Eq. (A.31), it is possible to preserve continuity of velocity and acceleration between (a) and (b):

$$s_1(0) = 0 \qquad s_2(0) = 0 \tag{A.37}$$

$$\dot{s}_1(0) = \dot{\overline{\alpha}} \qquad \dot{s}_2(0) = 0 \tag{A.38}$$

$$\ddot{s}_1(0) = 0 \qquad \ddot{s}_2(0) = 0 \tag{A.39}$$

$$s_1(T) = \alpha_2 \qquad s_2(T) = \beta_1 \tag{A.40}$$

$$\dot{s}_1(T) = 0 \qquad \dot{s}_2(T) = \dot{\overline{\beta}} \tag{A.41}$$

$$\ddot{s}_1(T) = 0 \qquad \ddot{s}_2(T) = 0 \tag{A.42}$$

$\dot{\overline{\alpha}}$ and $\dot{\overline{\beta}}$ respectively denote the angular velocity during the first and third step of the motion; these conditions can be easily retrieved by the polynomial law reported in Appendix A.2.4.

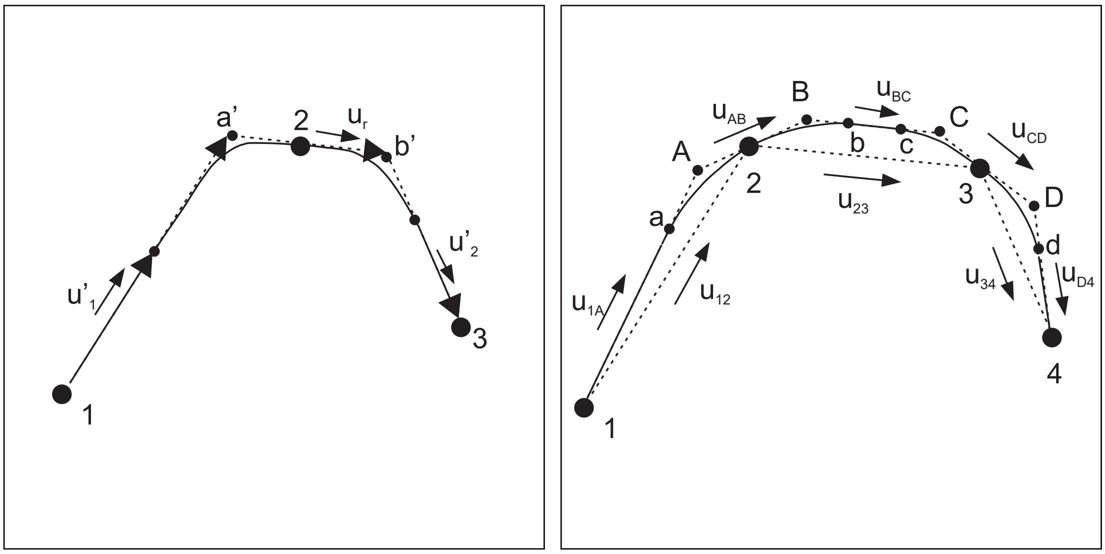

(a) (b)

Figure 98: (a) Exact trajectory connecting three different frames by using the intermediate poses (a') and (b'). (b) Exact trajectory connecting four frames by using the intermediate poses (A), (B), (C) and (D); extension to arbitrary number of poses is easily obtained by replication of the present scheme.

Exact method

In order to produce a trajectory that rotates frame (1) to (3), while passing exactly through frame (2), it is possible to replicate twice the algorithm described in the preceding paragraph.

At first (see Fig. 98a), an auxiliary rotation axis $\mathbf{u}_r$ is defined, so to be a weighted mean of $\mathbf{u}_1$ and $\mathbf{u}_2$:

$$\mathbf{u}_r = \frac{k_1\mathbf{u}_1 + k_2\mathbf{u}_2}{\|k_1\mathbf{u}_1 + k_2\mathbf{u}_2\|} \tag{A.43}$$

Then, chosen suitable rotation values α' e β', it is possible to generate the quaternions (a') e (b') by rotation around the axis $\mathbf{u}_r$. The intermediate auxiliary poses are determined as

$$\mathbf{q}_{0a'} = \mathbf{q}(\mathbf{u}_r, -\alpha')\mathbf{q}_{02} \qquad\qquad \mathbf{q}_{0b'} = \mathbf{q}(\mathbf{u}_r, \beta')\mathbf{q}_{02} \tag{A.44}$$

Finally, the 3-pose approximate algorithm is applied in two phases: the first connecting $(1) - (a') - (2)$ and the second connecting $(2) - (b') - (3)$.

A.2.3 Exact method for arbitrary number of rotations

The 3-pose exact algorithm can be extended to interpolate an arbitrary number of rotations. For each intermediate frame (i), i.e. from (2) to $(N-1)$, the fillet rotation axes are computed by weighted average of the axes connecting (i) with $(i-1)$ and $(i+1)$. Next, the auxiliary poses (A), (B), (C), …, (X) are chosen on the fillet axes by rotating of suitable desired angles. Finally, it is possible to compute the axes $\mathbf{u}_{1A}$, $\mathbf{u}_{BC}$, $\mathbf{u}_{D4}$, …, $\mathbf{u}_{X-1,X}$ and introduce the additional knots (a), (b), (c), …, (x) at desired angular position. For example, assuming 4 input rotations to be interpolated and referring to Fig. 98b, we can create the desired trajectory through the following steps:

$$\begin{aligned}
&\text{step 1:} && \mathbf{q} = \mathbf{q}_{01}\mathbf{q}(\mathbf{u}_{1A(1)}, \varphi_{1a}) \\
&\text{step 2:} && \mathbf{q} = \mathbf{q}_{0a}\mathbf{q}(\mathbf{u}_{1A(1)}, \varphi_{aA})\mathbf{q}(\mathbf{u}_{AB(2)}, \varphi_{A2}) \\
&\text{step 3:} && \mathbf{q} = \mathbf{q}_{02}\mathbf{q}(\mathbf{u}_{AB(2)}, \varphi_{2B})\mathbf{q}(\mathbf{u}_{BC(B)}, \varphi_{Bb}) \\
&\text{step 4:} && \mathbf{q} = \mathbf{q}_{0b}\mathbf{q}(\mathbf{u}_{BC(B)}, \varphi_{bc}) \\
&\text{step 5:} && \mathbf{q} = \mathbf{q}_{0c}\mathbf{q}(\mathbf{u}_{BC(B)}, \varphi_{cC})\mathbf{q}(\mathbf{u}_{CD(3)}, \varphi_{C3}) \\
&\text{step 6:} && \mathbf{q} = \mathbf{q}_{03}\mathbf{q}(\mathbf{u}_{CD(3)}, \varphi_{3D})\mathbf{q}(\mathbf{u}_{D4(D)}, \varphi_{Dd}) \\
&\text{step 7:} && \mathbf{q} = \mathbf{q}_{0d}\mathbf{q}(\mathbf{u}_{D4(D)}, \varphi_{d4}) \qquad \text{(A.45)} \\
& && \qquad \text{(A.46)}
\end{aligned}$$

This process can be repeated to interpolate any number of given rotations.

A.2.4 Polynomial motion laws

Here we summarize the quantities needed to define a five-degree polynomial motion law with assigned initial and final conditions of position, velocity and acceleration. If we name

- s_i, s_f: initial and final position
- v_i, v_f: initial and final velocity
- a_i, a_f: initial and final acceleration
- $\Delta s = s_f - s_i$

and we impose the following relations

$$\begin{aligned}
A &= s_i \\
B &= v_i \\
C &= \frac{a_i}{2} \\
D &= \frac{a_f - 3a_i}{2T} - \frac{6v_i + 4v_f}{T^2} + \frac{10\Delta s}{T^3} \\
E &= \frac{3a_i - 2a_f}{2T^2} + \frac{8v_i + 7v_f}{T^3} - \frac{15\Delta s}{T^4} \\
F &= \frac{a_f - a_i}{2T^3} - \frac{3(v_i + v_f)}{T^4} + \frac{6\Delta s}{T^5}
\end{aligned} \tag{A.47}$$

we may formulate the desired motion law and its derivatives as follows:

$$\begin{aligned}
s(t) &= Ft^5 + Et^4 + Dt^3 + Ct^2 + Bt + A \\
\dot{s}(t) &= 5Ft^4 + 4Et^3 + 3Dt^2 + 2Ct + B \\
\ddot{s}(t) &= 20Ft^3 + 12Et^2 + 6Dt + 2C
\end{aligned} \tag{A.48}$$

A.2.5 Source code

In the following, an implementation of the described quaternion algorithm is reported. Python language and Chrono::Engine API tools are used.

```
def compute_coeff_s(v_bound):
    # compute poly5 coefficients of duration T given
    # boundary position, speed and acceleration
    si = v_bound[0]
    vi = v_bound[1]
    ai = v_bound[2]
    sf = v_bound[3]
    vf = v_bound[4]
    af = v_bound[5]
    T = v_bound[6]
    ds = sf - si
    A = si
    B = vi
    C = ai / 2
    D = (af - 3*ai) / (2*T) - (6*vi + 4*vf) / (T**2)
        + 10*ds / (T**3)
    E = (3*ai - 2*af) / (2 * T**2)
```

```
        + (8*vi + 7*vf) / T**3 - 15*ds / (T**4)
    F = (af - ai) / (2* T**3) - 3 * (vi + vf) / (T**4)
        + 6*ds / (T**5)
    return [A, B, C, D, E, F]

def interpolate_s(coeff, t):
    # return [s, ds/dt, dds/ddt] position, speed, accel.
    # given polynomials computed in compute_coeff_s()
    s = coeff[0] + coeff[1] * t + coeff[2] * pow(t, 2)
        + coeff[3] * pow(t, 3) + coeff[4] * pow(t, 4)
        + coeff[5] * pow(t, 5)
    dsdt = coeff[1] + 2 * coeff[2] * t + 3 * coeff[3]
        * pow(t, 2) + 4 * coeff[4] * pow(t, 3)
        + 5 * coeff[5] * pow(t, 4)
    ddsddt = 2 * coeff[2] + 6 * coeff[3] * t + 12
        * coeff[4] * pow(t, 2) + 20 * coeff[5] * pow(t, 3)
    return [s, dsdt, ddsddt]

def compute_ur(q01, q02, q03, k1, k2):
    # compute fillet rotation axis respect to frame 2
    q10 = q01.GetConjugate()
    q20 = q02.GetConjugate()
    q12 = q10 * q02
    q23 = q20 * q03
    u1_1 = q12.Q_to_Rotv().GetNormalized() # NB: u1_2 = u1_1
    u2_2 = q23.Q_to_Rotv().GetNormalized() # NB: u2_2 = u2_3
    ur_2 = (u1_1 * k1 + u2_2 * k2).GetNormalized()
    return ur_2

def polySLERP_fillet(q_knot, u_fill, dr_fill, omega,
        Tfillet, tstart, t):
    '''
    polySLERP three poses interpolation. Useful
    for fillet phase of general method
    INPUT
        q_knot: quaternion knots of fillet phase
                (actual passage)
        u_fill: three axes of interpolation
        dr_fill: two fillet phases angles
        omega: starting and ending velocities
        Tfillet: two fillet phases times
        tstart: start time
```

```
    t: current time
OUTPUT
    q: current interpolated quaternion
'''
# Compute motion laws
# knot1 -> dummy1 -> knot2
coeff_s1 = compute_coeff_s(
    [0, omega[0], 0, dr_fill[0],
    0, 0, Tfillet[0]]) # si, vi, ai, sf, vf, af, T
coeff_s2 = compute_coeff_s(
    [0, 0, 0, dr_fill[0], (omega[0]
    + omega[1])/2, 0, Tfillet[0]]
    ) # si, vi, ai, sf, vf, af, T
# knot2 -> dummy2 -> knot3
coeff_s3 = compute_coeff_s(
    [0, (omega[0] + omega[1])/2,
     0, dr_fill[1], 0, 0, Tfillet[1]]
     ) # si, vi, ai, sf, vf, af, T
coeff_s4 = compute_coeff_s(
    [0, 0, 0, dr_fill[1], omega[1],
     0, Tfillet[1]]) # si, vi, ai, sf, vf, af, T

# Compute interpolated quaternion
if t <= tstart + Tfillet[0]:
    s1 = interpolate_s(coeff_s1, t - tstart)[0]
    s2 = interpolate_s(coeff_s2, t - tstart)[0]
    q = q_knot[0]
            * chrono.Q_from_AngAxis(
            s1, u_fill[0])
            * chrono.Q_from_AngAxis(
            s2, u_fill[1])
else:
    s3 = interpolate_s(coeff_s3, t -
            (tstart + Tfillet[0]))[0]
    s4 = interpolate_s(coeff_s4, t -
            (tstart + Tfillet[0]))[0]
    q = q_knot[1]
            * chrono.Q_from_AngAxis(s3, u_fill[1])
            * chrono.Q_from_AngAxis(s4, u_fill[2])

return q
```

```
def polySLERP(q_input, dr_array, T, Nsamp):
    '''
    polySLERP quaternion interpolation method
    INPUT
        q_input: input quaternion key frames
        dr_array: fillet angles (if one value given,
                assumed to be equal for all)
        T: time of interpolation
        Nsamp: interpolation sample points
    OUTPUT
        q_interp: np.array of interpolated quaternion
                components
    '''

    # Initialization
    deltaT = T / (len(q_input) - 1) # equally distrubute
        # time between given quaternions
    k1, k2 = 1, 1 # weights for fillet axes creation
    Ndr_check = 2 * (len(q_input) - 2) # check for consistent
        # given dr number
    q_rel, q_dummy, q_aux, q_interp = [], [], [], []
    u_rel, u_fill, u_aux, u_dir = [], [], [], []
    theta_dir = []
    Tdir, Tfill = [], []

    # If only 1 dr is input, use that angle for all fillets
    if (isinstance(dr_array, Number)):
        dr_array = [dr_array] * Ndr_check

    # Check if input fillet angles are of consistent number
    if (len(dr_array) != Ndr_check):
        raise ValueError('Inconsistent␣Nf')

    # Compute relative quaternions and axes
    # (q12, q23, ... and u12, u23, ...)
    for ii in range(0, len(q_input) - 1):
        q_rel.append(
            ~q_input[ii] * q_input[ii + 1])
        u_rel.append(
            (~q_input[ii]
            * q_input[ii + 1]).Q_to_Rotv().GetNormalized())
```

```
# Compute fillet axes (uAB, ...)
for ii in range(0, len(q_input) - 2):
    u_fill.append(
        (u_rel[ii] * k1
        + u_rel[ii + 1] * k2).GetNormalized())

# Compute dummy quaternions (q0A, q0B, ...)
for ii in range(0, len(q_input) - 2):
    q_dummy.append(
        q_input[ii + 1]
        * chrono.Q_from_AngAxis(-dr_array[2*ii],
        u_fill[ii]))
    q_dummy.append(
        q_input[ii + 1]
        * chrono.Q_from_AngAxis(+dr_array[2*ii + 1],
        u_fill[ii]))

# Compute starting and ending rotation axes
ustart = (~q_input[0]
    * q_dummy[0]).Q_to_Rotv().GetNormalized()
uend = (~q_dummy[-1]
    * q_input[-1]).Q_to_Rotv().GetNormalized()

# Compute auxiliary phase axes (u_bc, u_cd, ... )
for ii in range(1, len(q_dummy) - 1, 2):
    u_aux.append(
        (~q_dummy[ii]
        * q_dummy[ii + 1]).Q_to_Rotv().GetNormalized())

# Compute auxiliary quaternions (q0a, q0b, ...)
q_aux.append(q_dummy[0]
    * chrono.Q_from_AngAxis(-dr_array[0], ustart))
for ii in range(0, len(u_aux)):
    q_aux.append(
        q_dummy[2*ii + 1]
        * chrono.Q_from_AngAxis(dr_array[2*ii + 1],
         u_aux[ii]))
    q_aux.append(
        q_dummy[2*ii + 2]
        * chrono.Q_from_AngAxis(-dr_array[2*ii + 2],
        u_aux[ii]))
q_aux.append(q_dummy[-1]
```

```
    * chrono.Q_from_AngAxis(dr_array[-1], uend))

# Check for auxiliary quaternions interference
for ii in range(0, len(u_aux)):
    rel_angle = (~q_dummy[2*ii + 1]
            * q_dummy[2*ii + 2]).Q_to_Rotv().Length()
    if (rel_angle <= (dr_array[2*ii + 1]
            + dr_array[2*ii + 2])):
        raise ValueError('Exceeding␣distance')

# Compute direct phase angles (theta_1a, theta_bc, ..)
theta_dir.append((~q_input[0]
    * q_aux[0]).Q_to_Rotv().Length())
for ii in range(1, len(q_dummy) - 1, 2):
    theta_dir.append(
        (~q_dummy[ii] * q_dummy[ii + 1]).Q_to_Rotv().Length()
        - dr_array[ii] - dr_array[ii + 1])
theta_dir.append((~q_aux[-1]
    * q_input[-1]).Q_to_Rotv().Length())

# Compute direct phase times as proportions (T1a, Tbc, ...)
Tdir.append(theta_dir[0] / (theta_dir[0]
    + 2*dr_array[0]) * deltaT)
for ii in range(0, len(u_aux)):
    th_dir = (~q_aux[2*ii + 1]
            * q_aux[2*ii + 2]).Q_to_Rotv().Length()
    Tdir.append(
        th_dir / (2*dr_array[2*ii + 1]
        + th_dir + 2*dr_array[2*ii + 2])
        * deltaT)
Tdir.append(theta_dir[-1]
    / (2*dr_array[-1] + theta_dir[-1]) * deltaT)

# Compute half fillet phase times (Ta2, T2b, Tc3, T3d, ...)
Tfill.append(2*dr_array[0]
    / (theta_dir[0] + 2*dr_array[0]) * deltaT)
for ii in range(0, len(u_aux)):
    theta = 2*dr_array[2*ii+1]
            + theta_dir[ii+1] + 2*dr_array[2*ii+2]
    Tfill.append(
        2*dr_array[2*ii+1] / theta * deltaT)
    Tfill.append(
```

```
       2*dr_array[2*ii+2] / theta * deltaT)
Tfill.append(2*dr_array[-1]
    / (2*dr_array[-1] + theta_dir[-1]) * deltaT)

# Collect direct phase axes
u_dir = [ustart] + u_aux + [uend]

# Collect direct phase starting quaternions
q_dir = [q_input[0]]
for ii in range(1, len(q_aux), 2):
    q_dir.append(q_aux[ii])

# Collect interpolation times
times = [0]
for ii in range(0, len(q_input) - 2):
    times.append(times[-1] + Tdir[ii])
    times.append(times[-1] + Tfill[2*ii]
            + Tfill[2*ii + 1])
times.append(times[-1] + Tdir[-1])

phase, kk = 0, 0 # useful interpolation phase counters

# Perform interpolation
for t in np.linspace(0, T, Nsamp):
    tstart = times[phase]
    tend = times[phase + 1]

    # direct phase interpolation
    if phase % 2 == 0:
        q = q_dir[phase - kk] * chrono.Q_from_AngAxis(
            (t - tstart) / Tdir[phase - kk]
            * theta_dir[phase - kk], u_dir[phase - kk])

    # fillet phase interpolation
    else:
        qknot = [q_aux[phase - 1],
            q_input[phase - kk], q_aux[phase]]
        ufillet = [u_dir[phase - kk - 1],
            u_fill[phase - kk - 1], u_dir[phase - kk]]
        drfillet = [dr_array[phase - 1],
            dr_array[phase]]
        omega = [theta_dir[phase - kk - 1]
```

```
                / Tdir[phase - kk - 1], theta_dir[phase - kk]
                / Tdir[phase - kk]]
            Tfillet = [Tfill[phase - 1], Tfill[phase]]
            q = polySLERP_fillet(qknot, ufillet,
                drfillet, omega, Tfillet, tstart, t)

        # update phase
        if t >= tend:
            kk = phase - kk
            phase = phase + 1

        # add interpolated quaternion
        q_interp.append([q.e0, q.e1, q.e2, q.e3])

    return np.array(q_interp)
```

Appendix B

Mechanical Parts

B.1 Bill of materials

Table B.1: Size-90 drive bill of materials.

Item	Manufacturer	Model
BLDC motor	Maxon Motor	EC frameless 90 flat, 160 W
Controller	Maxon Motor	EPOS4 Compact 50/5 CAN
Gearing	Harmonic Drive SE	CSD-32-160-2A-GR-1
Motor shaft bearing	SKF	Ball bearing 61810-2RZ
Output shaft bearing	THK	Crossed roller RA9008
Absolute encoder	Renishaw	AksIM-2 MBD01_05-80
Solenoid	RS Components	177-0137

Table B.2: Size-60 drive bill of materials.

Item	Manufacturer	Model
BLDC motor	Maxon Motor	EC frameless 60 flat, 100 W
Controller	Maxon Motor	EPOS4 Compact 50/5 CAN
Gearing	Harmonic Drive SE	CSD-25-160-2A-GR-11
Motor shaft bearing	SKF	Ball bearing 61807-2RZ
Output shaft bearing	THK	Crossed roller RA7008
Absolute encoder	Renishaw	AksIM-2 MBD01_05-064
Solenoid	RS Components	177-0137

Table B.3: Size-45 drive bill of materials.

Item	Manufacturer	Model
BLDC motor	Maxon Motor	EC frameless 45 flat, 70 W
Controller	Maxon Motor	EPOS4 Compact 50/5 CAN
Gearing	Harmonic Drive SE	CSD-17-100-2A-R-1
Motor shaft bearing	SKF	Ball bearing 61805-2RZ
Output shaft bearing	THK	Crossed roller RA5008
Absolute encoder	Renishaw	AksIm-2 MBD01_05-049
Solenoid	RS Components	177-0137

Table B.4: End-effector bill of materials.

Item	Manufacturer	Model
BLDC motor	Maxon Motor	EC-i 30, 45 W
Controller	Maxon Motor	EPOS4 Compact 50/5 CAN
Gearing	Norelem	Worm gear 22500
Motor shaft bearing	SKF	Ball bearing W 628/6-2Z
Output shaft bearing	SKF	Ball bearing 628/8-2Z
Absolute encoder	Maxon Motor	ENC 16 EASY XT
Limit switch sensor	RS Components	PM-F25-C3

B.2 Drawings

In the following, the outline drawings of main robot components are reported.

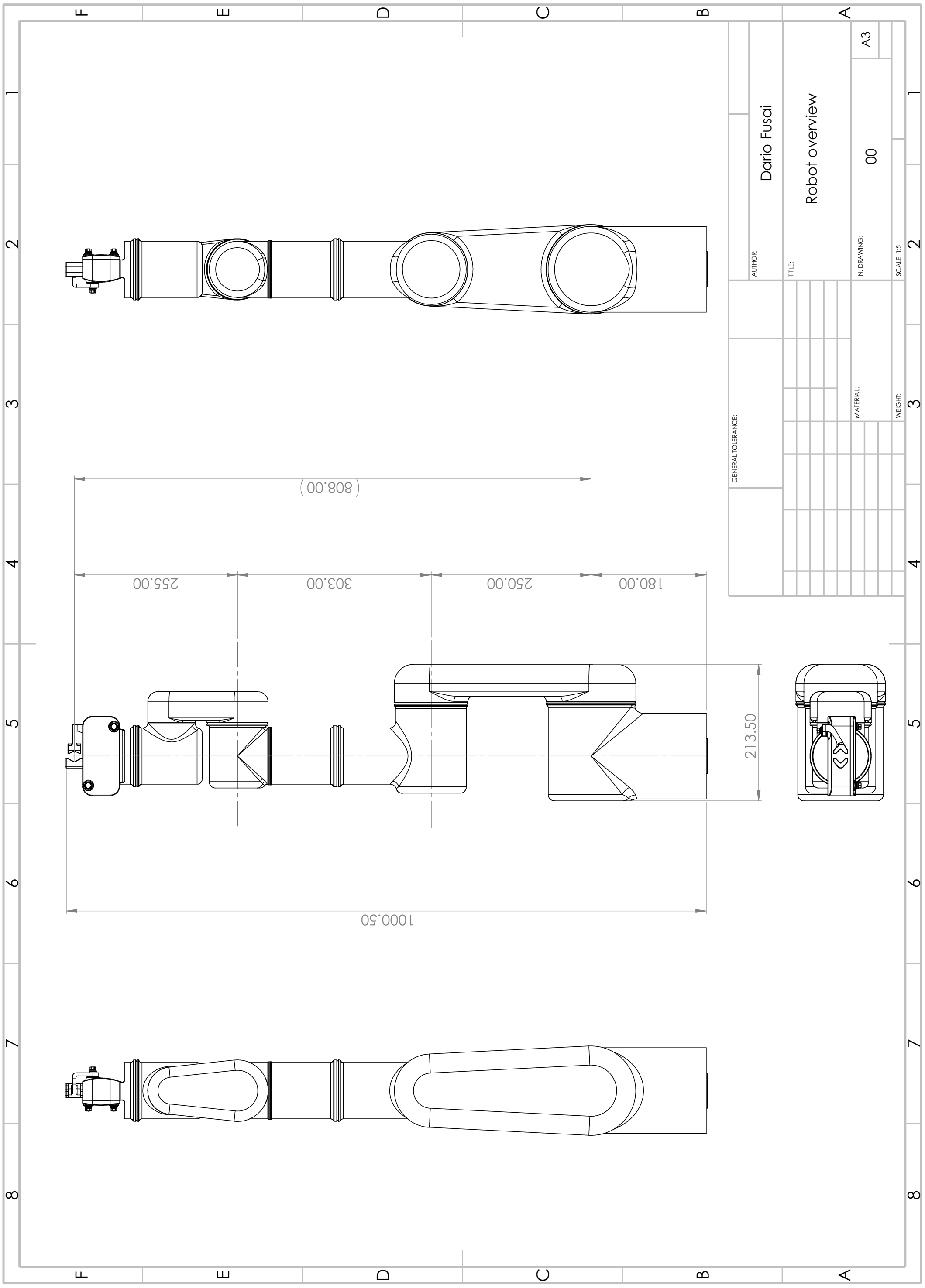
AUTHOR:
Dario Fusai
TITLE:
Robot overview
N. DRAWING:
00
SCALE: 1:5
A3
GENERAL TOLERANCE:
MATERIAL:
WEIGHT:
(808.00)
255.00
303.00
250.00
180.00
213.50
1000.50

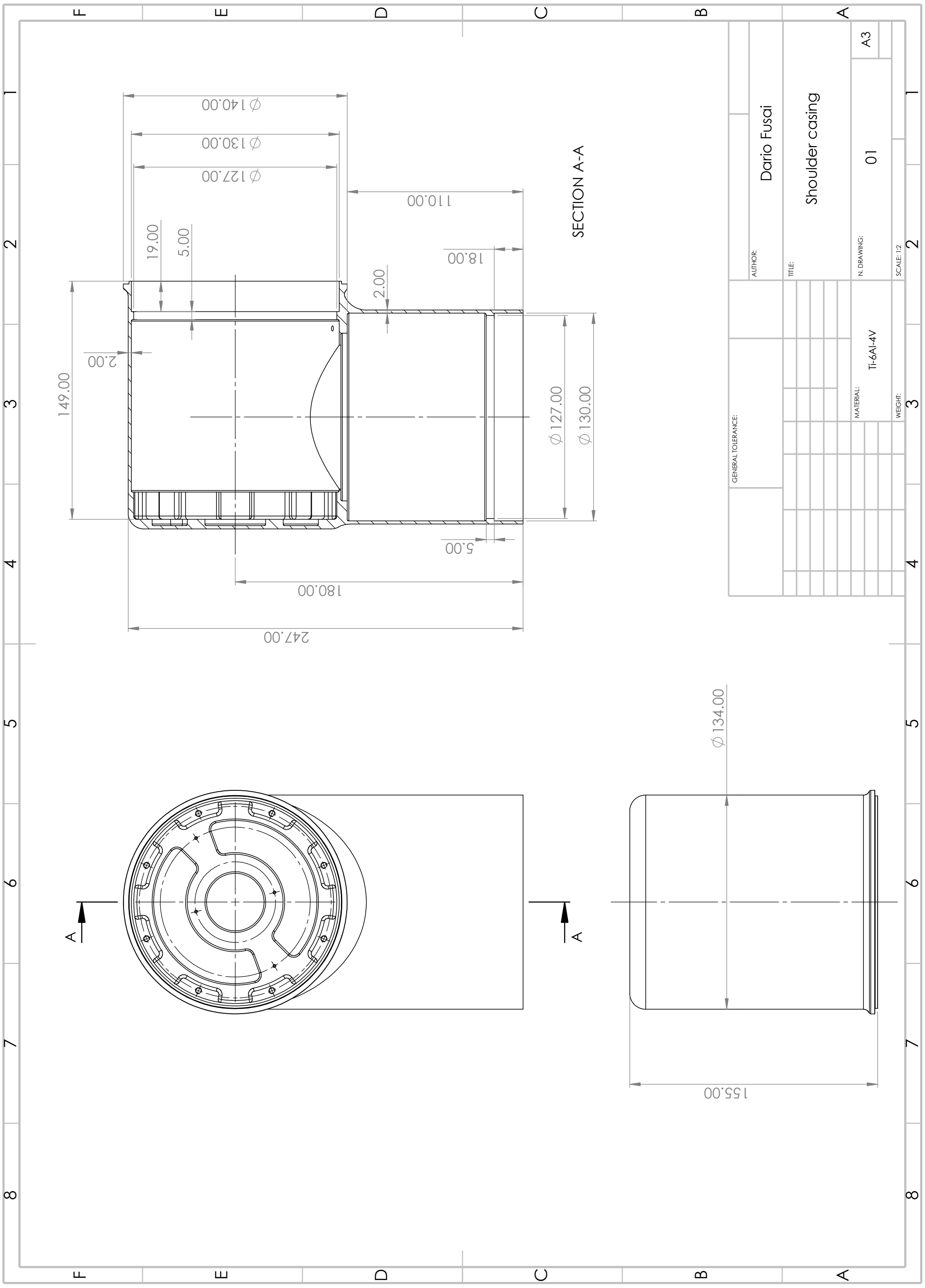
SECTION A-A
Ø 140.00
Ø 130.00
Ø 127.00
110.00
19.00
5.00
18.00
2.00
2.00
149.00
Ø 127.00
Ø 130.00
5.00
180.00
247.00
Ø 134.00
155.00
A
A
AUTHOR:
Dario Fusai
TITLE:
Shoulder casing
N. DRAWING:
01
SCALE: 1:2
A3
GENERAL TOLERANCE:
MATERIAL:
Ti-6Al-4V
WEIGHT:
A
B
C
D
E
F
1
2
3
4
5
6
7
8

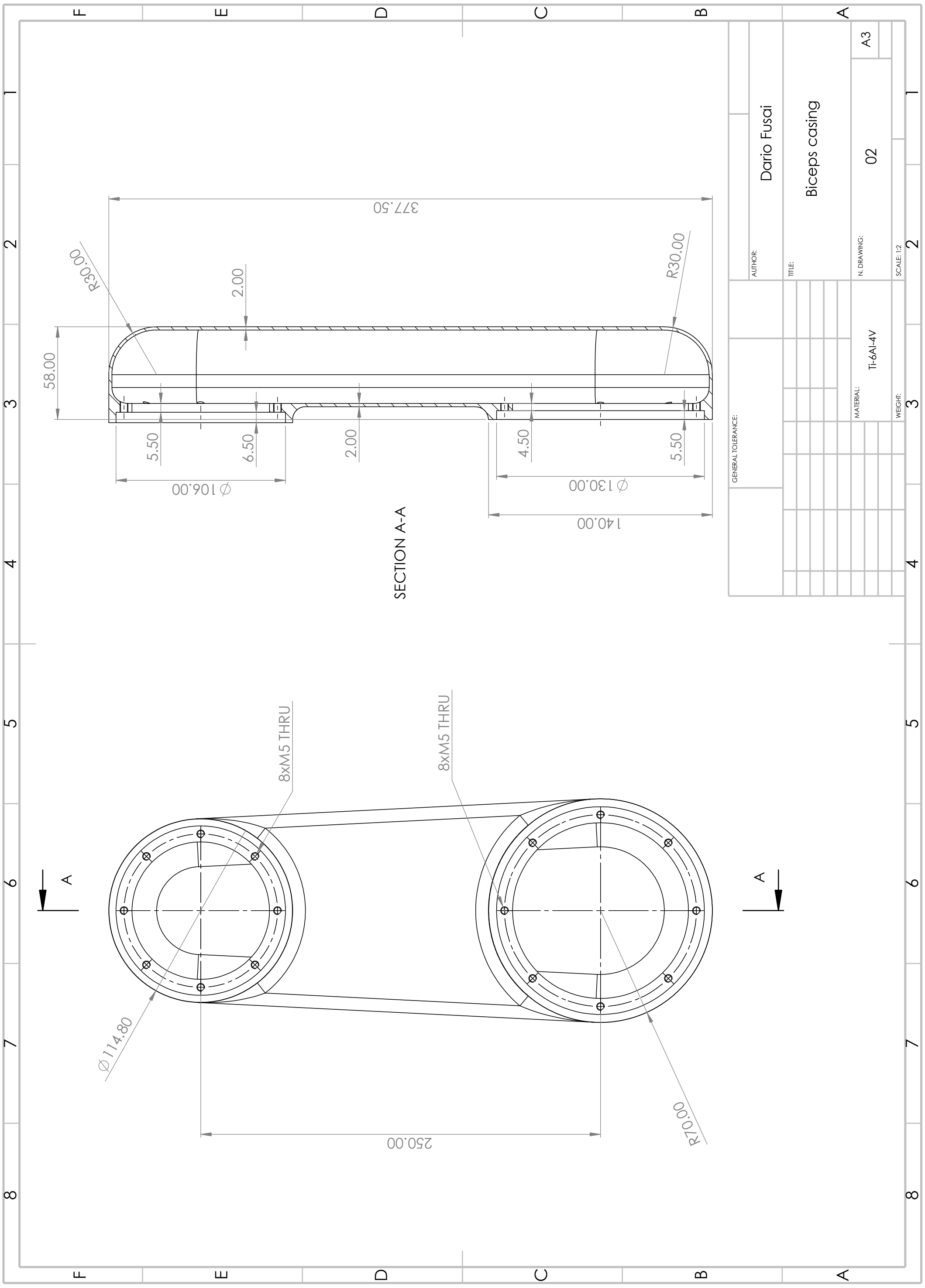
377.50
R30.00
R30.00
2.00
58.00
5.50
6.50
2.00
4.50
5.50
∅106.00
∅130.00
140.00
SECTION A-A
8xM5 THRU
8xM5 THRU
A
A
∅114.80
R70.00
250.00
AUTHOR:
Dario Fusai
TITLE:
Biceps casing
N. DRAWING:
02
SCALE: 1:2
A3
MATERIAL:
Ti-6Al-4V
WEIGHT:
GENERAL TOLERANCE:

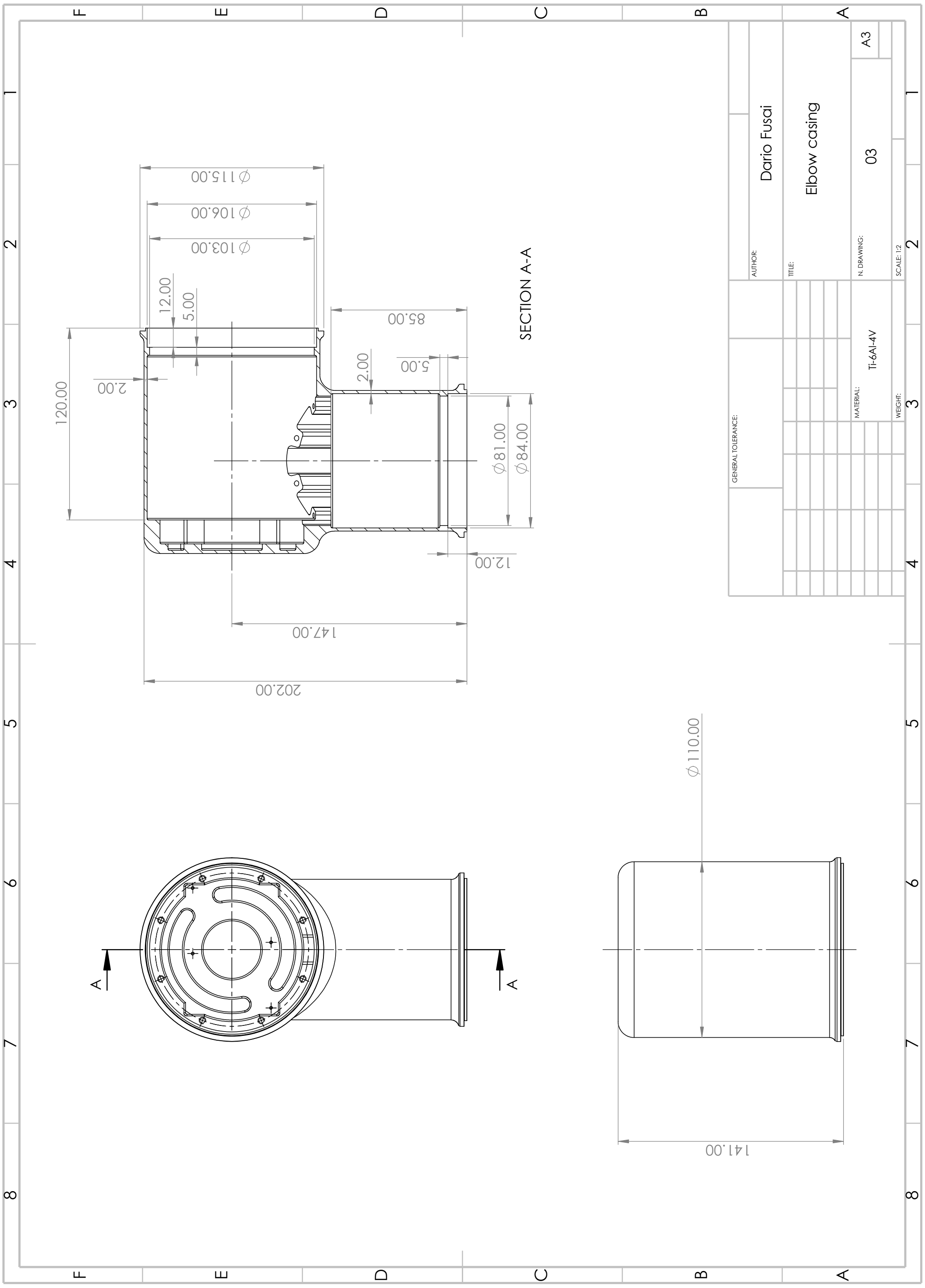
AUTHOR:
Dario Fusai
TITLE:
Elbow casing
N. DRAWING:
03
SCALE: 1:2
A3
MATERIAL:
Ti-6Al-4V
WEIGHT:
GENERAL TOLERANCE:
SECTION A-A
⌀115.00
⌀106.00
⌀103.00
12.00
5.00
2.00
120.00
85.00
2.00
5.00
⌀81.00
⌀84.00
12.00
147.00
202.00
⌀110.00
141.00
A
A
F
E
D
C
B
A
1
2
3
4
5
6
7
8

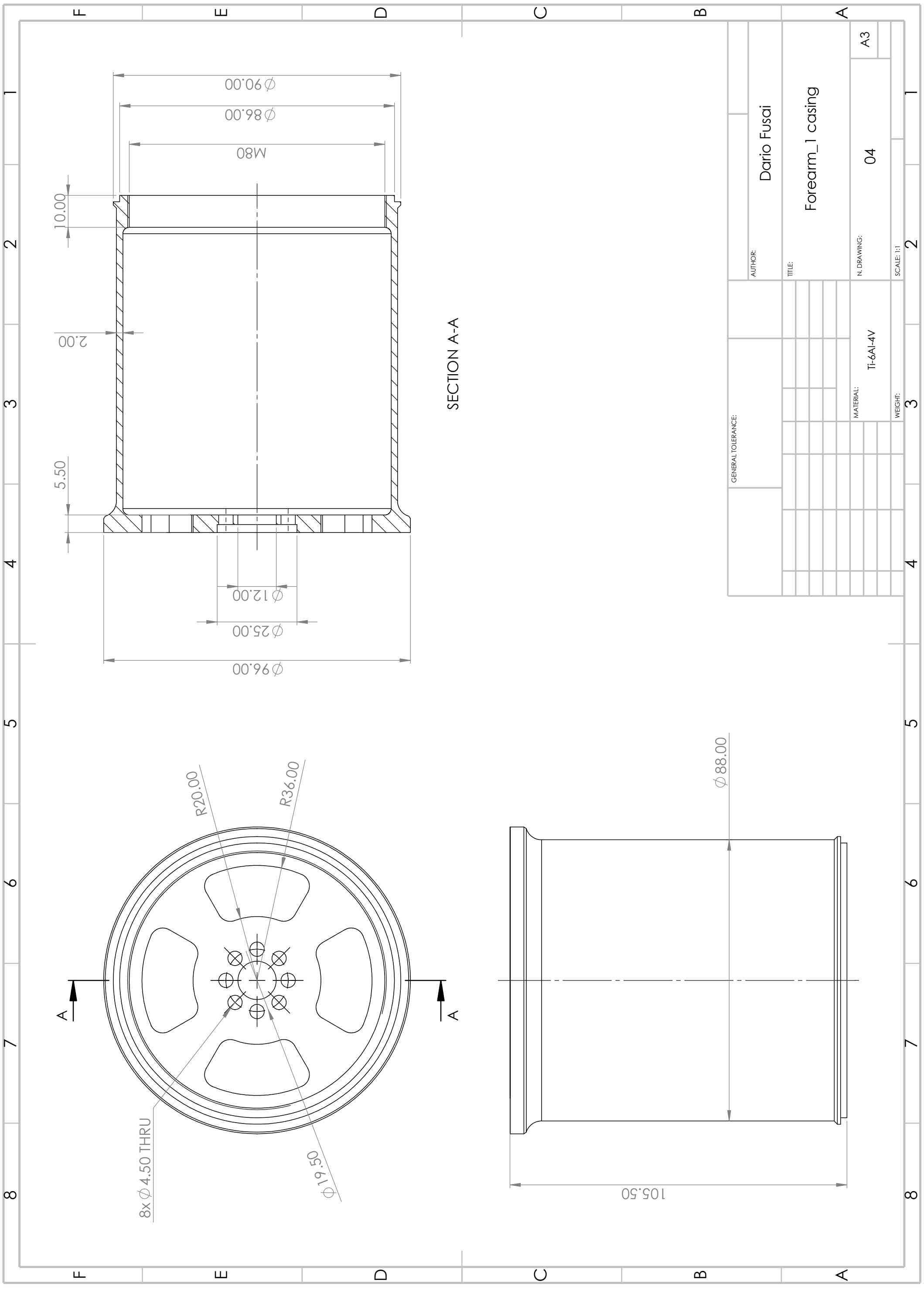
∅90.00
∅86.00
M80
10.00
2.00
5.50
∅12.00
∅25.00
∅96.00
SECTION A-A
R20.00
R36.00
A
A
8x ∅4.50 THRU
∅19.50
∅88.00
105.50
AUTHOR:
Dario Fusai
TITLE:
Forearm_1 casing
N. DRAWING:
04
SCALE: 1:1
A3
MATERIAL:
Ti-6Al-4V
WEIGHT:
GENERAL TOLERANCE:
A
B
C
D
E
F
1
2
3
4
5
6
7
8

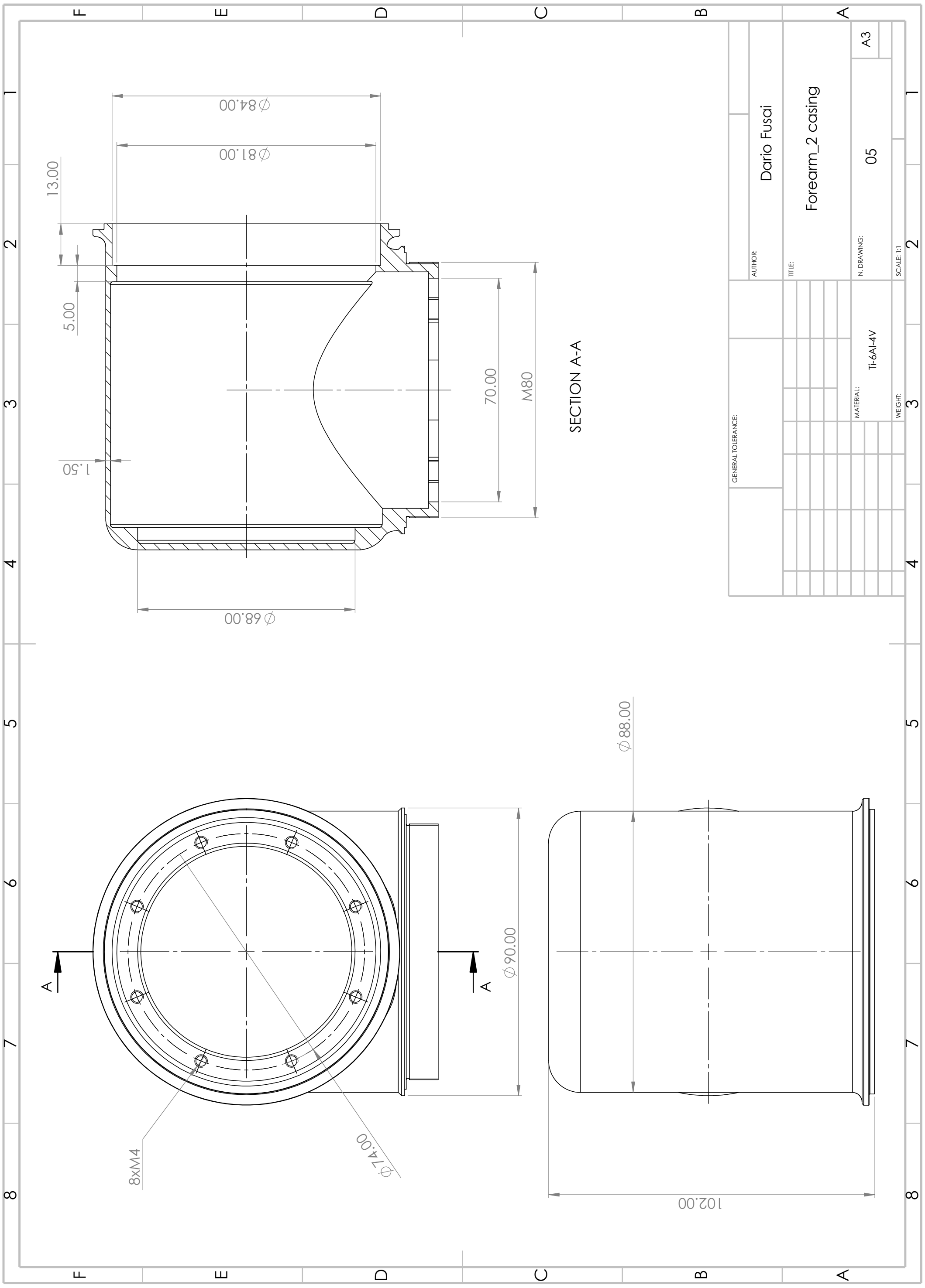
Ø84.00
Ø81.00
13.00
5.00
1.50
70.00
M80
Ø68.00
SECTION A-A
Ø88.00
Ø90.00
A
A
8xM4
Ø74.00
102.00
GENERAL TOLERANCE:
AUTHOR:
Dario Fusai
TITLE:
Forearm_2 casing
N. DRAWING:
05
SCALE: 1:1
MATERIAL:
Ti-6Al-4V
WEIGHT:
A3
F
E
D
C
B
A
1
2
3
4
5
6
7
8

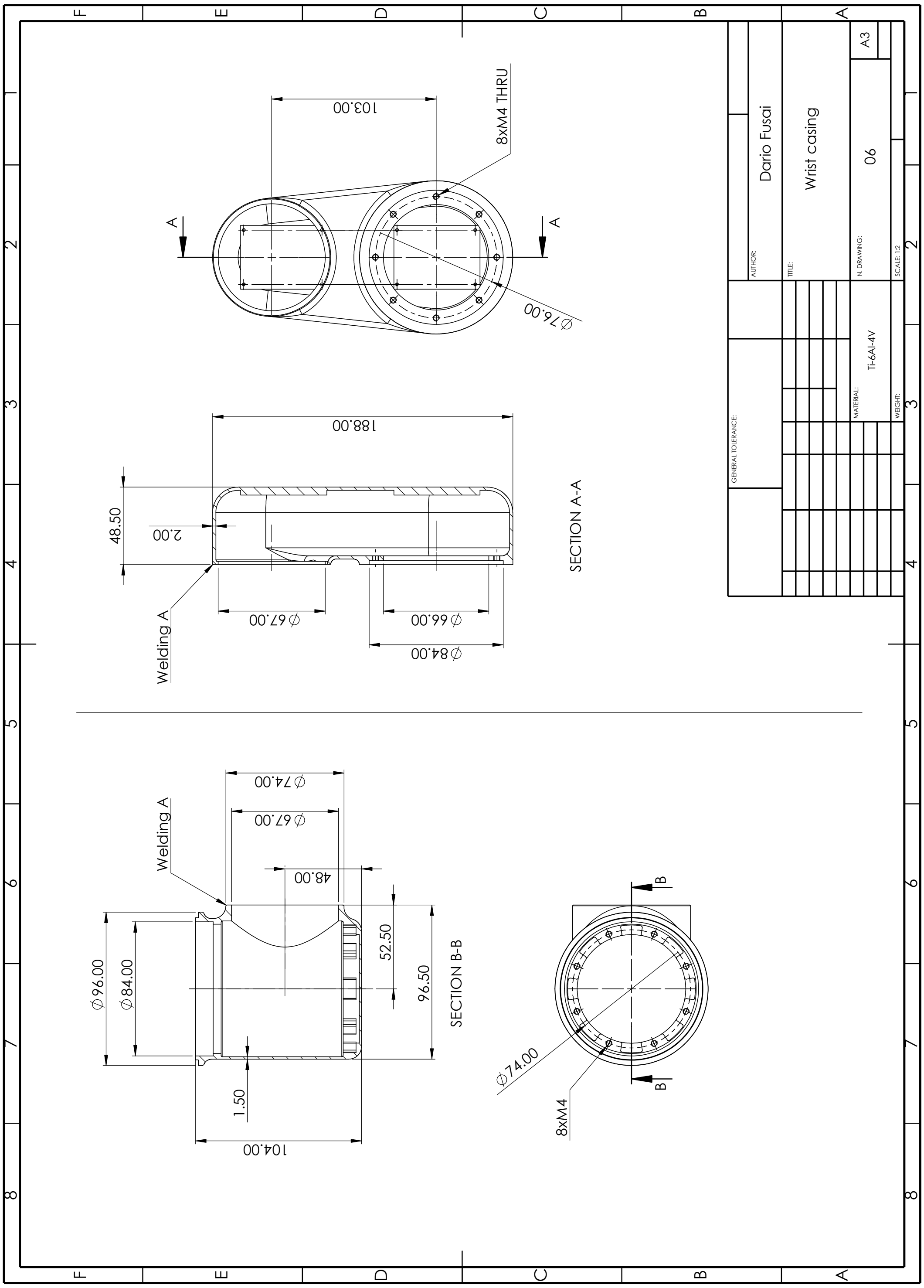
AUTHOR: Dario Fusai
TITLE: Wrist casing
N. DRAWING: 06
SCALE: 1:2
MATERIAL: Ti-6Al-4V
WEIGHT:
GENERAL TOLERANCE:
A3
103.00
8xM4 THRU
⌀76.00
A
A
188.00
48.50
2.00
Welding A
⌀67.00
⌀66.00
⌀84.00
SECTION A-A
⌀74.00
⌀67.00
Welding A
48.00
52.50
96.50
SECTION B-B
⌀96.00
⌀84.00
1.50
104.00
B
B
⌀74.00
8xM4

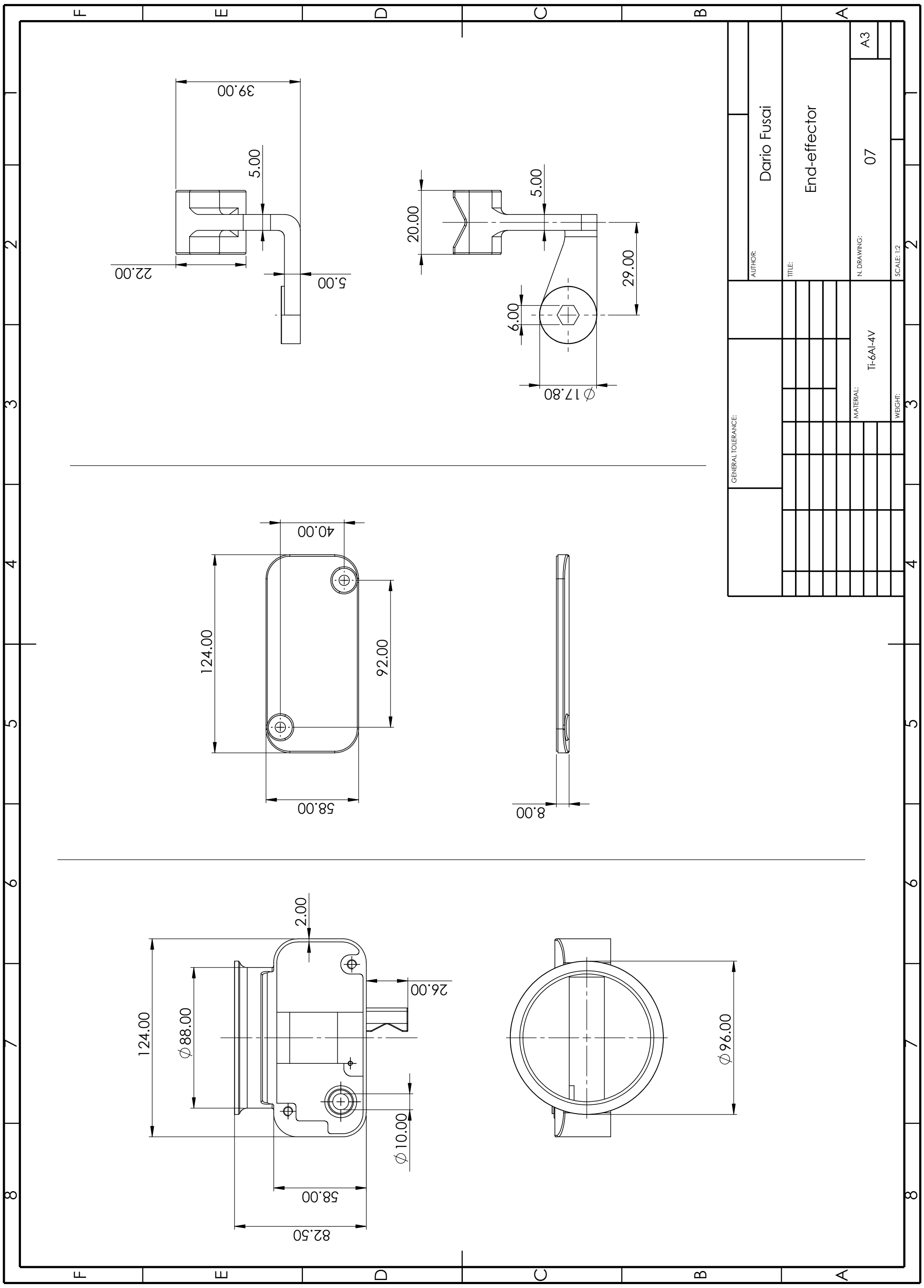
AUTHOR:
Dario Fusai
TITLE:
End-effector
N. DRAWING:
07
A3
SCALE: 1:2
MATERIAL:
Ti-6Al-4V
WEIGHT:
GENERAL TOLERANCE:
39.00
5.00
22.00
5.00
20.00
5.00
29.00
6.00
⌀17.80
40.00
124.00
92.00
58.00
8.00
2.00
26.00
124.00
⌀88.00
⌀10.00
58.00
82.50
⌀96.00

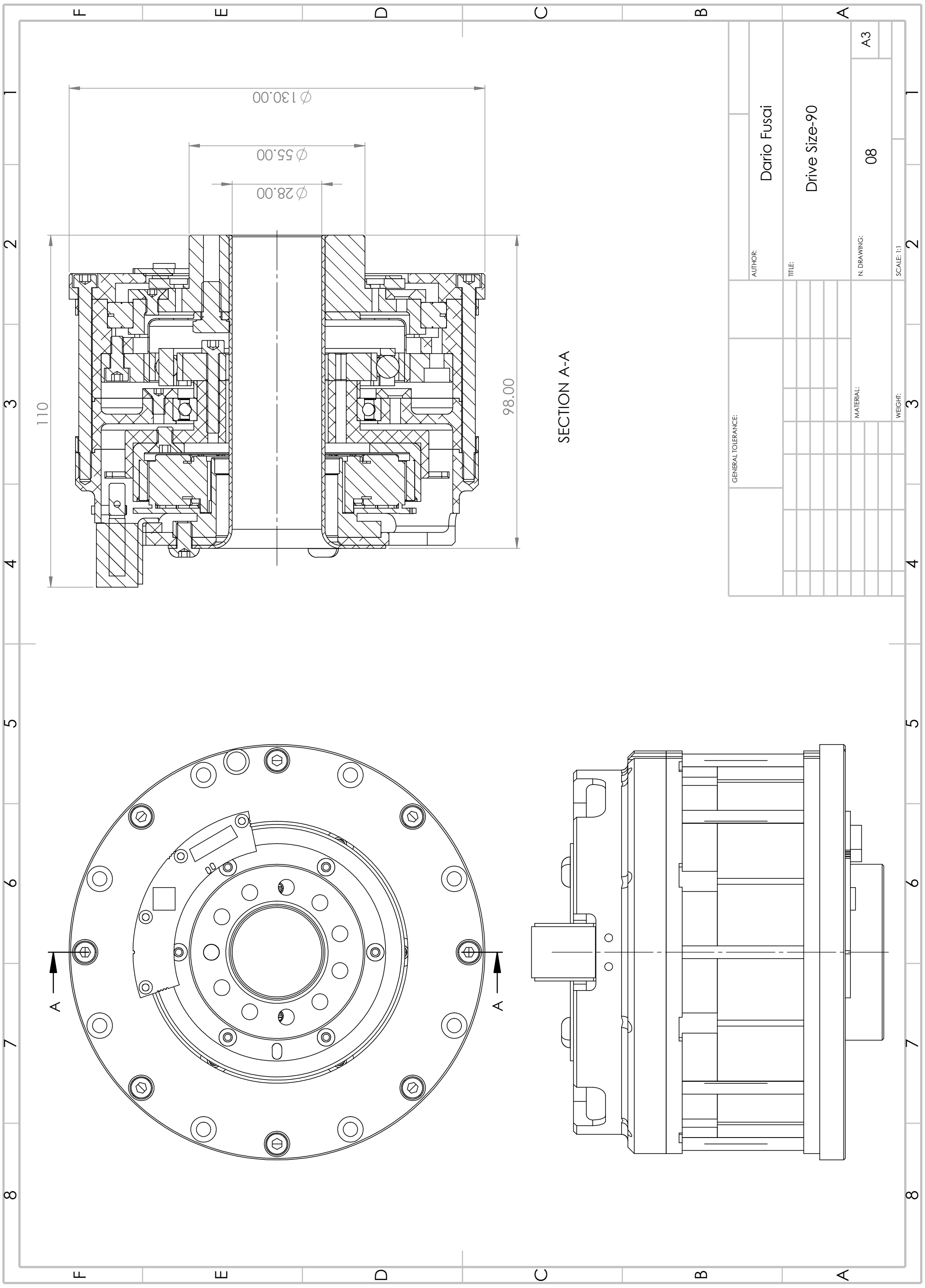
SECTION A-A
Ø130.00
Ø55.00
Ø28.00
110
98.00
A
A
AUTHOR:
Dario Fusai
TITLE:
Drive Size-90
N. DRAWING:
08
SCALE: 1:1
A3
MATERIAL:
WEIGHT:
GENERAL TOLERANCE:

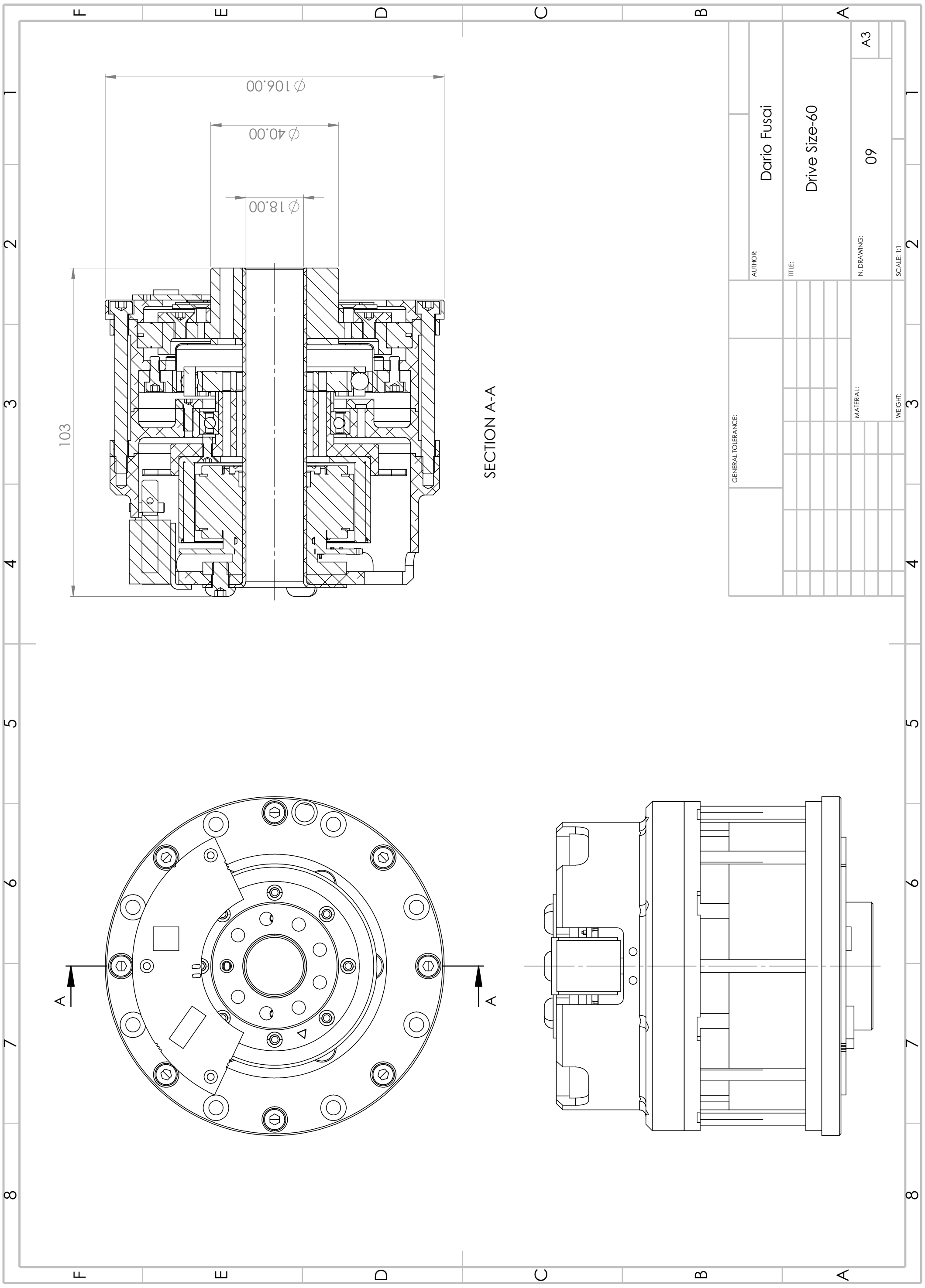
⌀106.00
⌀40.00
⌀18.00
103
SECTION A-A
A
A
AUTHOR:
Dario Fusai
TITLE:
Drive Size-60
N. DRAWING:
09
SCALE: 1:1
A3
GENERAL TOLERANCE:
MATERIAL:
WEIGHT:
F
E
D
C
B
A
1
2
3
4
5
6
7
8

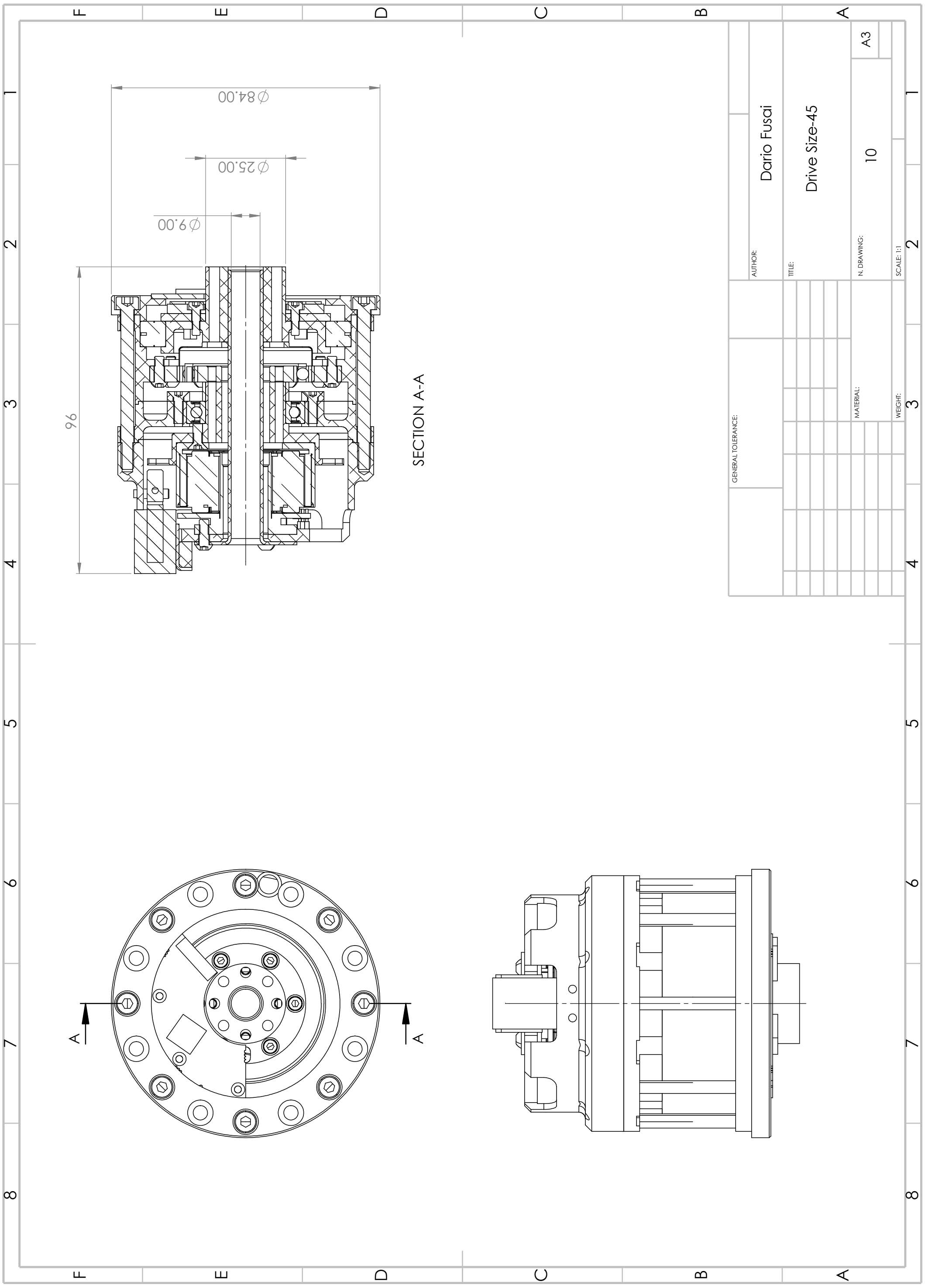
⌀84.00
⌀25.00
⌀9.00
96
SECTION A-A
A
A
GENERAL TOLERANCE:
AUTHOR:
Dario Fusai
TITLE:
Drive Size-45
N. DRAWING:
10
MATERIAL:
SCALE: 1:1
WEIGHT:
A3
F
E
D
C
B
A
1
2
3
4
5
6
7
8

Appendix C

Selected Calculations

C.1 Clamp unit

This section outlines the main results of a multibody simulation used to verify the sizing of robot clamp unit (refer to Section 3.5) with respect to yielding, buckling and local plastic deformation; in this regard, contact forces and stresses related to device assembling, operation, and disassembling phases are discussed.

From a computational point of view, the problem at hand is quite challenging, as it requires the concurrent solution of: multibody dynamics, unilateral constraints, collision detection, impulsive forces, interaction of rigid and flexible bodies. For the purpose, the system is modeled through a non-smooth dynamics approach in the Chrono::Engine simulation framework [107]. An innovative solver based on the Alternating Direction Method of Multipliers (ADMM) [106] [38] is employed, together with a Euler Semi-Implicit time integrator scheme (set to 5 ms timestep). By leveraging the axial symmetry of the clamp unit, only two bodies are considered: the cam-profiled disk and one of the eight flexible beams of the compliant disk. Given the planar nature of the problem, the system is modeled as two-dimensional contact profiles. This choice avoids the need for convex hull meshing of 3D bodies retrieved from CAD exported shapes; consequently, numerical stability is improved and computation time is dramatically reduced: more resources may be dedicated to lower the timestep, to the benefit of simulation accuracy.

The cam disk is modeled as a rotating rigid body, whose boundary profile is directly gathered from correspondent DXF vector drawing; as such, the set of related geometrical entities are faithfully reconstructed through a continuous path of straight and circular lines. A collision shape is hence attributed to this path, so to enable the computation of contact mechanics and prevent interpenetration with other simulation bodies. The compliant disk flexible beam is conversely modeled as a set of two linked entities. The former consists of a Euler-Bernoulli FEM cantilever beam (10 elements used), which encapsulates body elasticity; the latter, used to model component contact surfaces, is respectively made of a circular and a rectangular "envelope" rigid collision shape. Friction among the two bodies is modeled through a coefficient $f_s = 0.30$, representing a precautionary low value for dry steel-on-steel contact. Finally, the size of exposed beam entity and its relative position/orientation with respect to cam disk are linked to respective CAD drawing, so to automatically account for unit geometry modifications, if needed.

Fig. 99 illustrates the main phases of the simulation. At first (Fig. 99a), the cam disk (blue) is rotated in clockwise direction to represent the manual assembling of clamp unit. Next (Fig. 99b), the first contact is registered between cam tooth and beam rectangular section (black); the arising contact force is shown as a red segment, whose length is proportional to force magnitude. At this points, the beams starts to deflect in upward direction, until the peak of the tooth is crossed (Fig. 99c). Fig. 99d shows the main operative condition of the clamp unit: beam tip is pushed against the left part of cam tooth by springback effect. Therefore, if a suitable counter-clockwise torque is applied from cam disk to compliant disk, motion can be transmitted to downstream driven robot members. At last, Fig. 99e depicts the unit manual dismounting operation: a sufficient counter-clockwise torque is applied, so that beam tip begins to slide on cam tooth; after this incipient motion phase, the beam deflects upward and frees the two components (Fig. 99f).

Fig. 100 summarizes the main simulation results in function of time. In particular, upper Fig. 100a shows the angle traveled by cam disk from starting position to lock configuration (i.e. 12 °) and subsequent release; in correspondence to this motion, the lower part of the figure reports the torque profile applied on the cam disk. As described in Section 3.5, the unit must be able to

1. sustain, without dismounting, the maximum torque exerted by upstream drive during operation mode;

2. release the connection after the application of a suitable disassembling torque (inferior in magnitude to the maximum gearing sustainable value).

To model this scenario, the torque profile is defined in three tracts:

1. null setpoint tract, corresponding to the initial free rotation of the body;

2. application of motor torque $T_m = 100\,\mathrm{N\,m}$, precautionary doubled with respect to nominal value $51\,\mathrm{N\,m}$;

3. application of disassembling torque $T_d = 180\,\mathrm{N\,m}$ (with respect to gearing peak torque $T_{\max} = 261\,\mathrm{N\,m}$).

Since only one of the eight flexible beams is simulated, the described torque setpoint are scaled to a factor 1/8. Fig. 100b illustrates the displacement profile experienced by the tip of the beam; two peaks $d \approx 1.1\,\mathrm{mm}$ occur in correspondence of mounting

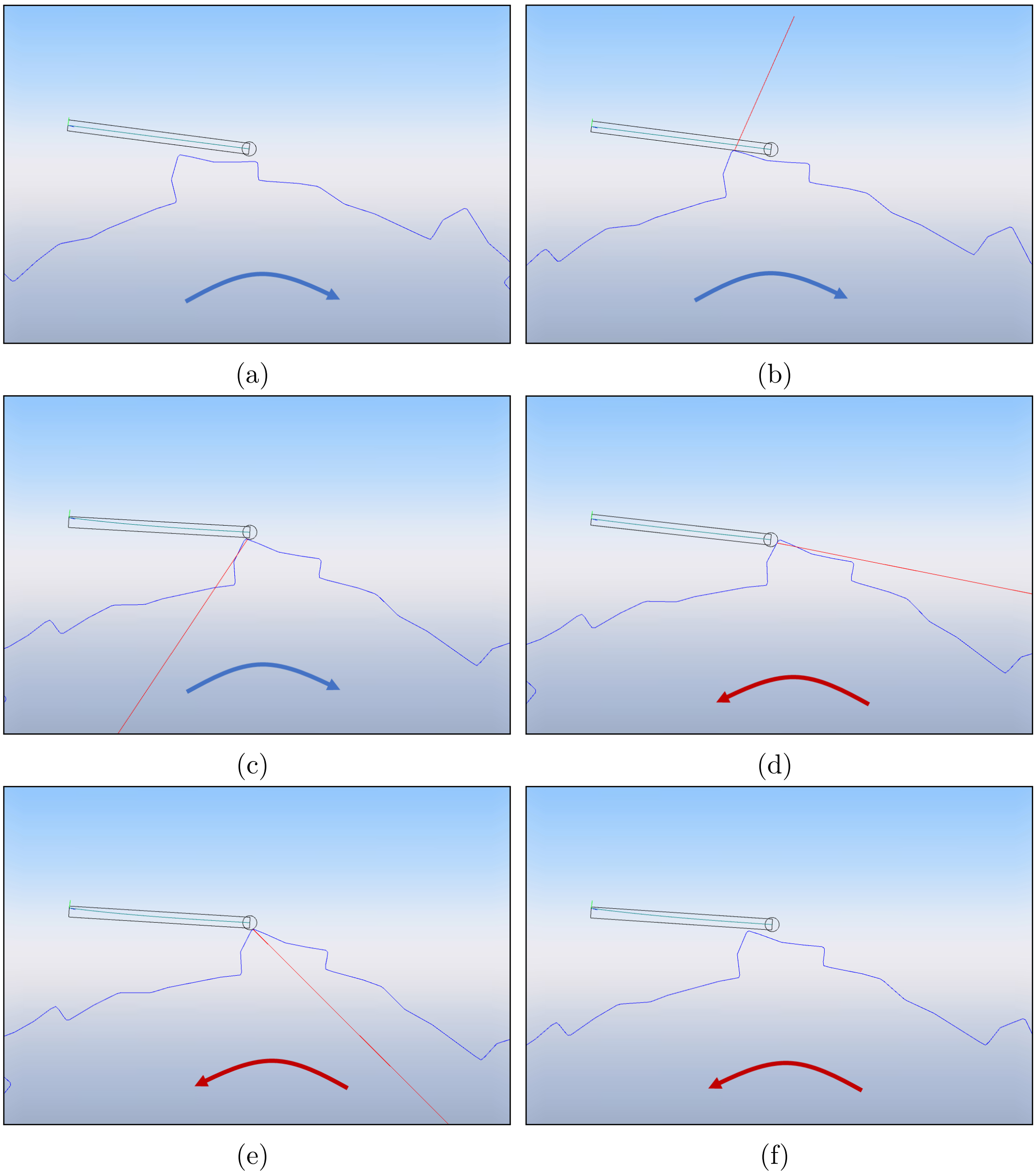

Figure 99: Simulation of compliant clamp unit operation. Flexible beam shown as dark green line (with black collision shape envelope), cam disk collision shape shown in blue, contact force shown in red, direction of motion drawn as blue/red curved arrow. Main phases are illustrated: (a) cam disk approach, (b) first assembling contact, (c) maximum beam tip deflection, (d) torque transmission, (e) dismounting torque, (f) unit disassembled.

and dismounting phases. Fig. 100c reports the actions exerted on the beam, respectively: cam-beam contact force, compression and shear force at fixture, bending

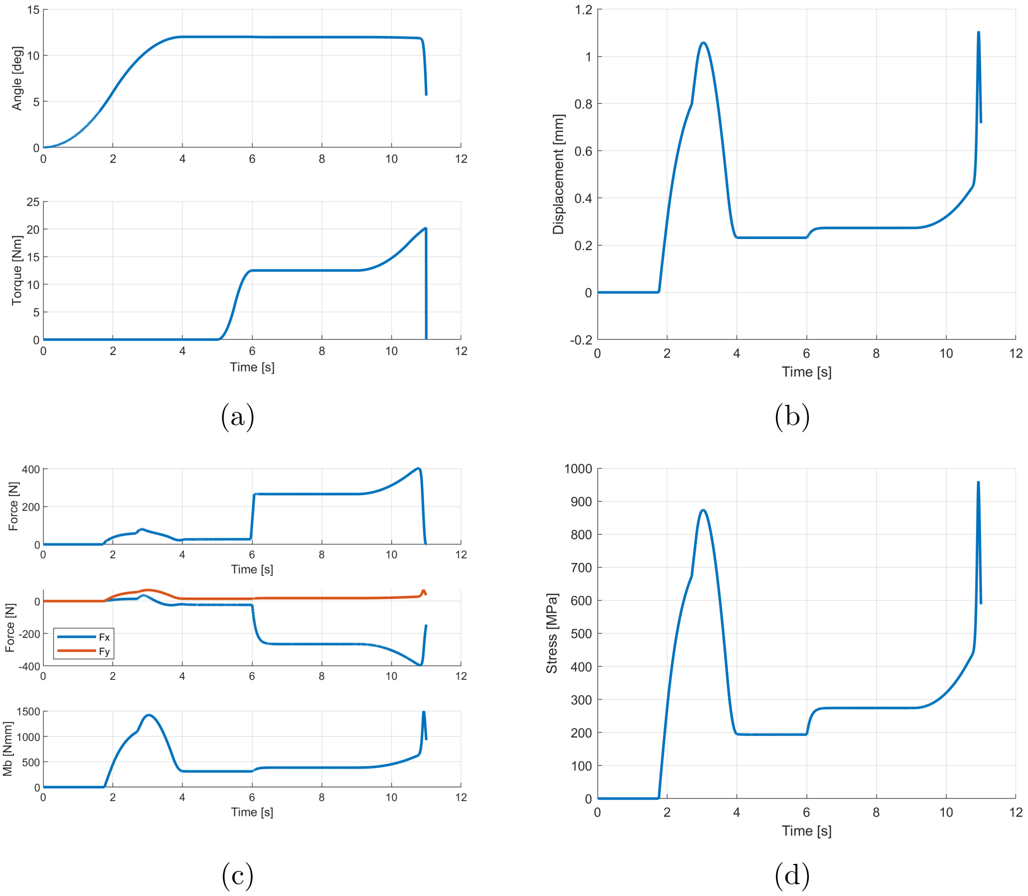

(a) (b)

(c) (d)

Figure 100: Output plots of clamp unit simulation: (a) motion profile, (b) beam tip displacement, (c) force-moment actions exerted on beam, (d) overall stress at beam fixture.

moment at fixture. Given the following data:

- beam length: $L = 23.2\,\mathrm{mm}$;
- beam thickness: $h = 1.4\,\mathrm{mm}$;
- beam width: $w = 5\,\mathrm{mm}$;
- beam tip diameter: $D = 1.8\,\mathrm{mm}$;
- material: X155CrVMo12-1KU (EN ISO 4957:2002);
- Young modulus: $E = 210\,\mathrm{GPa}$;
- Poisson ratio: $\nu = 0.30$;

- yield strength: $S_y = 1380\,\mathrm{MPa}$;

the maximum compression and bending stresses acting at fixture can be estimated as

$$\sigma_c = \frac{F_x}{A} = \frac{F_x}{wh} \tag{C.1}$$

$$\sigma_b = \frac{M_b}{I_b}\frac{h}{2} = \frac{M_b}{\frac{1}{12}wh^3}\frac{h}{2} \tag{C.2}$$

The maximum overall normal stress is thus obtained with

$$\sigma_{\mathrm{eq}} = \max(|\sigma_c|) + \max(|\sigma_b|) = 57.1 + 901.3\mathrm{MPa} \approx 960\,\mathrm{MPa} \tag{C.3}$$

which corresponds to the simulated stress presented in Fig. 100d. From the above analysis, it is apparent that the maximum stresses occur in correspondence of assembling and disassembling phases, rather than in operation mode. Since these two operations are seldom performed in the lifetime of the robot, beam static sizing is assessed as satisfactory with respect to yielding.

Next, it is possible to check if the slender beam is subjected to buckling failure. In the present case, characterized by one extreme fixed and the other free, we can express the Euler's critical load as

$$P_{\mathrm{cr}} = \frac{\pi^2 E I_b}{(2L)^2} = 1100.7\,\mathrm{N} \tag{C.4}$$

Since the maximum compression force is $F_c = 395.8\,\mathrm{N}$, we conclude that a safety factor 2.78 exist against buckling.

Finally, we may test beam resistance with respect to contact pressure. The calculation is performed in accordance to Hertz theory, with particular reference to the cylinder-on-plane contact scenario [72]. Given the sizes of the arising rectangular contact surface

$$a = w \tag{C.5}$$

$$b = \sqrt{\frac{4F(1-\nu^2)D}{\pi E w}} \tag{C.6}$$

the maximum Hertzian pressure is computed as

$$p_{\max} = \frac{2}{\pi}\frac{F}{ab} \tag{C.7}$$

being $F = 404.2\,\mathrm{N}$ the maximum contact force. From this, we can obtain the maximum contact stress through the Von Mises distortion energy approach, which leads to a value

$$\sigma_H = 0.56 p_{\max} = 1017.1\,\mathrm{MPa} \tag{C.8}$$

located at depth $z = 0.71b$ under contact surface. Since the value is inferior to the elastic limit of the material [72], the verification is held satisfactory.

C.2 FEM analysis of parts

In this section, a FEM analysis of the main robot parts is reported. The material used for casing components is Ti-6Al-4V, characterized by yield strength $S_y = 830\,\mathrm{MPa}$; the material used for drive internal components is aluminum 7075 alloy (Ergal), characterized by a yield strength $S_y = 550\,\mathrm{MPa}$.

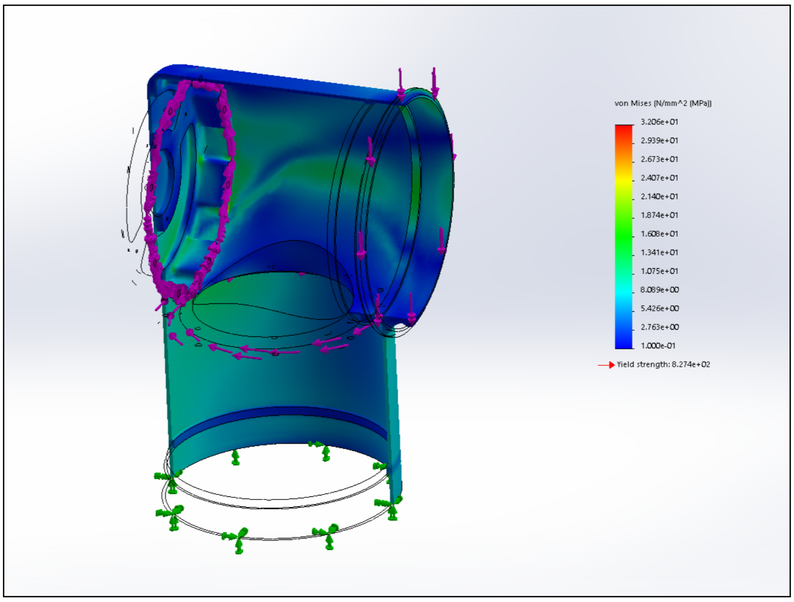

Figure 101: FEM analysis of shoulder casing. Loads: two torques corresponding to maximum value sustainable by CSD-32 gearing $T_G = 151\,\mathrm{N\,m}$; one force corresponding to equivalent weight of downstream arm $P = 90\,\mathrm{N}$.

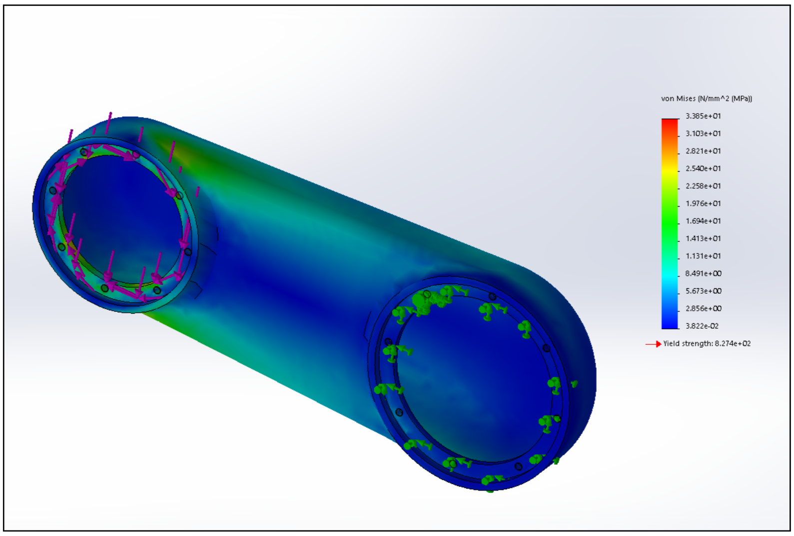

Figure 102: FEM analysis of biceps casing. Loads: one torque corresponding to maximum value sustainable by CSD-32 gearing $T_G = 151\,\mathrm{N\,m}$; one force corresponding to equivalent weight of downstream arm $P = 80\,\mathrm{N}$.

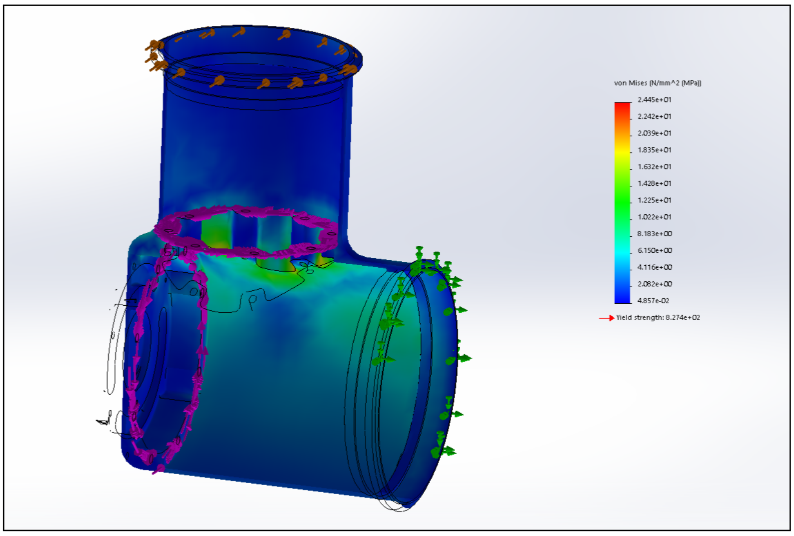

Figure 103: FEM analysis of elbow casing. Loads: two torque corresponding to maximum value sustainable by CSD-25 and CSD-17 gearing, respectively $T_{G1} = 75\,\mathrm{N\,m}$ and $T_{G2} = 27\,\mathrm{N\,m}$; one force corresponding to equivalent weight of downstream arm $P = 45\,\mathrm{N}$.

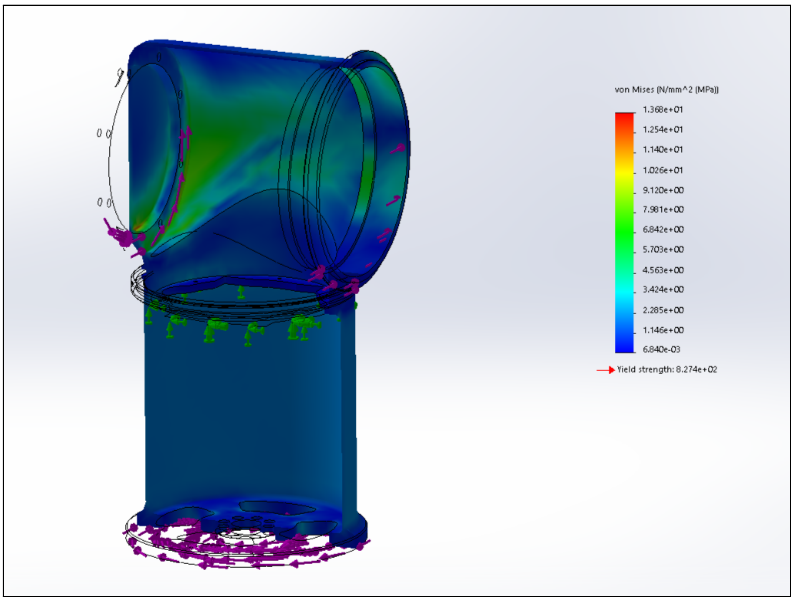

Figure 104: FEM analysis of forearm casing. Loads: two torque corresponding to maximum value sustainable vy CSD-17 gearing $T_G = 27\,\mathrm{N\,m}$; one force corresponding to equivalent weight of downstream arm $P = 28\,\mathrm{N}$.

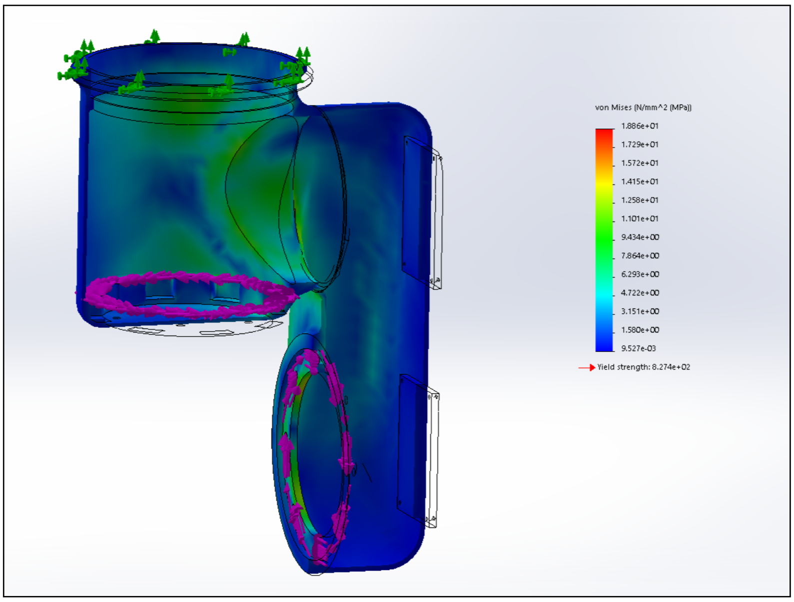

Figure 105: FEM analysis of wrist casing. Loads: two torques corresponding to maximum value sustainable by CSD-17 gearing $T_G = 27\,\mathrm{N\,m}$.

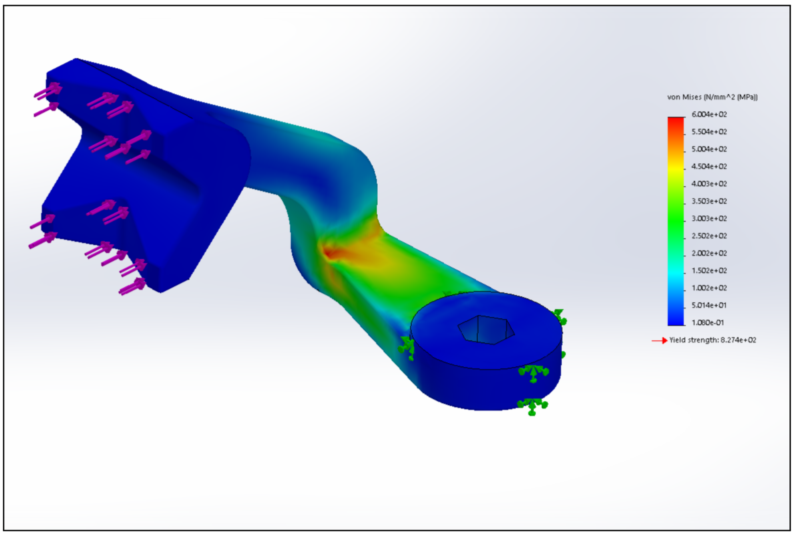

Figure 106: FEM analysis of end-effector claw. Loads: one force corresponding to 1.5x maximum claw grip torque value, i.e. $F = 180\,\mathrm{N}$.

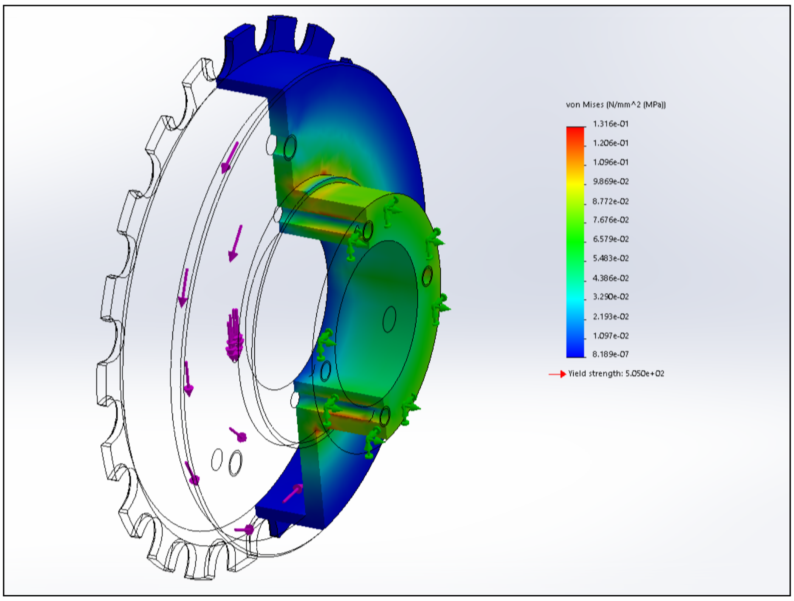

Figure 107: FEM analysis of shoulder Size-90 drive motor shaft. Loads: one torque corresponding to 2x maximum motor torque value, i.e. $T_m = 0.9\,\mathrm{N\,m}$.

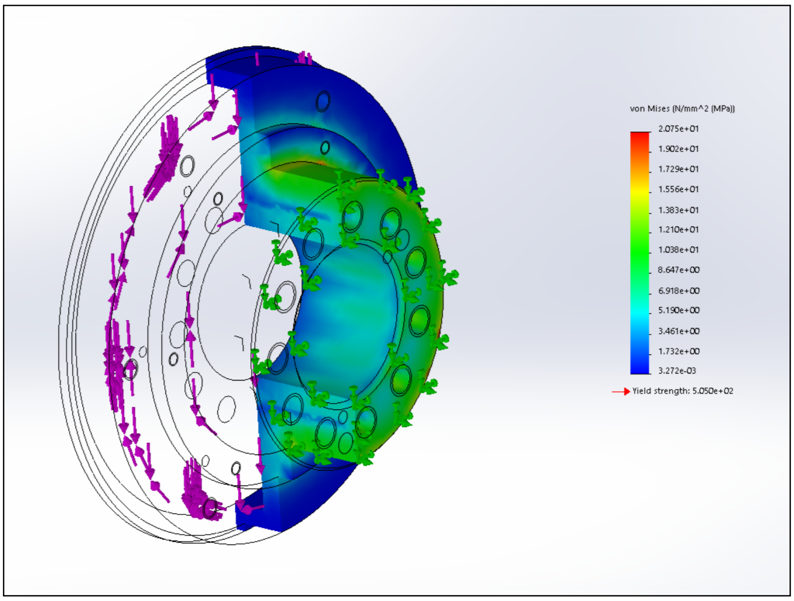

Figure 108: FEM analysis of shoulder Size-90 drive output shaft. Loads: one torque corresponding to CSD-32 gearing maximum sustainable value, i.e. $T_m = 151\,\mathrm{N\,m}$; one force corresponding to equivalent weight of downstream arm $P = 90\,\mathrm{N}$.

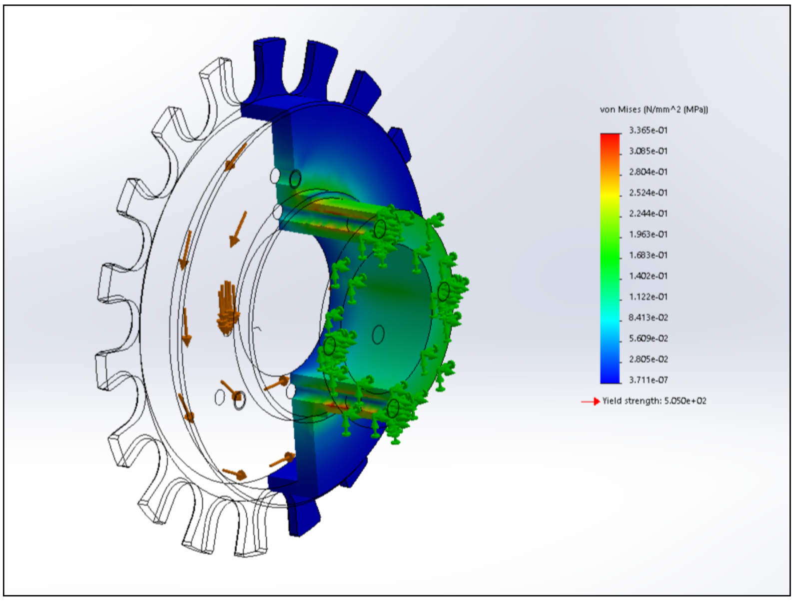

Figure 109: FEM analysis of shoulder Size-60 drive motor shaft. Loads: one torque corresponding to 2x maximum motor torque value, i.e. $T_m = 0.6\,\mathrm{N\,m}$.

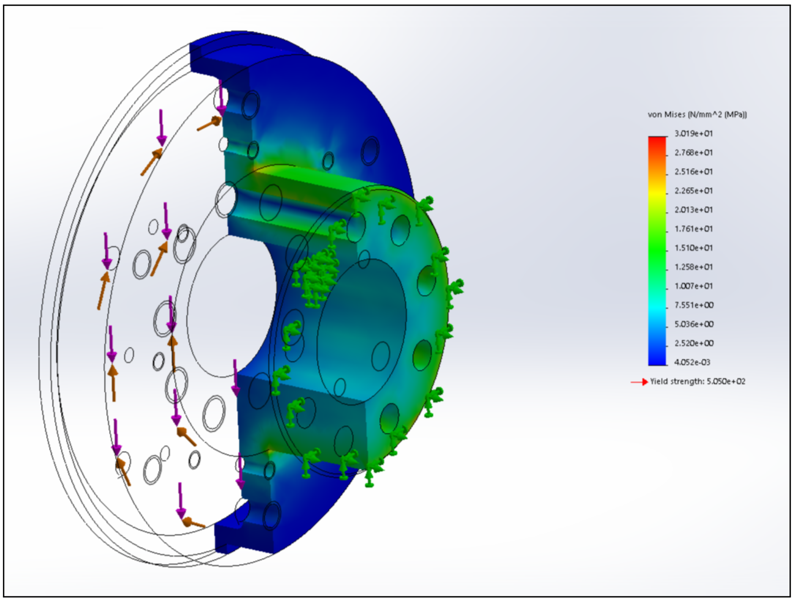

Figure 110: FEM analysis of shoulder Size-60 drive output shaft. Loads: one torque corresponding to CSD-25 gearing maximum sustainable value, i.e. $T_m = 75\,\mathrm{N\,m}$; one force corresponding to equivalent weight of downstream arm $P = 45\,\mathrm{N}$.

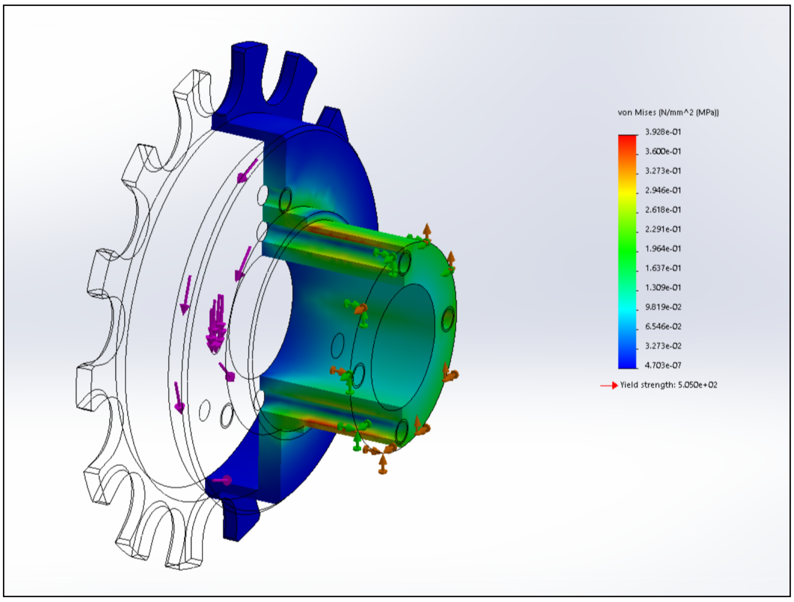

Figure 111: FEM analysis of shoulder Size-45 drive motor shaft. Loads: one torque corresponding to 2x maximum motor torque value, i.e. $T_m = 0.256\,\mathrm{N\,m}$.

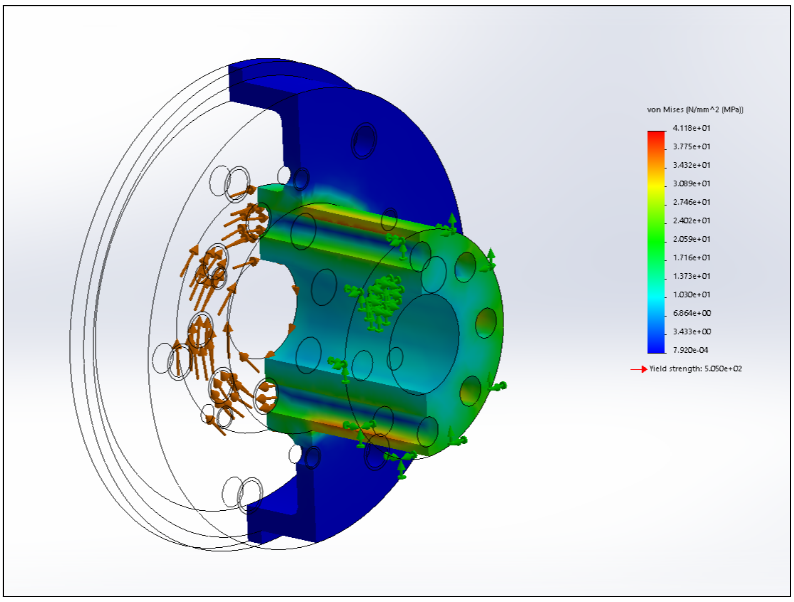

Figure 112: FEM analysis of shoulder Size-45 drive output shaft. Loads: one torque corresponding to CSD-17 gearing maximum sustainable value, i.e. $T_m = 27\,\mathrm{N\,m}$.

Bibliography

[1] ABB. IRB1300. https://new.abb.com/products/robotics/industrial-robots/irb-1300.

[2] O. Altan et al. Evaluation of machinability of aisi 304 and aisi 316 austenitic stainless steels. *Journal of Manufacturing Science and Engineering*, 2017.

[3] J. Angeles. *Fundamentals of robotic mechanical systems*. Springer, 2002.

[4] Angst+Pfister. O-Rings Basic Catalogue, 2009.

[5] ASTM F2026-17. Standard Specification for Polyetheretherketone (PEEK) Polymers for Surgical Implant Applications. Standard, American Society for Testing and Materials International, 2017.

[6] P. Austin and S. Timmerman. *Design and Operation of Clean Rooms*. Business New Publishing Company, 1965.

[7] K. Autumn et al. Adhesive force of a single gecko foot-hair. *Nature*, 405(6787):681–685, 2000.

[8] K. Autumn et al. Evidence for van der waals adhesion in gecko setae. *Proceedings of the National Academy of Sciences*, 99(19):12252–12256, 2002.

[9] Bal Seal Engineering Inc. Chrome plating: a guide for selecting the type of chrome plating for use in contact with Bal Seal spring-energized seals in rotary and reciprocating service. Technical report, Bal Seal Engineering Inc., 2016.

[10] A. Barr, B. Currin, S. Gabriel, and J. Hughes. Smooth interpolation of orientations with angular velocity constraints using quaternions. *ACM Siggraph Computer Graphics*, 26(2):313–320, 1992.

[11] W. Barthlott and C. Neinhuis. Purity of the sacred lotus, or escape from contamination in biological surfaces. *Planta*, 202(1):1–8, 1997.

[12] M. Basarab. Interpolating solid orientations with quaternion curves based on atomic functions and cardinal series. *Science & Military Journal*, 5(2):87, 2010.

[13] G. Betta et al. Understanding the impact of stainless steel finishing methods on cip effectiveness. European Hygienic Engineering and Design Group Yearbook 2017/2018, 2018.

[14] R. Budynas and J. Nisbett. *Shigley's Mechanical Engineering Design*. McGraw-Hill New York, 2011.

[15] P. Chuaybamroong et al. Efficacy of Photocatalytic HEPA Filter on Microorganism Removal. *Indoor Air*, 20(3):246–254, 2010.

[16] J. Craig. *Introduction to robotics: mechanics and control*. Pearson Education, 2009.

[17] B. Crossland. Friction welding. *Contemporary Physics*, 12(6):559–574, 1971.

[18] G. J. Curiel, G. Hauser, and D. A. Timperley. *Hygienic design of equipment for open processing*. European Hygienic Engineering and Design Group, 1996.

[19] E. Dam, M. Koch, and M. Lillholm. *Quaternions, interpolation and animation*, volume 2. Citeseer, 1998.

[20] J. David, R. Graves, and T. Szemplenski. *Handbook of aseptic processing and packaging*, volume 4. Crc Press, 2012.

[21] D. De Renzo. *Corrosion resistant materials handbook*. Noyes Data Corporation, 1985.

[22] T. Deák. Food technologies: sterilization. *Encyclopedia of Food Safety*, 2014.

[23] J. Denavit and R. Hartenberg. A kinematic notation for lower-pair mechanisms based on matrices. *Journal of Applied Mechanics*, 22:215–221, 1955.

[24] D. Denic, I. Randelovic, and G. Miljkovic. Recent trends of linear and angular pseudorandom encoder development. In *International Symposium on Power Electronics, Electrical Drives, Automation and Motion, 2006. SPEEDAM 2006.*, pages 746–750. IEEE, 2006.

[25] Denso. VS-050S2. `https://www.denso-wave.com/en/robot/product/iryou/VS-S2.html`.

[26] EC 10/2011. Plastics Materials and Articles intended to come in Contact with Food. Standard, Eurpean Community, January 2011.

[27] EC 1935/2004. Materials and Articles intended to come into Contact with Food. Standard, Eurpean Community, October 2001.

[28] EC 2023/2006. Good Manufacturing Practice for Materials and Articles intended to come in Contact with Food. Standard, Eurpean Community, December 2006.

[29] B. Eckel and C. Allison. *Thinking in C++*. Prentice Hall, 2004.

[30] N. Elmnasser et al. Pulsed-light system as a novel food decontamination technology: a review. *Canadian journal of microbiology*, 53(7):813–821, 2007.

[31] EN2006/42/EC. Directive 2006/42/EC of the European Parliament and of the Council of 17 May 2006 on machinery. Directive, European Parliament, Council of the European Union, May 2006.

[32] C. Faille et al. Influence of physicochemical properties on the hygienic status of stainless steel with various finishes. *Biofouling*, 15(4):261–274, 2000.

[33] Fanuc. LR-Mate-200iD/7WP. `https://www.fanuc.eu/it/it/robot/robot-filter-page/serie-lrmate/lrmate-200id-7wp`.

[34] FDA 177-2600. Rubber articles intended for repeated use. Standard, FDA, April 2011.

[35] FED-STD-209E. Federal Standard: Airborne Particulate Cleanliness Classes in Cleanrooms and Clean Zones. Standard, US General Services Administration, September 1992.

[36] R. Flitney. *Seals and sealing handbook*. Elsevier, 2011.

[37] A. P Fraise, P. A Lambert, and J.-Y. Maillard. *Russell, Hugo & Ayliffe's Principles and practice of Disinfection, Preservation and Sterilization*. John Wiley & Sons, 2008.

[38] D. Gabay and B. Mercier. A dual algorithm for the solution of nonlinear variational problems via finite element approximation. *Computers & mathematics with applications*, 1976.

[39] A. Ghassaei, P. Choi, and D. Whitaker. The design and optimization of a crank-based leg mechanism. Technical report, Pomona College Department of Physics and Astronomy, 2011.

[40] A. Goldenberg, B. Benhabib, and R. Fenton. A complete generalized solution to the inverse kinematics of robots. *IEEE Journal on Robotics and Automation*, 1(1):14–20, 1985.

[41] M Goldoni et al. Determination of hexavalent chromium in exhaled breath condensate and environmental air among chrome plating workers. *Analytica chimica acta*, 562(2):229–235, 2006.

[42] W.R. Hamilton. On quaternions; or on a new system of imaginaries in algebra. *The London, Edinburgh, and Dublin Philosophical Magazine and Journal of Science*, 25(163):10–13, 1844.

[43] Harmonic Drive AG. Engineering Data CSD-2A Component Sets, 2014.

[44] Y. Hedberg, N. Mazinanian, and I. Wallinder. Compliance tests of stainless steel as a food contact material using the coe test guideline. *Balance*, 204:S20431, 2014.

[45] S. Hillegas and A. Demirci. Inactivation of clostridium sporogenes in clover honey by pulsed uv-light treatment. In *2003 ASAE Annual Meeting*, page 1. American Society of Agricultural and Biological Engineers, 2003.

[46] J. Holah and H. Lelieveld. *Hygienic design of food factories*. Elsevier, 2011.

[47] A. Holder. Functional coatings for automation components in the food and beverage industry. European Hygienic Engineering and Design Group Yearbook 2017/2018, 2018.

[48] D. Holm. *Geometric Mechanics - Part II: Rotating, Translating And Rolling*. World Scientific, 2011.

[49] L. Horve. *Shaft seals for dynamic applications*. Crc Press, 1996.

[50] IEC 60529:1989. Degrees of protection provided by enclosures. Standard, International Electrotechnical Commission, 1989.

[51] Irrlicht. Irrlicht Engine. `https://irrlicht.sourceforge.io/`.

[52] ISO 14159:2002. Safety of machinery — Hygiene requirements for the design of machinery. Standard, International Organization for Standardization, April 2002.

[53] ISO 14644-1:2015. Cleanrooms and associated controlled environments — Part 1: Classification of air cleanliness by particle concentration. Standard, International Organization for Standardization, December 2015.

[54] ISO 29463-1:2017. High efficiency filters and filter media for removing particles from air — Part 1: Classification, performance, testing and marking. Standard, International Organization for Standardization, 2017.

[55] E. Jameson. *Electrical discharge machining*. Society of Manufacturing Engineers, 2001.

[56] P. Jha. *Inverse kinematic analysis of robot manipulators*. PhD thesis, Rourkela Institute of Technology, 2015.

[57] Kawasaki. MS-005N. `https://robotics.kawasaki.com/en1/products/robots/medical/MS005N/`.

[58] M.-J. Kim, M.-S. Kim, and S.Y. Shin. A C^2-continuous b-spline quaternion curve interpolating a given sequence of solid orientations. In *Proceedings Computer Animation*, pages 72–81. IEEE, 1995.

[59] Kuka. KR6-R900-HM. `https://www.kuka.com/-/media/kuka-downloads/imported/6b77eecacfe542d3b736af377562ecaa/0000228379_en.pdf`.

[60] G. Legnani, I. Fassi, A. Tasora, and D. Fusai. A practical algorithm for smooth interpolation between different angular positions. *Mechanism and Machine Theory*, 162, 2021.

[61] G. Legnani, I. Fassi, and A. Visioli. *Robotica industriale*. CEA Casa Editrice Ambrosiana, 2003.

[62] M. Lewan and E. Partington. Food processing equipment construction materials. In H. Lelieveld, J. Holah, and D. Napper, editors, *Hygiene in Food Processing (Second Edition)*, pages 142–154. Woodhead Publishing, second edition edition, 2014.

[63] C. Leyens and M. Peters. *Titanium and titanium alloys: fundamentals and applications*. Wiley Online Library, 2006.

[64] M. Long and H. Rack. Titanium alloys in total joint replacement — materials science perspective. *Biomaterials*, 19(18):1621–1639, 1998.

[65] M. Loomans et al. Experimental investigation into cleanroom contamination build-up when applying reduced ventilation and pressure hierarchy conditions as part of demand controlled filtration. *Building and Environment*, 176:106861, 2020.

[66] Alabdullah M. An investigation on machinability assessment of al-6xn and aisi 316 alloys: an assessment study of machining. *Machining Science and Technology*, 23(2):171–217, 2019.

[67] A. Ma, D. Liu, and X. Zhang. Influence of soft interlayers on fretting fatigue and fretting wear resistance of ti-6al-4v alloy. In *MATEC Web of Conferences*, volume 321. EDP Sciences, 2020.

[68] P. Magnani and G. Ruggeri. *Meccanismi per macchine automatiche.* Utet, 1986.

[69] K. Manickavelan, B. Singh, and N. Sellappan. Design, fabrication and analysis of four bar walking machine based on chebyshev's parallel motion mechanism. *European International Journal of Science and Technology*, 3(8), 2014.

[70] D. Manocha and J. Canny. Efficient inverse kinematics for general 6r manipulators. *IEEE transactions on robotics and automation*, 10(5):648–657, 1994.

[71] K. Mathia. *Robotics for Electronics Manufacturing: Principles and Applications in Cleanroom Automation.* Cambridge university press, 2010.

[72] H. Meerkamm. Technical Pocket Guide, 2014.

[73] C. Menon, M. Murphy, and M. Sitti. Gecko inspired surface climbing robots. In *2004 IEEE International Conference on Robotics and Biomimetics*, pages 431–436. IEEE, 2004.

[74] J. Milledge et al. The cleanability of stainless steel used as a food contact surface: an updated short review. *Food Science & Technology*, 24(4):27–28, 2010.

[75] Å. L. Möller. *International Standards for the Design of Cleanrooms*, chapter 2, pages 21–50. John Wiley & Sons, Ltd, 1999.

[76] P. Murray, Ken S. Rosenthal, and M. Pfaller. *Medical microbiology.* Elsevier Health Sciences, 2020.

[77] Akihiko Nagakubo and Shigeo Hirose. Walking and running of the quadruped wall-climbing robot. In *Proceedings of the 1994 IEEE International Conference on Robotics and Automation*, pages 1005–1012. IEEE, 1994.

[78] M. Neubauer and A. Müller. Smooth orientation path planning with quaternions using b-splines. In *2015 IEEE/RSJ International Conference on Intelligent Robots and Systems (IROS)*, pages 2087–2092. IEEE, 2015.

[79] L. Nie and Q. Huang. Inverse kinematics for 6-dof manipulator by the method of sequential retrieval. In *Proceedings of the International Conference on Mechanical Engineering and Material Science*, pages 255–258, 2012.

[80] Open Cascade. OCCT. https://www.opencascade.com/.

[81] E. Orihuel et al. Mechanical energy balance in surface cleaning by pressurized water spray: a simplified model. European Hygienic Engineering and Design Group Yearbook 2017/2018, 2018.

[82] R. Pack, J. Christopher, and K. Kawamura. A rubbertuator-based structure-climbing inspection robot. In *Proceedings of International Conference on Robotics and Automation*, volume 3, pages 1869–1874. IEEE, 1997.

[83] Christopher C Paige and Michael A Saunders. Solution of sparse indefinite systems of linear equations. *SIAM journal on numerical analysis*, 12(4):617–629, 1975.

[84] Filippo Parma. Design of a robotic gripper for aseptic environment. Master's thesis, University of Parma, 2019.

[85] L. Patnaik and L. Umanand. Kinematics and dynamics of jansen leg mechanism: A bond graph approach. *Simulation Modelling Practice and Theory*, 60:160–169, 2016.

[86] D. Pieper. *The kinematics of manipulators under computer control*. Stanford University, 1969.

[87] M. Ramstorp, M. Gustavsson, and A. Gudmundsson. Particle generation from humans-a method for experimental studie in cleanroom technology. In *10th International Conference on Indoor Air Quality and Climate (Indoor Air 2005)*, pages 1572–1576. Tsinghua University Press, 2005.

[88] R.L Hudson & Company. O-Rings design & material guide, 2011.

[89] F. Romano, S. Milani, and C. Joppolo. Airborne particle and microbiological human emission rate investigation for cleanroom clothing combinations. *Building and Environment*, 180:106967, 2020.

[90] R. Saha, R. Nandi, and B. Saha. Sources and toxicity of hexavalent chromium. *Journal of Coordination Chemistry*, 64(10):1782–1806, 2011.

[91] A. Sakudo. Inactivation methods for prions. *Current issues in molecular biology*, 36(1):23–32, 2020.

[92] B.-Z. Sandler. *Robotics: designing the mechanisms for automated machinery*. Academic Press, 1999.

[93] R. Schutz. Corrosion of titanium and titanium alloys. In *Corrosion: Materials*. ASM International, 2005.

[94] Ahmed A Shabana. *Dynamics of multibody systems*. Cambridge university press, 2003.

[95] Jaichandar Kulandaidaasan Sheba, Edgar Martínez-García, Mohan Rajesh Elara, and Le Tan-Phuc. Design and evaluation of reconfigurable klann mechanism based four legged walking robot. In *2015 10th International Conference on Information, Communications and Signal Processing (ICICS)*, pages 1–5. IEEE, 2015.

[96] K. Shoemake. Animating rotation with quaternion curves. In *Proceedings of the 12th annual conference on Computer graphics and interactive techniques*, pages 245–254, 1985.

[97] K. Shoemake. Quaternion calculus and fast animation. In *ACM SIGGRAPH*, 1987.

[98] L. Shuliang et al. A wall climbing robot with magnetic crawlers for sandblasting. spray-painting and measurement. *High Technology Letters*, 10:86–88, 2000.

[99] B. Siciliano et al. *Robotics: modelling, planning and control*. Springer, 2010.

[100] H. Sinner. *Über das Waschen mit Haushaltswaschmaschinen*. Haus und Heim Verlag, 1960.

[101] W. Smith, J. Hashemi, and F. Presuel-Moreno. *Foundations of materials science and engineering*. Mcgraw-Hill Publishing, 2006.

[102] Stäubli. TX2-60L-Stericlean. `https://www.staubli.com/en/robotics/product-range/industrial-robots/6-axis-robots/tx2-60/`.

[103] A. Tamime. *Cleaning-in-place: dairy, food and beverage operations*, volume 13. John Wiley & Sons, 2009.

[104] A. Tasora. Time integration in Chrono::Engine. White paper, Project Chrono, September 2017.

[105] A. Tasora. Rotations in Chrono::Engine. White paper, Project Chrono, January 2020.

[106] A. Tasora, D. Mangoni, S. Benatti, and R. Garziera. Solving variational inequalities and cone complementarity problems in nonsmooth dynamics using the alternating direction method of multipliers. *International Journal for Numerical Methods in Engineering*, 2021.

[107] A. Tasora, R. Serban, H. Mazhar, et al. Chrono: An open source multi-physics dynamics engine. In T. Kozubek, editor, *High Performance Computing in Science and Engineering – Lecture Notes in Computer Science*, pages 19–49. Springer, 2016.

[108] Tetra Laval Group. Sidel. https://www.sidel.com/en.

[109] The Qt Company. Qt. https://www.qt.io/.

[110] Trelleborg. O-Rings and Backu-up Rings, 2017.

[111] Trelleborg Sealing Solutions. Food & Beverage seals. https://www.trelleborg.com/en/seals/your-industry/food-and-beverage.

[112] J. Troelsen. A 100% hygienic welding procedure. European Hygienic Engineering and Design Group Yearbook 2015/2016, 2016.

[113] user:Jahobr. Omnidirectional wheel and movement. https://commons.wikimedia.org/wiki/File:Robot_omnidirectional_movement_speedvectors.PNG, 2007.

[114] A. Van den Brink and A. Van Schijndel. Improved control of the pressure in a cleanroom environment. In *Building Simulation*, volume 5, pages 61–72. Springer, 2012.

[115] Y. Wang, Y. Li, and L. Zhou. Pressure gradient control and energy-saving operation strategy study on a multi-zone cleanroom. *Procedia Engineering*, 121:1998–2005, 2015.

[116] W. Whyte. *An Introduction to the Design of Clean and Containment Areas*, chapter 1, pages 1–20. John Wiley & Sons, Ltd, 1999.

[117] L. Wu and J. Baghdachi. *Functional polymer coatings: principles, methods, and applications*. John Wiley & Sons, 2015.

Acknowledgements

This thesis gathers the most part of the work that I did during my PhD at University of Parma.

For this important accomplishment, I would first like to thank Prof. Alessandro Tasora, whose invaluable scientific guidance allowed me to achieve the results here presented. I would also like to express a word of thanks to Rossana Borgese, who provided the motivation to this work and supported me with precious insight of the impervious aseptic industrial world.

Finally, my warmest thanks to the lab colleagues Alessandro, Dario, Luca, Matteo and Simone, alongside whom I shared this amazing journey.

Dario Fusai
Parma, 2022